

RELATIONSHIPS BETWEEN METAMORPHISM AND  
DEFORMATION: EXAMPLES ON THE MICRO- TO MACRO-  
SCALE FROM THE WESTERN ALPS  
(CAMUGHERA-MONCUCCO UNIT AND  
MONTE ROSA NAPPE, N' ITALY)

Inauguraldissertation

zur

Erlangung der Würde eines Doktors der Philosophie  
vorgelegt der  
Philosophisch-Naturwissenschaftlichen Fakultät  
der Universität Basel

von

Lukas M. Keller  
aus Schaffhausen (Schweiz)  
Basel, 2004

---

Genehmigt von der Philosophisch-Naturwissenschaftlichen Fakultät

Auf Antrag von

Professor Dr. S. M. Schmid

Basel, den

---

(Dekan)



---

## INTRODUCTION

This combined structural and petrological study is subdivided into *four* chapters. These examine relationships between deformation and metamorphism on various scale and in the upper Penninic-Alps southwest of the Simplon line. The area investigated comprises the Camughera-Moncucco, the Antrona ophiolitic unit as well as the eastern parts of the Monte Rosa nappe.

**CHAPTER 1** addresses the metamorphic history of gneissic units from the upper Penninic-Alps and adjacent the Central Alps, for which it is still a matter of debate whether Barrovian P-T conditions were associated with or without substantial reheating that post-dated high-P overprint and decompression. In the case of the Camughera-Moncucco unit, it was even unclear whether it experienced an earlier high-pressure event at all. This study focuses on metapelites from gneissic units of the upper Penninic-Alps situated southwest of the Simplon line and discusses the nature and the reactions, which change white mica composition and form staurolite, an index mineral typical for the Barrovian metamorphism in the Lepontine dome and adjacent gneissic units of the upper Penninic-Alps situated southwest of the Simplon line. In addition, this study contributes towards the characterization of metamorphic areas that attained Barrovian P-T conditions in general and provides tools, which help to distinguish between prograde- and retrograde- Barrovian metamorphism.

**CHAPTER 2** presents a solution model for white mica, which was constructed in the course of this study. The solution model allows for explaining the P-T dependant systematic variation of white mica compositions and thus contributes to an improvement of white mica as a petrogenetic indicator in metapelites. Furthermore, the solid solution model provides a firm tool for revealing to what extent solid solution between phengite and paragonite influences the formation of other phases during decompression of pelitic rocks (see chapter 1).

Studies on the derivation of pressure-temperature-deformation paths for a specific area of the earth's crust, such as presented here, may help solving fundamental problems in orogeny but they do not consider processes, which are directly linked to deformation and associated metamorphism of a certain piece of rock. During the formation of faulted rocks such processes commonly include chemical alteration or metasomatic transformations, which are normally accompanied by fluid flow.

**CHAPTER 3** enlightens processes related to mineralogical and chemical transformations during syn-metamorphic shear zone formation. Among other findings the analysis gives insight into the chemical evolution of pore fluids during eclogite facies overprint of earlier metapelites and adds to the discussion of aluminium mobility during metamorphism.

**CHAPTER 4** is a structural study focusing on the area southeast of the Simplon line. This area is characterized by a metamorphic zonation with an eastward increase in metamorphic grade. The more western parts reached greenschist facies conditions during decompression upon a high-pressure stage.

---

In contrary, the more eastern parts reached Barrovian P-T conditions upon decompression from a high-pressure stage. This metamorphic pattern implies that the P-T history related to an individual deformation phase may be different from place to place. With the purpose of revealing relationships between deformation and regional metamorphic pattern this study subdivides macroscopic structural elements into deformation phases and correlates them with individual mineral assemblages obtained from microstructural observations in metapelites. From this correlation, and by using phase equilibrium diagrams, we obtain the P-T history corresponding to an individual deformation phase and conclude on the effect of deformation on the metamorphic evolution of metapelitic rocks on a regional scale.

This chapter 4 also contributes to the understanding of the nature of latestage backfolding and normal and/or strike slip faulting, which occurred in the Western Alps. The necessary prerequisite for such an understanding is the better knowledge of the location of the trace of the Vanzone antiform in the vicinity of the Simplon normal fault and the Centovalli fault zone. Hence, this study presents new structural data associated with the major Vanzone antiform. These allow for conclusions on the nature and the age of late stage backfolding and normal and/or strike slip faulting.

---

## **ORGANISATION OF THE THESIS AND CONTRIBUTIONS OF THE CO-AUTHORS**

This thesis is a “cumulative dissertation” and consists of four complete manuscripts. These manuscripts form four chapters of the thesis. The manuscripts have all been submitted to different international journals of geosciences (see below). One of them have been accepted by now. The text below outlines the contributions of the various co-authors.

### **CHAPTER 1**

#### **The phengite-paragonite solvus II: Influence of solid solution (phengite-paragonite) on the phase relations in metapelites during decompression (Monte Rosa nappe and Camughera – Moncucco unit, Western Alps).**

by L. M. Keller, R. Abart, S. M. Schmid and C. De Capitani

submitted to *Journal of petrology*

The first author did all the fieldwork and sampling necessary for performing this study. He also performed all microprobe analysis, thermodynamic calculations, figures and tables. Finally, he also wrote the complete manuscript.

The second- and third- authors carefully reviewed the manuscript. They also made some very useful suggestions and provided good discussions. This of course improved the manuscript. The fourth author helped with the thermodynamic calculations, microprobe analysis and also provided good discussion.

### **CHAPTER 2**

#### **The phengite-paragonite solvus I: A quaternary solution model for white micas based on natural coexisting phengite-paragonite pairs.**

by L. M. Keller, C. De Capitani and R. Abart

submitted to *Journal of petrology*

The first author did all the literature work, all the calculations and prepared all the figures and tables. The first author also wrote a first version of the complete manuscript. The second and third author carefully reviewed the manuscript and made very good suggestions, which improved the manuscript.

### **CHAPTER 3**

#### **Deformation, mass transfer and mineral reactions in an eclogite facies shear zone in a polymetamorphic metapelite (Monte Rosa nappe, western Alps)**

by L. M. Keller, R. Abart, H. Stünitz and C. De Capitani

*Journal of metamorphic geology*, 2004, 22, 97-118

The first author did all the sampling necessary for performing this study. He also performed all microprobe analysis, mass balance calculations, density measurements, thermodynamic calculations, figures and tables. The first author also wrote a first draft of the complete manuscript.

The second- and third- authors carefully reviewed the manuscript. They also made fundamental suggestions and provided good discussions, all of which substantially improved the manuscript. The third author also contributed a text section which deals with the microstructural aspects of the study. The

---

forth author helped with the thermodynamic calculations, microprobe analysis and also provided good discussion.

#### **CHAPTER 4**

### **Structural and metamorphic evolution of the Camughera-Moncucco- and the Monte Rosa- units southwest of the Simplon line**

by L. M. Keller, M. Hess, B. Fügenschuh and S. M. Schmid

submitted to *Eclogae geol. Helv.*

The first author did all the fieldwork and sampling necessary for performing this study. He also performed all microprobe analysis, thermodynamic calculations, figures and tables. Finally, he also wrote a complete first version of the manuscript.

The second author provided the fission-track age data, which give substantial support to the interpretation of major structural elements in the study area.

The third- and fourth- authors carefully reviewed the manuscript. They also made some very good suggestions and provided good discussions. These contributions substantially improved the manuscript

---

## ACKNOWLEDGMENTS

This study has been designed under the supervision of Stefan Schmid, Rainer Abart, Christian De Capitani and Holger Stünitz. Stefan Schmid supervised my fieldwork and introduced me to the problems concerning the regional geology. He explained many aspects of structural geology to me and he fundamentally helped with the interpretation of key outcrops. Thereby I gained additional knowledge in structural mapping and fieldwork in general. He also carefully reviewed the manuscripts dealing with regional aspects of metamorphic and structural geology. His criticism and suggestions led to discussions, which clarified many problems in terms of regional geology. Rainer Abart deeply participated in all aspects concerning processes in metamorphic petrology. He gave many useful methodical advices and also thoroughly reviewed the manuscripts dealing with metamorphic petrology and mineralogy. His very constructive criticism and stimulating suggestions clarified many problems and fundamentally improved the study. During the cooperation with Rainer Abart I improved my perception of metamorphic petrology. Christian De Capitani helped with the thermodynamic calculations and provided the idea of constructing a solution model for white mica. He was very cooperative and contributed many good discussions on metamorphism. Holger Stünitz was deeply involved in aspects dealing with the relationship between deformation and metamorphism. He gave good advice and provided good discussions about the interrelation between deformation and metamorphism. He carefully reviewed a manuscript, made very good suggestions and contributed a text section dealing with microstructural aspects. All four supervisors are deeply thanked for their help and cooperation.

Bernhard Fügenschuh was very interested in the tectonic aspects of the project and his discussions were always constructive. He also partly reviewed a manuscript and made very useful suggestions. Martin Engi provided advice and discussions, which very much helped during the start of the study. Alfons Berger provided discussions and also performed the micro-Raman analyses. Maurus Hess helped sampling the shear zone in the Monte Rosa nappe. W. Stern and H. Hürlimann from the Geochemical laboratory of Basel University performed the whole rock chemical analyses. Katy Waite helped with the microprobe analyses and made a first correction of the English writing. Furthermore I greatly acknowledge the contributions of the members of the Basel “Western Alps group” and “Monte Rosa group” (Romain Bousquet, Stefan Bucher, Stefano Ceriani and Julia Kramer), which helped clarifying my own thinking. A big thank also goes to Willi Tschuddin for supplying the thin sections in such a short time. After all I deeply thank Petra for all the beautiful things beside geology.

---

## CONTENTS

<b>1. The phengite-paragonite solvus II: Influence of solid solution (phengite-paragonite) on the phase relations in metapelites during decompression (Monte Rosa nappe and Camughera – Moncucco unit, Western Alps).</b>	
1.1 Abstract	1
1.2 Introduction	2
1.2 Geological setting	3
1.2.1 Tectonic context	3
1.2.2 High-pressure metamorphism	3
1.2.3 Low-pressure metamorphism	4
1.3 Methods of investigation	5
1.3.1 Petrography	5
1.3.2 Equilibrium phase diagrams	5
1.3.3 Whole rock chemistry	5
1.4 Sample description	6
1.4.1 Samples 1 and 4	7
1.4.2 Sample LK 48	8
1.4.3 Sample LK 13	11
1.4.4 Sample LK 45	11
1.4.5 Sample LK 76	12
1.5 Successive mineral assemblages and white mica compositions in metapelites	12
1.6 Equilibrium phase diagrams	13
1.6.1 Bulk rock chemistry	13
1.6.2 Stable assemblages and end-member isopleths of phe of the samples LK48, 4, 76	14
1.6.3 Stable assemblages in sample LK13	16
1.6.4 Stable assemblages in sample LK45	17
1.7 Mineral reactions	18
1.8 Discussion	21
1.8.1 Peak metamorphic conditions	21
1.8.2 P-T paths	22
1.8.3 End-member isopleths of phengite	23
1.8.4 Effects of decompression on the sodium content in phengite	24
1.8.5 Regional implication	25
1.9 Conclusions	25
1.10 Acknowledgments	26
1.11 References	27
<b>2. The phengite-paragonite solvus I: A quaternary solution model for white micas based on natural coexisting phengite-paragonite pairs.</b>	
2.1 Abstract	31
2.2 Introduction	32
2.3 Input data	33
2.3.1 Published solid solution models based on experimental data	33
2.3.2 End-member calculation of natural coexisting Paragonite – Phengite pairs	33
2.3.3 Phengite composition	34
2.3.4 Paragonite composition	35
2.4 Calculation procedure	35
2.4.1 Chemical potential expression	36
2.5 Comparison between the model Predictions and Observational data	38
2.6 Comparing our solution model with other models, application and discussion	41
2.6.1 Comparing our solution model with other models	41
2.6.2 Limits of the presented solution model	42
2.6.3 Application	42
2.6.4 Effects of pressure and temperature on the composition of phengite	43
2.7 Conclusion	45
2.8 Acknowledgments	45
2.9 References	46
<b>3. Deformation, mass transfer and mineral reactions in an eclogite facies shear zone in a polymetamorphic metapelite (Monte Rosa nappe, western Alps)</b>	
3.1 Abstract	50
3.2 Introduction	51
3.3 Geological setting	52
3.3.1 Pre-Alpine metamorphism	52
3.3.2 Alpine metamorphism	53
3.4 Geological framework of the investigated Shear zone	53

3.5 Methods of investigation	55
3.5.1 Strain estimates	55
3.5.2 Modal analysis and petrography	55
3.5.3 Whole rock chemistry	55
3.6 Microstructures and Mineral assemblages of the Samples	57
3.6.1 The protolith (sample 1)	57
3.6.2 Deformed metapelites (samples 2, 3, 4)	57
3.7 Mineral chemistry	60
3.7.1 Biotite	60
3.7.2 Plagioclase	61
3.7.3 White mica	62
3.7.4 Garnet	62
3.8 Physical conditions during metamorphism	62
3.8.1 Fluid-absent versus fluid-present metamorphism	62
3.8.2 Garnet growth	64
3.9 Mass transfer and reaction progress	65
3.9.1 Model mode	65
3.9.2 Volume reference frame	66
3.9.3 Mass transfer and bulk reactions	67
3.9.4 Mineral reactions in a closed system	70
3.9.5 Relationship between mass transfer and reaction progress	71
3.10 Discussion	72
3.10.1 Component mobility	73
3.10.2 Effects of the reaction on the deformation	74
3.10.3 Regional aspect	75
3.11 Conclusions	75
3.12 Appendix	76
3.12.1 Thermodynamic calculations	76
3.12.2 Quantification of the model mode	76
3.12.3 The method of Gresens and overall reactions	77
3.12.4 Overall reaction	77
3.12.5 Definition of mineral formulae used to quantify the reaction progress	77
3.12.6 Estimation of mass transfer from diff. between calc. and observed modal changes	78
3.13 Acknowledgments	78
References	79
<b>4. Structural and metamorphic evolution of the Camughera-Moncucco- and the Monte Rosa- units southwest of the Simplon line</b>	
4.1 Abstract	86
4.2 Introduction	87
4.3 Geological setting	89
4.4 Mapping of the Boundaries between tectonic units	89
4.5 Lithostratigraphy of the Camughera-Moncucco unit and the Antrona ophiolites	91
4.5.1 Camughera-Moncucco unit	91
4.5.2 Antrona ophiolite complex	92
4.6 Deformation history	93
4.6.1 D1/D2 structures	94
4.6.2 D3 structures and major folds	94
4.6.3 D4 structures	99
4.7 Axial traces and kinematic significance of major D4 folds	99
4.7.1 The eastern continuation of the major D4 Vanzone antiform within the CM unit	99
4.7.2 Major D4 folds mapped in Bognanco valley	101
4.7.3 Evidence for dextrally transpressive shearing during D4 deformation	101
4.8 Compilation of the orientation of stretching lineations and change in the kinematics of shearing	102
4.9 Late stage Brittle deformation associated with the Centovalli fault zone	106
4.10 Early stages of metamorphism related to top-N nappe stacking during D1/D2 deformation	106
4.11 Correlation between deformation and metamorphism during polyphase deformation	107
4.12 Tectonic and metamorphic evolution of the working area in a regional context	111
4.13 Chronology of Alpine structures	113
4.13.1 Top N-NW thrusting and nappe stacking (D1/D2)	113
4.13.2 First phase of backfolding (D3)	113
4.13.3 Second phase of backfolding and normal faulting along the Simplon line (D4)	116
4.14 Discussion	118
4.14.1 The eastwards continuation of the Simplon normal fault	118
4.15 Conclusions	120
4.16 Acknowledgments	121
4.17 References	122
4.18 Appendix	128

---

<b>5. Overall conclusions</b>	130
5.1 Conclusions concerning the history of deformation and metamorphism.	
5.1.1 D1/D2 Deformation	130
5.1.2 D3 Deformation	130
5.1.3 D4 Deformation	130
5.2 Conclusions regarding deformation, mass transfer and mineral reactions in a D1/D2 shear zone	130
5.3 The eastwards continuation of the Moncucco-Camughera unit	131
5.4 Conclusions regarding the regional metamorphism in general	131
5.5 Conclusions regarding a new solution model for white micas	132



# **1. THE PHENGITE-PARAGONITE SOLVUS II: INFLUENCE OF SOLID SOLUTION (PHENGITE-PARAGONITE) ON THE PHASE RELATIONS IN METAPELITES DURING DECOMPRESSION (MONTE ROSA NAPPE AND CAMUGHERA – MONCUCCO UNIT, WESTERN ALPS).**

L. M. Keller, R. Abart, S. M. Schmid and C. De Capitani

Department of Earth Sciences, Basel University, Bernoullistrasse 32, CH-4056 Basel

## **1.1 ABSTRACT**

Metapelites from the eastern part of the Monte Rosa nappe and the Camughera-Moncucco unit, both of them situated in the upper Penninic units southwest of the Simplon line, were investigated using microstructural relationships and equilibrium phase diagrams. The units under consideration experienced pre-Alpine amphibolite facies and went through a complex metamorphic evolution during the Alpine orogeny. Peak pressures during an early Alpine high-pressure stage were similar in the Monte Rosa nappe and Camughera-Moncucco unit at 12.5-16 kbar. A pronounced thermal gradient is indicated for the retrograde amphibolite facies overprint from the fact that decompression paths went through the chlorite, biotite, plagioclase stability field in the Monte Rosa nappe, through the staurolite in the easternmost Monte Rosa nappe and in the Camughera-Moncucco unit and through the sillimanite field in the eastern most Camughera-Moncucco unit.

In high-Al metapelites the initial formation of staurolite is related to continuous paragonite breakdown and associated formation of biotite. In the course of this reaction phengite becomes successively sodium enriched. In contrast in low-Al metapelites the initial staurolite formation occurs via the continuous breakdown of sodium-rich phengite. In both low- and high-Al- metapelites the largest volume of staurolite is formed during the continuous breakdown of sodium-rich phengite below P-T conditions of about 7-9.5 kbar at 600-650°C. During this reaction phengite becomes successively potassium enriched as sodium from phengite is used to form the albite component in plagioclase. For “normal” pelitic chemistries, phengite becomes Na-enriched during decompression through the breakdown of paragonite on an isothermal decompression path. The Na content in phengite reaches its maximum when paragonite is entirely consumed. During further decompression the paragonite component in phengite decreases again because Na is preferentially incorporated into the albite component of plagioclase.

*Keywords:* metapelites; white mica; high-pressure; equilibrium diagrams; Western Alps

## 1.2 INTRODUCTION

Regional Barrovian type metamorphism is commonly characterized by a sequence of mineral zones, which mimic progressive metamorphism from chlorite through biotite, staurolite, kyanite and sillimanite zones (Barrow, 1912). These mineral zones have been found in many areas and are typical for medium-pressure metapelites. Barrovian P-T conditions attained during prograde metamorphism along a medium pressure geotherm is for example reported from the Lukmanier in the northern realm of the central Alps of the classical Alpine collisional orogen (Fox, 1975) (P-T path 1 in Fig. 1). In this case the mineral zones characterize progressive metamorphism from Cld+Chl+Ky through St+Cld+Chl+Ky, Bt+St+Cld+Chl+Ky and Bt+St+Grt+Chl+Ky zones (Fox, 1975). However, Barrovian type metamorphism may also occur during decompression from a precursory high-pressure stage in collisional mountain belts as is reported for the southern parts of Adula nappe in the central Alps (Heinrich, 1986; Meyre, 1997; Meyre, 1999; Nagel et al., 2002) (P-T path 2 in Fig. 1). Barrovian P-T conditions attained during decompression are also reported from the southern Koralpe (eastern Alps) (Gregurek et al., 1997). In the case of the central Alps (Adula nappe) Nagel et al. (2002) propose the formation of index minerals such as staurolite, kyanite and sillimanite during approximately isothermal decompression. However, other workers suggest a heating pulse during a later stage of Tertiary metamorphism in southern parts Lepontine area (e.g. Becker, 1993; Engi et al., 1995; Todd & Engi, 1997). The modelling result of Engi et al. (2001b) suggest P-T paths from the Central Alps, which involve a heating stage after decompression, induced by accretion of radioactive continental crustal

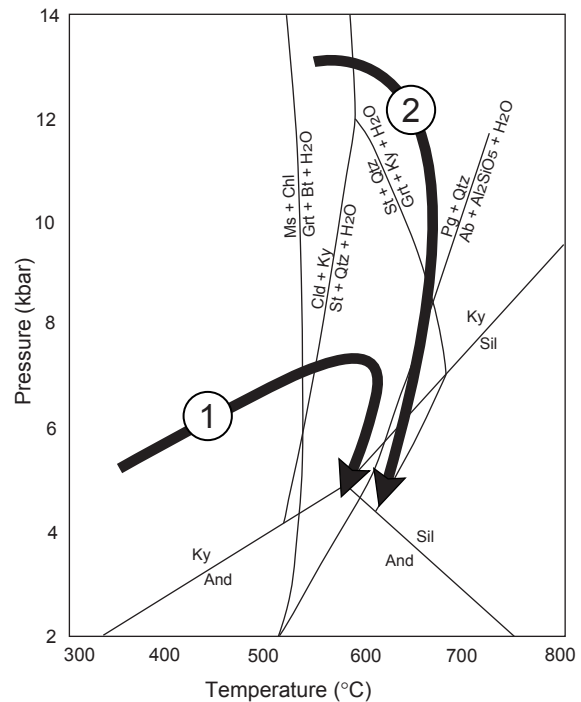


Fig. 1 Pressure-temperature grid and mineral reactions modified after Bucher & Frey (1994). The selected equilibria and P-T paths show that mineral assemblages sequences leading to Barrovian P-T conditions likely depend on the P-T history of a particular unit or area.

fragments. Hence, it is still a matter of debate whether Barrovian P-T conditions in the more southern part of the Central Alps and adjacent gneissic units of the upper Penninic-Alps are associated with or without substantial reheating that post-dates decompression. In order to discuss the nature of Barrovian metamorphism in the light of the above mentioned controversy this study focuses on gneissic units of the upper Penninic-Alps situated southwest of the Simplon line (Fig. 1), where the metamorphic characteristics are similar to that of the Adula nappe. In addition, this study contributes towards the characterization of metamorphic areas that attained Barrovian P-T conditions in general. Hence, it provides tools, which help to distinguish between prograde- and retrograde- Barrovian metamorphism. In the case of gneissic unit under consideration, the Camughera-Moncucco unit, it is even unclear whether it experienced an earlier high-pressure

event or not.

In order to unravel the metamorphic history of the gneissic units southwest of the Simplon line a sequence of stable mineral assemblages will be established on the basis of microstructural relationships. In addition mineral inclusions, as well as the variation of the paragonite and celadonite content of phengite, will be used to unravel the metamorphic history. Based on the solution model for white mica, introduced in part I, equilibrium phase diagrams and corresponding end-member isopleths of phengite are calculated. Phase relations will be investigated for different bulk rock compositions, in order to test the sensitivity of mineral assemblages to bulk rock compositions.

Our findings on the systematic variation of white mica compositions as a function of P and T will improve the use of white mica as a petrogenetic indicator in metapelites. Furthermore, it is important to know to what extent solution between phengite and paragonite influences the formation of other phases during decompression of pelitic rocks, i.e. what kind of reactions change white mica composition and form the index minerals typical for the Barrovian metamorphism in the Lepontine dome (Niggli & Niggli, 1965) and adjacent gneissic units of the upper Penninic-Alps situated southwest of the Simplon line (Merlyn, 1977). This study presents a series of mineral assemblages and corresponding white mica compositions reaching from a pre-Alpine metamorphic stage over the early Alpine high-pressure stage to subsequent stages during decompression. The mineral reactions leading to the compositional variation of phengite and the formation of index minerals will be inferred on the base of the solution model for white mica introduced in part I, combined with equilibrium

phase diagrams, end-member isopleths of phengite and mineral abundance isopleths

## 1.2 GEOLOGICAL SETTING

### 1.2.1 Tectonic context

Monte Rosa nappe, Antrona ophiolites and Camughera-Moncucco gneissic unit belong to the upper Penninic nappe pile west of the Lepontine dome and southeast of the Simplon line (Fig. 2). Due to S-vergent backfolding and associated axial plunge towards SW the former nappe pile can be seen as a distorted profile in map view (e.g. KLEIN, 1978; MILNES et al., 1981; ESCHER et al., 1997). The Camughera-Moncucco gneissic unit is the structurally deepest unit of this part of the western Alps, being situated in the core of the Vanzone antiform (e.g. Bearth, 1957) (Fig. 2). The so-called "Salarioli-Mulde" a series of aligned lenses of marbles and quartzites of possibly Mesozoic age separates the Camughera zone from the Moncucco zone (Bearth, 1939, 1956). The Camughera-Moncucco unit is mainly composed of pre-Mesozoic paragneisses and orthogneisses as well as a larger body of peridotite (e.g. Bearth, 1956; Laduron, 1976; Merlyn, 1977). The Antrona ophiolites separate the Camughera-Moncucco it from the Monte Rosa nappe, which itself is overlain by the Zermatt-Saas ophiolites (Fig. 2). The pre-Alpine protoliths of the Monte Rosa nappe consist of metapelitic paragneisses, intruded by post-Variscan granites at around 310 Ma and 270 Ma (HUNZIKER, 1970; FREY et al., 1976).

### 1.2.2 High-pressure metamorphism

According to the new metamorphic map of the Alps (Frey et al., 1999) the Zermatt-Saas ophiolites, Monte Rosa nappe and Antrona ophiolites all have undergone a regional high-

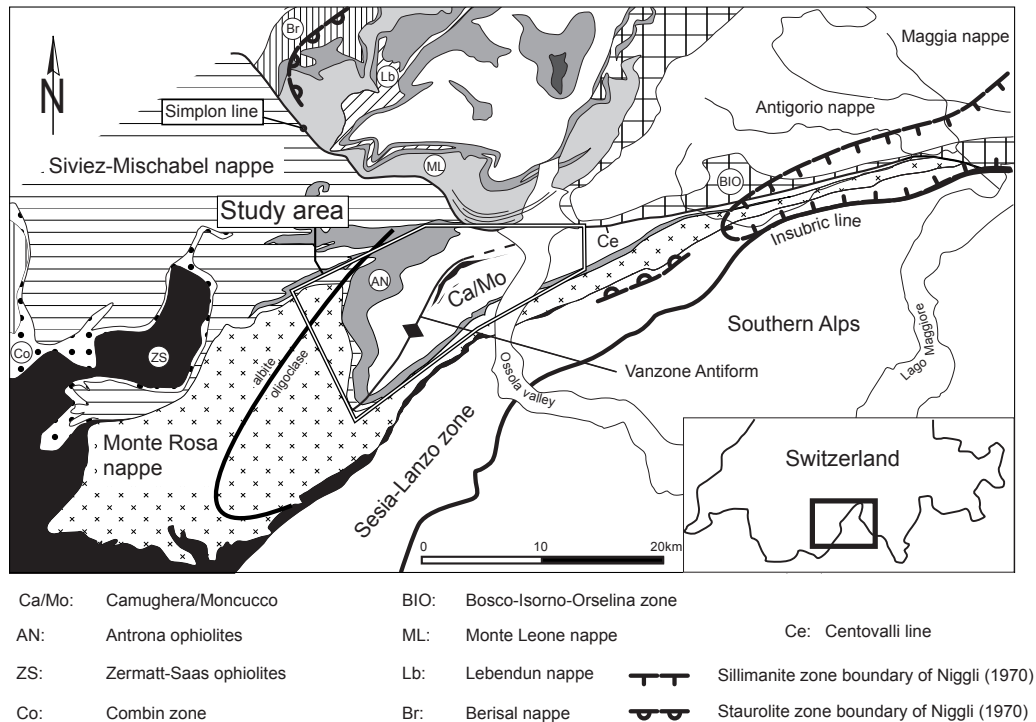


Fig. 2 Modified tectonic map of the western part of the Penninic Alps after Spicher (1976) and Keller & Schmid (2001) showing the outline of the study area and the mineral zone boundaries characteristic for the Barrovian metamorphism in the study area. Sillimanite and staurolite mineral zone boundaries after Niggli (1970). Albite-oligoclase isograde after Bearth (1958).

pressure metamorphism. Recent isotopic studies indicate an Early to Middle Eocene age for the high-pressure stage in the Zermatt-Saas ophiolites (Bowtell et al., 1994; Rubatto et al., 1997).

Concerning high-pressure metamorphism in the internal crystalline massifs (Dora Maira) ages ranging from the middle Eocene to the early Oligocene have been obtained (e.g. Duchene et al., 1997). Regarding P-T estimates for the high-pressure stage in the Monte Rosa nappe Dal Piaz & Lombardo (1986) derived (garnet-clinopyroxene thermometry) pressures in the range between 8-10 kbar and <14 kbar, at temperatures of 440-530°C. Also for the high-pressure stage, but based on the Grt-Phe geothermometer and the Si content in phengite, Borghi et al., (1996) derived P-T estimates in the range of 518-546°C at 11-14 kbar. Somewhat higher pressures (16 kbar at 500°C) are obtained by Chopin & Monié (1984) for an atypical mineral assemblage found in a pelitic

sample from the Monte Rosa nappe. For the high-pressure stage of the Antrona ophiolites Colombi & Pfeiffer (1986) inferred P-T conditions of >14 kbar at 500-700°C.

### 1.2.3 Low-pressure metamorphism

During a late stage of Alpine metamorphism the eastern part of the Monte Rosa nappe, the Antrona ophiolites and the Camughera-Moncucco unit experienced amphibolite facies conditions whereas the western part of the Monte Rosa nappe only reached the greenschist facies (Frey et al., 1999). This metamorphic zonation was first recognized by Bearth (1958) who mapped the albite-oligoclase boundary in the study area (Fig. 2) indicating a metamorphic field gradient with temperatures increasing from the west to the east. The temperatures estimated for the Antrona ophiolites range between 600-700°C (Colombi,

Table 1 Bulk rock compositions of the investigated samples and published average rock compositions of high-grade metapelites

	LK13	LK45	LK48	LK76	1	4	Medium- and high-grade pelites of Shaw (1956)	Amphibolite facies pelites of Ague (1991)
SiO <sub>2</sub>	57.17	44.37	59.47	60.63	49.04	59.04	60.26	56.25
Al <sub>2</sub> O <sub>3</sub>	19.25	32.41	22.38	20.55	29.84	21.96	20.64	20.18
FeO							5.49	
Fe <sub>2</sub> O <sub>3</sub>	9.10	11.11	6.42	8.45	8.60	7.78	1.41	9.31
MnO	0.10	0.12	0.09	0.07	0.15	0.11		0.18
MgO	3.93	2.04	1.88	2.60	2.05	2.01	1.93	3.23
CaO	1.34	0.35	0.21	0.35	0.33	0.50	0.52	1.54
Na <sub>2</sub> O	2.33	1.00	1.13	0.66	1.41	1.29	1.38	1.8
K <sub>2</sub> O	3.31	4.70	4.71	3.61	5.00	3.94	3.72	4.02
TiO <sub>2</sub>	0.90	1.08	0.89	0.94	1.07	0.84	1.05	1.05
P <sub>2</sub> O <sub>5</sub>	0.11	0.07	0.15	0.08	0.10	0.14		
Sum	97.54	97.25	97.33	97.94	97.59	97.60	96.4	97.56

1989, his Fig. 6-2E). Concerning the Camughera-Moncucco unit no quantitative P-T estimates are available so far and it is not known whether this unit underwent an early high-pressure metamorphic stage at all. Within the Camughera-Moncucco unit several occurrences of staurolite and kyanite are known (Merlyn, 1977, his Fig. 14). For the Monte Rosa nappe Engi et al. (2001a) provide monazite ages that are interpreted to date an early stage during decompression between 38-32 Ma ago. The same study also estimated *P-T* conditions of about 11 kbar at 650°C, interpreted to represent partial re-equilibration upon decompression.

## 1.3 METHODS OF INVESTIGATION

### 1.3.1 Petrography

The mineral compositions were determined with a JEOL JXA-8600 electron microprobe at 15kV acceleration voltage and 10 nA sample current and correcting with a PROZA routine. The mol fraction of end-members muscovite, paragonite, Mg-celadonite and Fe-celadonite in white mica were calculated by applying the method of least squares for the same set of equations as introduced

in part I.

### 1.3.2 Equilibrium phase diagrams

Equilibrium phase diagrams were calculated for the system K<sub>2</sub>O-Na<sub>2</sub>O-CaO-FeO-MgO-Al<sub>2</sub>O<sub>3</sub>-SiO<sub>2</sub>-H<sub>2</sub>O with the computer program DOMINO (De Capitani & Brown, 1987; De Capitani, 1994), using the database of Berman (1988, update 92). For staurolite and chloritoid the thermodynamic data of Nagel et al. (2002) was used. For garnet the solution model of Berman (1990) was used. Concerning biotite binary (Phl, Ann) ideal mixing on site (3) was assumed. For chlorite the solution model of Hunziker (2003), for feldspar the solution model of Fuhrman & Lindsley (1988), for omphacite we use the solution model of Meyre et al. (1997) and for staurolite the solution model of Nagel et al. (2002) was used. The solution model introduced in part I of this issue was used for white mica. Concerning chloritoid binary ideal mixing on site (1) was assumed.

### 1.3.3 Whole rock chemistry

Bulk rock compositions were determined on melted pellets by XRF using a Bruker AXS SRS-



3400 at the Geochemical Laboratory in Basel. From each sample one slice was cut. From these slices one thin section was prepared and from the remaining volume the layers containing the indicative mineral assemblages were extracted and analysed. Bulk rock chemistries of the described samples are presented in Table 1.

**1.4 SAMPLE DESCRIPTION**

Six metapelitic samples from the frontal part of the Monte Rosa nappe and from the Camughera-Moncucco unit are described in detail. In order to derive the P-T history of metapelitic rocks from the study area we selected samples comprising well-preserved microstructural relationships. The selected samples span a wide range of bulk rock compositions. Two of the six samples (sample 1 and 4) are those described by Keller et al. (in

press.) collected in the Monte Rosa nappe, and are representative of the high-pressure overprint of pre-Alpine metamorphic pelites during an early stage of Alpine metamorphism. This early stage marks the starting point for the subsequent decompression history. Hence the physical conditions and mineral chemistries related to this early high-pressure stage will be discussed in some detail. As will be demonstrated the remaining four samples from the Camughera-Moncucco unit record subsequent decompression stages during the Alpine metamorphic cycle.

Figure 3 presents the regional distribution of the index minerals staurolite and sillimanite and in addition shows the proposed staurolite and sillimanite mineral zone boundary for the gneissic units southwest of the Simplon line. The distribution pattern of index minerals and

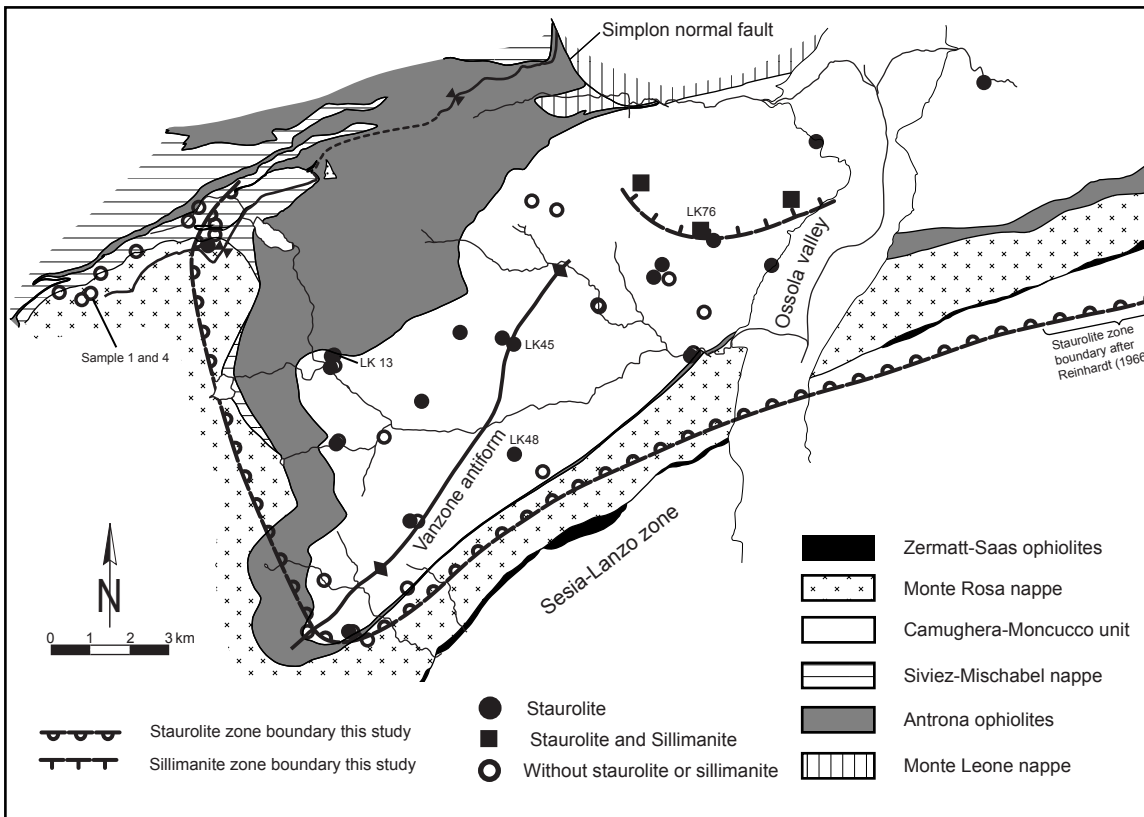


Fig. 3 Tectonic map of the study area outlined in Figure 1 presenting the distribution of staurolite and sillimanite and the location of their mineral zone boundaries. The southeastern fraction of the staurolite mineral zone boundary was mapped by Reinhardt (1966).

the resulting mineral zone boundaries indicate a metamorphic field gradient with increasing temperatures towards the east. This is in line with the albite-oligoclase isograd of Bearth (1958) (Fig. 2) and the pattern of regional isotherms established by Colombi (1989) and Todd & Engi (1997). The proposed staurolite mineral zone boundary is also constrained by the studies of Laduron (1976), Merlyn (1977) and Engi et al. (2001a), which report no staurolite bearing metapelites southwest of the proposed mineral zone boundary. The southeastern part of the mineral zone boundary was mapped by Reinhard (1966) (Fig. 3).

#### 1.4.1 Samples 1 and 4

These two samples are from the staurolite-absent mineral zone in the frontal Monte Rosa nappe (Fig. 3). At the sampling locality of both samples

a pre-Alpine foliation (sample 1) is continuously dragged into a shear zone. Thereby the pre-Alpine mineral assemblage is synkinematically replaced by an Alpine one in the case of sample 4.

The pre-Alpine foliation of sample 1 is composed of biotite, plagioclase, quartz, kyanite, garnet (1), phengite (1); accessory phases include ilmenite, rutile and tourmaline. P-T conditions for the formation of the pre-Alpine assemblage was estimated at about 720°C and 8.5 kbar (Keller et al. in press). Chlorite sporadically overgrows the pre-Alpine foliation and is interpreted as an alteration product of pre-Alpine biotite formed during late stages of Alpine metamorphism. Alpine metamorphism is indicated by a new garnet (2) and phengite (2) generation, both of which grow preferentially along the grain contacts between pre-existing biotite and plagioclase.

Sample 4 exhibits an early Alpine foliation,

Table 2 Selected microprobe analyses of white mica; end-member calculations see text

	Sample 1 Phe	Sample 4 Pg	Sample 4 Phe	LK 48 Phe (1)	Pg	Phe (2)	LK 13 Phe (core)	Pg incl. in Pl	Phe	LK 45 Phe	LK 76 Phe
SiO <sub>2</sub>	45.03	46.11	48.31	50.31	46.77	47.53	49.02	50.03	46.24	43.79	47.16
Al <sub>2</sub> O <sub>3</sub>	35.14	36.57	28.57	29.29	37.20	37.16	30.30	39.31	35.58	34.24	35.93
FeO	0.81	0.23	1.42	1.56	0.67	0.71	1.50	0.18	0.99	1.15	0.86
MnO	0.01	0.00	0.04	0.01	0.02	0.06	0.00	0.00	0.00	0.08	0.00
MgO	0.41	0.12	2.38	2.11	0.10	0.42	2.15	0.11	0.51	0.45	0.62
CaO	0.02	0.09	0.00	0.01	0.31	0.01	0.00	1.14	0.05	0.00	0.00
Na <sub>2</sub> O	0.72	7.16	0.84	1.20	6.61	2.40	0.92	7.07	1.59	1.57	1.49
K <sub>2</sub> O	10.73	0.90	9.77	9.77	1.33	8.45	10.14	0.83	9.83	8.81	9.62
TiO <sub>2</sub>	0.80	0.03	0.73	0.50	0.26	0.53	0.64	0.27	0.88	0.36	0.55
Sum	93.67	91.21	92.06	94.76	93.27	97.27	94.67	98.94	95.67	90.45	96.23
Si	3.05	3.08	3.32	3.35	3.06	3.07	3.28	3.08	3.06	3.06	3.09
Al	0.95	0.92	0.68	0.65	0.94	0.93	0.72	0.92	0.94	0.94	0.91
Sum	4.00	4.00	4.00	4.00	4.00	4.00	4.00	4.00	4.00	4.00	4.00
Al	1.86	1.95	1.63	1.65	1.93	1.89	1.67	1.93	1.84	1.88	1.86
Fe	0.05	0.01	0.08	0.09	0.04	0.04	0.08	0.01	0.05	0.07	0.05
Ti	0.04	0.00	0.04	0.03	0.01	0.03	0.03	0.01	0.04	0.02	0.03
Mn	0.00	0.00	0.00	0.00	0.00	0.00	0.00	0.00	0.00	0.00	0.00
Mg	0.04	0.01	0.24	0.21	0.01	0.04	0.21	0.01	0.05	0.05	0.06
Sum	1.99	1.98	2.00	1.98	1.99	2.00	2.00	1.96	1.99	2.01	2.00
Na	0.09	0.93	0.11	0.16	0.84	0.30	0.12	0.84	0.20	0.21	0.19
K	0.93	0.08	0.86	0.83	0.11	0.70	0.87	0.07	0.83	0.78	0.80
Ca	0.00	0.01	0.00	0.00	0.02	0.00	0.00	0.08	0.00	0.00	0.00
Sum	1.02	1.00	0.97	0.99	0.95	1.00	0.98	0.91	1.03	1.00	0.99
XM <sub>s</sub>	0.83	0.01	0.54	0.49	0.07	0.61	0.58	0.05	0.72	0.70	0.70
XPg	0.08	0.93	0.12	0.16	0.86	0.30	0.12	0.88	0.18	0.21	0.19
XMg-Cel	0.04	0.03	0.25	0.24	0.02	0.04	0.21	0.03	0.05	0.03	0.06
XFe-Cel	0.05	0.03	0.09	0.10	0.05	0.04	0.08	0.03	0.05	0.05	0.05

mainly composed of garnet (2), phengite (2) and paragonite, while minor amounts of biotite grow as retrograde alteration products along the grain boundary between garnet (2) and phengite (2). Pre-Alpine plagioclase, and kyanite can still be detected, but their modal amount is drastically reduced compared to sample 1. Pre-Alpine garnet (1) is only preserved as relics in this sample .

P-T conditions for the Alpine transformations are estimated at around 650°C and 12.5 kbar. Conservation of the pre-Alpine assemblage in sample 1 is probably due to the absence of an aqueous fluid within the undeformed country rock of the shear zone (Keller et al. in press).

During the transformation to the Alpine

assemblage the phengites became enriched in the Mg-celadonite content (0.2-0.35), whereas the Fe-celadonite content remained rather constant (Fig. 4, Tab. 2). In addition the paragonite content in phengite became slightly enriched during the Alpine transformation (Fig. 2, Tab. 2, see below). For the chemistry of the other minerals, related to this early stage of Alpine metamorphism, the reader is referred to Keller et al. (in press).

### 1.4.2 Sample LK 48

This sample is from the staurolite zone and is located in the Camughera-Moncucco unit (Fig. 3). It contains garnet, phengite, paragonite, biotite, staurolite, chlorite, turmaline as major

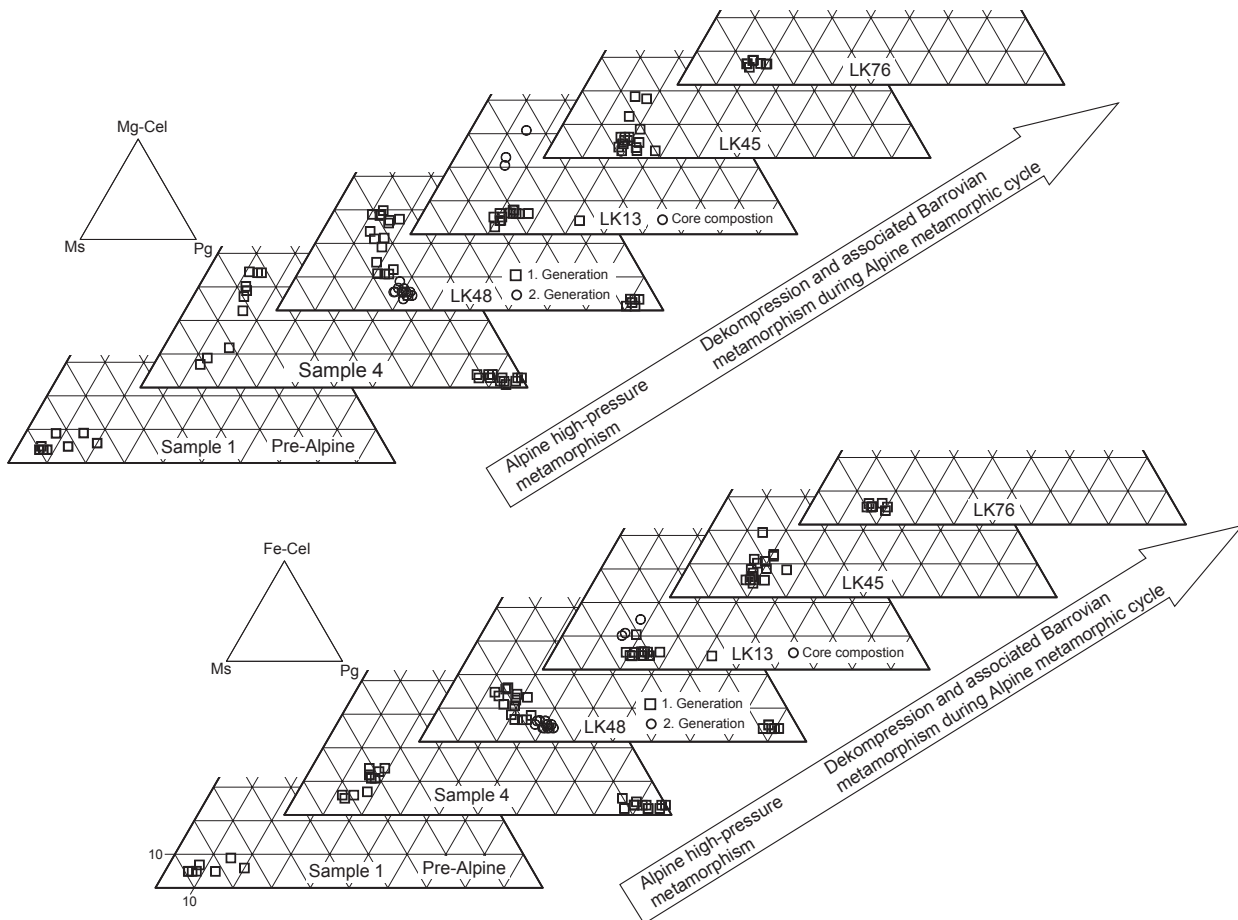


Fig. 4 White mica compositions for the investigated samples mentioned in the text given in the paragonite (Pg), muscovite (Ms) and Mg-celadonite (Mg-Cel) or Fe-celadonite (Fe-Cel) triangular plots. There is a pronounced increase of the Mg-celadonite component related to the early high-pressure stage while the Fe-celadonite component remains relatively constant. During subsequent decompression and Barrovian overprint the phengite composition changes systematically (see Fig. 6).



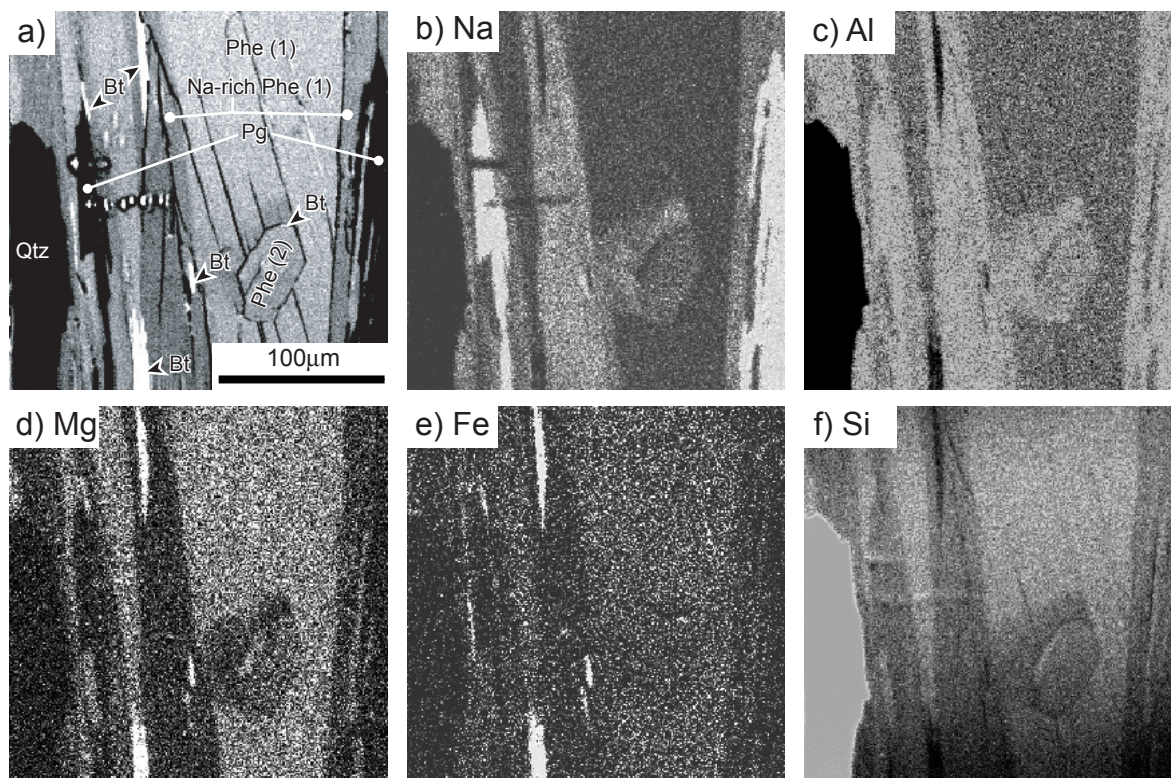


Fig. 5 Backscatter electron image (a) and corresponding X-ray maps (Na (b), Al (c), Mg (d), Fe, (e), Si (f)) illustrating the compositional variation of different white mica generations in sample LK48. Light colours correspond to high content of a given element. The contrast was adjusted to highlight the chemical variation. The composition of the first phengite generation (Phe (1)) varies parallel to the layers: i) layers rich in the Mg, Fe and Si (high celadonite content) and poor in Na and Al, ii) layers poor in Mg, Fe and Si and rich in Na and Al. A second phengite generation (Phe (2)) overgrows the first one and is poor in Mg, Fe and Si and rich in Na and Al. Note that biotite grows as exsolutions in layers of the first phengite generation. Because these layers are poor in Mg, Fe and Si and rich in Na and Al indicates that biotite grows on the expense of celadonite rich phengite (see text for further explanation).

minerals, and accessory opaque minerals. Two generations of phengite are observed. A first generation (Phe (1) in Fig. 5) is associated with paragonite, and laminae of phengite flakes show a compositional variation whereby both the celadonite (rich in Mg, Fe and Si) content and the paragonite (rich in Na and Al) content alternate parallel to the (001) plane (Fig. 5). Laminae with low celadonite content are Na enriched and are predominately associated with paragonite (Fig. 5). Compositional variation occurs also along the (001) plane (Fig. 5). From these observations it is interpreted that compositional adaption of major elements is likely to be parallel to the layers of phengite, as is assumed for hydrogen diffusion in white mica (Graham, 1981). In celadonite rich domains of phengite (1) the Mg-celadonite

content is enriched relative to the Fe-celadonite content (Fig. 4). A similar compositional variation of white mica is reported from the Monte Rosa nappe (Anzasca valley) situated slightly to the west of the study area (Laduron & Martin, 1969). A second phengite generation overgrows both phengite (1) and paragonite and the corresponding celadonite content is fairly constant (Fig. 4). The paragonite content of phengite (2) is higher compared to the celadonite rich laminae of phengite (1) (Figs 4, 5, Tab. 2). When biotite ( $Fe/(Fe+Mg) \approx 0.5$ ) occurs in form of exsolutions it is preferentially situated within domains of phengite (1), composed of low Mg, Fe and Si content and high Na and Al content (Fig. 5). Furthermore biotite overgrows paragonite, and it grows at the rim of garnets (Fig. 6a). More or less garnet-rich



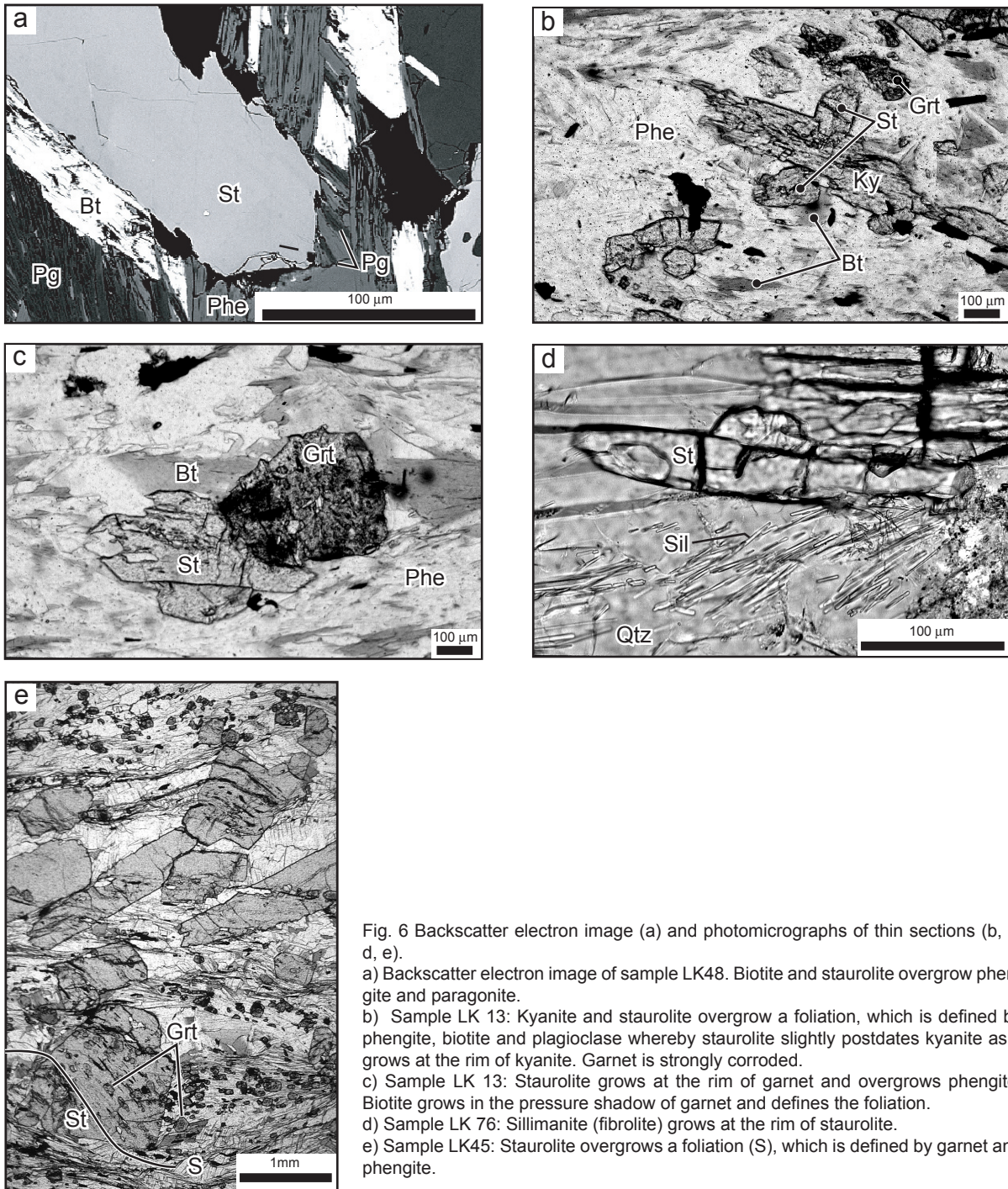


Fig. 6 Backscatter electron image (a) and photomicrographs of thin sections (b, c, d, e).  
 a) Backscatter electron image of sample LK48. Biotite and staurolite overgrow phengite and paragonite.  
 b) Sample LK 13: Kyanite and staurolite overgrow a foliation, which is defined by phengite, biotite and plagioclase whereby staurolite slightly postdates kyanite as it grows at the rim of kyanite. Garnet is strongly corroded.  
 c) Sample LK 13: Staurolite grows at the rim of garnet and overgrows phengite. Biotite grows in the pressure shadow of garnet and defines the foliation.  
 d) Sample LK 76: Sillimanite (fibrolite) grows at the rim of staurolite.  
 e) Sample LK45: Staurolite overgrows a foliation (S), which is defined by garnet and phengite.

layers define the foliation. The garnets are usually zoned. Where the zoning can be separated into two homogeneous parts one finds a core with slightly elevated grossular and relatively low almandine contents and a rim enriched in almandine and slightly reduced in grossular content. The pyrope content remains constant. The decrease of the grossular content corresponds to the increase in

the almandine content.

This same zoning pattern is also observed in garnets within pelitic rocks from the Monte Rosa nappe. There this pattern is interpreted as the result of a two-stage growth of garnet during the first stages of Alpine metamorphism (Keller et al. in press). High grossular in the garnet core reflects a the first growth stage, garnet locally

forming atrims of pre-Alpine plagioclase. Low grossular in the garnet rims reflects a second growth stage, during which garnet forms in a less Ca-rich bulk rock composition (Keller et al. in press). Staurolite is essentially unzoned with Mg/(Mg+Fe) of about 0.16 and it overgrows phengite (1) and paragonite, both of defining the foliation (Fig. 6a). No plagioclase is detected in sample LK 48. Chlorite overgrows the foliation and postdates staurolite.

From the microstructural relationships it is concluded that a first stage during Alpine metamorphism is represented by the assemblage Grt + Phe (1) + Pg + Qtz {1}. The exsolution of biotite within Na-enriched phengites indicates the breakdown of phengite (1) and paragonite (Fig. 4, see below). This leads to a second metamorphic stage represented by the assemblage Grt + Phe (2) + Pg + Bt + Qtz {2}. Evidently staurolite is produced during the breakdown of paragonite and phengite. This leads to a third metamorphic stage represented by the assemblage Grt + Phe (2) + Bt + St + Qtz {3}.

#### 1.4.3 Sample LK 13

This second sample from the staurolite mineral zone of the Camughera-Moncucco unit (Fig. 3) contains garnet, phengite, biotite, kyanite, staurolite, plagioclase, chlorite, epidote as major minerals and opaque minerals. The analysed garnets are unzoned. Paragonite occurs as inclusions in garnet and plagioclase. The sample contains abundant plagioclase ( $An \approx 0.27-0.31$ ) and biotite ( $Fe/(Fe+Mg) \approx 0.43-0.49$ ), both defining the foliation. Staurolite grows at the rim of kyanite, and both postdate the formation of the foliation (Fig. 6b). Because garnet predates staurolite, which grows at the rim of garnet, it is inferred that garnet did decompose during

staurolite formation (Fig. 6c). Chlorite and epidote occur as the latest minerals. Phengite grains may be zoned, and Si in the cores ranges from 3.3 to 3.4 p.f.u., whereas  $X_{MgCcl}$  ranges from 0.21 to 0.28 (Fig. 4, Tab. 2). Numerous small phengites show a Si content of about 3.1 p.f.u. (Fig. 4, Tab. 2).

From these observations the following metamorphic stages and corresponding assemblages are established: {1}: Grt + Phe + Bt + Pg + Pl; {2}: Grt + Phe + Bt + Pl; {3}: Grt + Phe + Bt + Pl + Ky; {4}: Grt + Phe + Bt + Pl + Ky + St

#### 1.4.4 Sample LK 45

This third sample from the staurolite mineral zone in the Camughera-Moncucco unit (Fig. 3) contains garnet, phengite, biotite, staurolite, plagioclase, chlorite and opaque phases as major minerals. Abundant staurolite overgrows the matrix foliation, which is well indicated by an internal foliation found in staurolite porphyroblasts (Fig. 6e). This internal foliation is slightly sigmoidal and can be traced into the matrix foliation indicating ongoing deformation during staurolite growth. Inclusion trails of garnet and opaque minerals define the internal foliation in staurolite. Phengite and biotite are also found as inclusions in staurolite (Fig. 6d). The analysed garnets show no zonation, neither in the matrix nor as inclusions in staurolite. Staurolite is unzoned with Mg/(Mg+Fe)  $\approx 0.20$ . Biotite is predominately found in the matrix and defines the foliation. Inclusions of biotite are frequently found in plagioclase and only rarely in staurolite. Plagioclase ( $An \approx 0.2-0.25$ ) grows as porphyroblasts and postdates garnet, phengite ( $Si \approx 3.0-3.24$  p.f.u) and biotite. Chlorite occurs as the latest mineral. Because the internal foliation of staurolite is devoid of biotite it is suggested that the initial grow of staurolite

predates the formation of biotite. However, the microstructural evidence is equivocal, particularly for the early stage assemblages. Hence we used an equilibrium phase diagram to interpret the mineral observed in this sample.

#### 1.4.5 Sample LK 76

Sample LK 76 is from an outcrop situated within the sillimanite zone of the Camughera-Moncucco unit (Fig. 3). It contains garnet, phengite, biotite, staurolite, sillimanite, plagioclase, rutile, chlorite and opaque minerals. Staurolite ( $Mg/(Mg+Fe) \approx 0.20$ ) and plagioclase ( $An \approx 0.28-0.35$ ) occur as porphyroblasts and define the foliation. Rutile can be observed as inclusions in staurolite. Rare sillimanite needles (fibrolite) occur in quartz, some of them growing at the grain boundary of staurolite (Fig. 6d). Occasionally garnet cores are resorbed giving rise to atoll structures. Small garnet grains occur as inclusions in both staurolite and plagioclase indicating that these two minerals postdate garnet. The analysed phengites have a fairly homogenous composition (Fig. 4). Chlorite is very rare and appears the as latest mineral.

### 1.5 SUCCESSIVE MINERAL ASSEMBLAGES AND WHITE MICA COMPOSITIONS IN METAPELITES

Figure (7) shows the relationships between phengite compositions (Fig. 4) and the mineral assemblages. In the pre-Alpine assemblage  $Grt + Phe + Pl + Bt + Ky + Qtz$  (sample 1) phengite composition is fairly close to the ideal muscovite composition (Figs 4, 7). During the Alpine HP overprint the pre-Alpine biotite, plagioclase and kyanite are decomposed, and the assemblage  $Grt + Phe + Pg + Qtz$  (sample 4) becomes stable. In the course of this overprint the paragonite content of phengite slightly increases, when compared

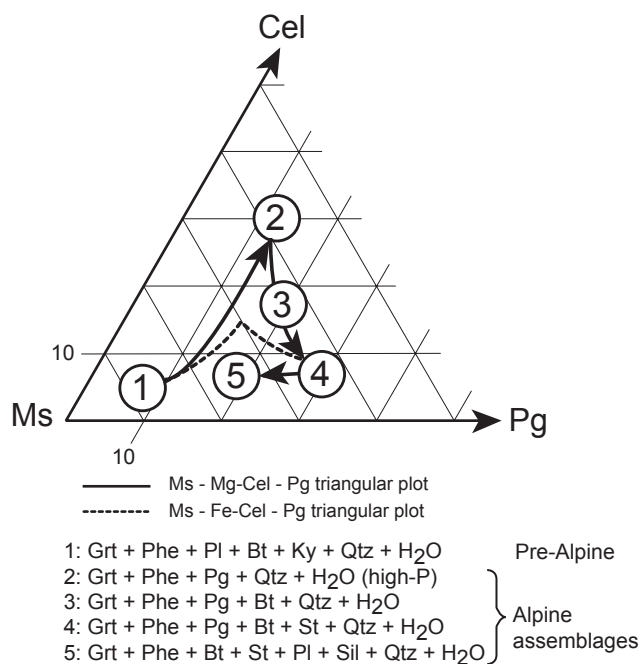
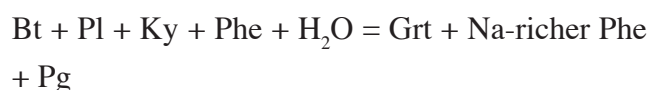


Fig. 7 Muscovite (Ms), paragonite (Pg), and celadonite (Cel) triangular plot illustrating the relationship between phengite composition and observed mineral assemblages. Encircled numbers refer to different mineral assemblages and are placed at the approximate phengite composition corresponding to the mineral assemblage (continuous line = Ms - Mg-Cel - Pg; stippled line = Ms - Fe-Cel - Pg triangular plot). In the high temperature medium pressure pre-Alpine assemblage (1) the phengite composition is close to ideal muscovite composition. During the early high-pressure overprint assemblage  $Grt + Phe + Pg + Qtz$  (2) becomes stable and phengite becomes enriched in its celadonite and paragonite component. Note that the Fe-celadonite content remains fairly constant when compared to the Mg-celadonite content. During Barrovian metamorphism biotite and staurolite become stable (assemblages 3 and 4) and phengite becomes enriched in its paragonite component and the celadonite is reduced. Subsequent retrogression leads to the formation of plagioclase and sillimanite (assemblage 5) and the white mica composition is shifted towards the muscovite end-member.

to pre-Alpine phengite. This indicates that Na of pre-Alpine plagioclase is partly stored within phengite (Figs 4, 7). In the HP assemblage the Mg-celadonite content in phengite is generally higher than the Fe-celadonite content, indicating that the substitution  $SiMg = Al^{IV} + Al^{VI}$  is preferred with respect to  $SiFe^{2+} = Al^{IV} + Al^{VI}$  (Figs 4, 7; see also Part I and Guidotti, 1984). The decomposition of the pre-Alpine assemblage and the concomitant increase in Na may be expressed by the following reaction:



During retrogression biotite grows at the expense



of garnet, paragonite and phengite (Fig. 5). This leads to the assemblage Grt + Phe + Pg + Bt + Qtz. In the course of biotite formation the muscovite and the celadonite contents in phengite decrease. This is probably due to the fact that K, Mg and Fe serve as nutrients for biotite formation (Fig. 5). During the growth of biotite the Na content of phengite increases, indicating that Na liberated during the breakdown of paragonite is stored within phengite (Fig. 5). The compositional change of phengite occurs by diffusional exchange of the first phengite generation and by the formation of a new phengite generation, i.e. by recrystallisation (Fig. 4). During ongoing retrogression staurolite, plagioclase, kyanite and sillimanite are formed and paragonite is decomposed. The highest Na content in phengite is observed in the assemblage Grt + Phe + Pg + Bt + St (sample LK48) in the absence of plagioclase (Figs 4, 5, 7). If phengite coexists with plagioclase (sample LK45, LK 13 and LK76) the Na content in phengite is reduced. In the assemblage Grt + Phe + Bt + St + Sil + Pl phengite contains the lowest Na content (Figs 4, 7).

## 1.6 EQUILIBRIUM PHASE DIAGRAMS

### 1.6.1 Bulk rock chemistry

In order to investigate the sensitivity of the stability fields to bulk rock compositions equilibrium phase diagrams were calculated for three bulk rock compositions. The bulk rock chemistries of the investigated samples are given Table 1. In addition average chemical compositions of medium- and high-grade pelitic rocks described by Shaw (1956, his Table 5) and by Ague (1991, his Table 2) are given. The bulk rock compositions are compared in the AFM projection (Thompson, 1957) of Figure 8. For calculating of the AFM coordinates the amounts of  $Al_2O_3$  bound by

CaO in anorthite and  $Na_2O$  in paragonite were subtracted from the total  $Al_2O_3$ , and the resulting projection is referred to as A'FM projection (Laduron, 1976). Interestingly, sample LK13 and the average composition of Ague (1991) plot at lower A' values than samples 4, LK48, LK76 and the average composition of Shaw (1956), despite the fact that all six bulk compositions contain almost the same amount of  $Al_2O_3$  (Tab. 1). This is explained by the fact that sample LK13 and the average composition of Ague (1991) are enriched in CaO and  $Na_2O$ , both binding  $Al_2O_3$  in specific minerals (anorthite and paragonite in our case) and thereby reducing the A' value in the A'FM plane. Thus, the CaO and  $Na_2O$  bulk contents may influence the development of assemblages, as it is indicated by the scattered distribution of bulk rock chemistries in the A'FM plane. The compositions of samples 4, LK48 and LK76 plot within a narrow field close to the average pelitic composition of Shaw (1956). Samples 1 and LK45 plot at higher

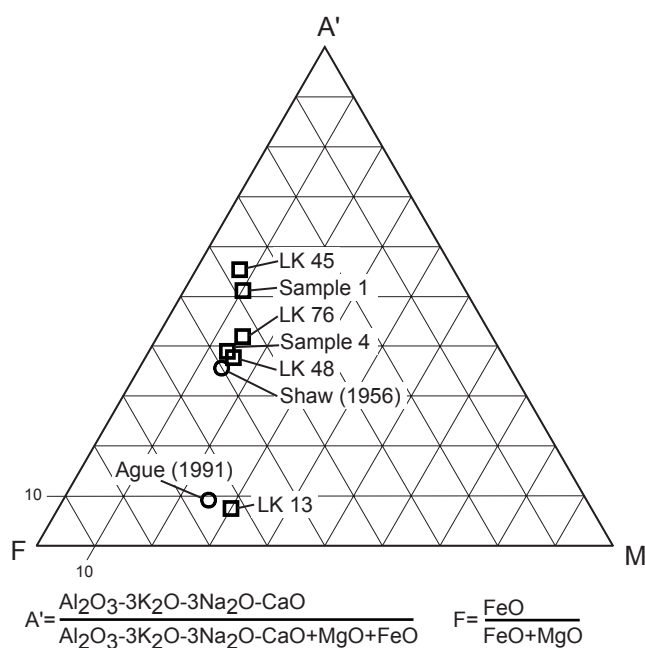


Fig. 8 A'FM triangular-plot derived from the classical AFM projection. The plot illustrates the bulk rock compositions of investigated samples and the published average pelitic composition of Shaw (1956) and Ague (1991).

A' values compared to the other samples. The composition of LK13 plots close to the average pelitic composition of Ague (1991), both having a lower A' value than the samples 4, LK48 and LK76. In order to account for these variable bulk compositions we computed equilibrium diagrams for the low-Al composition of sample LK13, the medium-Al composition of sample LK48, and the high-Al composition of sample LK45.

The composition of LK48 differs only slightly from the composition of samples 4 and LK76 and hence it is most likely that these three samples preserve assemblages corresponding to successive stages of the metamorphic history in the study area. Thus, the equilibrium diagram computed for the bulk composition of sample LK48 will also be used to interpret sample 4 and LK76. In order to interpret the wide range of observed phengite compositions in samples 4, LK48 and LK76 we also computed the end-member isopleths corresponding to the bulk rock composition of sample LK48. Because bulk rock chemistries of the samples LK48 and LK13 plot close to published average pelitic rock compositions we feel confident that the established equilibrium diagrams contain the desired general validity.

The use of single bulk rock chemistry for calculating equilibrium phase diagrams is based on assumption that the bulk rock chemistry remains constant during the modelled retrograde history. Hence, it excludes the removal or introduction of mobile components via a metamorphic fluid during decompression. Note also, that some components may be partly locked within growing phases (e.g. cores of zoned minerals), thereby modifying the effective bulk rock chemistry during decompression. In spite of this, the used method allows for a comparison between mineral parageneses obtained from

microstructural observations in a thin section and the corresponding equilibrium phase diagram calculated for the composition the same sample.

### 1.6.2 Stable assemblages and end-member isopleths of phengite of the samples LK48, 4 and LK76

Figure (9a) shows the equilibrium diagram calculated for the system  $K_2O-Na_2O-CaO-FeO-MgO-Al_2O_3-SiO_2-H_2O$ , given the bulk rock composition of sample LK48 and assuming a water activity of one. The corresponding end-member isopleths of phengite are given in Figure 9b. Shaded areas mark the successive stages of observed Alpine assemblages, while the stippled area designates the stability field of the pre-Alpine assemblage  $Grt + Phe + Pl + Bt + Ky + Qtz + H_2O$  observed in sample 1. At the P-T conditions defined by the pre-Alpine assemblage ( $\approx 720^\circ C$  at 8.5 kbar, Fig. 9a) calculated and measured phengite composition are in accordance and close to the ideal muscovite composition (Figs 4, 7, 9b).

The first Alpine assemblage  $Grt + Phe + Pg + Qtz + H_2O$  (assemblage 1 in Fig. 9a) is stable within a large area above about 12.5 kbar. This assemblage 1 is interpreted to reflect peak pressure conditions and is found in LK48 and 4. . The upper pressure limit ( $\approx 16$ kbar) is given by the stability of kyanite. Kyanite would become stable towards higher pressures, as ongoing Tschermak substitution would turn phengite towards less aluminous compositions, liberating aluminium for kyanite formation (Fig. 9a). Note that the end-member isopleths for phengite correctly predict the observed compositional change from pre-Alpine phengite towards Alpine high-pressure phengite. The latter is enriched in paragonite-

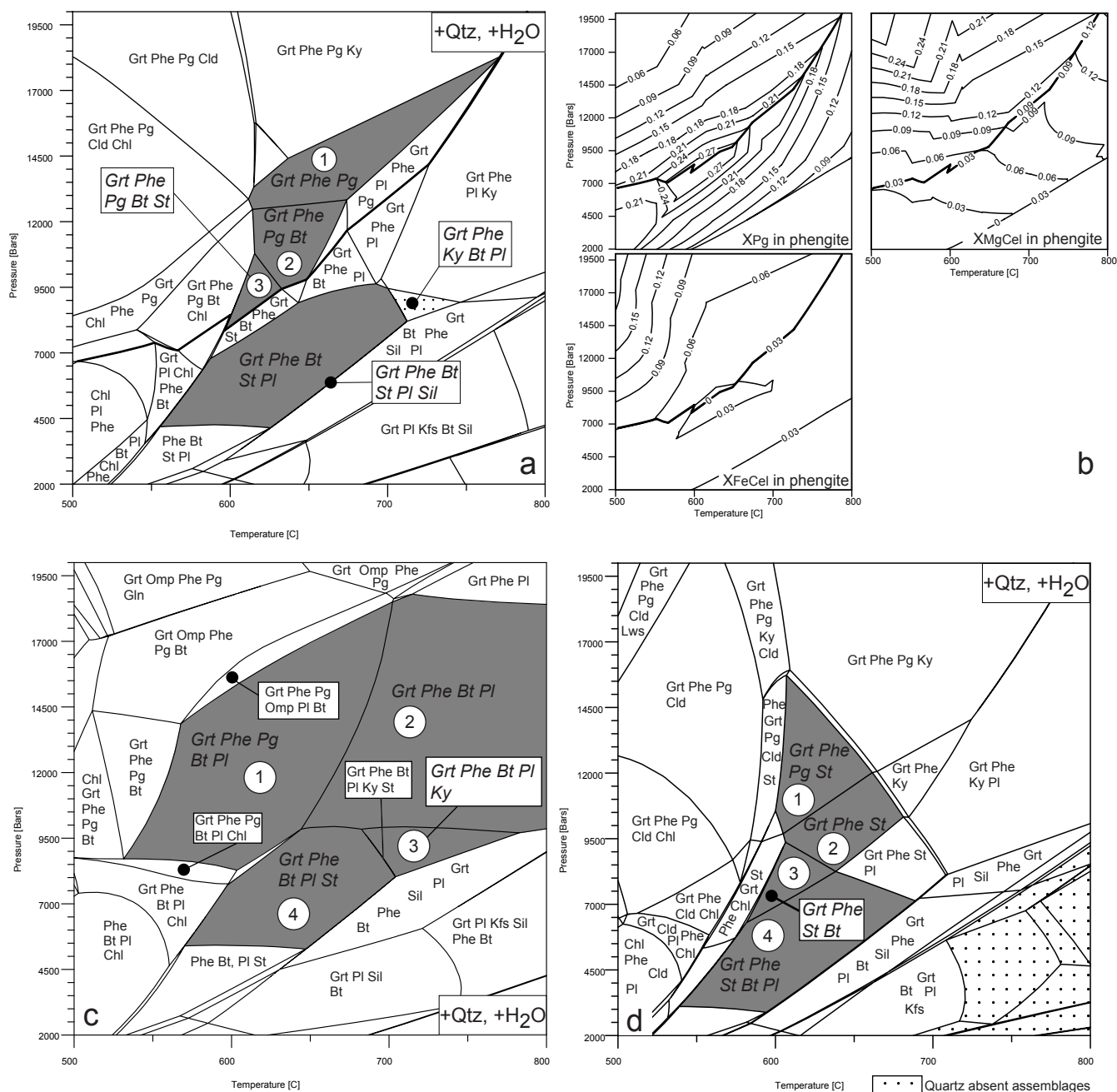


Fig. 9 Equilibrium phase diagrams for measured bulk rock chemistry of sample LK48, LK13 and LK45 and end-member isopleths of phengite corresponding to bulk rock chemistry of sample LK48. The diagrams are calculated with the program DOMINO (de Capitani, 1994) and they postulate distinct stable phase assemblages and corresponding mineral composition based on thermodynamic properties defined in the database (JUN92). Bulk rock chemistry is determined by powder X-ray diffraction and normalized to 100 cations while all iron is taken as Fe<sup>2+</sup>. The stability fields of successive mineral assemblages inferred from sample 4, LK48 and LK76 and mentioned in the text are marked by dark shading and italic letters. The low-pressure stability limit of paragonite is marked by the bold line.

(a) Equilibrium phase diagram for the specific bulk rock chemistry of sample LK 48 illustrating the stable mineral assemblages. Water and quartz are stable with all mineral assemblages. Numbers 1, 2, 3, indicate the mineral parageneses of sample LK48 mentioned in the text. The light grey area corresponds to the pre-Alpine assemblage observed in sample 1.

(b) End-member isopleths of paragonite, Mg-celadonite and Fe-celadonite in phengite corresponding to the bulk rock chemistry of LK48.

(c) Equilibrium phase diagram for the specific bulk rock chemistry of sample LK 13 illustrating the stable mineral assemblages. Water and quartz are stable with all mineral assemblages. Numbers 1, 2, 3, 4 indicate the mineral parageneses of sample LK13 mentioned in the text.

(d) Equilibrium phase diagram for the specific bulk rock chemistry of sample LK 45 illustrating the stable mineral assemblages. Water and quartz are stable with all mineral assemblages. Numbers 1, 2, 3, 4 indicate the mineral parageneses of sample LK45 mentioned in the text.

and celadonite- components, respectively (Figs 4, 7, 9b). Towards lower pressure the equilibrium phase diagram (Fig. 9a) correctly predicts

the occurrence of biotite. In accordance with the measured phengite composition the calculated end-member isopleths for phengite predict both

an increase in the paragonite and a decrease in the celadonite content of phengite, concomitant with biotite growth during decompression (Figs 5, 7, 9a). At P-T conditions of about 620°C and 9.5 kbar the aluminium liberated during continuous breakdown of paragonite and garnet can no longer be stored in phengite and the first staurolite begin to form. In the case of sample LK48 the formation of staurolite represents the latest stage of metamorphism, preserved in form of the assemblage Grt + Phe + Pg + Bt + St + Qtz ( $\approx$  620°C / 9.5 kbar, assemblage 3 in Fig. 9a). This assemblage 3 is limited towards lower pressure by the stability limit of paragonite, and the calculated phengite composition correctly predicts the highest Na-content in phengite (Fig. 9b bold line). This indicates that the second phengite generation, which is highest in Na, is in equilibrium with the assemblage 3 (i.e. Grt + Phe + Pg + Bt + St + Qtz ) in sample LK48, whereas the composition of the first phengite generation corresponds to earlier metamorphic stages and re-equilibration is incomplete. Towards lower pressure all paragonite is consumed by continuous reactions and the assemblage Grt + Phe + Bt + St + Qtz becomes stable. This illustrates that the final replacement of paragonite does not necessarily produce plagioclase as long as all sodium from paragonite can be stored in phengite. At higher P-T conditions (>650°C/9.5 kbar) the continuous breakdown of paragonite may form plagioclase because asymmetric K-Na mixing between phengite and paragonite decreases with increasing pressure, i. e. the maximum possible sodium content in phengite decreases with both increasing pressure and temperature because the Pg isopleths of phengite and the lower stability limit of paragonite have a different slope in P-T (Fig. 9a, b see also Part I).

Growth of plagioclase and sillimanite is only observed in sample LK76 and succeeds the latest metamorphic stage preserved in sample LK48. The equilibrium phase diagram predicts the formation of plagioclase towards a slightly lower pressures than those prevailing during the last metamorphic stage in sample LK48 (assemblage 3 in Fig. 9a). Comparison of the composition of the second generation of phengite in sample LK48 with the phengite composition of sample LK76 shows that phengite of the plagioclase-bearing sample LK76 is richer in K (Fig. 4). This can be explained by the growth of plagioclase grows at the expense of Na-rich phengite. Thereby phengite changes towards a K-richer composition, as Na is used for the formation of the end-member component albite in plagioclase. This is in line with the end-member isopleths predicting that K in phengite increases as plagioclase grows during decompression (Fig. 9a, b). Hence, it is likely that sample LK76 likely experienced decompression through the plagioclase-bearing stability field of the assemblage Grt + Phe + Bt + St + Pl + Qtz. The latest metamorphic stage is represented by the growth of sillimanite at staurolite grain boundaries in sample LK76 (Fig. 6d). This is corroborated by the equilibrium phase diagram, which predicts the growth of sillimanite at the expense of staurolite at and below the low-pressure stability limit of the assemblage Grt + Phe + Bt + St + Pl + Qtz (Fig. 9a).

### 1.6.3 Stable assemblages in sample LK13

Figure (9c) shows the equilibrium diagram calculated for the system  $K_2O$ - $Na_2O$ - $CaO$ - $FeO$ - $MgO$ - $Al_2O_3$ - $SiO_2$ - $H_2O$  for the low-Al bulk rock composition of sample LK13. The dark shaded areas mark the assemblages formed during successive stages of Alpine metamorphism.



The assemblage Grt + Phe + Pg + Pl + Bt + Qtz (assemblage 1 in Fig. 9c) occupies a large stability field, the upper pressure limit being given by the stability of plagioclase with respect to omphacite at pressures ranging between 14 kbar and 18 kbar. Assemblage 1 (Fig. 9c) is interpreted to reflect peak metamorphic conditions recorded in sample LK13. Note that plagioclase and biotite are stable at higher pressures given the bulk rock composition of sample LK13, when compared to for the stability fields of these minerals at the bulk rock composition of sample LK48 (Fig. 9a, c). As suggested by the A'FM projection (Fig. 8) the equilibrium diagrams verify that sample LK13 is “undersaturated” in Al in the sense that there is not sufficient Al for storing all univalent and divalent cations in “high aluminous minerals” such as garnet, phengite and paragonite. This increases the P-T area within which “low aluminous minerals” such as biotite and plagioclase are stable.

The subsequent assemblages 2, 3 and 4 in Figure 9c are correctly predicted by the equilibrium phase diagram. Assemblage 3 (Grt + Phe + Pl + Bt + Ky + Qtz) is limited towards lower P-T conditions by stability of kyanite with respect to staurolite; kyanite and staurolite coexist in a very narrow P-T interval (Fig. 9c). The growth of staurolite at the grain boundary of kyanite indicates the formation of staurolite at the expense of kyanite is indicated by (Fig. 6b). In sample LK13 this replacement is far from complete. This indicates that the assemblage Grt + Phe + Pl + Bt + Ky + St + Qtz either represents the latest metamorphic stage preserved in sample LK13, or alternatively, that the replacement of kyanite by staurolite is sluggish because of kinetic reasons. In the latter case the sample underwent further retrogression through the P-T area defined by the assemblage Grt + Phe + Pl + Bt + St + Qtz where kyanite

would be metastable. In any case, the observed mineral parageneses are in accordance with the prediction of the equilibrium phase diagram a retrogressive P-T path is indicated.

#### 1.6.4 Stable assemblages in sample LK45

Figure (9d) shows the equilibrium diagram calculated in the system  $K_2O-Na_2O-CaO-FeO-MgO-Al_2O_3-SiO_2-H_2O$  for the high-Al bulk rock composition of sample LK45. The dark shaded areas mark successive stages of the Alpine metamorphic evolution. In sample LK45 staurolite exhibits a sigmoidal internal foliation, that can be traced into the matrix foliation (Fig. 6e). This foliation is predominately defined by aligned garnet grains, whereas phengite and rare biotite are also found as inclusions in staurolite. In sample LK45 neither paragonite nor kyanite could be detected. From these observations, and provided that rare biotite inclusions represent incorporations during a late stage of staurolite growth, assemblage Grt + Phe + St + Qtz (assemblage 2 in Fig. 9d) can be interpreted to represent an early stage of metamorphism for sample LK45. In this case the internal foliation of staurolite would document progressive deformation and associated growth of staurolite during the early stages of metamorphism and deformation rather than growth of staurolite over a pre-existing Alpine foliation. Figure (9d) predicts assemblage 2 (Grt + Phe + St + Qtz) for a relatively restricted P-T area, the upper pressure limit being given by the stability of paragonite at pressures ranging between about 9.5 and 12 kbar. The stability of staurolite is limited towards higher P-T conditions where kyanite replaces staurolite (Fig. 9d). However, the assemblage inferred for the first Alpine stages in samples LK48 and LK13

point to somewhat higher pressures than those inferred from assemblage 2 in Figure 9d formed in sample LK45. Thus, it is possible that during an earlier metamorphic stage the assemblage of sample LK45 may also comprised paragonite, which would be stable towards higher pressures. If paragonite would indeed have been present in sample LK45 the assemblage Grt + Phe + Pg + St + Qtz (assemblage 1 in Fig. 9d) would reflect peak metamorphic conditions. Retrogression of sample LK45 is indicated by the porphyroblastic growth of plagioclase incorporating biotite. This is in accordance with the phase equilibrium diagram, which predicts the assemblages Grt + Phe + St + Bt + Qtz and Grt + Phe + St + Bt + Pl + Qtz as retrogressive stages of sample LK45 assemblages 3 and 4 in Fig. 9d).

### 1.7 MINERAL REACTIONS

It is clear that the considered 5- to 8-phase assemblages in the above 8-component system are at least divariant or even higher variant in terms of the phase rule. The high variance is largely due to the wide compositional variation of the phases present. In such high-variance assemblages the mineral reactions are continuous and mainly manifested by gradational modal- and compositional- changes of a restricted group of phases. In addition the distinct observed mineral parageneses and the equilibrium phase diagrams mutually indicate that the variance of the considered bulk composition affects the P-T relation of stable assemblages, whereby the A' value largely influences the formation of a specific assemblage. Based on these considerations we calculated mineral abundances diagrams for the bulk rock composition of sample LK48 in order to establish the mineral reactions, which cause the compositional change of phengite (Fig. 10). To

account for variable A' values we also calculated an isothermal P-A' binary phase equilibrium diagram and corresponding abundances isopleths of selected minerals (Fig. 11). These calculations are made by varying the Al-content of the bulk rock composition of sample LK48, whereby the atomic ratios of the remaining components are equal for each Al-content (i.e. equal as in sample LK48). A constant temperature (620°C) is justified because the mineral parageneses and equilibrium diagrams mutually indicate an approximately isothermal P-T path during retrogression (see discussion).

Figure (10) shows the mineral abundance isopleths of selected minerals corresponding to the equilibrium phase diagram of sample LK48 (Fig. 9a). The P-A' binary phase equilibrium diagram and corresponding mineral abundances isopleths are illustrated in Figure (11), whereby the A' values of the described and published pelitic compositions are indicated by arrows.

In sample 4 and LK48 biotite is seen to be the first retrogressive reactions product, which becomes stable towards lower pressures. In the stability field of the assemblage Grt + Phe + Pg + Bt + Qtz + H<sub>2</sub>O (assemblage 2 in Fig. 9a) the mineral abundance isopleths predict both the continuous formation of biotite and phengite and the continuous consumption of garnet and paragonite (Fig. 10a, b, c, f). From the mineral abundance isopleths, the end-member isopleths of phengite, and in accordance with microstructural observations (see above), the following biotite forming reaction may be formulated:



As a result of this continuous reaction phengite becomes Na and Al enriched towards lower pressure, which is in accordance with the

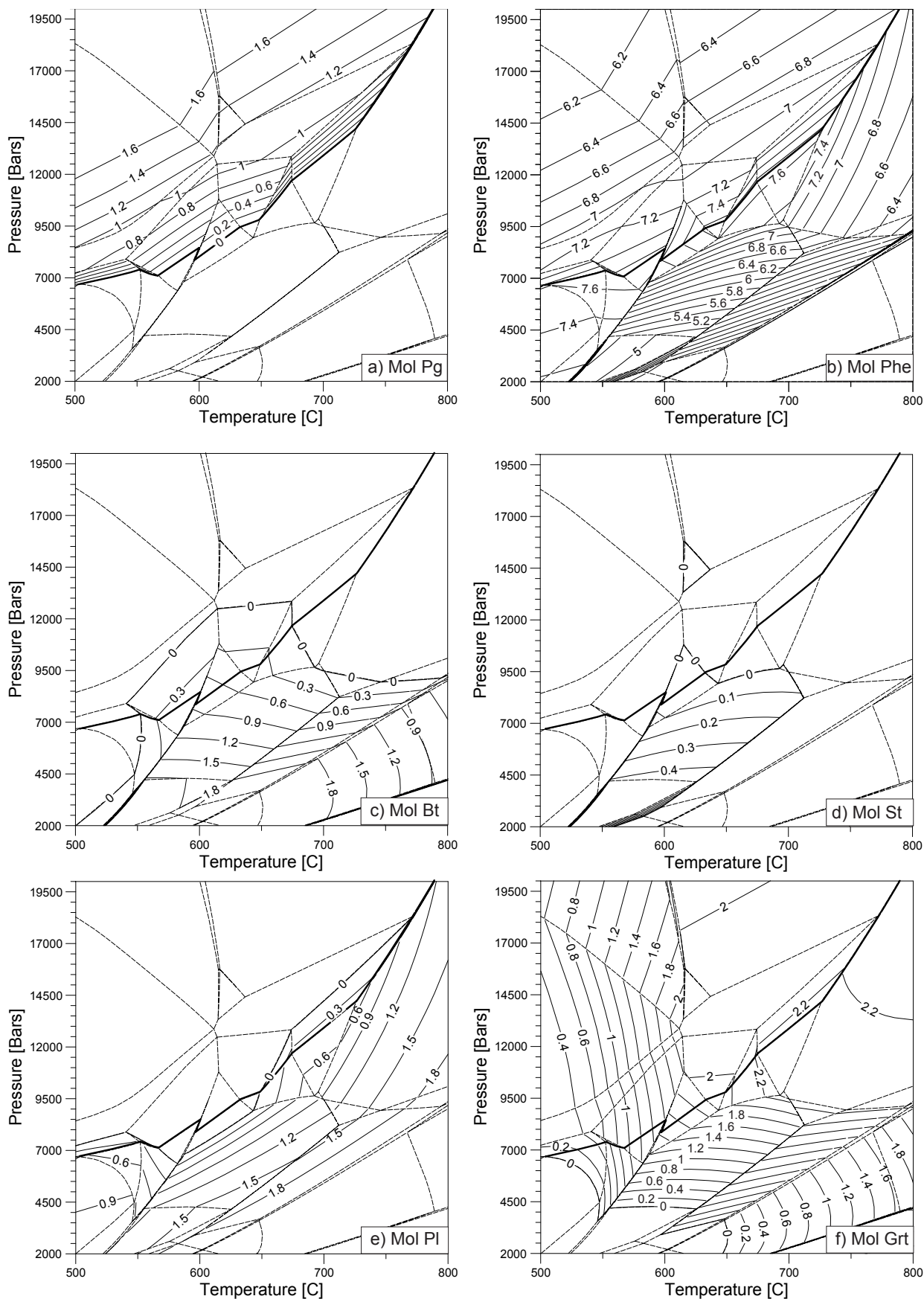


Fig. 10 Mineral abundance isopleths of paragonite (a), phengite (b), biotite (c), staurolite (d), plagioclase (e) and garnet (f). The diagrams are calculated for the measured bulk rock chemistry of sample LK48 with the program DOMINO (de Capitani, 1994) and they postulate isopleths of moles of a stable phase based on thermodynamic properties defined in the database (JUN92). Bulk rock chemistry is determined by powder X-ray diffraction and normalized to 100 cations while all iron is taken as Fe<sup>2+</sup>. The low-pressure stability limit of paragonite is marked by the bold line.



and garnet forms biotite (Fig. 11). This biotite formation is regardless of bulk composition (Fig. 11). As biotite grows on the expense of Na-rich phengite and garnet Na and Al is continually liberated and the mineral abundance isopleths indicate the formation of plagioclase (Fig. 10). Concerning metapelites with higher  $A'$  values, staurolite is formed in addition to plagioclase, and the following plagioclase and staurolite forming reaction may be formulated (Figs 10, 11):



This continuous reaction forms plagioclase in metapelites with higher  $A'$  values and takes place in the stability field of the assemblage  $\text{Grt} + \text{Phe} + \text{Bt} + \text{St} + \text{Pl} + \text{Qtz}$  found in sample LK76 and LK45 (Fig. 9a, d). In the course of the pressure driven reaction R4 phengite should become K-richer (Fig. 9b). In low-Al metapelites the P- $A'$  diagram and corresponding mineral abundance isopleths indicate the formation of the first staurolite via reaction R4, which in addition proceeds in the assemblage  $\text{Grt} + \text{Phe} + \text{Bt} + \text{St} + \text{Pl} + \text{Qtz}$  interpreted to be a late stage of sample LK13 (Figs 11, 9c). Hence, the assemblage  $\text{Grt} + \text{Phe} + \text{Bt} + \text{St} + \text{Pl} + \text{Qtz}$  and reaction R4 occurs over wide compositional range of pelitic compositions and mineral abundance isopleths indicate that staurolite is largely formed during the progress of reaction R4 (i.e. during phengite breakdown) (Figs 9, 10, 11). Paragonite breakdown, however, forms only a minor amount of staurolite, and in Al-rich bulk rock compositions only (Figs 10, 11).

## 1.8 DISCUSSION

### 1.8.1 Peak metamorphic conditions

The peak metamorphic conditions for the metapelites from the eastern part of the Monte

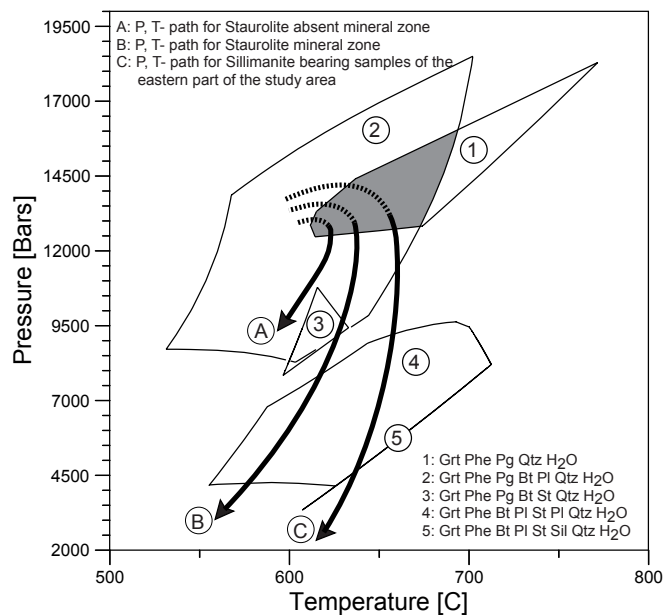


Fig. 12 Peak metamorphic conditions of the north-eastern part of the Monte Rosa nappe and the Camughera – Moncucco unit as well as P-T paths for investigated pelitic rocks corresponding to different metamorphic zones. Encircled numbers refer to stability fields of mineral assemblages extracted from the equilibrium diagrams of Figure 8a and 10. The peak metamorphic conditions (grey area) are inferred from the overlapping P, T-area of the first stage metamorphic mineral assemblage ((1) and (2)) of LK 48, LK4 and LK 13.

Rosa nappe and the Camughera-Moncucco unit are inferred from the overlapping part of the stability fields extracted from Fig. 9a, c (fields 1 and 2 in Fig. 12). These stability fields represent the earliest Alpine metamorphic mineral assemblages found in pelitic rocks with different bulk rock compositions. The overlapping P-T field (shaded in Fig. 12) allows constraining pressure and temperature within 12.5-16 kbar and 620-700°C respectively. This indicates a high-pressure metamorphic stage for the Camughera-Moncucco tectonic unit that remained undetected until now. Similar pressures (14-16 kbar) at somewhat lower temperatures (500-550°C) have been reported from the western part of the Monte Rosa nappe (Chopin & Monié, 1984; Borghi et al., 1996). This suggests that both the Monte Rosa nappe and the Camughera-Moncucco unit reached a similar depth during the high-pressure stage. Given the temperature difference the isotherms appear not to



have been parallel to the isobars during this early stage of metamorphism, implying that a lateral thermal gradient already existed during the early stages of Alpine orogenic metamorphism. This implication may appear rather weakly constrained because it is based on the geothermobarometric results obtained by different workers using various methods. However, according to Borghi et al. (1996) the Grt-Chl-Cld association commonly indicates high-pressure metamorphic conditions in metapelites of the western parts of the Monte Rosa nappe. After our calculations this association is always stable at temperatures lower than those indicated by the first stage assemblages found in our working area, comprising the eastern part of Monte Rosa nappe and the Camughera-Moncucco unit (Fig. 9a, d). Hence, the HP mineral assemblages in metapelites also indicate spatially different temperatures for the high-pressure metamorphism, supporting the suggestion of a thermal gradient during early stages of Alpine metamorphism.

Regarding the retrograde stages of Alpine metamorphism, a metamorphic field gradient is undoubtedly indicated by the mineral zones observed in the field area. Given the different temperatures inferred for the peak pressure stage we propose that this gradient is at least in part inherited from the high-pressure metamorphic stage. This is corroborated by our finding that the minerals assemblages, which are typical for Barrovian type metamorphism undoubtedly grew at the expense of the high-pressure mineral assemblages, which are stable at higher temperatures than those reported from the western part of the Monte Rosa nappe. A metamorphic field gradient that was already present during high-pressure metamorphism, and which was inherited during subsequent Barrovian metamorphism was

previously proposed for the Adula nappe (Central Alps) (Heinrich, 1986; Nagel et al., 2002) situated east of the Lepontine dome. This finding is new however, for our working area situated west of the Lepontine dome.

### 1.8.2 P-T paths

The P-T paths during decompression of the metapelites can be inferred from the mineral assemblages stable during the successive stages of decompression and are given by the stability fields extracted from Figure (9a, c) and shown in Fig. (12). Thereby we distinguish between three different mineral zones (see A, B and C in Fig. 12). The different mineral zones found in the field area indicate different P-T conditions during the retrograde part of the P-T paths. Except for its eastern part of its root zone the Monte Rosa nappe only marginally falls into to the staurolite mineral zone (Fig. 3).

The retrograde P-T path for metapelites from the staurolite-absent mineral zone (P-T path A in Fig. 12) does not cross P-T areas within which staurolite is stable. Hence, cooling during decompression is more pronounced in the case of the staurolite-absent mineral zone, where biotite, chlorite and plagioclase formed during retrogression of the metapelites. The mineral parageneses of metapelites from within the staurolite mineral zone indicates nearly isothermal decompression during the retrograde P-T path (P-T path B in Fig. 12). This path is constrained by the relatively small stability field of the mineral assemblage Grt + Phe + Pg + Bt + St + Qtz (assemblage 3 in Fig. 12) found in sample LK48. This assemblage gives P-T estimates of about 620°C at 9.5 kbar. Similar P-T estimates were obtained for staurolite bearing pelitic samples from the Monte Rosa nappe from within the staurolite mineral zone

(Engi et al., 2001a). Note, however, that in case of very high-Al metapelites it is entirely possible that staurolite belongs to the peak metamorphic assemblage formed at pressures >9.5 kbar. However, we emphasise the fact that staurolite formation is sensitive to bulk rock composition at least in the area under consideration. Moreover, staurolite formation is also strongly pressure driven and occurs by continuous reactions over a large P-interval. At low pressures ( $\approx <8$  kbar at  $600^\circ\text{C}$ ) massive staurolite formation by the continuous breakdown of Na-rich phengite and garnet is less sensitive to bulk composition (Figs 10, 11). Decompression during staurolite growth is additionally indicated by the chemical change of phengite. The paragonite content in phengite decreases from  $X_{\text{Pg}} \approx 0.3$  in assemblage 3 to  $X_{\text{Pg}} \approx 0.15-0.2$  in the assemblages 4 and 5, respectively (see definition of assemblages given in Fig. 12). This indicates a pressure decrease of about 5 kbar (Figs 4, 7, 9a, b). The formation of sillimanite in the eastern part of the study area may be explained by isothermal decompression at somewhat higher temperatures of about  $650^\circ\text{C}$  at 5 kbar (P-T path C in Fig. 12). In summary, the observed phase relations indicate that the eastern part of the Monte Rosa nappe and Camughera - Moncucco unit experienced amphibolite facies conditions during approximately isothermal decompression from peak P-T conditions, whereby substantial heating is not necessary in order to explain the observed mineral parageneses.

### 1.8.3 End-member isopleths of phengite

The isopleths calculated for the bulk composition of sample LK48, in combination with the highest Mg-celadonite content ( $X_{\text{MgCel}} \approx 0.3$ ) measured in the first phengite generation of this sample, point to higher pressures than those obtained from

first stage metamorphic mineral assemblages (Figs 4, 9a, b). The compositional zonation and the variance of measured compositions in the first generation of phengite in sample LK48 indicates, that phengite did probably not attain chemical equilibrium on thin section scale during progressive metamorphism (Figs 4, 5). Chemical equilibrium is achieved only locally, i. e. at the contact with other phases (e. g. biotite, paragonite; Fig. 5). Hence, the inference of quantitative P-T conditions from isopleths calculated for a bulk composition representing a whole thin section yields no unequivocal results for the high-pressure stage recorded in sample LK48. Also, the bulk rock composition relevant for defining the phengite composition might vary within thin section scale. This would additionally contribute to the variance in composition of first generation phengite. Despite the fact that phengite composition cannot be used for thermobarometry, given the profound disequilibrium within sample LK48, the observed mineral parageneses, combined with the equilibrium phase diagram (Fig. 9a), can be used to infer P-T conditions via equilibrium mineral assemblages. In addition, the calculated isopleths of phengites correctly predict the observed trend of phengite composition during decompression (Fig. 4, 5, 7, 9b). Moreover the measured composition of the second phengite generation ( $X_{\text{Pg}} \approx 0.3$ ,  $X_{\text{MgCel}} \approx 0.05$ ) agrees well with the phengite composition calculated for the latest assemblage (Grt + Phe + Pg + Bt + St + Qtz) observed in LK48 (Figs 4, 9a, b).

Furthermore, the calculated isopleths for phengite predict that the Fe-celadonite content in phengite depends on temperature rather than pressure at higher P-T conditions (Fig. 9d; see also part I). Hence, there should only be little change in Fe-celadonite content in phengite if decompression

is almost isothermal (see above). Indeed the measured Fe-celadonite contents in phengite only show little variation, and they are generally lower when compared to Mg-celadonite content (Figs 4, 7). Thus, the trend in the Fe-celadonite content of phengite is in accordance with the inferred P-T path, exhibiting almost isothermal decompression. However, the isopleths of Fe-celadonite should be only used qualitatively, since the determination of the Fe-celadonite in phengite is subject to uncertainties due to the unknown amount of Fe<sup>3+</sup> resulting from microprobe analysis.

#### 1.8.4 Effects of decompression on the sodium content in phengite

The chemical variation of phengite composition in response to changing P-T conditions and variable bulk rock compositions is discussed by Guidotti (1973), Guidotti & Sassi (1976) and in Keller et al. of part I. Hence, only a few points are discussed here. In order to test to what extend

the Na-content in phengite is sensitive to bulk rock composition, we calculated the end member isopleths of paragonite in phengite for the P-A' binary diagram as given in Figure (11). These isopleths depicted in Figure (13) reveal that the Na-content in phengite depends only slightly on the A' value (i.e. on the bulk Al-content), provided that the pelitic compositions have elevated A' values. The A' values of the bulk rock compositions for samples LK48, LK76, LK45, 4 and 1 and the average pelitic composition of Shaw (1956) are high enough, for the phengite composition to be more or less independent of bulk composition (Figs 11, 13). Concerning these samples, we feel confident that the observed compositional trend of phengite solely reflects the P-T history of the samples and is thus not affected the variance of bulk rock composition. In the case of the low-Al pelites, whose composition would for example correspond to that of sample LK13, or to the average pelitic composition of Ague (1991), the maximum possible Na-content in phengite would be sensitive to bulk rock composition the maximum possible Na-content in phengite decreasing with decreasing A' value. Hence, phengite should only be used in high-Al metapelites for deriving the P-T history of a particular metamorphic area.

The maximum possible paragonite content in phengite depends on pressure, temperature and bulk rock composition, defining a quite restricted P-T area close to the low-pressure stability limit of paragonite (Figs 9b, 11). Phengites from high-Al pelitic rocks are particularly Na-rich, if their retrograde PT path crosses a T-interval of around 550-650°C, where a maximum amount of paragonite content of phengite is predicted (Fig. 9b). Within this T-interval growth of biotite is concomitant with paragonite breakdown,

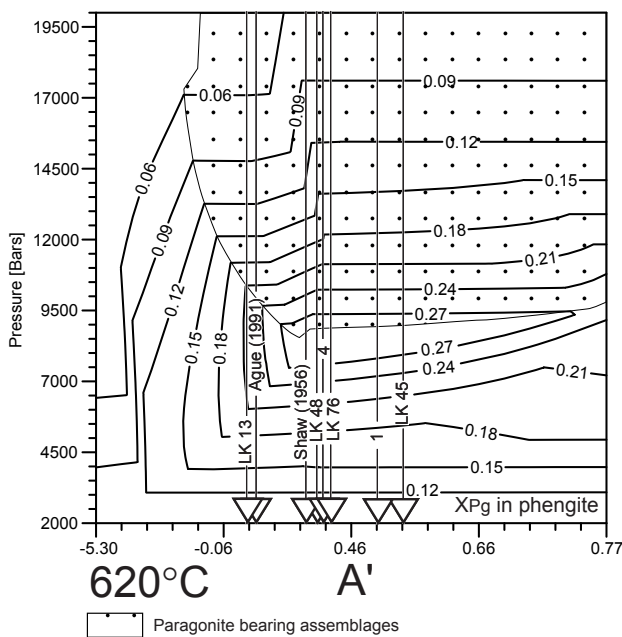


Fig. 13 End-member isopleths of paragonite in phengite corresponding to the P-A' binary equilibrium phase diagram presented in Figure 11. Along the horizontal axis the A' (for definition see Fig. 8) value is varied. Arrows indicate the A' values of the described samples and of published average pelitic compositions.



and the released sodium can be largely stored in phengite. Hence, plagioclase does not form during paragonite breakdown, but rather during the breakdown of Na-rich phengites. At higher temperatures and pressures, plagioclase becomes stable with respect to biotite, and paragonite breakdown forms plagioclase.

### 1.8.5 Regional implication

Recently Nagel et al. (2002) proposed that the mineral zone boundaries of Barrovian metamorphism in the Adula nappe (central Alps) do represent a reaction isograd, and that paragonite breakdown occurs in a relatively narrow P-T interval during decompression. These authors based their interpretation on equilibrium phase diagrams calculated with computer programs identical to those used in this study. However, they did not consider K-Na mixing between phengite and paragonite. Neglecting K-Na mixing between phengite and paragonite overestimates the calculated amount of paragonite at a given bulk composition. Consequently the final breakdown of paragonite is predicted to release far too much Al (i.e. far too much staurolite would be formed due to paragonite breakdown) compared to calculations that consider K-Na mixing between phengite and paragonite. In spite of this shortcoming, the growth of staurolite is undoubtedly related to paragonite breakdown also in the case of the Adula nappe. However, our study shows that paragonite breakdown may also occur by continuous reactions producing only minor amounts of staurolite, and that growth of staurolite related to paragonite breakdown is restricted to high-Al metapelites.

In our study area the continuous breakdown of phengite largely dominates the formation of staurolite and it occurs within a wide range of

pelitic compositions (Figs 9, 10, 11). Because the formation of staurolite is related to continuous reactions within high-variance assemblages, whose stability in P-T space is also sensitive to bulk rock composition, we conclude that, at least within our study area, the staurolite mineral zone boundary does not represent a simple reaction isograd indicating identical P-T conditions during staurolite growth all along its boundary trace in map view (Fig. 3). Slightly to the west of the staurolite mineral zone boundary paragonite is frequently found (Laduron & Martin, 1969; Laduron, 1976) while it can only rarely be found within this boundary. Hence, this relatively well-defined boundary could theoretically imply a reaction isograd. But given the results of this study that indicate almost isothermal decompression, continuous and pressure driven reactions did produce this well-defined mineral zone boundary a field area that exhibits a significant temperature gradient during staurolite formation.

## 1.9 CONCLUSIONS

1. The Camughera - Moncucco gneissic unit experienced peak high-pressure metamorphic conditions of about 600-650°C at 12.5-16.5 kbar, based on two overlapping stability fields for first stage metamorphic mineral assemblages found within pelitic rocks of different bulk rock compositions.
2. The mineral zones in the study are characterized by Chl, Bt, Pl through St and Sil mineral zones, indicating a metamorphic field gradient whereby temperatures increase towards the east during decompression. The observed mineral assemblages are compatible with almost isothermal decompression.

A heating pulse during later stages of the metamorphic history is not necessary or indicated.

3. The solution model for white mica introduced in part I and used here for calculating equilibrium diagrams, end-member isopleths of phengite and mineral abundance isopleths gives very reasonable results seeing that the calculations coincide with the observations in natural pelitic samples. It turns out that the solution model is an important link in modelling multicomponent equilibrium diagrams for pelitic rocks as it makes the processes understandable, which are related to the decomposition of paragonite and phengite during decompression of pelitic rocks originating from high-pressure areas.
4. At least for the gneissic units of the upper Penninic-Alps situated southwest of the Simplon line, this study shows that staurolite grows within a large P-interval during the continuous decomposition of paragonite and phengite, while the growth of staurolite is sensitive to bulk rock composition. The observed systematic chemical variation of phengite documents the P-T history of the study area.

This study is supported by the Swiss National Foundation Grant Nr. 20-61814.00.

#### **1.10 ACKNOWLEDGMENTS**

This work has benefited from comments and discussion with A. Berger, who performed also the micro-Raman analyses. W. Stern and H. Hürlimann from the Geochemical laboratory of Basel University performed the whole rock chemical analyses. K. Waite helped with the microprobe analyses. Furthermore we acknowledge the contributions of R. Bousquet, which were instrumental for our own thinking.

## 1.11 REFERENCES

- Ague, J. J. (1991). Evidence for major mass transfer and volume strain during regional metamorphism of pelites. *Geology* **19**, 855-858.
- Barrow, G. (1912). On the geology of lower Dee-side and the southern highland border. *Proceedings of the geologists' association*, 17pp.
- Bearth, P. (1939). Ueber den Zusammenhang von Monte Rosa- und Bernhard- Decke. *Eclogae Geologicae Helvetiae* **32**, 101-111.
- Bearth, P. (1956). Zur Geologie der Wurzelzone östlich des Ossolatales. *Eclogae Geologicae Helvetiae* **49**, 267-278.
- Bearth, P. (1957). Erläuterungen Blatt Saas und Monte Moro, Geologischer Atlas der Schweiz. Nr. **30, 31**. Schweizerische geologische Kommission, Basel.
- Bearth, P. (1958). Ueber den Wechsel der Mineralfazies in der Wurzelzone des Penninikums. *Mineralogische und Petrographische Mitteilungen*, **38**, 363-373.
- Becker, H. (1993). Garnet peridotite and eclogite Sm-Nd mineral ages from the Lepontine dome (Swiss Alps): New evidence for Eocene high-pressure metamorphism in the central Alps. *Geology*, **21**, 599-602.
- Berman, R. G. (1988). Internally-consistent Thermodynamic Data for Minerals in the System Na<sub>2</sub>O-K<sub>2</sub>O-CaO-FeO-Fe<sub>2</sub>O-Al<sub>2</sub>O<sub>3</sub>-SiO<sub>2</sub>-H<sub>2</sub>O-CO<sub>2</sub>. *Journal of Petrology*, **29**, 445-552.
- Berman, R. G. (1990). Mixing properties of Ca-Mg-Fe-Mn garnets. *American Mineralogist*, **75**, 328-344.
- Borghgi, A., Compagnoni, R. & Sandrone, R. (1996). Composite P-T paths in the internal Penninic massifs of the western Alps: Petrological constrains to their thermo-mechanical evolution. *Eclogae Geologicae Helvetiae* **89**, 345-367.
- Bowtell, S. A., Cliff, R. A. & Barnicoat, A. C. (1994). Sm-Nd isotopic evidence on the age of eclogitization in the Zermatt-Saas ophiolite. *Journal of Metamorphic Geology*, **12**, 187-196.
- Bucher, K. & Frey, M. (1994). *Petrogenesis of metamorphic rocks*. Berlin Heidelberg. Springer-Verlag.
- Chopin, C. & Monié, P. (1984). A unique magnesiochloritoid-bearing, high-pressure assemblage from the Monte Rosa, Western Alps: petrologic and <sup>40</sup>Ar-<sup>39</sup>Ar radiometric study. *Contributions to Mineralogy and Petrology* **87**, 388-398.
- Colombi, A. (1989). Métamorphisme et géochimie des roches mafiques des Alpes ouest-centrales (géoprofile Viège-Domodossola-Locarno). *Mém. Géol. Lausanne* **4**, 1-216.
- Colombi, A. & Pfeifer H-R. (1986). Ferrogabbroic and basaltic meta-eclogites from the Antrona mafic-ultramafic complex and Centovalli-Locarno region (Italy and Southern Switzerland)-first results. *Schweizerische Mineralogische und Petrographische Mitteilungen* **66**, 99-110.
- Dal Piaz, G. V. & Lombardo, B. (1986). Early Alpine eclogite metamorphism in the Penninic Monte Rosa- Gran Paradiso basement nappes of the northwestern Alps. Blueschists and Eclogites. *Geological society of America memoir* **164**, 249-265.
- De Capitani, C. & Brown, T. H. (1987). The computation of chemical equilibrium in complex systems containing non-ideal solutions. *Geochimica et Cosmochimica Acta*, **51**, 2639-2652.
- De Capitani, C. (1994). Gleichgewichts-Phasendiagramme: Theorie und Software. *Berichte der*

- Deutschen Mineralogischen Gesellschaft, Beihefte zum European Journal of Mineralogy*, **6**, 48.
- Duchene, S., Blichert-Toft, J., Luais, B., Télouk, P., Lardeaux, J. M. & Albarède, F. (1997). The Lu-Hf dating of garnets and the ages of Alpine high-pressure metamorphism. *Nature* **387**, 586-588.
- Engi, M, Todd, C. S. & Schmatz, D. R. (1995). Tertiary metamorphic conditions in the eastern Lepontine Alp. *Schweizerische Mineralogische und Petrographische Mitteilungen* **75**, 347-369.
- Engi, M., Scherrer, N. C. & Burri, T. (2001a). Metamorphic evolution of pelitic rocks of the Monte Rosa nappe: Constrains from petrology and single grain monazite age data. *Schweizerische Mineralogische und Petrographische Mitteilungen* **81**, 305-328.
- Engi, M., Berger, A. & Roselle, G. T. (2001b). Role of the tectonic accretion channel in collision orogeny. *Geology* **29**, 1143-1146.
- Escher, A., Hunziker, J. C., Marthaler, M., Masson, H., Sartori, M. & Steck, A. (1997). Geologic framework and structural evolution of the western Swiss-Italien Alps. In: Pfiffner, O. A., Lehner, P., Heitzmann, P., Mueller, St. & Steck, A., (eds). *Deep Structure of the Alps, Results of NRP 20*. Basel Boston Berlin: Birkhäuser, 205-222.
- Fox, J. S. (1975). Three-dimensional isograds from the Lukmanier Pass, Switzerland, and their tectonic significance. *Geological Magazine* **112**, 547-626.
- Frey, M., Hunziker, J. C., Neil, J. R. & Schwander, H. W. (1976). Equilibrium-Disequilibrium Relations in the Monte Rosa Granit, Western Alps: Petrological, Rb-Sr and Stable Isotope Data. *Contributions to Mineralogy and Petrology*, **55**, 147-179.
- Frey, M., Desmons, J. & Neubauer, F. (eds) (1999). Metamorphic maps of the Alps. Published by the editors and as enclosure to *Schweizerische Mineralogische und Petrographische Mitteilungen*, **79**.
- Fuhrman, M. L. & Lindsley, D. H. (1988). Ternary-feldspar modelling and thermometry. *American Mineralogist*, **73**, 201-215.
- Graham, C. M. (1981). Experimental Hydrogen Isotope Studies III: Diffusion of hydrogen in hydrous minerals, and stable isotope exchange in metamorphic rocks. *Contribution to Mineralogy and Petrology* **76**, 216-228.
- Gregurek, D., Abart, R. & Hoinkes, G. (1997). Contrasting Eoalpine P-T evolution in the southern Koralpe, Eastern Alps. *Mineralogy and Petrology* **60**, 61-80.
- Guidotti, C. V. (1973). Compositional variation of muscovite as a function of metamorphic grade and assemblages in metapelites from N. W. Main. *Contribution to mineralogy and petrology* **42**, 33-42.
- Guidotti, C. V. & Sassi, F. P. (1976). Muscovite as a petrogenetic indicator mineral in pelitic schists. *Neues Jahrbuch f. Mineralogie. Abhandlungen* **127**, 97-142.
- Guidotti, C. V. (1984). Micas in metamorphic rocks. In: Bailey, S. W. (ed.) Micas. Mineralogical society of America. *Reviews in mineralogy* **13**, 357-467.
- Heinrich, C. A. (1986). Eclogite facies regional metamorphism of hydrous mafic rocks in the central Alpine Adula nappe. *Journal of Petrology* **27**, 123-154.
- Hunziker, J. C. (1970). Polymetamorphism in the Monte Rosa, Western Alps. *Eclogae Geologicae Helvetiae*, **63**, 151-161.
- Hunziker, P. (2003). The stability of tri-octahedral Fe<sup>2+</sup>-Mg-Al chlorite. A combined experimental and theoretical study. *Ph. D., University of Basel*, 162pp.

- Keller, L. M. & Schmid, S. M. (2001). On the kinematics of shearing near the top of the Monte Rosa nappe and the nature of the Furgg zone in the Val Loranco Antrona valley, N. Italy : tectonometamorphic and paleogeographical consequences. *Schweizerische Mineralogische und Petrographische Mitteilungen*, **81**, 347-367.
- Keller, L. M., Abart, R., Stünitz, H. & De Capitani, C. (2003). Deformation, mass transfer and mineral reactions in an eclogite facies shear zone in a polymetamorphic metapelite (Monte Rosa nappe, western Alps). *Journal of Metamorphic Geology*, in press.
- Klein, J. A. (1978). Post-nappe folding southeast of the Mischabel Rückfalte (Pennine Alps) and some aspects of the associated metamorphism. *Leidse Geologische Mededelingen*, **51**, 233-312.
- Laduron, D. (1976). L'antiforme de Vanzone. Etude pétrologique et structurale dans la valle Anzasca (Province de Novara, Italie). *Mém. Inst. Géol. Univ. Louvain* **28**, 1-121.
- Laduron, D. & Martin, H. (1969). Coexistence de paragonite et muscovite et phengite dans un micaschist a gérnat de la zone du Mont-Rose. *Annales de la Société Géologique de Belgique* **T. 92**, 159-172.
- Merlyn, M. (1977). Structure et métamorphisme du complexe Camughera-Moncucco entre la Valle Anzasca et le Val Brevettola (Province de Novara, Italie). PhD thesis, *Université catholique de Louvain*.
- Meyre, C., De Capitani, C. & Partsch, J. H. (1997). A ternary solid solution model for omphacite and its application to geothermobarometry of eclogites from the middle Adula nappe (Central Alps, Switzerland). *Journal of metamorphic Geology* **15**, 687-700.
- Meyre, C., De Capitani, C., Zack, T. & Frey, M. (1999). Petrology of high-pressure metapelites from the Adula nappe (Central Alps, Switzerland). *Journal of Petrology* **40**, 199-213.
- Milnes, A. G., Grellier, M. & Müller, R. (1981). Sequenz and style of major post- nappe structures, Simplon- Pennine Alps. *Journal of Structural Geology*, **3**, 411-420.
- Nagel, T., De Capitani, C. & Frey, M. (2002). Isogrades and *P-T* evolution in the Southeastern Lepontine Dome (Graubünden, Switzerland). *Journal of Metamorphic Geology*, **20**, 309-324.
- Niggli, E. & Niggli, C. R. (1965). Karten einiger Mineralien der alpidischen Metamorphose in den Schweizer Alpen (Stilpnomelan, Alkali-Amphibol, Chloritoid, Staurolith, Disten, Sillimanit). *Eclogae Geologicae Helvetiae* **58**, 335-368.
- Niggli, E. (1970). Alpine Metamorphose und alpine Gebirgsbildung. *Fortschritt in Mineralogie* **47**, 16-26.
- Reinhardt, B. (1966). Geologie und Petrographie der Monte Rosa Zone, der Sesia Zone und des Canavese im Gebiet zwischen Valle d'Ossola und Valle Loana. *Schweizerische Mineralogische und Petrographische Mitteilungen*, **46**, 553-678.
- Rubatto, D., Gebauer, D. & Compagnoni, R. (1997). Dating the UHP/HP metamorphism in the western Alps Sesia-Lanzo and Zemat- Saas- Fee: Evidence for subductions events at the Cretaceous-Tertiary boundary in the Middle Eocene. Fifth Internat. Eclogite Conf. Ascona supplement No1 to *Terra Nova*, **9**, 30-31.
- Shaw, D. M. (1956). Geochemistry of pelitic rocks. Part 3: Major elements and general geochemistry. *Bulletin Geological Society of America* **67**, 919-934.
- Spicher, A. (1976). Tektonische Karte der Schweiz 1: 500'000. *Schweizerische geologische Kommission*.
- Thompson, J. B. (1957). The graphical analysis of the mineral assemblages in pelitic schists. *The*

## References

---

*American Mineralogist* **42**, 842-858.

Todd, C. S. & Engi, M. (1997). Metamorphic field gradients in the Central Alps. *Journal of metamorphic Geology* **15**, 513-530.

## **2. THE PHENGITE-PARAGONITE SOLVUS I: A QUATERNARY SOLUTION MODEL FOR WHITE MICAS BASED ON NATURAL COEXISTING PHENGITE-PARAGONITE PAIRS.**

L. M. Keller, C. De Capitani and R. Abart

Department of Earth Sciences, Basel University, Bernoullistrasse 32, CH-4056 Basel

### **2.1 ABSTRACT**

A thermodynamic model for the quaternary white mica solid solution with end-members muscovite - Mg-celadonite-paragonite - Fe-celadonite (Ms-MgCel-Pg-FeCel) is presented. The interaction energies for the MgCel-Pg join, the FeCel-Pg join and the ternary interactions were obtained from natural coexisting phengite-paragonite pairs. Phengite-paragonite pairs were selected based on the criteria that their chemical compositions may be represented as linear combination of the model end-member compositions and that the respective formation conditions (350°-650°C, 4-21 kbar) are accurately known. The excess free energy expression of Roux & Hovis (1996) was used for the binary Ms-Pg join and those of Massonne & Szpurka (1997) for the Ms-MgCel and Ms-FeCel binaries. The suggested mixing model was tested by calculating multicomponent equilibrium phase diagrams. It proved to be particularly well suited to reproduce compositional variations of white micas from amphibolite facies metapelites

*Keywords: white mica, solution model, equilibrium phase diagrams*



## 2.2 INTRODUCTION

White mica is an ubiquitous phase in low to medium grade metamorphic pelites. In the early work of J. B. Thompson (1957) white mica was treated as an excess phase of fixed (muscovite) composition giving rise to the well-known AFM projection. It was soon recognized (J. B. Thompson, 1957; Guidotti, 1973; Thompson & Thompson, 1976) that this treatment was too simplistic in many cases, because it did not account for the compositional variations of white micas and the coexistence of potassium and sodium rich white micas in metapelites.

Taking muscovite as an end-member, several chemical substitutions may occur in white mica (see Fig. 1). The compositional join between the muscovite ( $\text{KAl}_2(\text{AlSi}_3\text{O}_{10})(\text{OH})_2$ ) and paragonite ( $\text{NaAl}_2(\text{AlSi}_3\text{O}_{10})(\text{OH})_2$ ) end-members is represented by the Na=K substitution. Two Tschermak type substitutions,  $\text{SiMg} = \text{Al}^{\text{VI}} + \text{Al}^{\text{IV}}$  and  $\text{SiFe}^{2+} = \text{Al}^{\text{VI}} + \text{Al}^{\text{IV}}$  lead to the theoretical Mg-celadonite ( $\text{KAlMg}(\text{Si}_4\text{O}_{10})(\text{OH})_2$ ) and Fe celadonite ( $\text{KAlFe}(\text{Si}_4\text{O}_{10})(\text{OH})_2$ ) end-members. White micas with chemical compositions along the muscovite-celadonite join are common in metapelites and they are referred to as phengites. If these phengites are high in sodium the celadonite substitution is usually less pronounced (Guidotti & Sassi, 1976).

At high temperature there is a qualitative closing of the muscovite-paragonite solvus, whereas at low temperatures the solvus opens and a potassium and a sodium rich white mica may coexist (see also Guidotti, 1984). The temperature dependence of the K/Na partitioning works well as qualitative geothermometer, whereas its use as a quantitative geothermometer is not very successful (e. g. Guidotti & Sassi, 1976; Guidotti, 1984). Experiments showed that the solvus on

the ideal Ms - Pg join widens with increasing pressure (e. g. Chatterjee & Flux, 1986). Guidotti et al. (1994a) showed that pressure alone cannot account for the opening of the solvus between potassium and sodium rich white micas, and that the celadonite component in phengites also has an influence on the Na/K partitioning between coexisting paragonite and phengite.

Since the pioneering work of Guidotti & Sassi (1976) it has been known that the solvus between sodium and potassium rich white micas opens with increasing celadonite component. This is documented by the fact that the phengite limb of the solvus approaches successively more potassium rich compositions with increasing celadonite component (Katagas & Baltazis, 1980; Enami, 1983; Grambling, 1984; Guidotti, 1984). The celadonite content in phengite, in turn, increases with increasing pressure but is sensitive to mineral assemblages additional (Guidotti & Sassi, 1998).

Mixing models exist for the binary muscovite-paragonite (Eugster et al., 1972; Chatterjee & Flux, 1986; Chatterjee & Froese, 1975; Roux & Hovis, 1996) and the muscovite-celadonite joins (Massonne & Szpurka, 1997; Coggon & Holland, 2002). A quaternary model that covers the entire composition space that spans the muscovite, paragonite, Mg-celadonite and Fe-celadonite end-members, has, however, not been calibrated so far.

We suggest a quaternary mixing model that covers the entire composition space of phengites and paragonite. Our model is based on existing binary interaction parameters from the literature and additional binary and ternary interaction terms, which were derived from the analysis of coexisting phengite and paragonite from natural rocks. Our model accounts for the combined



pressure and bulk rock composition effect on the K/Na partitioning between coexisting Phe and Pg. Application of our model in phase equilibrium calculations yields correct descriptions of phase relations in metapelites and will foster the petrologic analysis of white mica bearing assemblages by means of geothermobarometry and phase diagram calculations. This particularly concerns pelitic schists at high-pressure metamorphic conditions where sodium and potassium are mainly stored within Phe and Pg.

## 2.3 INPUT DATA

### 2.3.1 Published solid solution models based on experimental data

The shape of the solvus in the quaternary white mica system strongly depends on the three binary solvi on Ms – Pg, Pg – MgCel and Pg – FeCel joins. At low temperature conditions, each of the three binary joins exhibits miscibility gaps. It is found that the Ms – Pg solid solution model of Roux & Hovis (1996) best fits the compositional data from our samples. This is particularly true for pairs of coexisting Phe – Pg from Al-rich high-grade (c. 600°C/c. 7 kbar) pelitic rocks from the Lepontine Alps. The model of Raux & Hovis (1996) predicts a relatively narrow miscibility gap. The miscibility gap of solution models from earlier workers (e.g. Chatterjee & Froese, 1975) is too wide to reproduce natural data (Roux & Hovis, 1996; Blencoe et. al., 1994 their Fig. 3). For the two binaries Ms – MgCel and Ms – FeCel we used the solution model of Massonne & Szpurka (1997).

### 2.3.2 End-member calculation of natural coexisting Paragonite – Phengite pairs

We investigated 63 coexisting Pg-Phe pairs from 56 samples (Table 1). Data were taken from

the literature and from our own work. Sample selection was based on the following criteria: 1) The P-T conditions of Pg - Phe equilibration must be known accurately. 2) The chemical composition of the white micas must be a linear combination of the end-members Ms, Pg, MgCel and FeCel.

The mol fractions of the end-members Ms , Pg , MgCel and FeCel were calculated by applying the method of least squares to the following set of equations:

$$\begin{bmatrix} 3 & 3 & 4 & 4 \\ 3 & 3 & 1 & 1 \\ 0 & 0 & 0 & 1 \\ 0 & 0 & 1 & 0 \\ 1 & 0 & 1 & 1 \\ 0 & 1 & 0 & 0 \end{bmatrix} \times \begin{bmatrix} X_{Ms} \\ X_{Pg} \\ X_{MgCel} \\ X_{FeCel} \end{bmatrix} = \begin{bmatrix} Si \\ Al \\ Fe \\ Mg \\ K \\ Na \end{bmatrix}$$

where the matrix to the left contains the stoichiometric coefficients of Si, Al, Fe, Mg, K, and Na in end member compositions (columns), and the column vector on the right hand side gives the measured white mica composition.  $X_{Ms}$ ,  $X_{Pg}$ ,  $X_{MgCel}$  and  $X_{FeCel}$  are the end-member mol fractions. The element concentrations of each sample were re-calculated from the end member contents and compared to the element concentrations analysed by microprobe. Theoretically there should be a 1:1 correlation between re-calculated and analysed element concentrations. In actual fact, small discrepancies between analysed and re-calculated element concentrations occur, which are due to the analytical uncertainty inherent in microprobe analysis and to the fact that the four endmembers cannot fully account for white mica compositions. Assuming that the deviation of the re-calculated from the analysed element concentration is normally distributed, we calculated the  $1\sigma$  standard deviation for each element. Then in our analyses we only considered those samples, which fall within a  $3\sigma$  band around the 1:1 correlation

Table 1. Source of data and P/T conditions of coexisting phengite and paragonite pairs

Sample	T(°C)	P(kbar)	Ref.	n
<b>low-T, low-P</b>				
71a	350	4*	1	2
140c	350	4*	1	2
187c	350	4*	1	2
764 MR	350	5	2	2
51/57	475*	7*	3	2
114/70	475*	7*	3	2
157/70	475*	7*	3	2
131/70	475*	7*	3	2
33-1H	480-500	7	4	2
33-5A	480-500	7	4	2
34-3A	480-500	7	4	2
3-6A	480-500	7	4	2
8-6A	480-500	7	4	2
26-3B	480-500	7	4	2
39-3A	480-500	7	4	2
?	425*	8.9*	5	2
Total				32
<b>low-T, medium-P</b>				
Z3th	420	>11	6	2
Care0041	365	13	7	4
AL269	510	13.5	8	2
P80/36	450	17	9	2
P82/46	450	17	9	2
6.298c	420**	14**	10	2
Total				14
<b>high-T, low-P</b>				
77-244c	580*	4*	11	2
81-42	580*	4*	11	2
M.76.2W	530	5	12	2
A271	580-610*	6*	13	2
A40	580-610*	6*	13	2
510	580-610*	6*	13	2
T10	600	7	14	2
KL264	600	7	14	2
KL285	600	7	14	2
KL185	600	7	14	2
KL98	600	7	14	2
Al 235	625	<7	15	2
Al 280	625	<7	15	2
Al 286	625	<7	15	2
Al 389	625	<7	15	2
Al 365	625	<7	15	2
Total				32
<b>high-T, medium-P</b>				
OP-08	c.600	c.10	16	2
CHM1	c.650	10-11	17	2
3	650	12.5	18	6
4	650	12.5	18	10
PD-162	580	13	19	2
PD-167A	580	13	19	2
PD-189C	580	13	19	2
Ad85	>550	>15	20	2
88DM143	500-600	15	21	2
3M	600	15	22	2
KL283	600-700**	9-15**	23	2
KL409	600-700**	9-15**	23	2
Total				36
<b>high-T, high-P</b>				
Z6-50-12	<700	18-21	17	2
24-23	580-640	18-24	24	2
43-3	580-640	18-24	24	2
82092801	580-640	18-24	24	2
KL264	>580**	>17**	23	2
92-17A	600-650	20.5-21.5	25	2
Total				12
Overall sum				126
(1) Katagas (1980)			(13) Hoffer (1978)	
(2) Franceschelli et al. (1989)			(14) Koch (1982)	
(3) Höck (1974)			(15) Irouschek (1983)	
(4) Ferry (1992)			(16) Enami (1983)	
(5) Ahn et al. (1985)			(17) Meyre (1999)	
(6) Gili Ibaraguchi & Dallmeyer (1991)			(18) Keller et al. (in prep.)	
(7) Bucher (unpub. data and pers. com.)			(19) Feininger (1990)	
(8) Okay (1989)			(20) Heinrich (1982)	
(9) Theye & Seidel (1991)			(21) Chopin et al. (1991)	
(10) Chopin (1979)			(22) Brown & Forbes (1986)	
(11) Grambling (1984)			(23) Nagel (2002b)	
(12) Aswirth & Evrigen (1984)			(24) Hirajima et al. (1988)	
			(25) Zhang et al. (1994)	
* P and/or T after Guidotti et al. (1994a)				
** P and T after Vidal et al. (2001)				
* P after the present author				
**P/T after the present author				

three pairs from Nagel (2002b), the 5 almost binary Phe – Pg pairs ( $X_{\text{FeCel}}$  in phengite  $\leq 0.01$ ,  $X_{\text{MgCel}}$  in phengite  $\leq 0.05$ ) of Irouschek (1983) and one pair, of which phengite composition gives negative end-members values were only used for comparative purposes and model testing.

### 2.3.3 Phengite composition

For the phengites the measured chemical compositions are compared with the compositions recalculated from the end-members in Fig. 1. Fig. 2a shows that in our data set  $X_{\text{Cel}}$  ( $X_{\text{MgCel}} + X_{\text{FeCel}}$ ) in Phe is correlated with the Si content. This indicates that the Si content is predominately controlled by the Tschermak substitution ( $\text{SiMg}/\text{Fe}^{2+} = \text{Al}^{\text{VI}} + \text{Al}^{\text{IV}}$ ). The pyrophyllitic substitution ( $(\text{Na}/\text{K})\text{Al} = \square\text{Si}$ ) (e. g. Bousquet et al., 2002) has only a minor effect on the Si-content in Phe. This is supported by the fact that the generally high K+Na content in Phe does not depend on  $X_{\text{Cel}}$  ( $X_{\text{MgCel}} + X_{\text{FeCel}}$ ) (Fig. 2b). The recalculated Mg content in Phe shows rather good correlation with the measured Mg content (Fig. 1c). In contrast, the recalculated Fe content of Phe is systematically lower than the measured Fe content (Fig. 1d). This discrepancy suggests that most of the selected phengites contain ferric iron. The largest differences between recalculated and analysed Fe contents indicate maximum ferric iron contents of 0.06  $\text{Fe}^{3+}$  atoms p.f.u. Most of the phengites contain less than 0.04  $\text{Fe}^{3+}$  atoms p.f.u. (Fig. 2c). The phengites show a good correlation between the measured and the recalculated Al content. This suggests that the  $\text{Fe}^{3+}$  content of the selected phengites does not result from the substitution of  $(\text{Fe}^{3+})^{\text{VI}}$  for  $\text{Al}^{\text{VI}}$ . Possibly the  $\text{Fe}^{3+}$  content in the phengites can be explained by the substitution  $\text{Fe}^{2+} + \text{H} = \text{Fe}^{3+} + \square$  (see Guidotti 1984). In addition, Fig. 1c, d indicate that the substitution

for each element ( $3\sigma$  (atoms p.f.u): Si=0.066, Al=0.025, Fe=0.056, Mg=0.054, K=0.083, Na=0.086). Based on this criterion we had to exclude 14 Phe - Pg pairs. For the remaining 49 Phe-Pg pairs only 33 were used for the calibration of a mixing model.

Our own seven pairs form unpublished data,

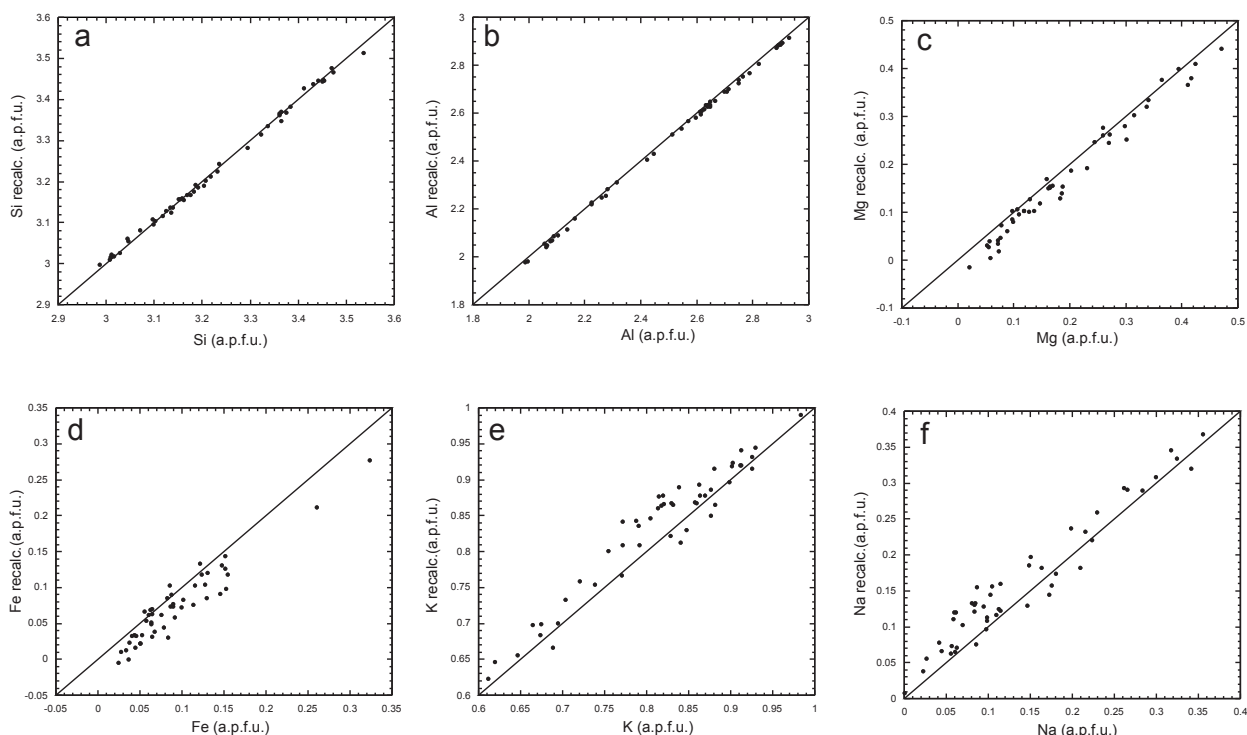


Fig. 1 Correlation between chemical composition of phengites and their end-member composition. The measured content of Si (a), Al (b), Mg (c), Fe (d), K (e) and Na (f) (a.p.f.u.) is plotted versus their content recalculated from the end-members. An analysis representing a true linear combination of the four considered end-members should lie on the bold lines.

$\text{SiMg} = \text{Al}^{\text{VI}} + \text{Al}^{\text{IV}}$  is preferred with respect to the substitution  $\text{SiFe}^{2+} = \text{Al}^{\text{VI}} + \text{Al}^{\text{IV}}$  particularly in phengites with high Si content.

### 2.3.4 Paragonite composition

It has repeatedly been reported (Guidotti, 1984) that, in contrast to phengite, paragonite generally contains very little or no Mg,  $\text{Fe}^{2+}$  or  $\text{Fe}^{3+}$ . Guidotti et al. (2000) claim that the incorporation of minor amounts of these cations into paragonite does not depend on pressure. Substitution of substantial amounts of magnesium and ferric or ferrous iron would destabilize paragonite due to crystallochemical constraints (Guidotti, 1984). In addition, it was shown experimentally that magnesium substitution is very limited in paragonite (Franz & Althaus, 1976). These findings are in line with our observations. In our data set the measured Mg,  $\text{Fe}_{\text{tot}}$  concentrations and the calculated celadonite contents in paragonite are very low.

## 2.4 CALCULATION PROCEDURE

In the quaternary system Ms-MgCel-Pg-FeCel we estimated the binary interaction parameters on the MgCel - Pg and on the FeCel - Pg joins and all ternary interaction parameters from the available information on compositions and formation conditions of coexisting Pg - Phe pairs (Tables 1, 2). The remaining interaction parameters were taken from the literature.

Table 2 Margules excess terms

System	Ms - MgCel - Pg - FeCel		
	WH (J)	WS (J/K)	WV (J/bar)
W112*		15.920	0.187
W122*		58.598	0.735
W113**	6150		0.452
W133**	15050		0.452
W114*=W144*		24.083	0.3394
W223=W233	<b>14224</b>		<b>0.520</b>
W334=W344	<b>16620</b>		<b>0.340</b>
W123=Q123	<b>24824</b>	<b>37.260</b>	<b>1.430</b>
W124=Q124		<b>61.340</b>	<b>0.800</b>
W134=Q134	<b>27220</b>	<b>24.083</b>	<b>1.130</b>
W234=Q234	<b>30844</b>		<b>0.860</b>

Note :  $W_G = W_H - W_S T + W_V P$

\* Excess terms after Masson and Szpurka (1997)

\*\* Excess terms after Roux and Hovis (1996)

Parameter labeling after equation (2)

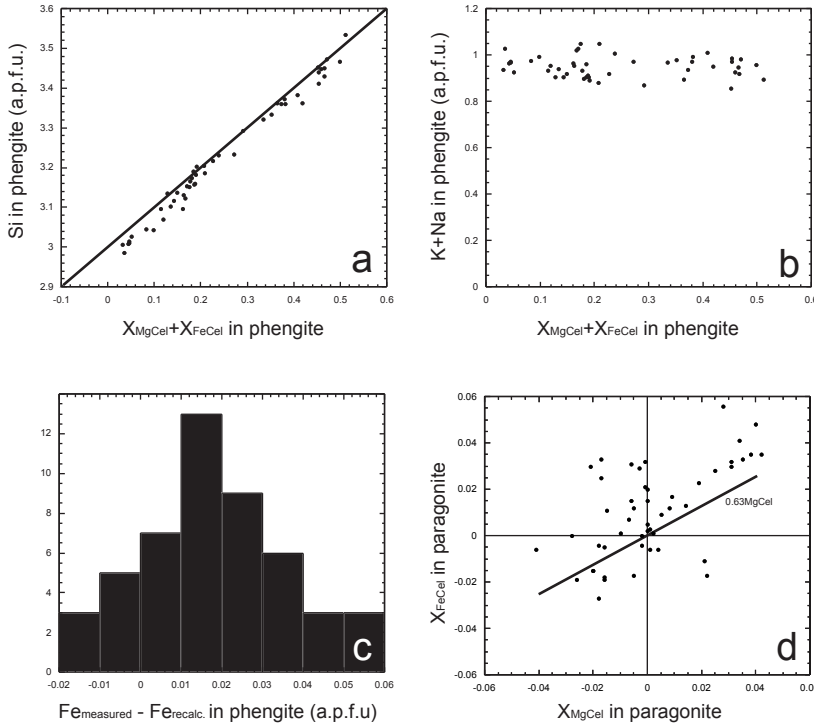


Fig. 2

a) Si content of phengite versus calculated celadonite content. An analysis which represents a true linear combination of the four considered end-members and which results from true Tschermak substitution should lie along the bold line.

b) K + Na content of phengite versus calculated celadonite content. If the Si content in phengite is also controlled by pyrophyllitic substitution there should be a dependence between the K+Na content of phengite and celadonite content.

c) Frequency diagram of the difference between the measured and the recalculated Fe content in phengite (a.p.f.u.). For further explanation the reader is referred to the text.

d) X<sub>FeCel</sub> in paragonite versus X<sub>MgCel</sub> in paragonite. The celadonite content in paragonite is very small. The linear equation represents a constant ratio between X<sub>FeCel</sub> and X<sub>MgCel</sub> calculated from all data points. For further explanation the reader is referred to the text.

### 2.4.1 Chemical potential expression

If the quaternary solutions are described in terms of their end-members, the following expression gives the Gibbs free energy as a function of the respective end-member concentrations, where  $\Delta G_{\text{ex}}$  accounts for molecular non-ideal mixing.

$$\Delta G_{\text{mix}} = \sum_i^n x_i \mu_i^\circ + RT \sum_i^n x_i \ln x_i + \Delta G_{\text{ex}} \quad (1)$$

where  $\mu_i^\circ$  is the chemical potential of end-member  $i$  at standard state and  $X_i$  is the mole fraction of end-member  $i$ :  $1 = \text{Ms}$ ,  $i : 2 = \text{MgCel}$ ,  $i : 3 = \text{Pg}$  and  $i : 4 = \text{FeCel}$ .

For  $\Delta G_{\text{ex}}$  we used the quaternary expansion of Jackson (1989), which is based on the ternary equation of Wohl (1946, 1953). The following relation gives the quaternary excess function ( $\Delta G_{\text{ex}}$ ).

$$\begin{aligned} \Delta G_{\text{ex}} = & X_1 X_2 (X_3 W_{112} + X_2 W_{122}) \\ & + X_1 X_3 (X_1 W_{113} + X_3 W_{133}) \\ & + X_1 X_4 (X_1 W_{114} + X_4 W_{144}) \\ & + X_2 X_3 (X_2 W_{223} + X_3 W_{233}) \\ & + X_2 X_4 (X_2 W_{224} + X_4 W_{244}) \\ & + X_3 X_4 (X_3 W_{334} + X_4 W_{344}) \\ & + X_1 X_2 X_3 Q_{123} + X_1 X_2 X_4 Q_{124} \\ & + X_1 X_3 X_4 Q_{134} + X_2 X_3 X_4 Q_{234} \end{aligned} \quad (2)$$

where

$$Q_{ijk} = 0.5(W_{ij} + W_{ji} + W_{ik} + W_{ki} + W_{jk} + W_{kj}) - C_{ijk} \quad (3)$$

In our treatment we set the ternary Wohl  $C_{ijk}$  terms to zero. Because there are no indications of an asymmetric miscibility gap between MgCel – Pg and between FeCel – Pg a symmetric Margules mixing model was used for these binary joins ( $W_{223} = W_{233}$ ,  $W_{334} = W_{344}$ ). We assume ideal Fe-Mg mixing on the MgCel–FeCel binary join (Coggen & Holland, 2002) thus  $W_{224}$  and  $W_{244}$  are set to zero. These simplifications yield an excess function:

$$\begin{aligned} \Delta G_{\text{ex}} = & X_1 X_2 (X_1 W_{112} + X_2 W_{122}) \\ & + X_1 X_3 (X_1 W_{113} + X_3 W_{133}) \\ & + X_1 X_4 (X_1 W_{114} + X_4 W_{144}) \\ & + X_2 X_3 (X_2 W_{223} + X_3 W_{233}) \\ & + X_3 X_4 (X_3 W_{334} + X_4 W_{344}) \\ & + X_1 X_2 X_3 (0.5W_{112} + 0.5W_{122} + 0.5W_{113} + 0.5W_{133} + 0.5W_{223} + 0.5W_{233}) \\ & + X_1 X_2 X_4 (0.5W_{112} + 0.5W_{122} + 0.5W_{114} + 0.5W_{144}) \\ & + X_1 X_3 X_4 (0.5W_{113} + 0.5W_{133} + 0.5W_{114} + 0.5W_{144} + 0.5W_{334} + 0.5W_{344}) \\ & + X_2 X_3 X_4 (0.5W_{223} + 0.5W_{233} + 0.5W_{334} + 0.5W_{344}) \end{aligned} \quad (4)$$

The binary interaction parameters  $W_{112}$ ,  $W_{122}$ ,  $W_{114}$ ,  $W_{144}$ ,  $W_{113}$  and  $W_{133}$  were taken from the literature (Roux and Hovis, 1996; Massonne & Szpurka, 1997). As we assumed symmetric mixing between MgCel – Pg and between FeCel – Pg there remain two unknown parameters in equation (4):  $W_{223}$  ( $=W_{233}$ ) and  $W_{334}$  ( $=W_{344}$ ). The chemical potentials can be calculated from the following relation:

$$\mu_m = \Delta G_{\text{mix}} + \frac{\partial \Delta G_{\text{mix}}}{\partial x_m} - \sum_{i=1}^n x_i \frac{\partial \Delta G_{\text{mix}}}{\partial x_i} \quad (5)$$

where  $\mu_m$  is the chemical potential of any end-member. The second term in (5) is given by the following expression:

$$\frac{\partial \Delta G_{\text{mix}}}{\partial x_m} = \mu_m^\infty + RT \ln x_m + RT + \frac{\partial \Delta G_{\text{ex}}}{\partial x_m} \quad (6)$$

and the third term in (5) is given by:

$$\begin{aligned} \sum_{i=1}^n x_i \frac{\partial \Delta G_{\text{mix}}}{\partial x_i} = \\ \sum_{i=1}^n \mu_i^\infty x_i + RT \sum_{i=1}^n x_i \ln x_i + RT \sum_{i=1}^n x_i + \sum_{i=1}^n x_i \frac{\partial \Delta G_{\text{ex}}}{\partial x_i} \end{aligned} \quad (7)$$

by considering:

$$RT \sum_{i=1}^n x_i = RT \quad (8)$$

and combining (1), (3), (4) and (5) the chemical potential can be expressed as:

$$\mu_m = \mu_m^\infty + RT \ln x_m + \Delta G_{\text{ex}} + \frac{\partial \Delta G_{\text{ex}}}{\partial x_m} - \sum_{i=1}^n x_i \frac{\partial \Delta G_{\text{ex}}}{\partial x_i} \quad (9)$$

Then for the quaternary system at a given P and T, two coexisting Phe – Pg pairs must meet the following equilibrium conditions:

$$\begin{aligned} \mu_{\text{Ms}}^{\text{Phe}} &= \mu_{\text{Ms}}^{\text{Pg}} \\ \mu_{\text{MgCel}}^{\text{Phe}} &= \mu_{\text{MgCel}}^{\text{Pg}} \\ \mu_{\text{Pg}}^{\text{Phe}} &= \mu_{\text{Pg}}^{\text{Pg}} \\ \mu_{\text{FeCel}}^{\text{Phe}} &= \mu_{\text{FeCel}}^{\text{Pg}} \end{aligned} \quad (10)$$

By substituting the derivations of equation (4) into equation (9), which is subsequently substituted into equations (10) and collecting all unknown parameters, one obtains a system of four equations in two unknowns. The unknown interaction energies  $W_{223}$  ( $=W_{233}$ ) and  $W_{334}$  ( $=W_{344}$ ) for 33 selected coexisting Phe – Pg pairs were calculated at the corresponding P-T conditions by applying the method of least squares to the equation system (10). From the pressure dependence of the obtained interaction energies we fitted  $W_V$  for the unknown interaction parameters. A temperature dependent term  $W_S$  was not considered. This is motivated by the fact that the shift of the Phe-limb of the solvus can be correlated to a pressure induced increase of the ferromagnesian content of Phe (Guidotti et al., 1994a) indicating that the non-ideality of the Phe – Pg solvus depends primarily on pressure and not on temperature.

When minerals with close to end-member compositions are used, the calculated interaction energies are very sensitive to uncertainties in the determination of end-member contents. In this respect, the celadonite content in paragonite poses a problem, because the mole fractions of  $X_{\text{MgCel}}$  and  $X_{\text{FeCel}}$  in paragonite are generally small. To avoid this problem, a constant value for  $X_{\text{MgCel}}$  and  $X_{\text{FeCel}}$  in paragonite was assumed for all the phengite – paragonite pairs that were used



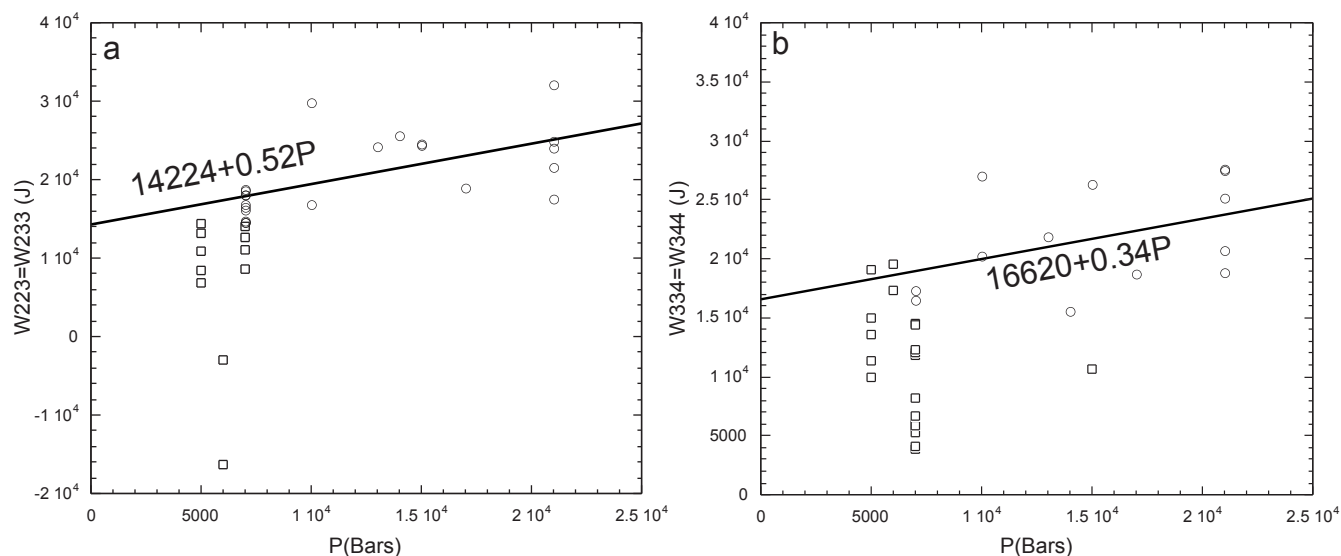


Fig. 3 Calculated interaction energies versus pressure and the resulting fit of the interaction parameters. Open circles are interaction energies used in order to fit the interaction parameters. Open rectangles are omitted interaction energies. Note that  $\leq 7$  kbar the calculated interaction energies scatter over a wide range and do not linearly depend on pressure. a) Interaction energies and parameters for the binary paragonite-Mg-celadonite join. b) Interaction energies and parameters for the binary paragonite-Fe-celadonite join.

for the calculation of interaction energies. The mean celadonite content of the 49 paragonites is 1.2 mol %, where the average proportions of Fe- and Mg celadonite are ( $X_{\text{FeCel}}/X_{\text{MgCel}} = 0.63$ ) (Fig. 2d). On average this yields 0.7 mol % Mg-celadonite and 0.5 mol % for Fe-celadonite content in paragonite. The major problem of fitting the interaction parameters on the MgCel-Pg join and the FeCel-Pg join is the lack of data of Phe with compositions near both binary joins. However, the calculated interaction energies for the MgCel-Pg join ( $W_{223}$ ,  $W_{233}$ ) and the FeCel-Pg join ( $W_{334}$ ,  $W_{344}$ ), in particular for coexisting Phe-Pg pairs where the celadonite content in phengite is high, cause a miscibility gap at corresponding P-T conditions. Consequently we used binary interaction energies, which are high enough to produce a miscibility gaps in order to fit for both  $W_{223}(=W_{233})$  and  $W_{334}(=W_{344})$  (open circles in Fig. 3a,b). Note that the used binary interaction energies correspond to Phe-Pg pairs equilibrated at  $\geq 7$  kbar where the interaction energy is a linear function of pressure. Below 7 kbar the calculated interaction energies scatter over a wide range and

most interaction energies are too small in order to produce miscibility gaps.

## 2.5 COMPARISON BETWEEN THE MODEL PREDICTIONS AND OBSERVATIONAL DATA

To test our model, we re-calculated the phengite composition of the coexisting 33 Phe-Pg pairs we used to derive interaction energies. In addition we compared model predictions and measured compositions for the samples of Irouschek (1983). These Phe-Pg pairs may be regarded as true linear combination of the model end-members and the P-T condition of equilibration are accurately known. The thermodynamic calculations were done with the computer program THERIAK (De Capitani & Brown, 1987; De Capitani, 1994), which calculates the stable mineral assemblage and the composition of the solid solutions for fixed values of P, T and given bulk composition. In this case the stable mineral assemblage is always composed of Phe and Pg. For the bulk composition we used the composition defined by a 1:1 mixture of the measured compositions of

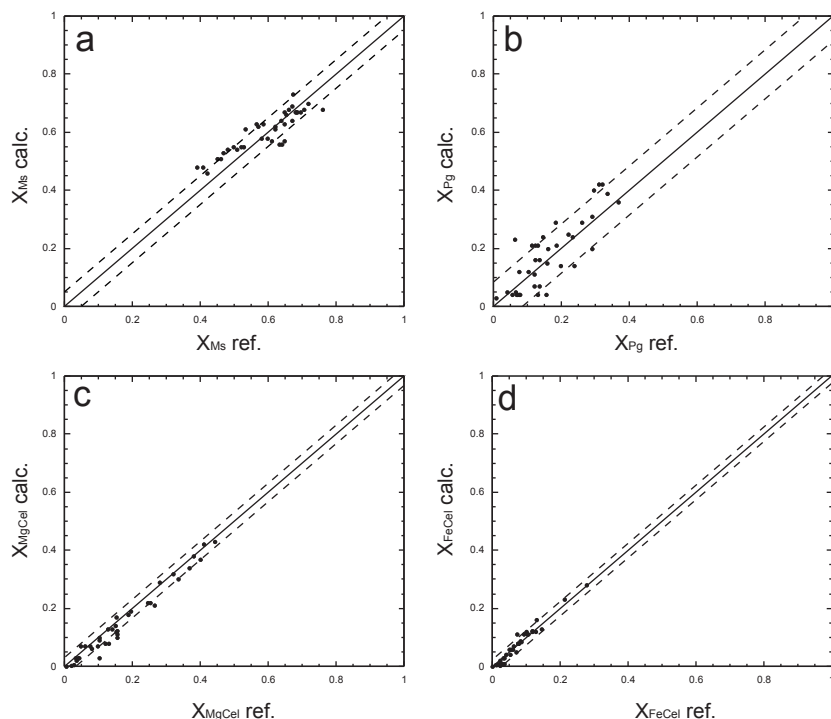


Fig. 4 Calculated end-member compositions of phengite versus reference compositions ( $X_{Msref}$ ,  $X_{MgCelref}$ ,  $X_{Pgref}$  and  $X_{FeCelref}$ ) vs. ( $X_{Mscalc}$ ,  $X_{MgCelcalc}$ ,  $X_{Pgcalc}$  and  $X_{FeCelcalc}$ ). The compositions are calculated at the reference P, T-conditions of each coexisting phengite and paragonite pair for the bulk composition corresponding to a 1:1 mixture of the measured compositions of the coexisting phengite and paragonite. The dashed line is  $2\sigma$  of the deviation between the calculated and the reference end-member compositions.  
 a) Calculated muscovite content versus reference muscovite content ( $2\sigma=0.05$ ).  
 b) Calculated paragonite content versus reference paragonite content ( $2\sigma=0.08$ ).  
 c) Calculated Mg-celadonite content versus reference Mg-celadonite content ( $2\sigma=0.03$ ).  
 d) Calculated Fe-celadonite content versus reference Fe-celadonite content ( $2\sigma=0.02$ )

the coexisting phengite and paragonite. The results and  $2\sigma$  of the difference between the reference composition and the calculated composition are given in Fig. 4. The good correlation between measured and re-calculated compositions in Fig. 4 shows that the model correctly reflects white mica phase relations.

To further test our model we calculated isothermal/isobaric sections of the ternary Phe-Pg (Ms-MgCel-Pg) miscibility gap and compared these with natural data (Fig. 5). For the sake of simplicity data points, which lie inside the quaternary composition space are projected onto the Ms-MgCel-Pg ternary plane from the FeCel apex. Because this projection deviates from a thermodynamic projection and in order to obtain an idea of the geometry of the quaternary solvus we also projected sectional parts of the quaternary Phe-Pg (Ms-MgCel-Pg-FeCel) miscibility gap onto the Ms-MgCel-Pg ternary plane; the sections correspond to a constant  $X_{FeCel}$  in phengite.

To illustrate the effect of P and T on the ternary solvus calculations were done for five different

P-T regimes. The coexisting phengite-paragonite pairs were divided into five P-T categories (Table 1, Fig. 5). The ternary sections were calculated with the computer program THERTER (De Capitani, 1994) using the thermodynamic end-member properties for Ms, MgCel and Pg of Berman (1988, update 92). Because the solvus varies only slightly within the P-T range of a distinct P-T category the sections were calculated for the lower and upper P-T boundary limiting the categories (Fig. 5). Fig. 5 shows that our model is compatible with most natural data.

The effect of the Cel component on the Phe-Pg solvus is most pronounced at high-T and low-P conditions and only if  $X_{MgCel}$  in Phe is relatively low ( $X_{MgCel} < 0.2$ ) (Fig. 5b). Towards lower temperatures the above effect decreases (Fig. 5a, b). As pressure increases the solvus widens and consequently the effect of the MgCel component becomes less pronounced at high pressure (Fig. 5c, d).

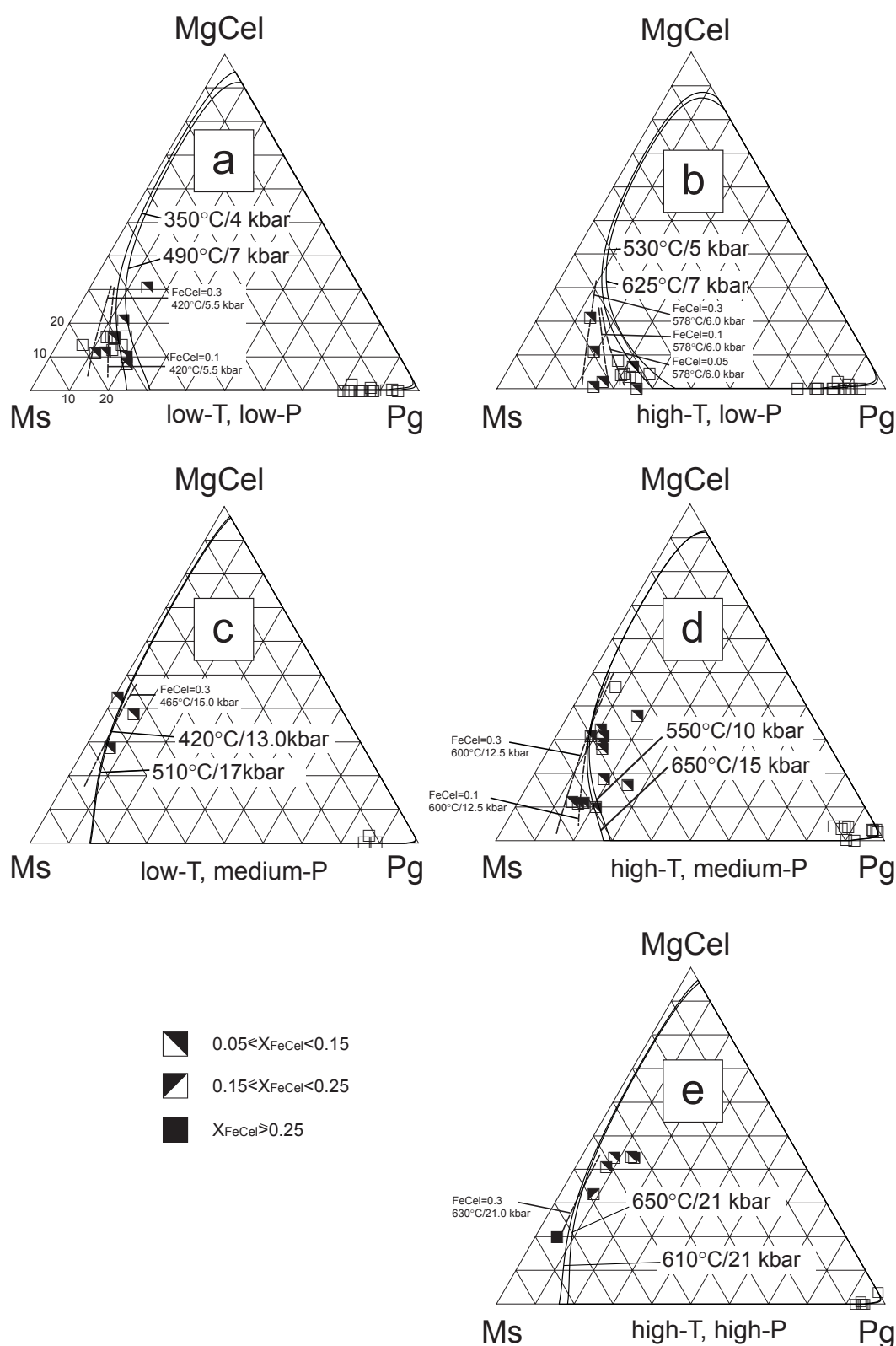


Fig. 5 Comparison of the ternary solvi, calculated from our model with the natural data of coexisting phengite – paragonite pairs.. The data are subdivided into 5 P, T-dependent categories according to Table (1): (a) low-T, low-P; (b) high-T, low-P; (c) low-T, medium-P; (d) high-T, medium-P; (e) high-T, high-P. Stippled lines indicate sectional parts of the quaternary Phe-Pg solvus. These sections are calculated for a constant  $X_{FeCel}$  in phengite and at P-T conditions lying in between the lower and upper P-T boundary of the P-T categories and are projected onto the ternary plane.

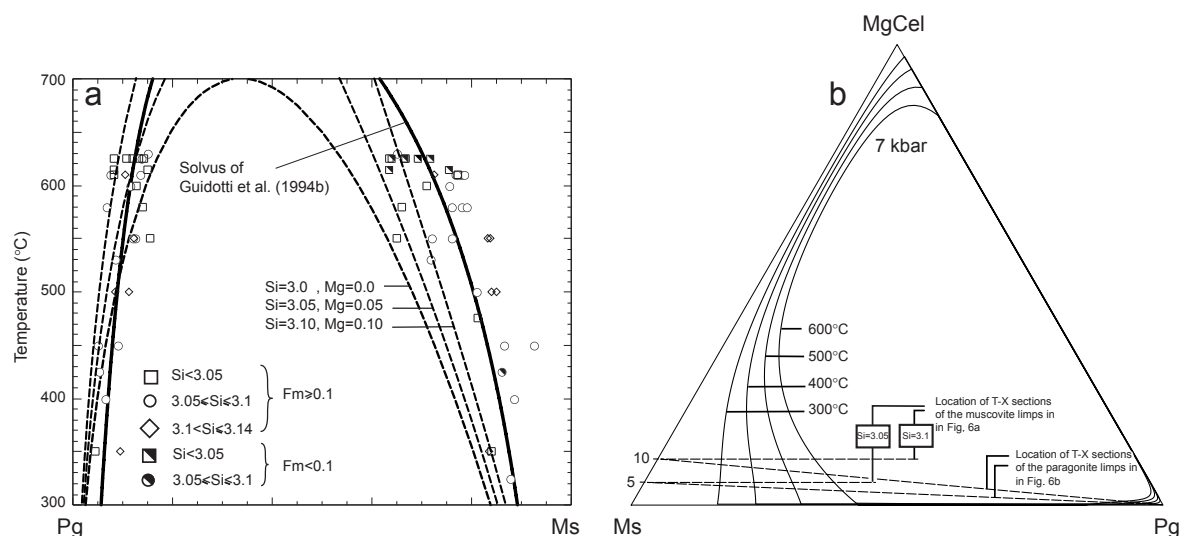


Fig. 6

a) Comparison of the solvus of Guidotti et al. (1994b) with T-X sections through the ternary solvus calculated for Si content in phengite of 3.0, 3.05 and 3.1 at the reference pressure of 7 kbar given by Guidotti et al. (1994b) for their solvus. The data points corresponds to the compilation of Guidotti et al. (1994b) whereas the composition are close to the muscovite-paragonite join. The data points are subdivided due to the Si and ferromagnesian content in phengite. b) Ternary solvi calculated at 300°C, 400°C, 500°C and 600°C at 7 kbar showing the location of the T-X sections. Note that for a constant Si content in phengite the T-X sections can-not be calculated on a sections between ideal paragonite and phengite.

## 2.6 COMPARING OUR SOLUTION MODEL WITH OTHER MODELS, APPLICATION AND DISCUSSION

### 2.6.1 Comparing our solution model with other models

Because the effect of the MgCel component on the Phe-Pg solvus is most pronounced for low MgCel contents in Phe we compare our model with the Pg-Ms solvus established by Guidotti et al. (1994b). These authors used natural coexisting Pg-Ms pairs with compositions (Fig. 6a, Guidotti et al., 1994b; their Table A1) near the ideal Pg-Ms join in order to establish parametric equations, which describe the T-X form of the solvus. The Ms compositions used by the former authors deviate slightly from the ideal composition (Fig. 6a, Si=3.0-3.14 a.p.f.u; Fm(Fe<sup>2+</sup>+Mg+Fe<sup>3+</sup>)=0.02-0.26 a.p.f.u). To compare predictions from our model with the model of Guidotti et al. (1994b) we calculated three binary T-X-sections through the ternary solvus. These sections were calculated with the computer program DOMINO (De

Capitani & Brown, 1987; De Capitani, 1994) for the reference pressure of 7 kbar given by Guidotti et al. (1994b) for their solvus. The locations of the T-X sections are shown in Fig. 6b. A constant Si content in Phe is achieved by calculating the T-X sections on sections of constant X<sub>MgCel</sub> (Fig. 6b). In T-X sections between ideal Pg and Phe the Si content in Phe is not constant (Fig 6b). In our case it decreases with increasing temperature and K-Na mixing in Phe is overestimated towards higher temperature if it is compared to sections where the Si content in Phe is constant (Fig. 6b). The Pg limb is calculated on sections with the end-members of ideal Pg and Phe (Fig. 6b). For a celadonite (MgCel) content in the range of 0.05-0.1 (Si=3.05-3.1 p.f.u) there is good agreement between the data of Guidotti et al. (1994b) and the model presented here (Fig. 6a). In addition there is good agreement between the Ms limb of the solvus of Guidotti et al. (1994b) and the Ms limb of our model corresponding to a celadonite (MgCel) content of 0.1 (Fig. 6a).

Up to know the only thermodynamic

considerations, which account for the effect of the celadonite component in Phe were recently given by Coggon & Holland (2002) for the system  $\text{Na}_2\text{O}-\text{K}_2\text{O}-\text{MgO}-\text{Al}_2\text{O}_3-\text{SiO}_2-\text{H}_2\text{O}$ . These authors propose 52 kJ to be the interaction energy on the binary Pg-MgCel join. This high interaction energy causes a miscibility gap on the binary Pg-MgCel join, which is very wide over a large P-T range and thus may restrict the position and shape of the ternary solvus to within a relatively small compositional range. In contrast, our investigations point to a much lower interaction energy and the ternary isothermal/isobaric sections calculated for

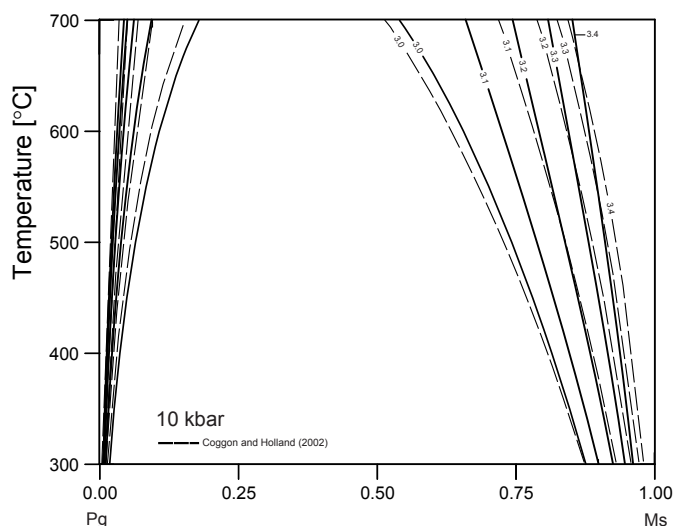


Fig. 7 Comparison of the solvi of Coggon & Holland (2002) with T-X sections through the ternary solvus calculated for Si content in phengite of 3.1, 3.2, 3.3 and 3.4 at pressure of 10 kbar. The location of the T-X sections are defined as in Fig. 6b.

the P-T range of the natural data presented herein indicate that much lower interaction energy suffices to cause a miscibility gap on the binary Pg-MgCel join. In order to compare the results obtained by Coggon & Holland (2002; their Fig. 5b) with our model we calculated T-X sections through the ternary Ms-MgCel-Pg solvus. These were calculated for different Si contents in Phe. In general there is agreement between the results of Coggon & Holland (2002) (their Fig. 5b) and our model (Fig. 7). But by comparing the Ms limbs of

our model with the Ms limbs of the model Coggon & Holland (2002) it is obvious that the latter are restricted to a relatively small compositional range particularly at higher Si (>3.2) content in Phe (Fig. 7). As stated above this is caused by the high interaction energy on the Pg-MgCel join.

### 2.6.2 Limits of the presented solution model

Because the model is calibrated for pressures up to 21 kbar at about 650°C we do not recommend an extrapolation towards much higher pressures. At low pressures and high temperatures the solution model allows complete mixing between Pg-Ms and between Pg-Cel (MgCel, FeCel). As this occurs outside the high-temperature low-pressure stability limit of paragonite, which may be given by the assemblage phengite + paragonite + sillimanite + quartz (Grambling, 1984; see Guidotti, 1984 for further discussion) complete mixing on the above binary joins is regarded as a mathematical artefact of our model.

### 2.6.3 Application

It is well known that the compositions of phengites in pelitic rocks are affected by the metamorphic conditions (Guidotti, 1973; Guidotti & Sassi, 1976; Guidotti, 1984; Guidotti & Sassi, 1998). Therefore it is interesting to see. In order to test whether our model predicts the compositional trends observed in phe of pelitic rocks, we calculated the equilibrium phase diagram (Fig. 8) and the end-member isopleths of white mica (Fig. 9) for the bulk composition corresponding to the average of 18 pelitic rock samples described by Shaw (1956) ( $\text{SiO}_2=61.37$ ,  $\text{TiO}_2=0.98$ ,  $\text{Al}_2\text{O}_3=19.25$ ,  $\text{FeO}=6.91$ ,  $\text{MnO}=0.7$ ,  $\text{MgO}=2.03$ ,  $\text{CaO}=0.46$ ,  $\text{Na}_2\text{O}=1.3$ ,  $\text{K}_2\text{O}=3.58$ ). Nagel et al. (2002a) also used this composition to discuss aspects of phase relations concerning



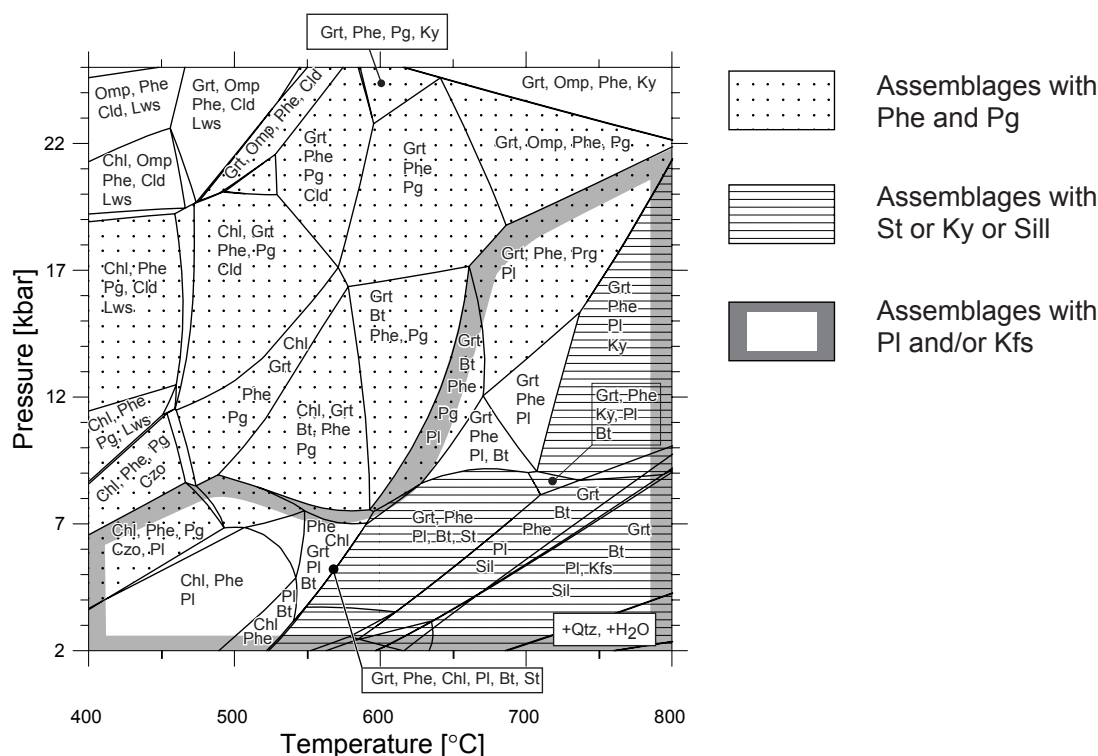


Fig. 8 Equilibrium phase diagram computed for an average pelitic bulk rock composition. The diagram is calculated with the program DOMINO (De Capitani, 1994) and it postulates distinct stable phase assemblages and corresponding mineral composition and mineral abundances based on thermodynamic properties defined in the database of Berman (1988, update 92). Bulk rock chemistry is normalized to 100 cations while all iron is taken as Fe<sup>2+</sup>. Water and quartz are stable with all mineral assemblages. The stippled area outlines assemblages where phengite coexists with paragonite; the area outlined with a grey bar corresponds to assemblages where feldspar is stable; the horizontal ruled area outlines assemblages where either staurolite, kyanite or sillimanite are stable (Mineral symbols after Kretz 1983)

metapelites, which experienced decompression from eclogite facies conditions to amphibolite facies conditions. The calculation was done in the system  $K_2O-Na_2O-CaO-FeO-MgO-Al_2O_3-SiO_2-H_2O$  with the computer program DOMINO (De Capitani & Brown, 1987; De Capitani, 1994) using the database of Berman (1988, update 92). For staurolite and chloritoid we used the data of Nagel et al. (2002a). For garnet we used the solution model of Berman (1990), for biotite binary (Phl, Ann) ideal mixing on site (3) was assumed, for chlorite the solution model of Hunziker (2003) was used. For feldspar we used the solution model of Fuhrman & Lindsley (1988), for staurolite the solution model of Nagel et al. (2002a) and for omphacite we used the model of Meyre et al. (1997).

Fig. 8 presents the equilibrium phase diagram and Figs 9a, b, c, d show the corresponding

compositional variation of Phe given by its end-member isopleths. The stippled area in the above figures represents the P-T field where Pg and Phe coexist.

#### 2.6.4 Effects of pressure and temperature on the composition of phengite

From Fig. 9a it can be seen that as temperature and pressure increases Phe becomes Na-enriched up to a maximum amount. Further temperature and pressure increase has the opposite effect as the Na content decreases and the K content increases in Phe (Fig. 9a, b). The conditions of maximum Na content in Phe are shifted towards higher temperatures as pressure increases. At the same time the maximum amount of Na decreases (see also Guidotti & Sassi, 1976, their Fig. 13). Because the Phe-Pg solvus widens in response to both a pressure increase and an increase of the

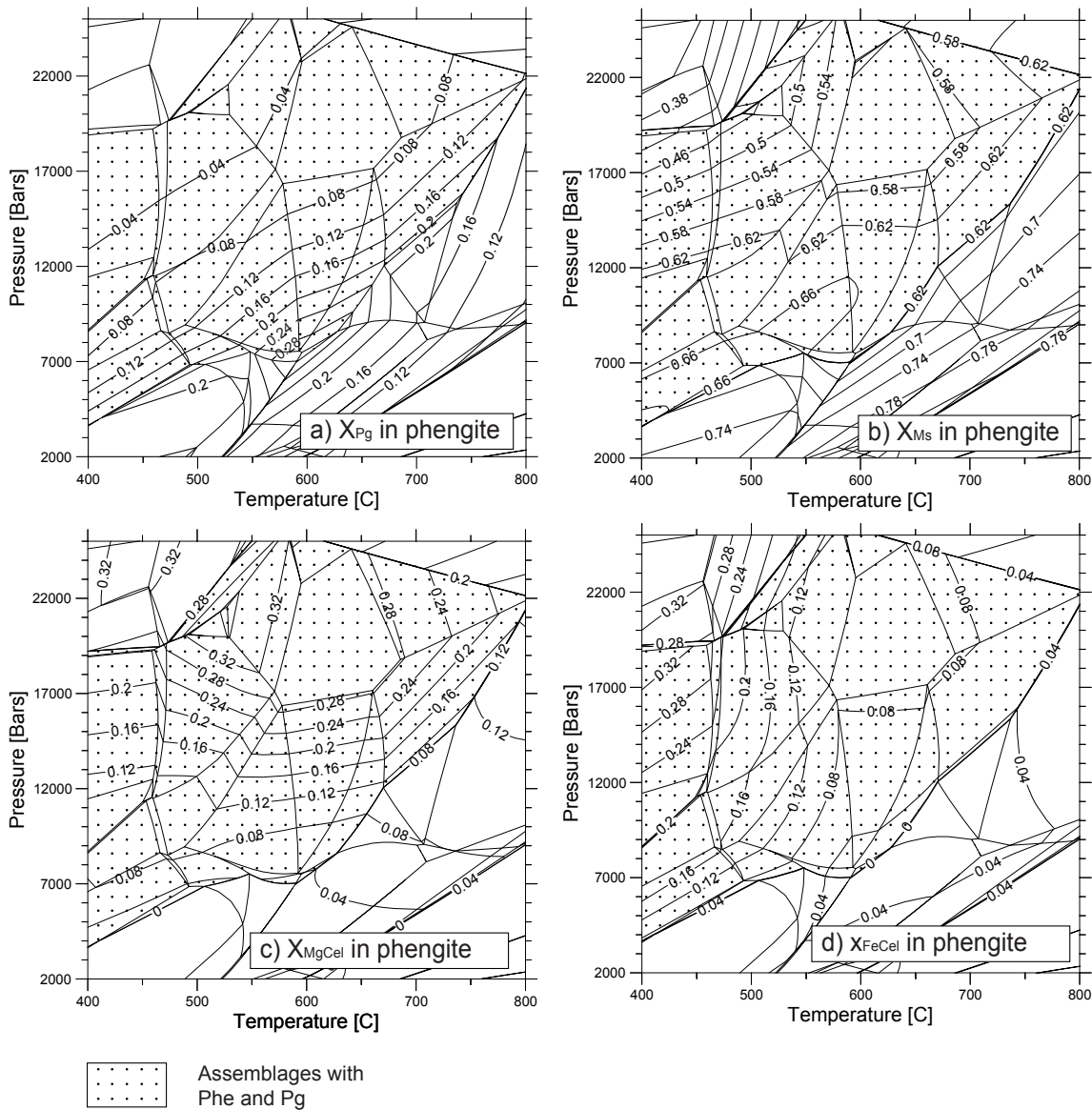


Fig. 9 End-member isopleths of phengite computed for the same average pelitic bulk rock composition as in Fig. 8. The diagram is calculated with the program DOMINO (De Capitani, 1994) based on the presented solution model and on thermodynamic properties defined in the database of Berman (1988, update 92). The stippled area outlines assemblages where phengite coexists with paragonite. a) Paragonite content in phengite; b) Muscovite content in phengite; c) Mg-celadonite content in phengite; d) Fe-celadonite content in phengite

celadonite content in Phe the amount of maximum Na content in Phe decreases as pressure increases. The P-T conditions of maximum Na content in Phe are defined by the low-pressure stability limit of Pg whereas the most Na-rich Phe can be found in the P-T range where the above stability limit starts shifting towards higher pressures (Figs 8, 9a). Similar compositional trends are described by Guidotti & Sassi (1976, their Figs 7, 13 and 14). At relatively low P-T conditions

the Na-enrichment in Phe may be caused by the continuous and temperature induced decomposition of chlorite (Chl) (Guidotti & Sassi, 1976; their reactions 8 and 9). This is in line with our calculations since the Na content in Phe increases during the progressive decomposition of chlorite (Figs 8, 9a). During this decomposition Grt, Bt and St may be formed whereas K in Phe is used as a nutrient for the formation of Bt. Thus Phe should become more Na-rich (Figs 8, 9a, b).

At higher pressures in absence of Pl but in the presence of Pg the effect of Chl decomposition on the Na content in Phe is less pronounced as the Na-content in Phe is mainly controlled by K-Na mixing between Phe and Pg (Figs 8, 9a). At high T and low P conditions within the stability range of phases such as St, Ky and sillimanite (Sil) (Fig. 8, area with horizontal ruling) the Na content in Phe decreases as temperature increases and increases as pressure increases (Fig. 9a). The thermally induced decrease of the Na content in Phe is likely caused by the breakdown of Na-rich Phe, which releases Al, forms Pl and produces K-enriched Phe (Guidotti & Sassi, 1976; their reaction 7). This is in accordance with our calculation as the abundance of Phe decreases within the stability fields of St, Ky and Sill (Fig. 9b of part II).

The equilibrium diagram (Fig. 8) predicts that the thermally driven reaction progress forming high Al phases so typical for the progressive Barrow-type metamorphism may occur in very small T intervals where continuous and discontinuous reactions take place (e. g. breakdown of Chl and St). But in collision mountain belts the formation of high Al phases may occur during approximately isothermal decompression from high-pressure conditions, which has recently been discussed for the central Alps (Leontine Dome) by Nagel et al. (2002a) (see part II for further discussion).

Fig. 9c, d shows the P-T induced variation of the celadonite content. The isopleths of the MgCel content in Phe are predominately functions of pressure within most assemblages whereas the FeCel content in Phe decreases as temperature increases particularly at higher pressures (Fig. 9c, d) (see also part II). By combining the compositional variation of the two celadonite end-members the variation of the celadonite content coincides with the one discussed in Guidotti &

Sassi (1976, their Fig. 12). These authors state that: i) particularly at low temperatures the celadonite content increases as pressure increases, ii) particularly at higher pressures the celadonite content decreases as temperature increases. By comparing the isopleths of  $X_{\text{FeCel}}$  in Phe with calculated abundance of Grt it is indicated that the FeCel content in Phe likely decreases during thermally driven growth of Grt (see Figs 9b, 10f of part II).

## 2.7 CONCLUSION

We suggest that the presented model represents an improvement over existing solution models for white micas as it accounts for the effect of the celadonite component on the Phe-Pg solvus. When the model is used to calculate the P-T dependant compositional variation of Phe in multicomponent systems it gives reasonable and consistent results in quantitative and qualitative respects at least for metapelites. The model should be particularly useful in modelling the phase relations and corresponding white mica composition for distinct pelitic bulk compositions particularly for high-grade metamorphic conditions where the white micas can usually be described in terms of the end-members Ms, Pg, MgCel and FeCel.

## 2.8 ACKNOWLEDGMENTS

This study is supported by the Swiss National Foundation Grant Nr. 20-61814.00.

We thank S. Bucher for providing us with his unpublished data. In addition we had support from K. Waite and R. Bousquet.

## 2.9 REFERENCES

- Ahn, J., Peacor, D. R. & Essene, E. J. (1985). Coexisting paragonite-phengite in blueschist eclogite: a TEM study. *American Mineralogist* **70**, 1193-1204.
- Ashworth, J. R. & Evirgen, M. M. (1984). Garnet and associated minerals in the southern margin of the Menderes Massif, southwest Turkey. *Geological Magazine* **121**, 323-337.
- Berman, R. G. (1988). Internally-consistent Thermodynamic Data for Minerals in the System Na<sub>2</sub>O-K<sub>2</sub>O-CaO-FeO-Fe<sub>2</sub>O-Al<sub>2</sub>O<sub>3</sub>-SiO<sub>2</sub>-H<sub>2</sub>O-CO<sub>2</sub>. *Journal of Petrology* **29**, 445-552.
- Berman, R. G. (1990). Mixing properties of Ca-Mg-Fe-Mn garnets. *American Mineralogist* **75**, 328-344.
- Blencoe, J. G., Guidotti, C. V. & Sassi, F. P. (1994). The paragonite-muscovite solvus: II. Numerical geothermometers for natural, quasibinary paragonite-muscovite pairs. *Geochimica et Cosmochimica Acta* **58**, 2277-2288.
- Bousquet, R., Goffé, B., Oberhänsli, R. & Patriat, M. (2000). The tectono-metamorphic history of the Valaisan domain from the Western to the Central Alps: New constraints on the evolution of the Alps. *Geological Society of America Bulletin* **114**, 207-225.
- Brown, E. H. & Forbes, R. B. (1986). Phase petrology of the eclogitic rocks in the Fairbanks district, Alaska. In: Evans, B. W. & Brown, E. H. (eds) Blueschists and Eclogites. *Geological Society of America Memoir* **164**, 155-167.
- Chopin, C. (1979). De la Vanois au massif du Grand Paradis, une approche pétrographique et radiochronologique de la signification géodynamique du métamorphisme de haute pression. *Ph. D., Université Paris VI*, 145pp.
- Chopin, C., Henry, C. & Michard, A. (1991). Geology and petrology of the coesite-bearing terrain, Dora Maira massif, Western Alps. *European Journal of Mineralogy* **3**, 263-291.
- Chatterjee, N. D. & Froese, E. (1975). A Thermodynamic Study of the Pseudobinary Join Muscovite-Paragonite in the System KAlSi<sub>3</sub>O<sub>8</sub>-NaAlSi<sub>3</sub>O<sub>8</sub>-Al<sub>2</sub>O<sub>3</sub>-SiO<sub>2</sub>-H<sub>2</sub>O. *American Mineralogist* **60**, 985-993.
- Chatterjee, N. D. & Flux, S. (1986). Thermodynamic mixing properties of muscovite-paragonite crystalline solutions at high temperatures and pressures, and their geological applications. *Journal of Petrology* **27**, 677-693.
- De Capitani, C. & Brown, T. H. (1987). The computation of chemical equilibrium in complex systems containing non-ideal solutions. *Geochimica et Cosmochimica Acta* **51**, 2639-2652.
- De Capitani, C. (1994). Gleichgewichts-Phasendiagramme: Theorie und Software. Berichte der Deutschen Mineralogischen Gesellschaft. *Beihefte zum European Journal of Mineralogy* **6**, 48.
- Coggon, R. & Holland, T. J. B. (2002). Mixing properties of phengitic micas and revised garnet-phengite thermobarometers. *Journal of metamorphic Geology* **20**, 683-696.
- Eugster, H. P., Albee, A. L., Bence, A. E., Thompson, J. B. & Waldbaum, D. R. (1972). The two-phase

region and excess mixing properties of paragonite-muscovite crystalline solutions. *Journal of Petrology* **13**, 147-179.

Enami, M. (1983). Petrology of pelitic schists in the oligoclase-biotite zone of the Sanbagawa metamorphic terrain, Japan: phase equilibria in the highest grade zone of a high-pressure intermediate type of metamorphic belt. *Journal of metamorphic Geology* **1**, 141-161.

Feininger, T. (1980). Eclogite and related high-pressure regional metamorphic rocks from the Andes of Ecuador. *Journal of Petrology* **21**, 107-140.

Ferry, J. M. (1992). Regional metamorphism of the Waits River Formation, Eastern Vermont: Delineation of a new type of giant hydrothermal system. *Journal of Petrology* **33**, 45-94.

Franceschelli, M., Mellini, M., Memmi, I. & Ricci, C. A (1989). Sudoite, a rock-forming mineral in Verrucano of the northern Apennines (Italy) and the sudoite-chloritoid-pyrophyllite assemblage in prograde metamorphism. *Contribution to mineralogy and petrology* **101**, 274-279.

Franz, C. & Althaus, E. (1976). Experimental investigation on the formation of solid solutions in sodium-aluminum-magnesian micas. *Neues Jahrbuch f. Mineralogie. Abhandlungen* **126**, 233-253.

Fuhrman, M. L. & Lindsley, D. H. (1988). Ternary-feldspar modelling and thermometry. *American Mineralogist* **73**, 201-215.

Gil Ibarra, J. I. & Dallmeyer, R. D. (1991). Hercynian blueschist metamorphism in north Portugal: tectonothermal implications. *Journal of metamorphic Geology* **9**, 539-549.

Grambling, J. A. (1984). Coexisting paragonite and quartz in sillimanite rocks from New Mexico. *American Mineralogist* **69**, 79-87.

Guidotti, C. V., Sassi, F. P., Comodi, P., Zanazzi, P. F. & Blencoe, J. G. (2000). The contrasting response of muscovite and paragonite to increasing pressure: petrological implications. *The Canadian Mineralogist* **38**, 707-712.

Guidotti, C. V. & Sassi, F. P. (1998). Petrogenetic significance of Na-K white mica mineralogy: recent advances for metamorphic rocks. *European journal of mineralogy* **10**, 815-854.

Guidotti, C. V., Sassi, F. P., Sassi, R. & Blencoe, J. G. (1994a). The effects of ferromagnesian components on the paragonite-muscovite solvus: a semiquantitative analysis based on chemical data for the natural paragonite-muscovite pairs. *Journal of metamorphic Geology* **12**, 779-788.

Guidotti, C. V., Sassi, F. P., Blencoe, J. G. & Selverstone, J. (1994b). The paragonite-muscovite solvus: I. P-T-X limits derived from the Na-K composition of natural, quasibinary paragonite-muscovite pairs. *Geochimica et Cosmochimica Acta* **58**, 2269-2275.

Guidotti, C. V. & Sassi, F. P. (1976). Muscovite as a petrogenetic indicator mineral in pelitic schists. *Neues Jahrbuch f. Mineralogie. Abhandlungen* **127**, 97-142.

Guidotti, C. V. (1973). Compositional variation of muscovite as a function of metamorphic grade and assemblages in metapelites from N. W. Main. *Contribution to mineralogy and petrology* **42**, 33-42.



- Guidotti, C. V. (1984). Micas in metamorphic rocks. In: Bailey, S. W. (ed.) Micas. Mineralogical society of America. *Reviews in mineralogy* **13**, 357-467.
- Heinrich, C. A. (1982). Kyanite-eclogite to amphibolite facies evolution of hydrous mafic and pelitic rocks, Adula nappe, Central Alps. *Contribution to mineralogy and petrology* **81**, 30-38.
- Hirajima, T., Shohei, B., Yoshikuni, H. & Yoshihide, O. (1988). Phase petrology of eclogites and related rocks from the Motalafiella high-pressure metamorphic complex in Spitsbergen (Arctic Ocean) and its significance. *Lithos* **22**, 75-97.
- Hoffer, E. (1978). On the "late" formation of paragonite and its breakdown in pelitic rocks of the southern Damara orogen (Namibia). *Contribution to mineralogy and petrology* **67**, 209-219.
- Höck, V. (1974). Coexisting phengite, paragonite and margarite in metasediments of the Mittlere Hohe Tauern, Austria. *Contribution to mineralogy and petrology* **43**, 261-273.
- Hunziker, P. (2003). The stability of tri-octahedral Fe<sup>2+</sup>-Mg-Al chlorite. A combined experimental and theoretical study. *Ph. D., University of Basel*, 162pp.
- Irouschek, A. (1983). Mineralogie und Petrographie von Metapeliten der Simano-Decke unter besondere Berücksichtigung Cordieritführender Gesteine. *Ph. D., University of Basel*, 205 pp.
- Jackson, S. L. (1989). Extension of Wohl's ternary asymmetric solution model to four and n components. *American Mineralogist* **74**, 14-17.
- Katagas, C. & Baltatzis, E. (1980). Coexisting celadonite muscovite and paragonite in chlorite zone metapelites. *Neues Jahrbuch für Mineralogie Mh. H.* **5**, 206-214.
- Koch, E. (1982). Mineralogie und plurifazielle Metamorphose der Pelite in der Adula-Decke (Zentralalpen). *Ph. D., University of Basel*, 201pp.
- Kretz, R. (1983). Symbols for rock-forming minerals. *American Mineralogist* **68**, 277-279.
- Massonne, H. J. & Szpurka, Z. (1997). Thermodynamic properties of white micas on the basis of high-pressure experiments in the system K<sub>2</sub>O-MgO-Al<sub>2</sub>O<sub>3</sub>-SiO<sub>2</sub>-H<sub>2</sub>O and K<sub>2</sub>O-FeO-Al<sub>2</sub>O<sub>3</sub>-SiO<sub>2</sub>-H<sub>2</sub>O. *Lithos* **41**, 229-250.
- Meyre, C., De Capitani, C., Zack, T. & Frey, M. (1999). Petrology of high-pressure metapelites from the Adula nappe (Central Alps, Switzerland). *Journal of Petrology* **40**, 199-213.
- Meyre, C., De Capitani, C. & Partsch, J. H. (1997). A ternary solid solution model for omphacite and its application to geothermobarometry of eclogites from the middle Adula nappe (Central Alps, Switzerland). *Journal of metamorphic Geology* **15**, 687-700.
- Nagel, T., De Capitani, C. & Frey, M. (2002a). Isogrades and P-T evolution in the Southeastern Lepontine Dome (Graubünden, Switzerland). *Journal of metamorphic Geology* **20**, 309-324.
- Nagel T. (2002b). Metamorphic and structural history of the southern Adula nappe (Graubünden, Switzerland). *Ph. D., University of Basel*, 103pp.

- Okay, A. I. (1989). An exotic eclogite/blueschist slice in a barrovian-style metamorphic terrain, Alanya Nappes, Southern Turkey. *Journal of Petrology* **30**, 107-132.
- Roux, J. & Hovis, G. L. (1996). Thermodynamic mixing models for muscovite-paragonite solutions based on solution calorimetric and phase equilibrium data. *Journal of Petrology* **37**, 1241-1254.
- Shaw, D. M. (1956). Geochemistry of pelitic rocks. Part 3: Major elements and general geochemistry. *Bulletin Geological Society of America* **67**, 919-934.
- Theye, T. & Seidel, E. (1991). Petrology of low-grade high-pressure metapelites from the external Hellenides (Crete, Peloponnese) a case study with attention to sodic minerals. *European Journal of Mineralogy* **3**, 343-366.
- Thompson, J. B. (1957). The graphical analysis of the mineral assemblages in pelitic schists. *The American Mineralogist* **42**, 842-858.
- Thompson, J. B. & Thompson, A. B. (1976). A model system for mineral facies in pelitic schists. *Contribution to Mineralogy and Petrology* **58**, 243-277.
- Vidal, O., Para, T. & Trotet, F. (2001). A Thermodynamic model for Fe-Mg aluminous chlorite using data from phase equilibrium experiments and natural pelitic assemblages in the 100°C to 600°C, 1 to 25 kb range. *American Journal of Science* **301**, 557-592.
- Wohl, K. (1946). Thermodynamic evaluation of binary and ternary liquid systems. *Transaction of the American Institute of Chemical Engineers* **42**, 215-249.
- Wohl, K. (1953). Thermodynamic evaluation of binary and ternary liquid systems. *Chemical Engineering Progress* **49**, 218-219.
- Zhang, R. & Liou, J. G. (1994). Coesite-bearing eclogite in Henan Province, central China: detailed petrography, glaucophane stability and P-T path. *European Journal of Mineralogy* **6**, 217-233.

### **3. DEFORMATION, MASS TRANSFER AND MINERAL REACTIONS IN AN ECLOGITE FACIES SHEAR ZONE IN A POLYMETAMORPHIC METAPELITE (MONTE ROSA NAPPE, WESTERN ALPS)**

L. M. Keller, R. Abart, H. Stünitz and C. De Capitani

Department of Earth Sciences, Basel University, Bernoullistrasse 32, CH-4056 Basel

#### **3.1 ABSTRACT**

This study analyses the mineralogical and chemical transformations associated with an Alpine shear zone in polymetamorphic metapelites from the Monte Rosa nappe in the upper Val Loranco (N-Italy). In the shear zone, the pre-Alpine assemblage plagioclase + biotite + kyanite is replaced by the assemblage garnet + phengite + paragonite at eclogite facies conditions of about 650°C at 12.5 kbar. Outside the shear zone, only minute progress of the same metamorphic reaction was attained during the Alpine metamorphic overprint and the pre-Alpine mineral assemblage is largely preserved. Textures of incomplete reaction, such as garnet rims at former grain contacts between pre-existing plagioclase and biotite, are preserved in the country rocks of the shear zone. Reaction textures and phase relations indicate that the Alpine metamorphic overprint occurred under largely anhydrous conditions in low strain domains. In contrast, the mineralogical changes and phase equilibrium diagrams indicate water saturation within the Alpine shear zones. Shear zone formation occurred at approximately constant volume but was associated with substantial gains in silica and losses in aluminium and potassium. Changes in mineral modes associated with chemical alteration and progressive deformation indicate that plagioclase, biotite and kyanite were not only consumed in the course of the garnet- and phengite-producing reactions, but were also dissolved “congruently” during shear zone formation. A large fraction of the silica liberated by plagioclase, biotite and kyanite dissolution was immediately re-precipitated to form quartz, but the dissolved aluminium- and potassium-bearing species appear to have been stable in solution and were removed via the pore fluid. The reaction causes the localization of deformation by producing fine-grained white mica, which forms a mechanically weak aggregate.

Key words: eclogites; ductile deformation; mass balance; pelites; reaction progress

### 3.2 INTRODUCTION

Fault rocks are often mineralogically, chemically and isotopically distinct from their precursors (White & Knipe, 1978; Brodie & Rutter, 1985; Selverstone *et al.*, 1991; Selverstone, 1993). If a metamorphic transformation associated with rock deformation is isochemical, changes in mineral modes will reflect the progress of net-transfer mineral reactions. These reactions tend towards thermodynamic equilibrium, which for a given chemical composition of the rock is governed by the  $P$ - $T$  conditions (e.g. Gilotti, 1989). If the reactions occur during deformation, e.g. in a shear zone, and are associated with chemical and isotopic alteration, it usually indicates interaction with an externally derived fluid (e.g., Dipple *et al.*, 1990; Selverstone *et al.*, 1991; Dipple & Ferry, 1992; Matthey *et al.*, 1994; Früh-Green, 1994; McCaig, 1997, his Table 9.1). Chemical transport associated with fluid flow may be facilitated by transient permeability enhancement during deformation (McCaig *et al.*, 1990; Dipple & Ferry, 1992; Stünitz, 1993), and chemical alteration is frequently observed to be associated with fault rock formation. Material gains and losses during rock alteration may be quantified from mass balance considerations (Gresens, 1967; Grant, 1984; Potdevin & Marquer, 1987; Cesare, 1999; Abart *et al.*, 2001). In the case of allochemical metamorphic or metasomatic transformations, changes in mineral modes may be a function of both the progress of mass-conserving, net-transfer mineral reactions and of mass transfer due to fluid transport.

For an understanding of fault rock formation it is important to know to what extent observed mineralogical patterns are controlled by (1) material gains/losses and by (2) net transfer reactions. In the context of syn-metamorphic

shear zone formation, this information can only be obtained from the combined analysis of petrographic data (including modal analysis by point counting), mineral and bulk rock chemistry, and density measurements. In this paper, such an empirical approach is used to distinguish between the effects of isochemical net transfer reactions and of material gains/losses applied to a suite of progressively deformed rocks from a shear zone from the Monte Rosa nappe.

The shear zone under consideration formed under eclogite facies conditions in pelitic basement rocks during the Alpine metamorphic event. This study is based on the quantification of changes in mineral modes, mass transfer and net transfer reactions that occurred during syn-metamorphic rock alteration. A model is presented to describe the simultaneous mineralogical and chemical alteration associated with the shear zone formation. On the basis of a comparison between calculated and observed changes in mineral modes, it is possible to ascribe observed material gains/losses to “congruent” dissolution and to the precipitation of specific minerals. Our analysis gives insight into the chemical evolution of pore fluids during an eclogite facies overprint of earlier metapelites and adds to the discussion of aluminium mobility during metamorphism. We also analyse the phase relations and reaction microstructures from the fault rocks and their undeformed equivalents and discuss implications for the polyphase metamorphic evolution of the Monte Rosa nappe. With respect to the Alpine metamorphic event low strain-domains can be distinguished, where the mineral reactions proceed under largely anhydrous conditions, reaction textures indicate transport-controlled growth, and thermodynamic equilibration only occurred on a subgrain scale. In contrast, there are high-strain domains, where

global thermodynamic equilibration was attained under fluid-present conditions.

There is a wealth of published geochemical studies concerned with major and trace element changes in shear zones, but the combination of mass balance, quantification of reaction progress and phase petrology has received less attention.

### 3.3 GEOLOGICAL SETTING

The Monte Rosa nappe belongs to the upper Penninic nappe pile west of the Lepontine dome and is situated southeast of the Simplon line (Fig. 1a). Large south-vergent backfolds with axial plunge towards the SW define the shape of the Monte Rosa nappe. (e.g. Klein, 1978; Milnes *et*

*al.*, 1981; Escher *et al.*, 1997) (Fig. 1b). Zermatt-Saas ophiolites lie structurally above and Antrona ophiolites below the Monte Rosa nappe (Fig. 1b). The Monte Rosa nappe consists of pre-Mesozoic metapelitic paragneisses, which are intruded by granites at around 310 Ma and 270 Ma (HUNZIKER, 1970; FREY *et al.*, 1976). After its emplacement the nappe pile was overprinted by backfolding. The shear zone studied is situated at the northeastern margin of the Monte Rosa nappe and lies within the northern limb of the Antrona synformal backfold (Fig. 1).

#### 3.3.1 Pre-Alpine metamorphism

In the following context of this study, the terms

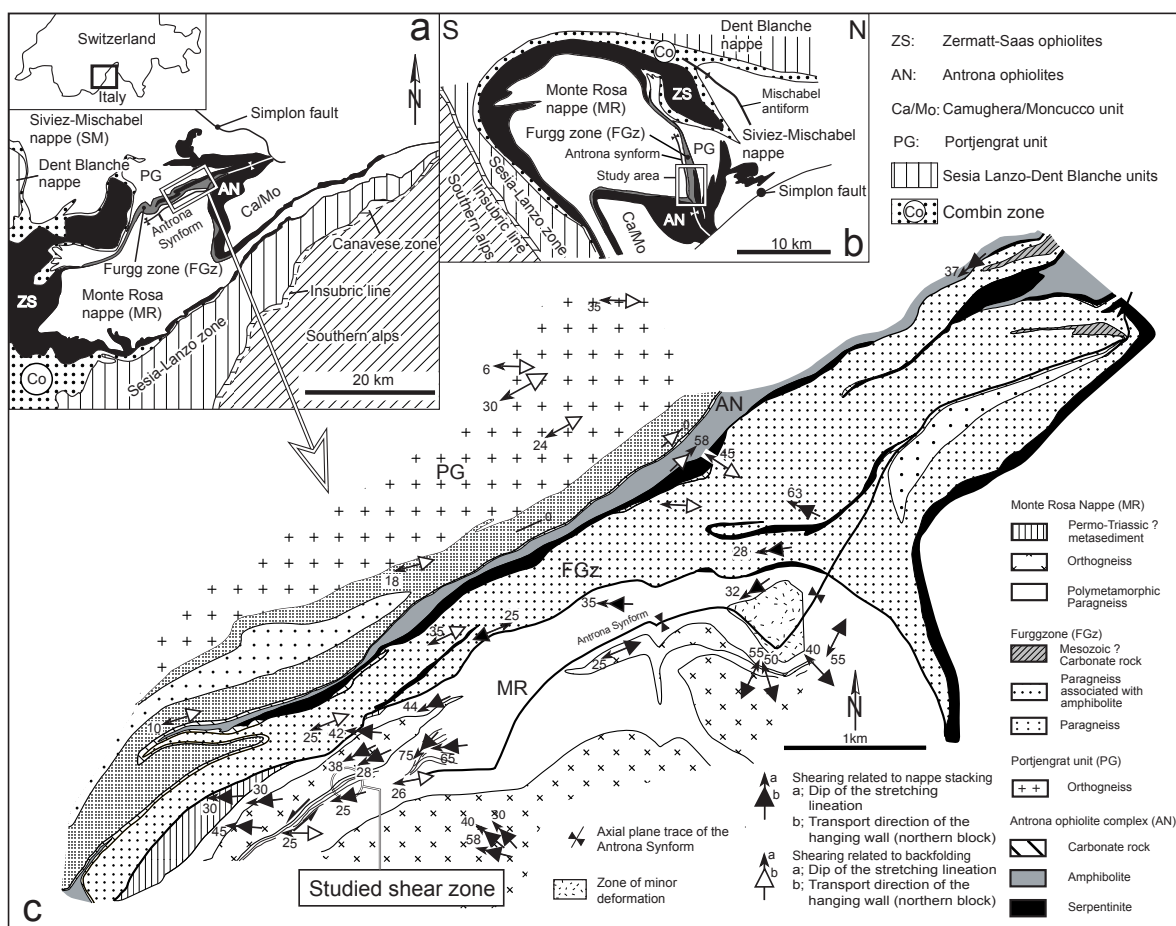


Fig. 1. Geological framework and sense of shear within the study area (outlined by rectangle).

a) Modified tectonic map of the western part of the upper Penninic Alps after Sartori (1987), Steck (1989), Pfeifer *et al.* (1989) and Keller & Schmid (2001). b) Synthetic cross section modified after Milnes *et al.* (1981).

c) Modified tectonic map after Keller & Schmid (2001) showing the transport directions of the hanging wall. Note that all tectonic contacts dip to the north.



Alpine and pre-Alpine refer to the Alpine event and older events, respectively. The relict pre-Alpine mineral assemblages in the Monte Rosa metapelites consist predominantly of biotite-sillimanite-garnet-quartz-K-feldspar-plagioclase and of garnet-biotite-muscovite-sillimanite-plagioclase (BEARTH, 1957; DAL PIAZ & LOMBARDO, 1986). The *P-T* conditions that prevailed during pre-Alpine metamorphism are not known exactly. According to Bearth (1952) cordierite grew at the expense of biotite during pre-Alpine metamorphism in the Monte Rosa metapelites; cordierite was later pseudomorphed by sillimanite, and the oldest discernable mineral assemblage garnet + biotite + sillimanite was formed.

### 3.3.2 Alpine metamorphism

According to the metamorphic map of the Alps (Frey *et al.*, 1999) the Zermatt-Saas ophiolites, the Monte Rosa nappe and the Antrona ophiolites all have undergone eclogite facies metamorphism. Recent isotopic studies indicate an Early to Middle Eocene age for the high-pressure stage in the Zermatt-Saas ophiolites (Bowtell *et al.*, 1994; Rubatto *et al.*, 1997).

During later stages of the Alpine metamorphic cycle and under conditions of lower pressures the eastern part of the Monte Rosa nappe, the Antrona ophiolites and the Camughera-Moncucco unit have undergone amphibolite facies metamorphism whereas the western part of the Monte Rosa nappe reached only greenschist facies (Frey *et al.*, 1999). This metamorphic zonation, which exhibits a temperature increase from the west to the east, was firstly recognized by Bearth (1958) who mapped the albite-oligoclase boundary in the study area.

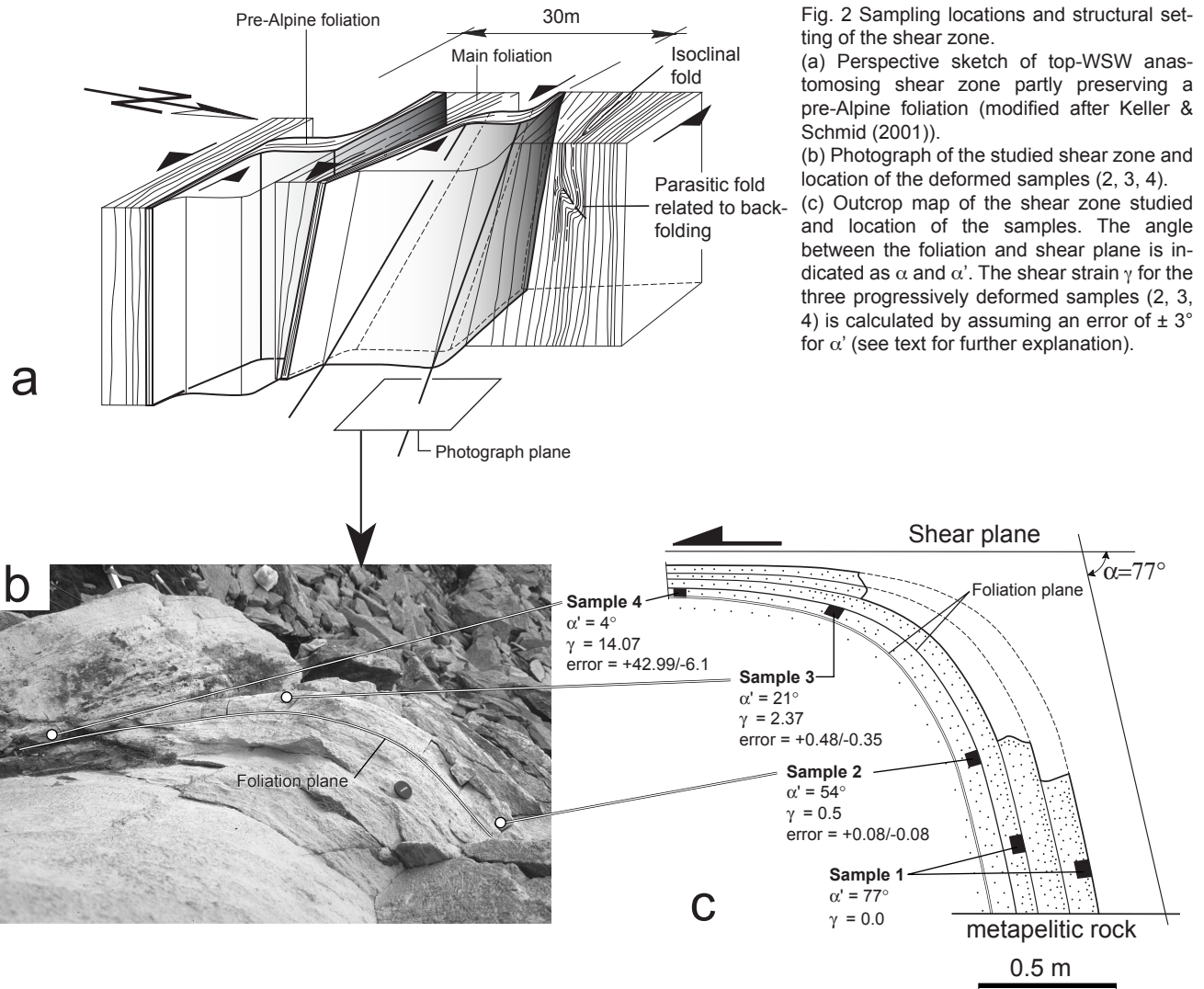
Recently Engi *et al.* (2001) estimated *P-T*

conditions of about 11 kbar at 650°C, interpreted to represent partial re-equilibration upon decompression.

### 3.4 GEOLOGICAL FRAMEWORK OF THE INVESTIGATED SHEAR ZONE

Three types of Tertiary ductile shearing and folding have been documented in the Penninic units (STECK, 1984, 1987; STECK & HUNZIKER, 1994). The oldest type of shear zones is related to SE-NW oriented underthrusting of the European plate below the Adriatic margin and is contemporaneous with the formation of the nappe pile (e.g. STECK, 1984, 1987; LACASSIN, 1987; STECK & HUNZIKER, 1994). A second and younger type of shearing is linked to overturned limbs of megascopic backfolds. In the study area this shearing has taken place with a top-ENE (i.e. dextral in map view) shear sense and is related to the northern limb of the Antrona synform (JABOYEDOFF *et al.*, 1996; Keller & Schmid, 2001) (Fig. 1c). A third type of shearing is related to the large scale Simplon ductile shear zone, which started to be active at about 35 *Ma* (STECK, 1984, 1987, 1990; STECK & HUNZIKER, 1994). This shear event and the associated Miocene Simplon normal fault (MANCKTELOW, 1992) have produced WSW-ENE oriented orogen-parallel extension and top-WSW shearing since the Oligocene.

The shear zone of this study belongs to the oldest shear zone type and is associated with top-N nappe stacking, which in the study started under eclogite facies conditions (Keller & Schmid, 2001). Due to the subsequent refolding (Antrona synform) the shear zone indicates top-WSW shearing today (Keller & Schmid, 2001; Fig. 1c). The shear zone is part of a network of anastomosing shear zones where a pre-Alpine foliation of the Monte Rosa metapelites is overprinted. Only domains as



wide as 10 m are unaffected by Alpine straining and preserve the pre-Alpine foliation (Fig. 2a). The new Alpine foliation within central parts of the shear zone is parallel to the main foliation of the frontal part of the Monte Rosa nappe and can laterally be traced for several hundreds of metres (Fig. 1c). Minor isoclinal folds within the mylonitic foliation have formed contemporaneous with the shear zone formation (Keller & Schmid, 2001) whereas open asymmetric folds, which overprint the mylonitic foliation, are related to subsequent backfolding (Fig. 2a).

Together with the gradual deflection of the pre-Alpine foliation into parallelism with the shear zone there is gradual change in mineralogy from the pre-Alpine garnet-biotite-plagioclase-

kyanite schist in the wallrock to an eclogite facies garnet-white-mica-schist. The breakdown of pre-Alpine biotite in the shear zone gives the rock a lighter colour compared to the wallrock. However, the eclogite facies rocks are preserved only in the marginal parts of the shear zone. In the central parts the mylonitic foliation consists of greenschist facies mineral assemblages and shearing is also top-WSW (Keller & Schmid, 2001). Based on this observation Keller & Schmid (2001) interpret that whole shear zone history is related to decompression and that active deformation started under eclogite facies conditions and was successively localised during subsequent deformation increments in the centre

of the shear zone. This interpretation suggests that the more marginal parts of the shear zone preserve the earlier deformation history formed under low-strain/eclogite facies conditions (e.g. Means, 1995). For this study only the outer parts of the shear zone displaying high-pressure shearing and mineral assemblages were sampled and analysed.

### 3.5 METHODS OF INVESTIGATION

#### 3.5.1 Strain estimates

Four samples of the shear zone (Fig. 2b, c) were studied in detail and document progressive stages of the syn-deformational reaction. During deformation by heterogeneous simple shear at constant volume, the shear strain  $\gamma$  of any passive plane that enclosed an angle  $\alpha$  with the shear plane prior to deformation and an angle  $\alpha'$  after deformation is given by (Ramsay, 1980):

$$\gamma = \cot \alpha' - \cot \alpha \quad (1)$$

The foliation in the undeformed wallrock is regarded as a passive marker plane. Towards the shear zone it is progressively rotated into parallelism with the shear plane (Fig. 2b, c). In the context of syn-metamorphic shear zones, the condition of constant volume during deformation is an assumption. To account for potential volume change during deformation, the angle  $\alpha'$  is regarded as a function of both the shear strain  $\gamma$  and the volume change. Because strain estimates are afflicted by large errors resulting from the uncertainties in measuring small angles, an error range of  $\pm 3^\circ$  for  $\alpha'$  is assumed.

#### 3.5.2 Modal analysis and petrography

Mineral modes were measured by counting 3000 points per thin section cut parallel to lineation and normal to foliation (Table 1).

Table 1  
Mode in area %  
(Counting 3000 points per thin section)

Sample	1	2	3	4
Bt	23.27	10.93	7.63	4.90
Pl	14.73	8.17	3.00	0.77
Qtz	24.83	30.23	19.00	28.33
Ky	12.27	8.07	7.37	0.03
Ilm/Rt	3.37	1.27	0.53	1.17
Grt 1	4.47	10.83	14.37	13.90
Grt 0	1.50	0.93	0.03	0.17
White mica	15.07	29.27	47.93	50.57
Tur/Chl	0.50	0.30	0.13	0.17
$\Sigma$	100.01	100.00	99.99	100.01

Densities of rock powders were measured using a pycnometer (Hutchinson, 1974). With three-four measurements obtained for each sample, the  $1\sigma$  of repetitive measurements ranges between 0.01-0.02 g/cm<sup>3</sup>. Air was removed from the powder with a vacuum pump while a pycnometer was placed in an ultrasonic bath. Mineral compositions were determined with a JEOL JXA-8600 electron microprobe at 15 kV acceleration voltage and 10 nA sample current and correcting with a PROZA routine. The compositions of the rock-forming minerals are given in Table 2.

#### 3.5.3 Whole rock chemistry

For accurately determining the whole rock chemistry of the protolith (sample 1), duplicate analyses for two samples containing identical mineralogy and approximately within the same layer as the deformed samples have been obtained (Fig. 2b, c). In order to ascertain that the protolith is the same as the deformed rock, all the deformed samples were taken along a single foliation plane, which can be traced from the wall rock into the most intensely deformed parts of the shear zone (Fig. 2b, c). An attempt was made to take samples only from petrographically homogeneous regions. This bias limited the sample size to 20 to 200 g.

Table 2  
Mean mineral compositions

	White mica analyses										Biotite analyses										Plagioclase analyses										Garnet analyses									
	1		2		3		4		1		2		3		4		1		2		3		4		1		2		3		4									
	Phe	N	Phe	N	Phe	N	Phe	N	pA	N	A	N	A	N	N=10	N=11	N=12	N=13	N=14	N=21	N=22	N=23	N=24	N=25	N=11	N=12	N=13	N=14	N=15	N=16	N=17	N=18	N=19							
SiO <sub>2</sub>	46.23	48.64	47.07	47.66	46.40	46.40	46.40	34.98	39.27	37.34	37.20	35.41	35.41	66.38	66.38	66.44	67.05	68.25	66.38	66.38	66.44	67.05	68.25	27.63	27.63	27.63	27.63	27.63	27.63	27.63	27.63	27.63								
Al <sub>2</sub> O <sub>3</sub>	35.07	30.22	31.07	37.65	37.06	37.06	37.06	18.34	20.75	19.32	18.41	18.79	18.79	20.95	20.95	20.30	20.55	19.75	20.95	20.95	20.30	20.55	19.75	21.04	21.04	21.04	21.04	21.04	21.04	21.04	21.04	21.04								
TiO <sub>2</sub>	0.59	0.87	0.53	0.12	0.16	0.16	0.16	2.43	0.91	3.19	1.39	2.89	2.89	0.06	0.06	0.07	0.07	0.06	0.06	0.06	0.07	0.07	0.06	0.41	0.41	0.41	0.41	0.41	0.41	0.41	0.41	0.41								
MgO	0.52	2.18	1.93	0.11	2.24	1.55	0.34	9.29	11.73	10.52	12.91	11.71	11.71	0.02	0.02	0.19	0.15	0.06	0.02	0.02	0.19	0.15	0.06	2.06	2.06	2.06	2.06	2.06	2.06	2.06	2.06	2.06								
FeO	0.94	1.56	1.22	0.24	0.34	0.34	0.34	21.90	14.66	15.20	15.88	18.59	18.59	0.13	0.13	0.47	0.25	0.19	0.13	0.13	0.47	0.25	0.19	34.16	34.16	34.16	34.16	34.16	34.16	34.16	34.16	34.16								
MnO	0.02	0.02	0.01	0.01	0.01	0.01	0.01	0.07	0.05	0.05	0.02	0.06	0.06	0.03	0.03	0.02	0.02	0.02	0.03	0.03	0.02	0.02	0.02	2.67	2.67	2.67	2.67	2.67	2.67	2.67	2.67	2.67								
CaO	0.01	0.02	0.01	0.01	0.01	0.01	0.01	0.10	0.02	0.09	0.00	0.06	0.06	3.12	3.12	1.88	1.34	1.58	3.12	3.12	1.88	1.34	1.58	5.66	5.66	5.66	5.66	5.66	5.66	5.66	5.66	5.66								
Na <sub>2</sub> O	0.88	0.75	1.01	7.19	0.87	0.93	0.93	0.15	0.15	0.32	0.23	0.19	0.19	9.57	9.57	10.70	10.73	10.67	9.57	9.57	10.70	10.73	10.67	0.03	0.03	0.03	0.03	0.03	0.03	0.03	0.03	0.03								
K <sub>2</sub> O	10.62	10.26	9.88	0.99	9.84	1.35	1.35	9.21	7.04	8.37	8.24	7.52	7.52	0.35	0.35	0.49	0.66	0.27	0.35	0.35	0.49	0.66	0.27	0.22	0.22	0.22	0.22	0.22	0.22	0.22	0.22	0.22								
Σ	94.88	94.52	94.39	93.49	92.08	92.52	92.52	96.47	94.58	94.40	94.28	95.22	95.22	100.61	100.61	100.61	100.82	100.85	100.61	100.61	100.61	100.82	100.85	103.88	103.88	103.88	103.88	103.88	103.88	103.88	103.88	103.88								

	Cations on the basis of 110										Cations on the basis of 80										Cations on the basis of 120																	
	Si	Al	Σ	Al	Fe	Ti	Mn	Mg	Σ	X <sub>Al</sub>	Si	Al	Σ	Ca	Na	K	Mn	Mg	Σ	X <sub>Al</sub>	Si	Al	Σ	Ca	Mg	Fe <sup>3+</sup>	Ti	Σ	Ca	Mg	Fe <sup>2+</sup>	Mn	Σ					
Si	3.09	3.26	3.26	3.06	3.28	3.06	3.06	3.06	3.06	0.26	2.67	2.86	2.78	2.78	2.66	2.66	2.66	2.66	2.66	2.66	2.66	2.90	2.91	2.91	2.90	2.91	2.91	2.91	2.91	2.91	2.91	2.91	2.91	2.91	2.91			
Al	0.91	0.74	0.74	0.94	0.72	0.94	0.94	0.94	0.94	1.34	1.33	1.14	1.22	1.22	1.34	1.34	1.34	1.34	1.34	1.34	1.34	1.08	1.05	1.05	1.08	1.05	1.05	1.05	1.05	1.05	1.05	1.05	1.05	1.05	1.05	1.05		
Σ	4.00	4.00	4.00	4.00	4.00	4.00	4.00	4.00	4.00	4.00	4.00	4.00	4.00	4.00	4.00	4.00	4.00	4.00	4.00	4.00	4.00	3.98	3.96	3.96	3.98	3.96	3.96	3.96	3.96	3.96	3.96	3.96	3.96	3.96	3.96	3.96	3.96	
Al	1.85	1.66	1.71	1.95	1.66	1.94	1.94	1.94	1.94	0.64	0.31	0.64	0.47	0.40	0.32	0.32	0.32	0.32	0.32	0.32	0.32	0.15	0.09	0.09	0.15	0.09	0.09	0.09	0.09	0.09	0.09	0.09	0.09	0.09	0.09	0.09		
Fe	0.05	0.09	0.07	0.01	0.09	0.02	0.02	0.02	0.02	0.89	1.40	0.89	0.95	0.99	1.17	1.17	1.17	1.17	1.17	1.17	1.17	0.81	0.91	0.91	0.81	0.91	0.91	0.91	0.91	0.91	0.91	0.91	0.91	0.91	0.91	0.91	0.91	
Ti	0.03	0.04	0.03	0.01	0.03	0.01	0.01	0.01	0.01	0.14	0.14	0.05	0.18	0.08	0.16	0.16	0.16	0.16	0.16	0.16	0.16	0.02	0.03	0.03	0.02	0.03	0.03	0.03	0.03	0.03	0.03	0.03	0.03	0.03	0.03	0.03	0.03	
Mn	0.00	0.00	0.00	0.00	0.00	0.00	0.00	0.00	0.00	0.00	0.00	0.00	0.00	0.00	0.00	0.00	0.00	0.00	0.00	0.00	0.00	0.01	0.01	0.01	0.01	0.01	0.01	0.01	0.01	0.01	0.01	0.01	0.01	0.01	0.01	0.01	0.01	
Mg	0.05	0.22	0.19	0.01	0.23	0.02	0.02	0.02	0.02	1.27	1.05	1.27	1.17	1.44	1.31	1.31	1.31	1.31	1.31	1.31	1.31	0.99	1.06	1.06	0.99	1.06	1.06	1.06	1.06	1.06	1.06	1.06	1.06	1.06	1.06	1.06	1.06	
Σ	1.99	2.01	2.00	1.98	2.01	1.98	1.98	1.98	1.98	2.86	2.91	2.86	2.77	2.91	2.97	2.97	2.97	2.97	2.97	2.97	0.99	1.06	1.06	0.99	1.06	1.06	1.06	1.06	1.06	1.06	1.06	1.06	1.06	1.06	1.06	1.06	1.06	
Na	0.11	0.10	0.13	0.91	0.12	0.89	0.89	0.89	0.89	0.02	0.02	0.02	0.05	0.03	0.03	0.03	0.03	0.03	0.03	0.03	0.03	0.15	0.08	0.08	0.15	0.08	0.08	0.08	0.08	0.08	0.08	0.08	0.08	0.08	0.08	0.08	0.08	
K	0.91	0.88	0.84	0.08	0.86	0.11	0.11	0.11	0.11	0.90	0.90	0.65	0.79	0.79	0.72	0.72	0.72	0.72	0.72	0.72	0.72	0.83	0.86	0.86	0.83	0.86	0.86	0.86	0.86	0.86	0.86	0.86	0.86	0.86	0.86	0.86	0.86	0.86
Ca	0.00	0.00	0.00	0.01	0.00	0.01	0.01	0.01	0.01	0.01	0.01	0.00	0.01	0.00	0.01	0.01	0.01	0.01	0.01	0.01	0.01	0.02	0.02	0.02	0.02	0.02	0.02	0.02	0.02	0.02	0.02	0.02	0.02	0.02	0.02	0.02	0.02	0.02
Σ	1.02	0.98	0.98	0.99	0.98	1.00	1.00	1.00	1.00	0.93	0.93	0.67	0.85	0.82	0.75	0.75	0.75	0.75	0.75	0.75	0.75	0.02	0.02	0.02	0.02	0.02	0.02	0.02	0.02	0.02	0.02	0.02	0.02	0.02	0.02	0.02	0.02	0.02
X <sub>Al</sub> <sup>Ms</sup>	0.78	0.59	0.59	0.14	0.57	0.06	0.06	0.06	0.06	0.57	0.57	0.41	0.45	0.41	0.47	0.47	0.47	0.47	0.47	0.47	0.47	0.15	0.08	0.08	0.15	0.08	0.08	0.08	0.08	0.08	0.08	0.08	0.08	0.08	0.08	0.08	0.08	
X <sub>Al</sub> <sup>Pg</sup>	0.10	0.11	0.14	0.81	0.12	0.88	0.88	0.88	0.88	0.43	0.43	0.59	0.55	0.59	0.53	0.53	0.53	0.53	0.53	0.53	0.53	0.83	0.86	0.86	0.83	0.86	0.86	0.86	0.86	0.86	0.86	0.86	0.86	0.86	0.86	0.86	0.86	
X <sub>Al</sub> <sup>Mg,Ca</sup>	0.06	0.21	0.20	0.03	0.22	0.03	0.03	0.03	0.03	0.01	0.01	0.00	0.01	0.00	0.01	0.01	0.01	0.01	0.01	0.01	0.01	0.02	0.02	0.02	0.02	0.02	0.02	0.02	0.02	0.02	0.02	0.02	0.02	0.02	0.02	0.02	0.02	
X <sub>Al</sub> <sup>Fe,Ce</sup>	0.06	0.08	0.07	0.03	0.08	0.03	0.03	0.03	0.03	0.93	0.93	0.67	0.85	0.82	0.75	0.75	0.75	0.75	0.75	0.75	0.75	0.02	0.02	0.02	0.02	0.02	0.02	0.02	0.02	0.02	0.02	0.02	0.02	0.02	0.02	0.02	0.02	0.02

X<sub>Al</sub><sup>Ms</sup>, X<sub>Al</sub><sup>Mg,Ca</sup>, X<sub>Al</sub><sup>Fe,Ce</sup> and X<sub>Al</sub><sup>Fe</sup> are determined by the method of least squares by regarding the elements Si, Al, Fe, Mg, Na and K.

Major element compositions were determined on melted pellets by XRF using a Bruker AXS SRS-3400. The volatile content was determined by loss on ignition (LOI). Whole rock chemistries are given in Table 3.

Table 3  
Bulk-rock chemical data for the analysed metapelitic rocks and bulk rock atomic ratios

Sample	1	2	3	4
	Mean N=4			
SiO <sub>2</sub>	49.40	57.44	51.29	59.04
Al <sub>2</sub> O <sub>3</sub>	28.76	23.81	26.36	21.96
Fe <sub>2</sub> O <sub>3</sub>	8.97	8.12	10.21	7.78
MnO	0.11	0.16	0.17	0.11
MgO	2.20	1.90	2.28	2.01
CaO	0.50	0.68	0.62	0.50
Na <sub>2</sub> O	1.23	1.43	1.21	1.29
K <sub>2</sub> O	5.04	3.90	4.55	3.94
TiO <sub>2</sub>	1.15	0.83	1.06	0.84
P <sub>2</sub> O <sub>5</sub>	0.12	0.14	0.13	0.14
LOI	2.36	1.48	2.01	2.27
Σ	99.84	99.89	99.89	99.87
Density (g/cm <sup>3</sup> )	2.99	2.97	3.04	2.93
Si/Al	1.47	2.05	1.65	2.28
Fe/Al	0.20	0.22	0.25	0.23
Mn/Al	0.00	0.00	0.00	0.00
Mg/Al	0.09	0.10	0.11	0.12
Ca/Al	0.01	0.03	0.02	0.02
Na/Al	0.07	0.10	0.08	0.10
K/Al	0.19	0.18	0.19	0.19
Ti/Al	0.02	0.02	0.03	0.02
Fe/Mg	2.07	2.16	2.26	1.96

### 3.6 MICROSTRUCTURES AND MINERAL ASSEMBLAGES OF THE SAMPLES

#### 3.6.1 The protolith (sample 1)

In this study the term protolith refers to the rock, which is unaffected by the shear zone-related strain. The major minerals in the protolith are biotite, plagioclase, quartz, kyanite, garnet, phengite and chlorite; accessory phases include ilmenite, rutile and tourmaline. Garnet and white mica occur in two generations. As a first metamorphic overprint during the Alpine metamorphism, a second garnet (2) and phengite (2) generation have grown predominantly along grain contacts between pre-existing plagioclase and biotite (Figs

4a, 6a). The garnet rims are between 0.05 and 0.1mm wide. Garnet (2) and phengite (2) have also formed within aggregates of fine-grained kyanite. New phengite (2) grains are much finer grained (c. 30 to 60  $\mu$ m) than the pre-Alpine phengites (up to 1.2 mm long). Garnet (2) also formed locally along ilmenite grain boundaries. Chlorite occurs sporadically and overgrows the pre-Alpine foliation. Chlorite does not occur in the deformed samples. Reaction textures suggest that chlorite has formed during unroofing late stages of Alpine metamorphism replacing pre-Alpine biotite.

The pre-Alpine foliation and quartz microstructures are well preserved in sample 1. Aligned biotite and ilmenite grains and pure quartz layers define the foliation. Plagioclase and garnet are mainly porphyroblasts in the biotite- phengite matrix (Fig. 3a). The quartz grain boundaries are generally straight with stepped, low crystallographic index segments indicating complete annealing of the pre-Alpine microstructures (Fig. 3b). Subgrains and other internal deformation features are virtually absent in quartz and biotite. This observation is evidence that the Alpine deformation has not affected the microstructures of the protolith (sample 1).

#### 3.6.2 Deformed metapelites (samples 2, 3, 4)

Sample 2 is the least deformed sample and contains biotite, plagioclase, quartz, kyanite, garnet (1), garnet (2) and phengite; accessory phases include ilmenite, rutile and tourmaline. The more deformed samples 3 and 4 also contain paragonite. The modal amount of the protolith minerals increases with increasing macroscopic strain (Table 1). Locally garnet (2) grows along the ilmenite grains, which themselves are also replaced by rutile (Fig. 4e). A late generation



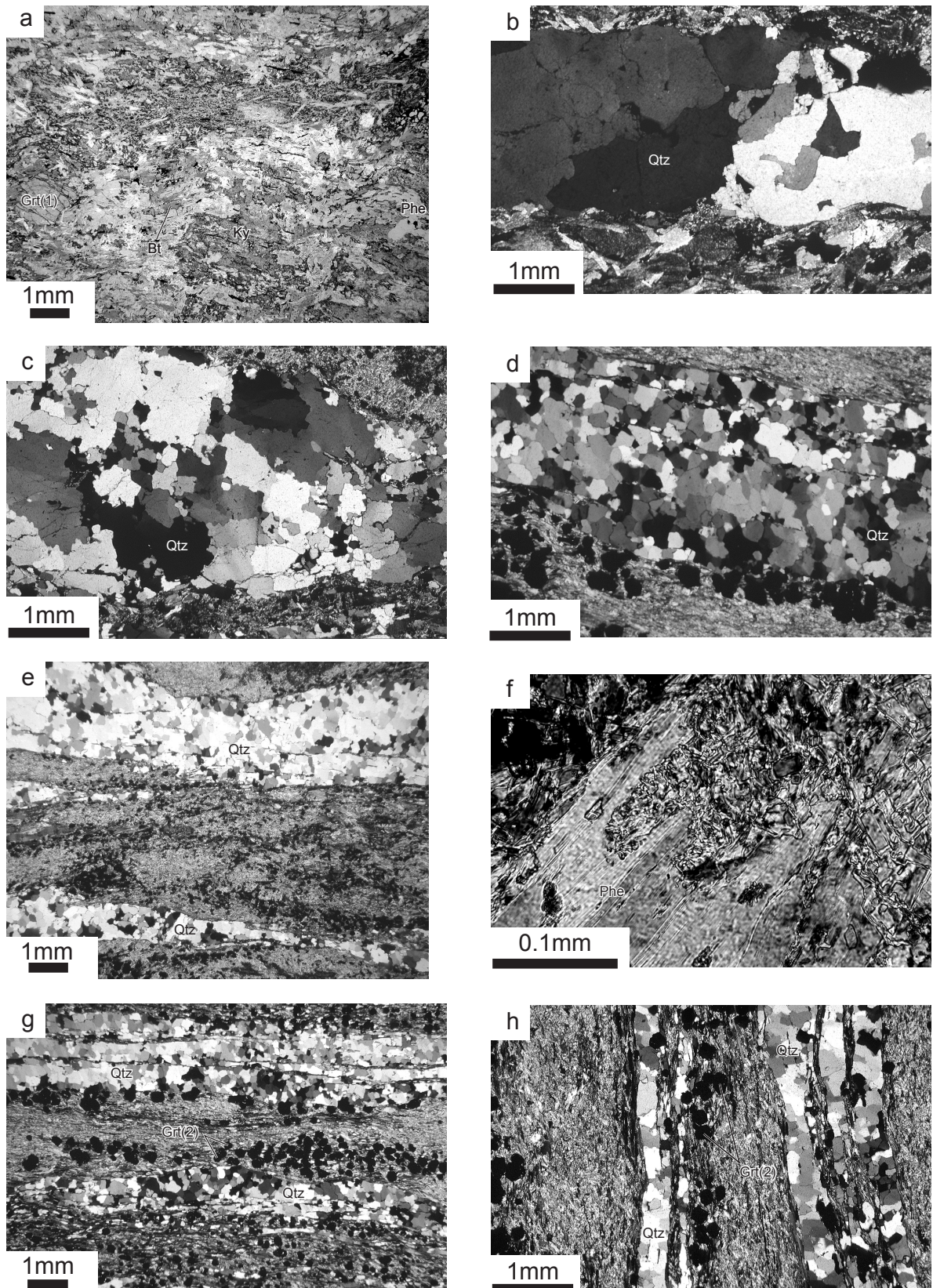


Fig. 3 Microstructures of the shear zone

(a) Overview of the pre-Alpine structures (sample 1). (b) Pre-Alpine quartz microstructures show large grains with straight, annealed grain boundaries. (c) Quartz microstructures of weak Alpine deformation (sample 2) show partial recrystallization by grain boundary migration recrystallization. (d) Completely recrystallized quartz microstructures (sample 4). Note grain size refinement compared to the pre-Alpine quartz (b). (e) Overview of quartz and mica aggregates after moderate Alpine deformation (sample 3). Quartz layers show pinch and swell structures in the micaceous matrix. (f) Partial dynamic recrystallisation of white mica porphyroclasts. Recrystallized grains show a random orientation. (g) Overview of the most strongly deformed sample 4. Lenses of quartz and garnet-mica are interlayered with a largely micaceous matrix. (h) Detail of the micaceous matrix in sample 4 showing domains without preferred orientation of the (001) planes of the white mica.



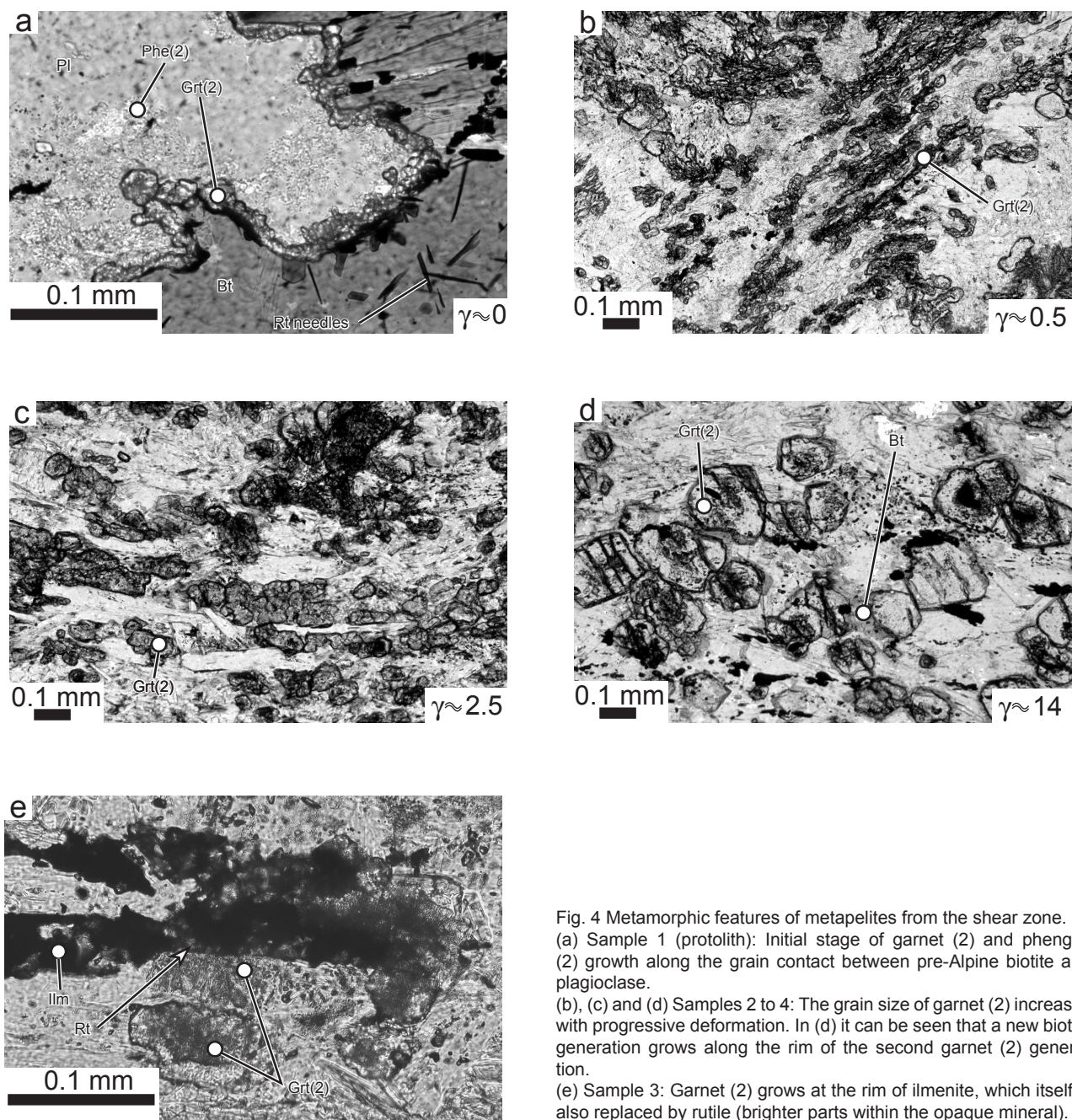


Fig. 4 Metamorphic features of metapelites from the shear zone. (a) Sample 1 (protolith): Initial stage of garnet (2) and phengite (2) growth along the grain contact between pre-Alpine biotite and plagioclase. (b), (c) and (d) Samples 2 to 4: The grain size of garnet (2) increases with progressive deformation. In (d) it can be seen that a new biotite generation grows along the rim of the second garnet (2) generation. (e) Sample 3: Garnet (2) grows at the rim of ilmenite, which itself is also replaced by rutile (brighter parts within the opaque mineral).

of biotite with different composition grows preferentially along the rims of the second generation of garnet (Figs 4d, 5a) and is interpreted as a late, post-deformational retrograde product, which has formed at the expense of garnet and white mica. Based on microstructural observations in the undeformed sample 1 and the mineralogical change observed during the transitions from the undeformed sample 1 to the paragonite-bearing samples 3 and 4, it is inferred that the following

mineral reaction has produced the replacement of the pre-Alpine assemblage



The increasing reaction progress in samples 2, 3, and 4 corresponds to a progressive deformational overprinting of the microstructures. In sample 2, quartz shows partial dynamic recrystallization (Fig. 3c), which is complete in samples 3 and 4

(Fig. 3d). A large number of chessboard subgrains is observed in quartz of sample 2 and is evidence for high temperature recovery (Blumenfeld *et al.*, 1986; Mainprice *et al.*, 1986; Kruhl, 1996). The recrystallization mechanism is grain boundary migration recrystallization (Fig. 3c), which is also indicative of high temperature and/or slow strain rate deformation (Hirth & Tullis, 1992; Stipp *et al.*, 2002). The larger part of the grain boundaries is fairly straight and indicates partial annealing of the Alpine quartz microstructures (Fig. 3d). The pure quartz aggregates display pinch-and-swell-structures and become boudinaged (Fig. 3e) demonstrating that quartz is mechanically stronger than the largely micaceous matrix in the shear zone.

The mica aggregates largely consist of fine grained white mica (grain size approximately 5 to 60  $\mu\text{m}$ ), in which some larger porphyroclasts (up to 1 mm long) are embedded (Fig. 3f). Many of the mica grains are not very elongated but are almost equant (Fig. 3f). In some cases, it is not clear whether the grain size reduction is due to dynamic recrystallization or whether it constitutes a metamorphic reaction. In sample 4, the white mica between newly formed small garnet grains is always of a larger size (up to 0.4 mm long) than the more mica-rich matrix surrounding it (grain size approximately 20 to 200  $\mu\text{m}$ ). These garnet-mica mixtures form lens-shaped boudins within the mica-rich matrix (Fig. 3g), which shows domains without a preferred orientation of the mica (001)-planes (Fig. 3h). All these microstructures demonstrate that the mica-dominated aggregates (more than 90% mica) forming the shear zone matrix are the most strongly deformed and thus the mechanically weakest domains of the rock,

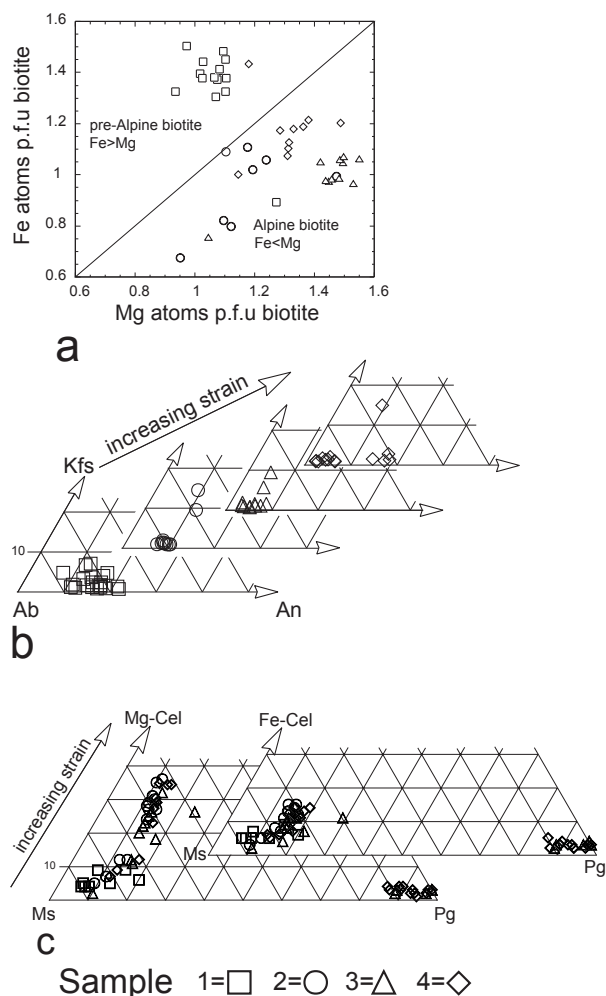


Fig. 5 Biotite, plagioclase and white mica compositions  
 (a) Two biotite generations shown by Fe and Mg contents. Pre-Alpine biotite with Fe > Mg. Late Alpine retrograde biotite Fe < Mg, forming rims around the second generation of garnet (see also Figs 4d & 6c).  
 (b) Plagioclase compositions. Note trend of albite enrichment with increasing strain linked to growth of a second garnet generation, which consumes the anorthite component of plagioclase.  
 (c) White mica compositions. There is a pronounced increase of the Mg-celadonite component with increasing strain while the Fe-celadonite component remains relatively constant.

### 3.7 MINERAL CHEMISTRY

#### 3.7.1 Biotite

Biotite occurs in all samples, and its modal amount decreases with increasing strain (Tables 1, 4). Two generations of biotite are distinguished: the first is a pre-Alpine biotite with Fe > Mg (atoms per formula unit) and the second (a late product of retrograde reactions) shows a composition characterized by Fe < Mg (Fig. 5a, Table 2). In contrast to the second biotite generation the pre-Alpine biotite show exsolution of rutile needles.



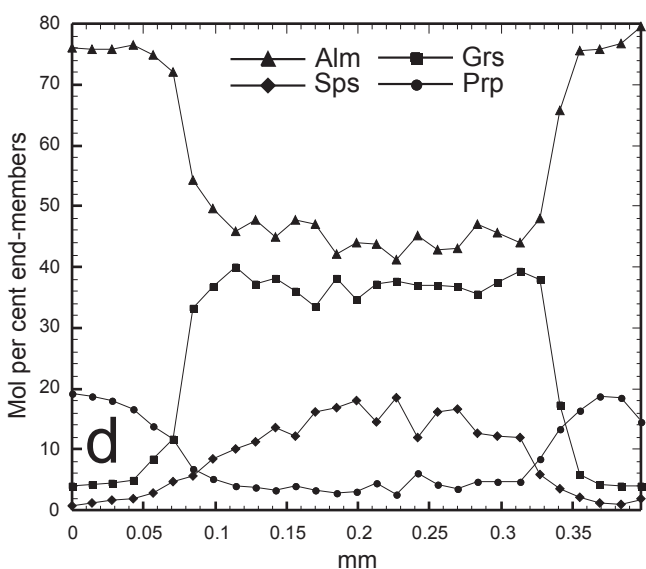
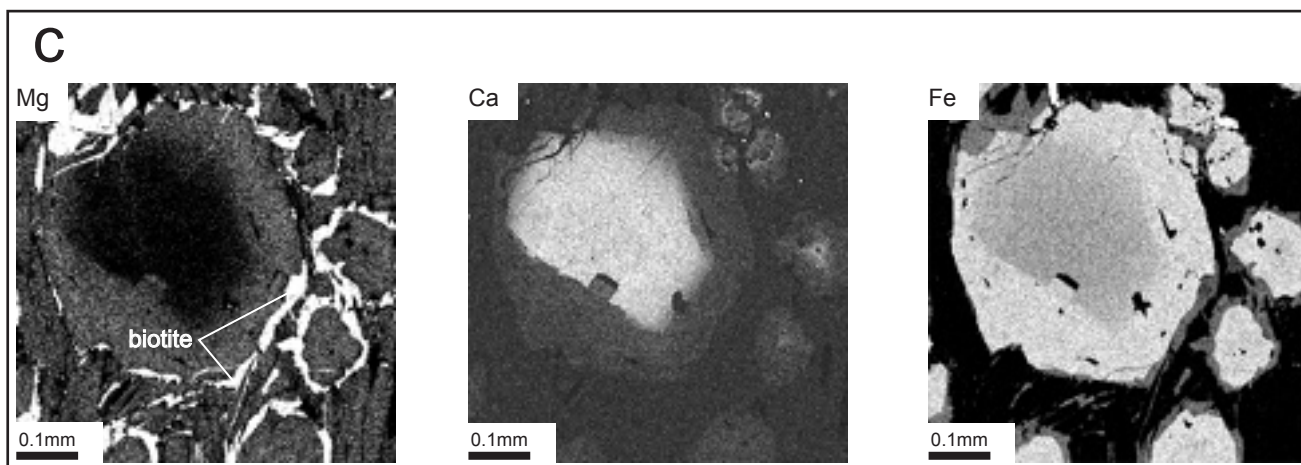
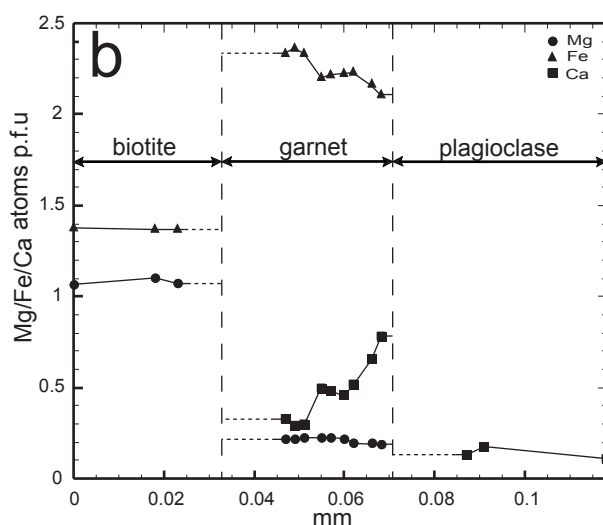
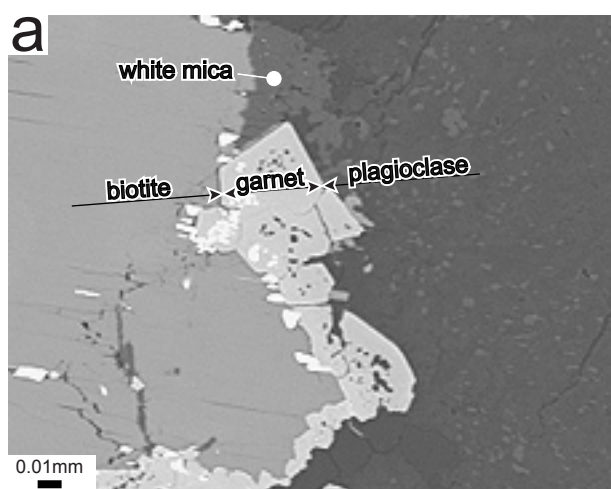


Fig. 6 Garnet composition

(a) Backscatter image of garnet (2) within an undeformed protolith (sample 1). Garnet (2) and white mica crystals along the grain boundaries between pre-existing plagioclase and biotite. (b) Compositional profile (profile trace is indicated in Fig. 6a) gives the element distribution of Fe, Mg and Ca in garnet (1). Note asymmetric zoning, with high Ca content towards plagioclase and high Fe content towards biotite. (c) X-ray maps (Mg, Ca, Fe) of a zoned garnet within the most deformed sample 4. Light colours correspond to high content of a given element. The contrast was adjusted to highlight the zoning. The zoning consists of two homogeneous parts: i) a core rich in grossular, intermediate in almandine, enriched in spessartine and poor in pyrope, ii) a rim poor in grossular and in spessartine, rich in almandine and enriched in pyrope. The second retrograde generation of biotite can be seen along the garnet rims (high Mg-contents). (d) Quantitative garnet zoning profile corresponding to the garnet in Fig. 6c.

### 3.7.2 Plagioclase

All samples contain plagioclase. Its composition in the deformed samples tends to be more albitic

than the undeformed sample (Fig. 5b, Table 2). However, the plagioclase composition of sample 4 shows two distinct groups of composition, which

probably reflects the peristerite gap (Fig. 5b). The modal amount of plagioclase decreases with progressive deformation (Table 1). This is in line with the suggestion of Spear *et al.*, (1991), who predicted both an increase in albite component of the plagioclase and a net consumption of plagioclase during the growth of garnet in pelitic lithologies.

### 3.7.3 White mica

All samples contain white mica. In the unaltered sample 1, white mica is coarse grained and chemically homogeneous with a muscovite-rich composition (Fig. 5c). With increasing strain white mica becomes enriched in the Mg-celadonite-component (Fig. 5c) and a general trend towards elevated Si contents ranging from 3.2 to 3.4 atoms p. f. u. is observed. A concomitant increase in the FeCel-component is less pronounced. The increase in celadonite component occurs at low strain at the transition from sample 1 to 2 in our sampling profile. Within the shear zone, there is no further increase of the celadonite component with increasing strain, but the modal amount of white mica increases with progressive deformation (Table 1). It is important to note that paragonite is restricted to the most deformed samples 3 and 4 (Fig. 5c, Table 2).

### 3.7.4 Garnet

There are two garnet generations: large garnet (1) ( $\approx 0.5$  cm) with corroded rims is part of the pre-Alpine mineral assemblage, whereas small garnet (2) ( $< 1$  mm) represents the product of Alpine metamorphism. In the undeformed sample 1, garnet (2) growth started at grain contacts between pre-existing plagioclase and biotite (Figs 4a, 6a). Such a garnet has high Ca towards plagioclase and high Fe towards biotite (Fig. 6b).

This dependence of the garnet compositions on the nature of the neighbouring minerals indicates that the chemical environment was heterogeneous on a grain scale during garnet growth. The diameters of the second garnet generation increase with progressive deformation (Fig. 4a-d). The larger garnet (2) grains ( $\approx 0.3$  mm) are typically zoned, with a core of intermediate grossular and almandine, low pyrope and a slightly elevated spessartine, and a rim with high almandine, low grossular, low spessartine and slightly elevated pyrope (Fig. 6c, d). The decreases in grossular and spessartine are respectively linked to increases in almandine and pyrope (Fig. 6d).

## 3.8 PHYSICAL CONDITIONS DURING METAMORPHISM

### 3.8.1 Fluid-absent versus fluid-present metamorphism

In order to test for the possible effect of bulk compositions on the stability of mineral assemblages different bulk rock compositions were used as input for the calculation of equilibrium phase diagrams. The bulk rock composition of sample 4 was used to establish the  $P$ - $T$  conditions of the final assemblage in the shear zone (Fig. 7a). The bulk rock composition of the protolith (sample 1) is used to calculate an equilibrium phase diagram of the metamorphic conditions in the wallrock of the shear zone prior to deformation (Fig. 7b). Phase relations in the KNCFMASH system calculated for the bulk rock composition of sample 4, assuming water saturation ( $a_{H_2O}=1$ ) are shown in Fig. 7a. The  $P$ - $T$  estimates for the pre-Alpine and Alpine metamorphic events are indicated by grey shading and the black circle, respectively. The stability field for the observed pre-Alpine assemblage garnet, biotite, phengite, plagioclase,



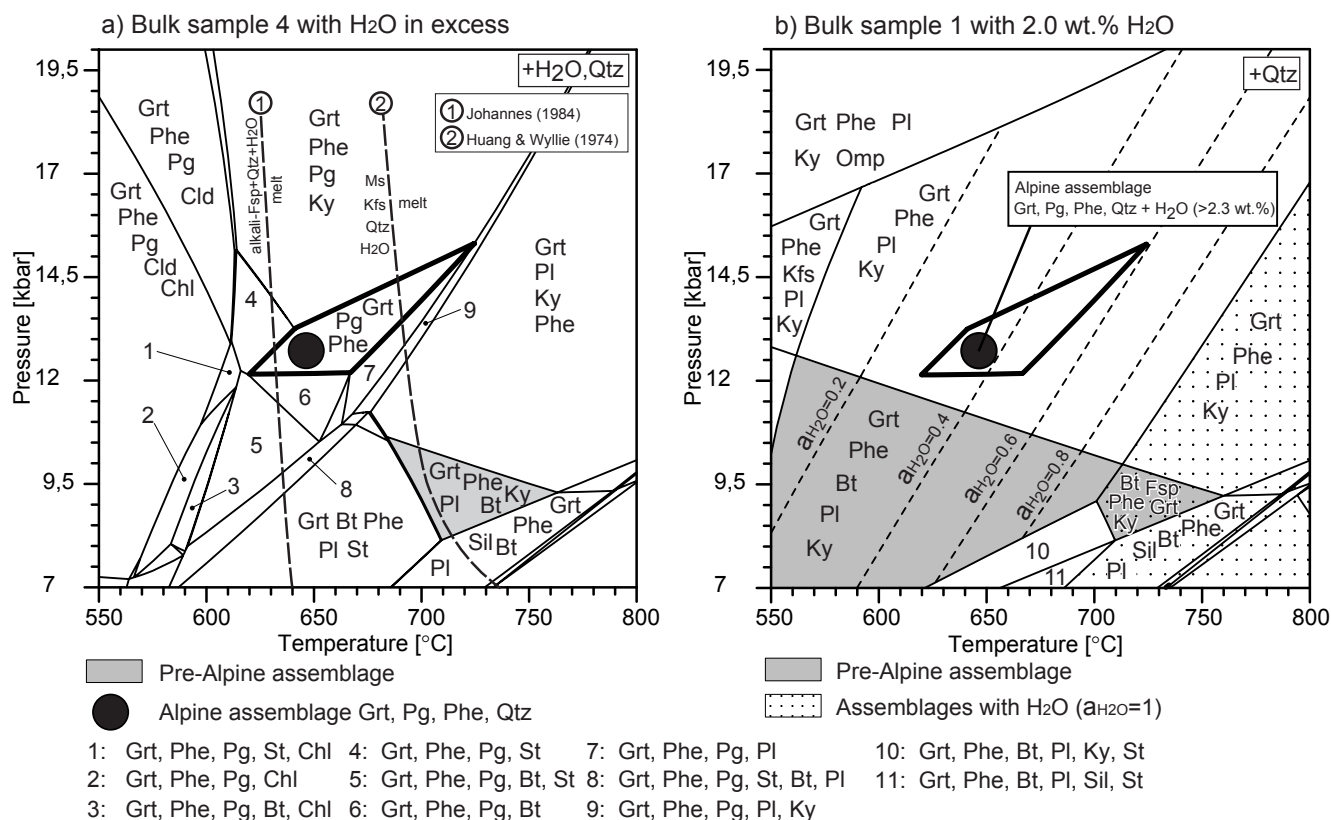


Fig. 7 Equilibrium phase diagrams for specific bulk rock chemistries illustrating the stable mineral assemblages.

(a) Computed for the specific bulk rock composition of sample 4 and the presence of excess water and quartz. There is no overlap between the stability fields of the pre-Alpine assemblage garnet, biotite, phengite, feldspar, kyanite (grey area) observed in unaltered rock (sample 1) and the Alpine assemblage garnet, phengite and paragonite from the fault rock (sample 4). The wet solidus of granite is taken from Huang & Wyllie (1974) and Johannes (1984).

(b) Computed for the bulk rock composition of sample 1; the water content is fixed at 2 wt.% to represent hydrous phases, which are stable with an aqueous fluid at the presumed peak  $P$ - $T$  conditions of the pre-Alpine event (grey area in Fig. 7a, grey and stippled area in Fig. 7b). For this bulk rock water content the pre-Alpine assemblage becomes undersaturated with respect to water and defines water activities  $< 1$  towards lower temperatures and higher pressures. At low water activities the stability field for the pre-Alpine assemblage is extended (grey area) as compared to the water-saturated conditions shown in Fig. 7a. Quartz is stable with all mineral assemblages.

(Grt = garnet, Bt = biotite, Phe = phengite, Pl = plagioclase, Ky = kyanite, Pg = paragonite, St = staurolite, Chl = chlorite, Sil = sillimanite, Cld = chloritoid, Omp=omphacite, Kfs=K-feldspar, Ms= muscovite, Qtz=quartz)

kyanite and quartz is around  $720^{\circ}\text{C}/8.5$  kbar. The Alpine metamorphic assemblage garnet-phengite-paragonite-quartz has its stability field at about  $650^{\circ}\text{C}$  and  $> 12$  kbar. In the study area no evidence for Alpine crustal anatexis has been found in the Monte Rosa nappe, limiting  $P$ - $T$  to below the wet solidus for granite, which is between  $630$ - $700^{\circ}\text{C}$  at 12.5 kbar (Huang & Wyllie, 1974; Johannes, 1994). At higher pressures white mica becomes successively less aluminous, and so for the bulk rock compositions of the fault rocks under consideration this would lead to the formation of kyanite resulting from the liberation Al. The lack of kyanite in the metamorphic Alpine assemblage

garnet-phengite-paragonite-quartz of the fault rocks limits pressures  $< 15$  kbar. As a result we favour  $P$ - $T$  conditions of about  $650^{\circ}\text{C}/12.5$  kbar for the of Alpine metamorphism. Finally, the growth of biotite (second generation in Figs 4d, 5a) is predicted from Fig. 7a at the expense of white mica and garnet during the retrograde stage of the Alpine metamorphic cycle.

The stability field of the pre-Alpine assemblage is quite restricted in the presence of a free aqueous fluid (grey shaded area in Fig. 7a, stippled and grey shaded area in Fig. 7b). Towards lower temperatures, staurolite is expected to form if an aqueous fluid is present in excess.

Retrograde staurolite formation is suppressed and the stability field of the observed pre-Alpine assemblage is significantly extended if the rocks are undersaturated with respect to H<sub>2</sub>O. The grey shaded area in Fig. 7b represents the stability field of the pre-Alpine assemblage if the bulk rock water content is set to 2.0 wt.%, i.e. which is the water content corresponding to the hydroxyl-bearing phases of the observed assemblage only. For this water content, the pre-Alpine assemblage is stable to significantly lower temperatures and higher pressures, defining successively lower water activities with decreasing temperature (Fig. 7b). The preservation of the pre-Alpine assemblage in the country rocks of the Alpine shear zones may thus be interpreted as an indication of low water activity ( $\leq 0.5$ ) in these domains during the Alpine evolution. The equilibrium phase diagram (Fig. 7b) calculated for the bulk composition of the protolith (sample 1) indicates that at the *P-T* conditions of the Alpine metamorphism (approximately 650°C/12.5 kbar) a pressure increase may produce the observed breakdown of biotite, whereas plagioclase would remain stable if the rock were undersaturated with respect to water. The observed decomposition of plagioclase requires the introduction of H<sub>2</sub>O, which is also indicated by the formation of paragonite (in the assemblage of samples 3 and 4). Thus, the formation of the observed Alpine assemblage not only reflects the overprint of the pre-Alpine assemblage at somewhat lower temperatures and higher pressures, but it also indicates infiltration of an aqueous fluid because sample 4 must contain a minimum amount of about 2.3 wt. % H<sub>2</sub>O in order to obtain the Alpine metamorphic assemblage garnet-phengite-paragonite-quartz (Fig. 7a).

### 3.8.2 Garnet growth

The chemical zonation of porphyroblasts such as garnet may reflect the *P-T* evolution during their growth (Spear *et al.*, 1991). In the present context, where the progress of a garnet-forming reaction correlates more with deformation intensity than with metamorphic grade, the chemical zoning of garnet may reflect changes in the local chemical environment and/or the kinetics of growth. The garnet zoning profiles observed within the investigated shear zones may be interpreted as the result of two stages of garnet growth: A first stage is characterized by the formation of garnet along biotite-plagioclase grain contacts. These garnet rims are chemically heterogeneous on a small scale and their composition appears to be controlled by the local chemical environment. A second stage of garnet growth is associated with deformation and fluid infiltration in the Alpine shear zones. In this stage, the earlier formed garnet is overgrown by garnet with comparatively low Ca and Mn contents. We interpret the chemical differences between the two growth stages of garnet to be due to a change in the size of equilibration domains. During the first growth stage, chemical equilibrium was only attained locally at garnet-biotite and at garnet-plagioclase interfaces. Provided that garnet grew simultaneously at both interfaces, the difference in garnet composition at garnet-biotite and garnet-plagioclase interfaces indicates, however, that chemical potential gradients persisted across the garnet rim during growth. This implies that the equilibration domains were small compared to the grain size during the first stage of garnet growth. Garnet composition was controlled by the environment on a local, grain- or sub-grain scale. This compositional pattern indicates low efficiency of chemical transport during the relatively “dry” and more-or-less static

Alpine metamorphic overprint of the pre-Alpine assemblage in the wallrocks of the Alpine shear zones.

In contrast, the rates of material transport were probably significantly enhanced due to the influx of an aqueous fluid in the course of Alpine deformation and shear zone formation allowing material re-distribution and thermodynamic equilibration over length scales that are large compared to the grain size of the rocks during the second stage of garnet growth.

To test this hypothesis the composition of garnet solid solutions was calculated at 650°C/12.5 kbar for different equilibration domains. To represent equilibration on a sub-grain scale the layer boundary composition of 1 mole plagioclase ( $\text{Ca}_{0.2}\text{Na}_{0.8}\text{Al}_{1.2}\text{Si}_{2.8}\text{O}_8$ ), 1 mole biotite ( $\text{K}(\text{Fe}_{1.68}\text{Mg}_{1.32})[\text{Si}_3\text{AlO}_{10}](\text{OH})_2$ ) and 0.005 mole  $\text{H}_2\text{O}$  were used for the initial growth stage (K-feldspar was not considered in this calculation). To account for bulk equilibration during the second growth stage the bulk rock composition of sample 4 was used and the water activity was set to unity. In agreement with the observations, these calculations yield intermediate (Grs=0.51, Prp=0.05, Alm=0.44) and low (Grs=0.07, Prp=0.27, Alm=0.68) grossular contents for the first and second garnet growth stages, respectively. Accordingly, the relatively high grossular contents in the garnet core of Fig. 6d are interpreted as a product of the initial stage of garnet growth, where the Ca from the consumption of plagioclase fractionated into the garnet. The abrupt decrease of the grossular content may either reflect complete consumption of the anorthite component in the reactant plagioclase or a sudden change in the chemical environment. The latter is compatible with a change in the effective rock composition due to a sudden increase of the equilibration domain size

associated with the change from water-deficient to water-saturated conditions. It should be noted that garnet compositions not only depend on the location of garnet nucleation within the protolith (see e.g. Chernoff & Carlson, 1997), but are also a function of the time of nucleation relative to the onset of deformation.

### 3.9 MASS TRANSFER AND REACTION PROGRESS

Equilibrium phase diagrams suggest that the metamorphic transition in the shear zone is mainly due to the infiltration of an aqueous fluid. Infiltration metamorphism may be accompanied by chemical alteration or metasomatism. The following section examines relations among mineral reactions, changes in mineral modes, chemical alteration and deformation (including volume strain) that occurred during shear zone formation.

#### 3.9.1 Model mode

One way to quantify the progress of net-transfer reactions and associated mass transfer is by analysing the systematics of mineral modes together with information on mineral chemistry in a transition from the precursor to the reacted rock. The point counting method cannot usually distinguish chemically distinct generations of a specific mineral. For the investigated shear zones, this problem is encountered with white mica and garnet, both of which occur in two chemically distinct generations, which are difficult to separate optically. Thus there is combined information from point counting, mineral chemistry and bulk rock chemistry to estimate the modal proportions of individual phases and phase components. The procedure used largely follows the method of Ferry (1984) and is described in detail in the appendix.

The following phases and phase components are considered: almandine, pyrope, grossular, phengite, paragonite, biotite, plagioclase, kyanite, and quartz; accessory phases are ilmenite and rutile. The modal amounts of biotite, kyanite and plagioclase determined by point counting combined with their chemical composition were taken as input data for calculations of the modes of the remaining phases and phase components. The modal amount of the remaining phases and phase components was estimated from mass balance considerations that take into account mineral and whole rock chemistry. As the simultaneous estimation of the modal amount of ilmenite and rutile yields unreasonable results, ilmenite is a reactant phase in the protolith and rutile as a product phase in the deformed samples. The first garnet generation (Table 1) was neglected because of its small modal abundance. Calculated modal amounts in Vol. % for the four samples are listed in Table 4 and illustrated in Fig. 8. It can be seen from Fig. 8 that major changes in mineral modes occur during the transition from the wallrock into

Table 4  
Model mode in volume % (Italic=Calculated)

Sample	1	2	3	4
Biotite	23.27	10.93	7.63	4.90
Plagioclase	14.73	8.17	3.00	0.77
Quartz	10.84	28.20	18.25	26.74
Kyanite	12.27	8.07	7.37	0.03
Ilmenite	0.41			
Rutile		0.13	0.49	0.20
Pyrope	2.33	2.97	1.56	5.27
Almandine	8.88	12.69	11.58	14.46
Grossular	0.03	1.10	1.28	1.03
Total Garnet	11.24	16.77	14.42	20.76
Phengite	27.15	27.74	41.48	34.00
Paragonite	0.00	0.00	7.36	12.60
Total White mica	27.15	27.74	48.83	46.60
$\Sigma$	100.00	100.00	100.00	100.00
H <sub>2</sub> O in wt. %	2.08	1.64	2.38	2.29

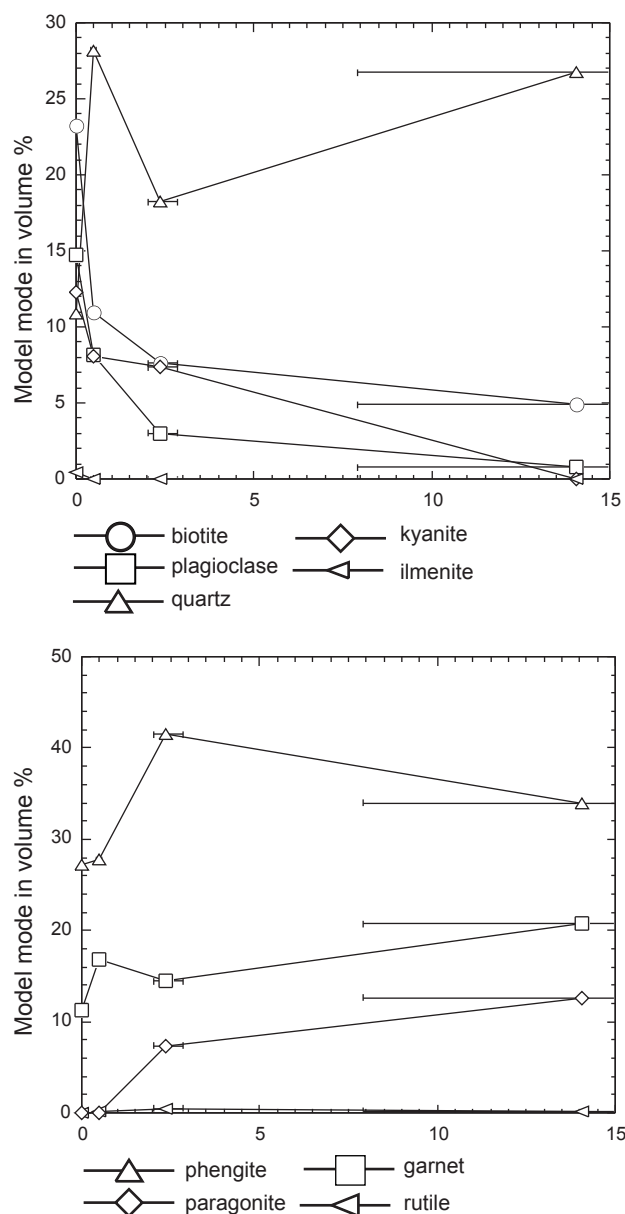


Fig. 8 The calculated modes from Table 4 are plotted vs. strain. The large error bars for high strain results from the uncertainty of the measurements of small foliation angles with the shear plane.

the outer, low-strain part of the shear zone.

### 3.9.2 Volume reference frame

Material gains or losses associated with metasomatism may be quantified if the geochemical behaviour of at least one component or the associated volume change is known (Gresens, 1967; Grant, 1986; Baumgartner & Olsen, 1995). In practice, geometric features such as bedding, fossils and pebbles may serve as strain markers. Such markers usually are absent

in medium and high-grade metamorphic rocks. In such cases, immobile elements, if present, may provide a reference frame for calculation of material gains and losses during chemical alteration (e. g. Thompson, 1975; Kerrich *et al.*, 1977; Ferry, 1983). Alternatively, the modal amount of minerals that are stable during chemical alteration can be used, as a reference frame (Gratier, 1984; Markl *et al.*, 2003). In our study, mineral modes are used rather than component concentrations as input data for the Gresens equation in order to derive relations among changes in mineral modes and volume change.

When mineral reactions proceed during shear zone formation it is reasonable to assume that the abundance of any product phase does not decrease during the transition from the protolith to the deformed equivalents. On the basis of this assumption we define a “minimum product reference frame” (see section below), which allows constraining the volume change associated with chemical alteration. For the Gresens method and the calculation of the bulk reaction the reader is referred to the appendix.

### 3.9.3 Mass transfer and bulk reactions

The relationship between changes in mineral modes and bulk rock element gains are illustrated in Fig. 9. The bulk rock compositions are calculated from mineral modes given in Table 4 and the rock densities listed in Table 3. The bulk rock element gains and losses has also been carried out using bulk rock chemical analyses. The resulting diagrams are practically identical to those of Fig. 9b and thus are omitted here. For the conversion of mineral gains and losses into chemical components the average mineral compositions of Table 2 were used for all phases except for garnet. For garnet the end-member

formula (see Appendix) was used with the addition of Ti but Mn was neglected for the sake of simplicity.

For the observed metamorphic transformation garnet, phengite and paragonite are the product phases. The “minimum product reference frame” is defined as follows: the product phase whose mass change line intersects the horizontal line (=zero mass change) at the smallest  $f_v$  (=volume change) is used to define the “minimum product reference frame”, i.e. it is the critical product phase, which defines the minimum possible volume change during the reaction (Fig. 9a). Selecting the critical product phase for constraining the volume change provides that the mass of all product phases increases or remains at least equal during the metamorphic reaction (the necessary conditions for reaction progress). As outlined above and for the transitions from sample 1 to 2 and 4 the product mineral phengite is critical for constraining the volume change (Fig. 9a, c). For the transition from sample 1 to 3 the product mineral garnet is the critical phase (Fig. 9b). The “minimum product reference frame” yields the maximum possible volume loss ranging between 3 and 21%. The increasing values may reflect the reaction progress and progressive volume loss during reaction and deformation (Fig. 9a). With respect to the “minimum product reference frame” the volume loss during transition from sample 1 to 2 does not exceed 3%. Such a small volume loss represents quasi-constant volume conditions. For a constant volume reference frame Al, K, Ti and Si show consistent results if component gains/losses are measured as bulk rock chemistries and for calculated gains and losses from modal changes throughout the shear zone (Fig. 10). The behaviour of Fe, Na, Ca and Mg is erratic whereas the mass changes of Na, Ca and Mg are small particularly



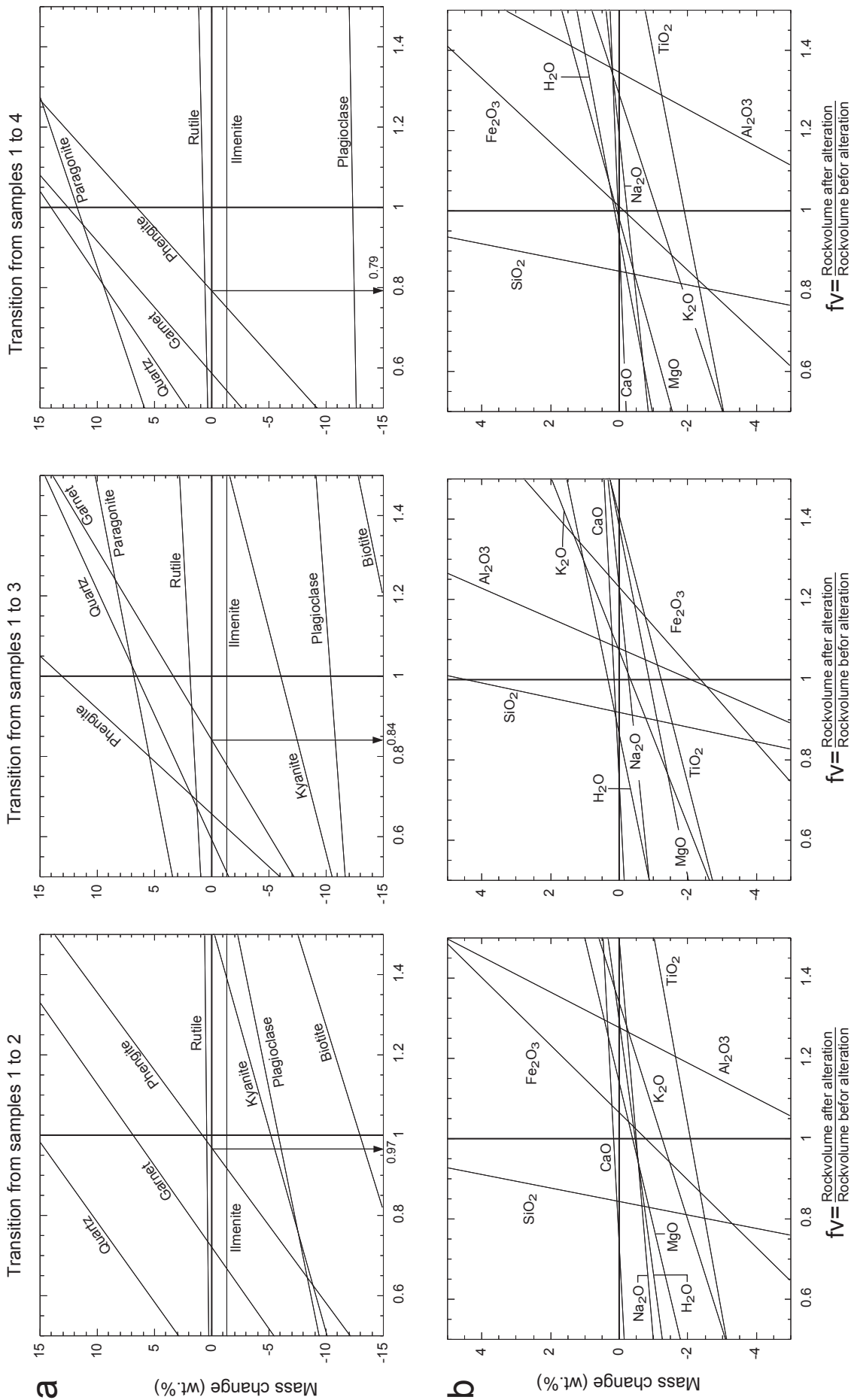


Fig. 9 Comparison of mineralogical mode between the protolith (sample 1) and the progressively deformed samples (2, 3, 4) using the method of Gresens (1967). The Gresens plots are based on modal analyses of Table (4) and mineral compositions (Table 2) considering the mass involved during the breakdown of biotite, plagioclase, kyanite, hematite and quartz to form the products garnet, phengite and paragonite. (a) Volume dependent loss or gain of constituent minerals from sample 1 to 2, 3, 4. The maximum possible volume decrease in the sense of the "minimum product reference frame" is indicated by arrows. (b) The volume-dependant gain and loss of oxides obtained by converting the mineral compositions into oxides. This gives the loss or gain of mass.

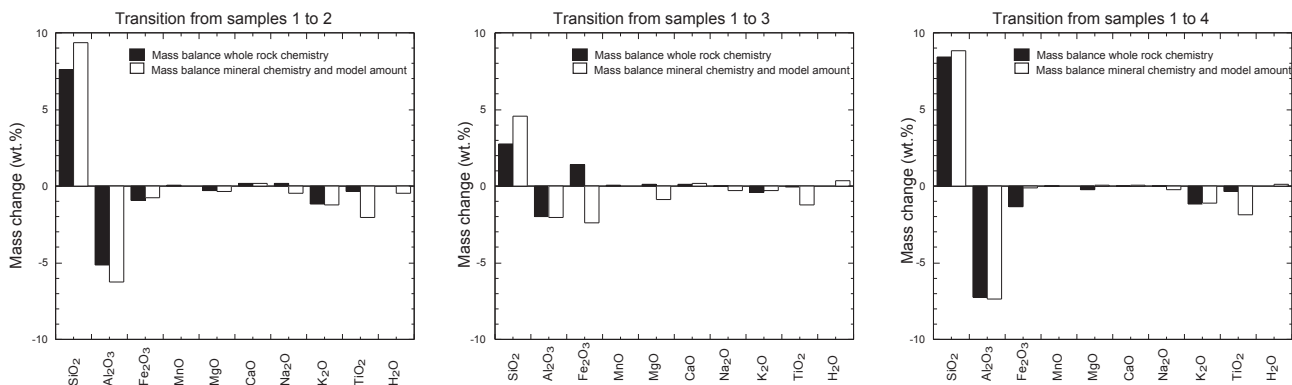
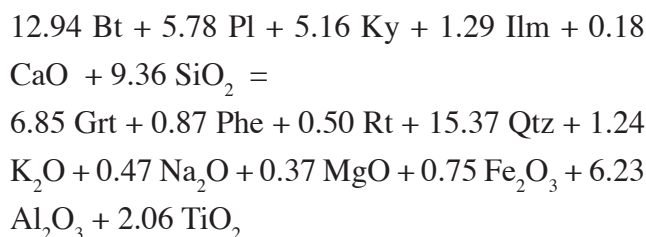


Fig. 10 Mass balance calculations applying the equation of Gresens (1967) and assuming a volume factor  $f_v = 1$ : black columns give the mass transfer by using whole rock chemistry, white columns give the mass change by using modal analyses. Note that both calculations predict at least similar behaviour for Si, Al, K and Ti.

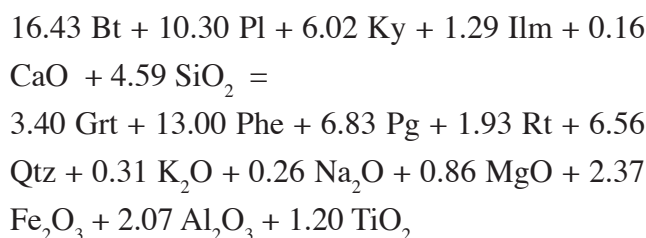
when material gains and losses are measured as bulk rock chemistries. For other volume factors, e.g. for volume increase at constant Al-content, the measured and calculated gains and losses of elements differ and are not consistent. The overall consistency of the behaviour of Al, K, Si and Ti at constant volume in transition from sample 1 to 2 suggest that deformation and the associated metamorphic transformation occurred at approximately iso-volumetric conditions and Al, K and Ti are removed from the rock whereas Si is introduced. The removal of Al may appear against conventional wisdom, which often assumes Al to be immobile. For the shear zone under consideration the bulk rock atomic ratios of Table 3 could imply the immobility of Al because most element vs. Al ratios, with the exception of Si/Al, are relatively constant across the shear zone. If Al were immobile, a volume gain in the range of about 10-35% would have occurred during deformation and reaction (Fig. 9b). Such a volume increase is contrary to the trend of iso-volumetric transition between sample 1 and 2. Since the mineral reaction is the same in all samples and only different reaction progress is recorded, it is very unlikely that the same reaction occurs isovolumetrically initially and produces volume increase at later stages. The consistent trend of element gains/losses,

together with the consistent results from the model bulk chemistry from modal analysis and the measured bulk chemistry for a constant volume reference frame suggest that the shear zone developed at approximately isovolumetric reaction and deformation. Concerning bulk rock atomic ratios there is an increase of the Si/Al and minor increase of Fe/Al, Mg/Al, Ca/Al and Na/Al ratios during the transitions from sample 1 to 2, 3 and 4, whereas the ratio of K/Al and Ti/Al remains rather constant (Table 3). These element trends are in accordance with the inferred removal of Al expecting an increase of most element/Al ratios. Except for Fe in the transition from sample 1 to 3 (see below), there is good agreement between the bulk rock and mineral mode methods of estimating material gains and losses. This consistency indicates that calculated model modes are accurate to a degree that they may serve as a reliable measure to determine the progress of net-transfer reactions. For the constant volume reference frame, the overall reactions that produced samples 2, 3, and 4 from sample 1 (see Appendix) have the following stoichiometries (in mass units):

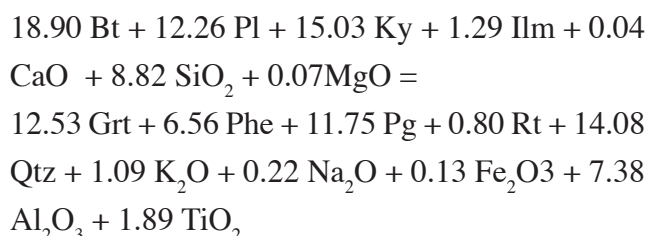
Transition from sample 1 to 2:



Transition from sample 1 to 3:



Transition from sample 1 to 4:



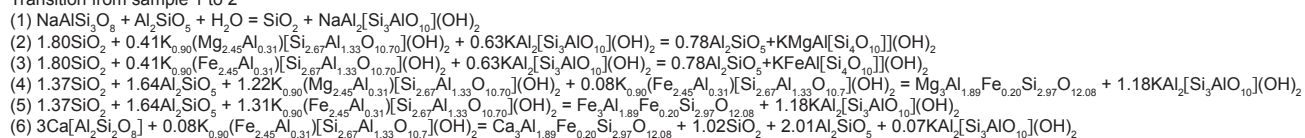
### 3.9.4 Mineral reactions in a closed system

Cation exchange reactions do not change mineral modes (Thompson, 1982). Thus, only net-transfer reactions are considered in the quantification of reaction progress. Calculations are done in the KNCFMASH system; Mn and Ti are neglected for the sake of simplicity. Linearly independent

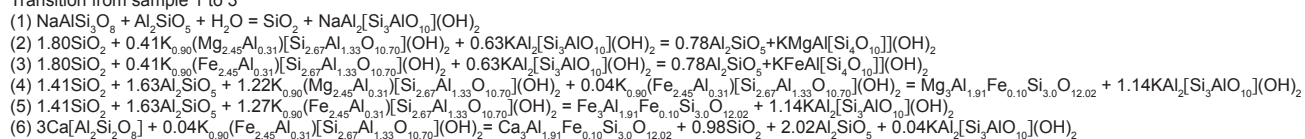
stoichiometric relations are formulated to represent the observed mineral reactions that produced garnet, K-white mica and paragonite from plagioclase, biotite and kyanite (Table 5). The compositions of plagioclase and white mica show systematic variations with increasing reaction progress, and garnet is chemically zoned. Following the suggestions of Ferry (1986), phases with variable compositions are treated in terms of their end-member mole fractions (see Table 5). To account for the variable compositions of solid solutions, separate equations were formulated for paragonite, the Mg- and Fe-celadonite components of K-white mica and for the pyrope, grossular and almandine components of garnet. This procedure yields a total of six net transfer reactions, taking into account the observed mineral chemistries (see Appendix). The initial growth of garnet and K-white mica likely occurred under fluid-deficient conditions. The corresponding reaction equations were thus formulated so as to conserve water. The occurrence of paragonite in the most deformed samples is ascribed to the breakdown in the albite component in plagioclase in the presence of a metamorphic fluid. The progress of the mineral reaction that produces the product

Table 5  
Net-transfer reactions for pelitic rocks. The following relations give the endmembers produced by each individual net-transfer reaction. (1) = paragonite (2) = Mg-celadonite, (3) = Fe-celadonite, (4) = pyrope, (5) = almandine, (6) = grossular.

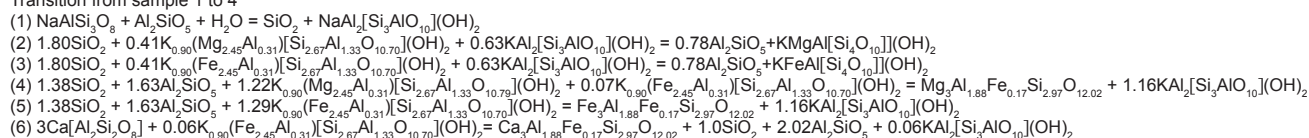
Transition from sample 1 to 2



Transition from sample 1 to 3



Transition from sample 1 to 4



phase or phase component  $j$ ,  $\xi_j$ , was calculated for each progressively deformed sample by using the relationship (Ferry, 1984, Eq. 4) (Table 6):

$$\xi_j = f_v(n_j)_{\text{faultrock}} - (n_j)_{\text{protolith}} \quad (2)$$

Where  $n_j$  gives the amount of phase or phase component  $j$  in the protolith (sample 1) and the altered samples (samples 2, 3, and 4) in mol/m<sup>3</sup>. From mass balance considerations approximately iso-volumetric conditions are inferred and the

Table 6  
Amount (progress  $\xi$ ) of endmember produced by net-transfer reactions for deformed samples (2, 3, 4) during transition from undeformed stage (Sample 1) (mol/m<sup>3</sup>)

Sample	2	3	4
$\xi_1$ (paragonite)	25.43	670.69	938.32
$\xi_2$ (Mg-celadonite)	302.37	670.69	938.32
$\xi_3$ (Fe-celadonite)	43.17	107.25	107.85
$\xi_4$ (pyrope)	56.98	-67.69	260.12
$\xi_5$ (almandine)	331.23	234.77	485.14
$\xi_6$ (grossular)	85.47	99.44	79.39

volume factor  $f_v$  in equation (2) is set to unity. The amount of plagioclase, biotite and kyanite required for the formation of the observed product assemblage in a hypothetical closed system may be derived from the calculated reaction progress and the stoichiometries of the corresponding reaction equations.

### 3.9.5 Relationship between mass transfer and reaction progress

The relationship between mass transfer and the progress of net-transfer reactions is obtained by a comparison of calculated and observed changes in mineral modes. Changes in the modes of the reactant phases in these reactions were calculated for a hypothetical closed system; thus, any discrepancy between observed and calculated variations in these modes must be accounted for by component gains or losses. The differences

between the observed and calculated consumption of the phase components representing plagioclase, biotite, muscovite and kyanite are given in column 2 of Table 7. The bulk mass transfer obtained from these data is illustrated in Fig. 11. Comparison of Figs 10 and 11 shows that mass balance calculated from both, the discrepancies between observed and calculated modal changes and from bulk rock chemistries and densities yield similar trends for all progressively deformed samples. In general, a mass gain is indicated for Si and a mass loss is indicated for Al and K. The good agreement (apart from Fe) between the two methods of calculation suggests that the calculated changes in mineral modes reflect the reaction progress.

Concerning Fe, the two methods consistently indicate the removal of Fe during the transitions from sample 1 to 2 and 4. Mass balance calculations for modal changes indicate that the removal of Fe is probably connected with the reactant mineral biotite (Figs 10, 11, Table 7). During the transition from sample 1 to 3 the behaviour of Fe differs between the two methods applied, whereas mass balance calculations based on bulk rock chemistry indicate that Fe is introduced into the rock (Figs 10, 11). Ilmenite is not considered in

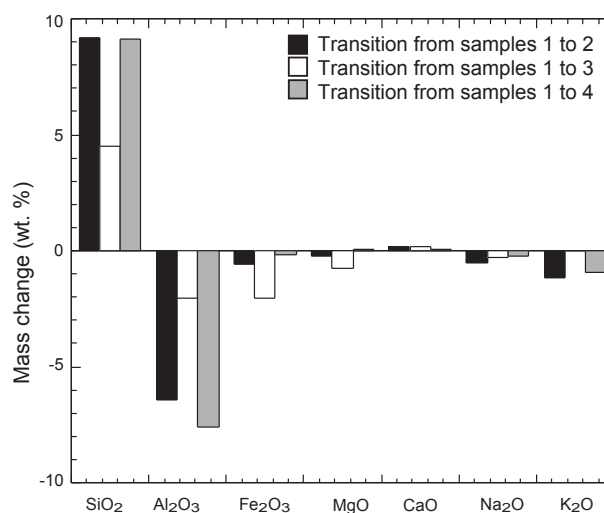


Fig. 11 Mass balance calculation based on reaction progress.

the mass balance calculations for modal changes. Its modal amount decreases during the transition from sample 1 to 3. Hence, neglecting ilmenite is not the reason for of the discrepancy between the two methods. Probably, other Fe-oxides exist in sample 3. The consistent behaviour of Fe during the transitions from sample 1 to 2 and 4 suggests a removal of Fe during deformation.

It is interesting to note that more quartz is present in the deformed rocks than would be expected if its abundance were only controlled by net transfer reactions in a closed system (Table 7, Figs 9, 10). From inspection of Fig. 9 it is seen, however, that the silica gains in the course of mass transfer are too small to fully account for the observed increase in modal quartz. The silica required for the observed increase in modal quartz must be internally derived. The most likely process that may provide silica internally is the dissolution of plagioclase and kyanite. Such a process is corroborated by the fact that less plagioclase and kyanite are present in the deformed rocks than would be expected if their abundance were only controlled by closed system net transfer reactions (Table 7). This leads

us to speculate that plagioclase, kyanite and biotite from the pre-Alpine mineral assemblage are not only consumed in the garnet-, phengite- and paragonite- forming metamorphic reactions, but were in part stoichiometrically dissolved into the metamorphic fluid. Whereas  $\text{SiO}_2$  derived from such dissolution reactions appears to have been immediately re-precipitated to form quartz, other components, such as aluminium and potassium, appear to have been removed via the pore fluid.

### 3.10 DISCUSSION

The metapelites experienced a pre-Alpine metamorphic history, where dehydration reactions produced a relatively “dry”, largely anhydrous assemblage where  $\text{H}_2\text{O}$  was restricted and occurred structurally bound in biotite and phengite. The Alpine metamorphic reactions commenced under fluid-absent conditions as indicated in the undeformed sample 1, where garnet (2) grew along former plagioclase-biotite grain contacts. The garnet rims are interpreted as corona structures or reaction bands in the sense of Joesten (1977). The high degree of

Table 7  
Massbalanced reaction progress for deformed samples (2, 3, 4) during the transition from the undeformed stage (sample 1)

Transition from sample 1 to 2			CaO	$\text{Al}_2\text{O}_3$	$\text{SiO}_2$	$\text{Na}_2\text{O}$	$\text{Fe}_2\text{O}_3$	$\text{K}_2\text{O}$	MgO
Mineral	balanced gain/loss mol/m <sup>3</sup>	wt.%	wt.%	wt.%	wt.%	wt.%	wt.%	wt.%	wt.%
Anorthite	101.49	0.19	0.35	0.41					
Albite	-492.31		-0.85	-2.99	-0.51				
Annite	-83.69		-0.24	-0.45		-0.55	-0.12		
Phlogopite	-66.95		-0.19	-0.36			-0.10	-0.22	
Kyanite	-733.50		-2.52	-1.48					
Quartz	8688.44			17.58					
Muscovite	-579.68			-2.98				-0.92	
Total		0.19	-6.42	9.18	-0.51	-0.55	-1.13	-0.22	
Transition from sample 1 to 3			CaO	$\text{Al}_2\text{O}_3$	$\text{SiO}_2$	$\text{Na}_2\text{O}$	$\text{Fe}_2\text{O}_3$	$\text{K}_2\text{O}$	MgO
Mineral	balanced gain/loss mol/m <sup>3</sup>	wt.%	wt.%	wt.%	wt.%	wt.%	wt.%	wt.%	wt.%
Anorthite	96.24	0.18	0.32	0.38					
Albite	-283.81		-0.48	-1.68	-0.29				
Annite	-320.84		-0.88	-1.69		-2.05	-0.45		
Phlogopite	-241.31		-0.67	-1.28			-0.34	-0.78	
Kyanite	-838.39		-2.81	-1.66					
Quartz	3808.93			7.53					
Muscovite	493.92			2.93				0.77	
Total		0.18	-2.03	4.53	-0.29	-2.05	-0.01	-0.78	
Transition from sample 1 to 4			CaO	$\text{Al}_2\text{O}_3$	$\text{SiO}_2$	$\text{Na}_2\text{O}$	$\text{Fe}_2\text{O}_3$	$\text{K}_2\text{O}$	MgO
Mineral	balanced gain/loss mol/m <sup>3</sup>	wt.%	wt.%	wt.%	wt.%	wt.%	wt.%	wt.%	wt.%
Anorthite	23.53	0.05	0.08	0.10					
Albite	-210.03		-0.37	-1.29	-0.22				
Annite	-23.01		-0.07	-0.13		-0.15	-0.03		
Phlogopite	17.43		0.05	0.10			0.03	0.06	
Kyanite	-1221.95		-4.25	-2.51					
Quartz	8021.04			16.45					
Muscovite	-581.17			-3.03				-0.93	
Total		0.05	-7.58	9.14	-0.22	-0.15	-0.94	0.06	



spatial organization of the garnet rims indicates diffusion-controlled growth. Diffusion control on the grain scale typically occurs under fluid-absent conditions (e.g. Ashworth, 1993; Koons *et al.*, 1986). In fluid-saturated systems, intergranular diffusion is significantly enhanced and one would expect porphyroblastic reaction microstructures instead of coronas (Carlson, 2002). We thus conclude that the first stage of Alpine garnet growth occurred at low water activities. Koons *et al.*, (1986) observed similar corona structures related to fluid-absent metamorphism in granitoids of the Sesia zone.

Equilibrium phase diagrams and component mobilities suggest that the introduction of an aqueous fluid exerted a major control on the studied metamorphic transformation. This view is corroborated by an increase in H<sub>2</sub>O content during the transition of sample 1 to 3 and 4. The increase in water content resulted in the formation of paragonite at the expense of the albite component in plagioclase. It is interesting to note that mass balance calculations indicate a decrease in the H<sub>2</sub>O content during the transition from sample 1 to 2. In this case the decrease of the amount of water bound in hydrated phases is most likely due to the increase in quartz content, which “dilutes” the content of hydrous phases in the rock.

### 3.10.1 Component mobility

Mobility of aluminium, alkali metals and silica at *P-T* conditions between 350 and 500°C and 1 to 2.5 kbar has been demonstrated experimentally for the assemblage quartz-albite-paragonite (Woodland & Walther, 1987). High pressure, experiments indicate enhanced mobility of Al, Fe and Ti (Feenstra & Wunder, 2002). Gains in silica and the mobility of aluminium and alkali metals have been reported from eclogite and amphibolite

facies shear zones in quartz-, feldspar- and mica-bearing rocks (Dipple *et al.*, 1990; Früh-Green, 1994; Matthey *et al.*, 1994). This is in line with our results on the mobility of aluminium, alkali metals and silica due to the solubility of feldspar, mica and kyanite. It must be noted that gains in silica during shear zone formation are not a general rule. In several cases the removal of large amounts of silica has been reported (O’Hara, 1988; Selverstone *et al.*, 1991). In contrast to the investigated shear zone, where deformation was approximately iso-volumetric, the latter examples are all associated with large volume loss.

The differences in the behaviour of silica, aluminium and alkali metals during shear zone formation are not immediately obvious from experimental work or from theoretical calculations. We speculate that the apparent immobility of silica is due to the fact that the infiltrating fluid was already saturated with respect to SiO<sub>2</sub> before fluid-rock interaction. In contrast, the fluid appears to have been undersaturated with respect to aluminium and alkali metals before it was involved in chemical alteration during shear zone formation. The different saturation states of the fluid with respect to silica, aluminium and alkali metals may either be due to differences in the *P-T* dependence of the solubilities of the respective components, or, alternatively, it may be due to the geochemical environment from which the alteration fluid was derived.

Even if the reason for the different geochemical behaviour of the major components cannot be resolved, reaction associated with shear zone formation in metapelites at eclogite facies conditions is a viable mechanism to introduce aluminium-bearing species into an aqueous pore fluid. During reaction such a fluid gains the potential for the precipitation of aluminium

silicates during later stages of its migration through the crust. Aluminosilicate bearing quartz veins are a widespread phenomenon in medium to high-grade metamorphosed basement units (Klein, 1976; Kerrick, 1988; Kerrick, 1990 his Chap. 10). Fluids that were involved in reactions of metapelites in the eclogite facies shear zone formation are certainly a potential source for such vein-forming fluids.

The loss of Fe and Ti during shear zone formation is probably due to the breakdown of pre-Alpine biotite, which contains abundant fine rutile needles.

The model modes and phase diagrams (Table 4, Figs 7, 9b) indicate an increase in the H<sub>2</sub>O content with reaction. Experimentally, it has been shown that fluid-saturated assemblages may locally form even in fluid-deficient systems (Stünitz & Tullis, 2001). The small amount of fluid on the grain boundary produces fluid-saturated conditions locally. Continuing fluid penetration into the shear zone may produce a completely fluid-saturated assemblage or, as in the shear zone investigated here, successive stages of more and more hydrated assemblages. The key factor is the continuing influx of H<sub>2</sub>O into the shear zone and thus to the reaction sites.

### 3.10.2 Effects of the reaction on the deformation

So far, only the effect of the deformation on the reaction progress has been considered but the reaction is also expected to have an enhancing effect on the deformation process. The white mica matrix is the mechanically weakest component. Consequently, the reaction progress forming white mica introduces more weak material to the rock and thus is expected to weaken the reacted material and to promote the localization of shear

deformation.

Weakening of basement rocks by sericitization has been inferred by several authors, especially at lower temperatures in the middle to upper crust (Dixon & Williams, 1983; Janecke & Evans, 1988; Mitra, 1992; Evans & Chester, 1995; Wintsch *et al.*, 1995; Wibberley, 1999). In most of the described cases the weakening is inferred to result from a switch in deformation mechanism from frictional sliding to either diffusion creep or to dislocation creep. In the case presented here, the shear zone formation is a high temperature deformation process, so that the early deformation increments, before a potential mechanism switch has occurred, are unlikely to be frictional.

Mica itself is a mechanically weak phase (Mares & Kronenberg, 1993) and the increasing mica content in experimentally deformed mica-quartz aggregates decreases the strength (Shea & Kronenberg, 1993; Tullis & Wenk, 1994). In these experiments, the deformation mechanism of the mica is dislocation creep involving slip on the (001) plane producing a strong crystallographic preferred orientation of the mica (Tullis & Wenk, 1994). However, many of the mica grains in the fine grained aggregates in the investigated shear zone tend to be rather equant and some domains do not show a well developed preferred orientation of the (001) planes (Fig. 3f, h). Given the small size of the mica in these aggregates (down to 5  $\mu\text{m}$ ), it is likely that the deformation takes place, at least in part, by a diffusion creep mechanism. The fine grain size partly results from the metamorphic reaction forming white mica. Diffusion creep deformation induced by nucleation of fine grained reaction products has been described by, e.g., Rubie (1983), Brodie & Rutter (1985), Gilotti (1989), Stünitz & FitzGerald (1993), Stünitz & Tullis (2001). There probably is

at least a partial transition from dislocation creep to diffusion creep as a result of the white mica forming reaction. Thus, the reaction causes a localization of deformation in the shear zone after minor initial shearing under high pressure/ high temperature metamorphic conditions.

### 3.10.3 Regional aspect

The *P-T* conditions of 720°C and 8.5 kbar obtained from the pre-Alpine assemblage in the undeformed country rocks of the Alpine shear zones probably reflect the highest-pressure conditions that were reached during pre-Alpine metamorphism of the crystalline basement of the Monte Rosa nappe. The assemblages biotite-sillimanite-garnet-quartz-K-feldspar-plagioclase and garnet-biotite-muscovite-sillimanite-plagioclase observed in other parts of the of the Monte Rosa nappe (BEARTH, 1957; DAL PIAZ & LOMBARDO, 1986), point to somewhat lower pressures. We prefer to interpret aggregates of fine-grained kyanite needles as the products of static recrystallization of sillimanite during a late stage of the pre-Alpine metamorphic evolution suggesting that the assemblages described by BEARTH (1957) and by DAL PIAZ & LOMBARDO (1986) belong to an early stage of pre-Alpine metamorphism, whereas the assemblages preserved in the wallrock of the shear zone would represent a late stage of the pre-Alpine evolution.

### 3.11 CONCLUSIONS

Reaction progress in a shear zone in metapelites from the Monte Rosa nappe is intimately linked to shearing deformation, and is restricted to deformed parts of the rock. Shear zone formation facilitated the influx of aqueous fluids into the rock and was the prerequisite for substantial metamorphic reaction progress. A gain of silica and losses of Al

and K during shear zone formation are indicated by consistent results of two different methods of mass transfer calculations, demonstrating the interplay between mass transfer and net-transfer mineral reactions. Assuming that the marginal parts of the shear zone record the earlier parts of the deformation history than the more central parts, the observed mass transfer and modal changes largely occurred during early stages of progressive deformation. The combined infiltration of Si and net transfer mineral reactions cannot account for the observed modal increase of quartz. The Si needed to account for the observed change in modal quartz was largely derived from the dissolution of plagioclase, kyanite and biotite, which released Si, Al and K into the fluid. The Si was immediately re-precipitated within the shear zone, but Al and K remained in the solution and were removed via the pore fluid. Petrological and microstructural data, together with the phase equilibrium diagrams suggest that the scales over which chemical equilibrium was attained differed between the low- and high-strain domains. Chemical equilibrium was only attained on a sub-grain scale in the low-strain domains, where the Alpine metamorphic overprint occurred at water activities of  $\leq 0.5$ . Bulk equilibration was attained on a hand specimen scale within the shear zone, where the metamorphic transformation occurred under  $H_2O$  saturated conditions. The  $H_2O$  influx suggests that deformation has increased permeability and turned the system from fluid-undersaturated into fluid-saturated conditions. High water activities enhanced intergranular diffusion of chemical elements (Carlson, 2002) and thus allowed for chemical homogenisation on a hand specimen scale within the shear zone.

### 3.12 APPENDIX

#### 3.12.1 Thermodynamic calculations

Equilibrium phase diagrams were calculated for specified bulk rock compositions in the system KNCFMASH. Calculations were made with the DOMINO software (De Capitani & Brown, 1987; De Capitani, 1994). Most thermodynamic data were taken from Berman (1988, update 92); staurolite and chloritoid data are from Nagel *et al.* (2002), while garnet uses the solution model of Berman (1990). For the biotite binary (Phl, Ann) ideal mixing on three mixing sites, and for chlorite binary (clinocllore, daphnite) ideal mixing on four mixing sites were considered. For feldspar the solution model of Fuhrman & Lindsley (1988), for staurolite the solution model of Nagel *et al.* (2002) and for phengite the solution models of Massonne & Szpurka (1997) with a ternary expansion after Kohler (1960) was used. For muscovite/paragonite the solution model of Chatterjee & Froese (1975) was used, and for chloritoid binary ideal mixing on one mixing site was used.

#### 3.12.2 Quantification of the model mode

The amount of an element  $i$  relative to Al in a rock is related to the compositions and the abundances of its constituent minerals by (Ferry, 1984):

$$i/Al = \left( \sum_j \alpha_{i,j} \times n_j \right) / \left( \sum_j \alpha_{Al,j} \times n_j \right) \quad (1)$$

where  $i/Al$  is a whole rock atomic ratio (Table 3),  $\alpha_{i,j}$  gives the number of atoms  $i$  per formula unit of mineral  $j$  (Table 2) and  $n_j$  is the number of moles of mineral  $j$  in the rock. In order to solve for the six unknown mineral abundances,  $n_j$ , with  $j =$  pyrope, almandine, grossular, phengite, quartz and ilmenite in sample 1, four equations of type

(1) were written for the components  $i =$  Si, Ca, K, Ti. A fifth equation was formulated to account for the observed garnet composition:

$$Fe/Mg = \left( \sum_j \alpha_{Fe,j} \times n_j \right) / \left( \sum_j \alpha_{Mg,j} \times n_j \right) \quad (2)$$

where  $Fe/Mg$  refers to the relative atomic amounts of Fe and Mg in the rock (Table 3). A sixth equation is derived from normalization to a specified volume of rock:

$$\sum_j n_j \times V_j = 1,000,000 \text{ cm}^3 / \text{m}^3 \quad (3)$$

where  $V_j$  is the molar volume of mineral  $j$  in  $\text{cm}^3/\text{mole}$ . Volumetric data were taken from the database of Berman (1988; update 92) for standard state conditions. The molar volumes for biotite and phengite were calculated from weighted end-member data to account for solid solutions. In sample 2 the same equations were used for the same unknowns as in sample 1 with the exception that the abundance of rutile was solved for instead of ilmenite. In samples 3 and 4 four equations of type (1) ( $i =$  Si, Ca, K, Na, Ti) were used, as well as equations (2) and (3) to solve for the six unknown  $n_j$ ' with  $j =$  pyrope, almandine, grossular, phengite, paragonite, quartz and rutile.

Substantial differences between observed and calculated amounts of quartz and phengite in sample 1 are probably due to the use of mean whole rock composition in equations (1, 2, 3). Sensitivity tests revealed that the calculated model mode is very sensitive to variations of the whole rock composition within the analytical error. If the rock composition is changed by increasing the Si/Al ratio by  $1\sigma$  and reducing the other atomic ratios by  $1\sigma$  a good agreement is obtained between calculated and measured

values. This implies that the modal analysis of sample 1 was performed from a thin section with a slightly elevated Si content as compared to the mean whole rock composition.

End-members amounts are calculated from the relation:

$$n_k = n_j \times X_{k,j} \quad (4)$$

where  $n_k$  is the amount of end member  $k$  = annite, phlogopite, muscovite, paragonite, Mg-celadonite, Fe-celadonite, anorthite and albite in the rock,  $X_{k,j}$  is the mole fraction of end member  $k$  (Table 2) in mineral  $j$  = biotite, two white micas and plagioclase and,  $n_j$  is the modal amount calculated or measured from Table (5).

### 3.12.3 The method of Gresens and overall reactions

Gresens (1967) derived an equation that relates material gains/losses during rock alteration to associated volume changes:

$$\Delta C = C_2 \times f_v \times (\rho_2 / \rho_1) - C_1 \quad (5)$$

The subscripts 1 and 2 refer to the protolith and its altered equivalent.  $\rho_1$  and  $\rho_2$  and  $C_1$  and  $C_2$  are the corresponding densities and element concentrations or abundances of the various constituent oxides or minerals. The volume factor,  $f_v$ , is defined as the ratio of equivalent rock volumes before and after alteration. Depending on whether the  $C$  parameters refer to the concentrations of chemical components or modal mineral abundances,  $\Delta C$  may represent material gains/losses or changes in the amount of mineral phases present.

### 3.12.4 Overall reaction

Consider a rock that undergoes a metamorphic transformation, which involves both, isochemical net transfer reactions and mass transfer. The bulk reaction stoichiometric coefficient of the mineral  $j$ ,  $v_j$ , (in mass units) is obtained from comparison of the mass of mineral  $i$  in the precursor and its equivalent product rock:

$$v_j = n_j^{\text{product}} \times f_v \times \rho_2 / \rho_1 - n_j^{\text{reactant}} \quad (6)$$

where  $n_j$  is the wt. % of mineral  $j$  in the rock.

The stoichiometric coefficient of the oxide component  $i$ ,  $v_i$ , is obtained from:

$$v_i = \sum_j \alpha_i^{j, \text{reactant}} \times n_j^{\text{reactant}} - f_v \times (\rho^{\text{product}} / \rho^{\text{reactant}}) \times \sum_j \alpha_i^{j, \text{product}} \times n_j^{\text{product}} \quad (7)$$

where  $\alpha_{i,j}$  gives the number of atoms  $i$  per formula unit of mineral  $j$  and  $n_j$  is the number of moles of mineral  $j$  in the rock. The products  $\alpha_i \times n_j$  have to be converted into wt. %.

### 3.12.5 Definition of mineral formulae used to quantify the reaction progress

The plagioclase composition is expressed in terms of the anorthite ( $\text{CaAl}_2\text{Si}_2\text{O}_8$ ) and albite ( $\text{NaAlSi}_3\text{O}_8$ ) end-members; the orthoclase component ( $\text{KAlSi}_3\text{O}_8$ ) in plagioclase was neglected. The composition of white mica is expressed in terms of the muscovite ( $\text{KAl}_2[\text{Si}_3\text{AlO}_{10}](\text{OH})_2$ ), paragonite ( $\text{NaAl}_2[\text{Si}_3\text{AlO}_{10}](\text{OH})_2$ ), Mg-celadonite ( $\text{KMgAl}[\text{Si}_4\text{O}_{10}](\text{OH})_2$ ) and Fe-celadonite ( $\text{KFeAl}[\text{Si}_4\text{O}_{10}](\text{OH})_2$ ) phase components. To account for the substitution of Al by  $\text{Fe}^{3+}$  on the six-fold coordinated site the garnet compositions was expressed in terms of mol fraction of  $\text{Mg}_3\text{Al}_{i_\alpha}\text{Fe}_\alpha\text{Si}_\alpha\text{O}_x$ ,  $\text{Fe}_3\text{Al}_{i_\alpha}\text{Fe}_\alpha\text{Si}_\alpha\text{O}_x$  and  $\text{Ca}_3\text{Al}_{i_\alpha}\text{Fe}_\alpha\text{Si}_\alpha\text{O}_x$  where  $i_\alpha$  is the mean amount of



element  $i=Al, Fe^{3+}$  and Si atoms p. f. u. in garnet of each sample. Biotite composition were expressed in terms of  $K_{\alpha}(Fe)_{Fe\alpha+Mg\alpha}(Al)_{\alpha}[Si_{\alpha}Al_{\alpha}O_x](OH)$  and  $K_{\alpha}(Mg)_{Fe\alpha+Mg\alpha}(Al)_{\alpha}[Si_{\alpha}Al_{\alpha}O_x](OH)$  where  $i_{\alpha}$  is the mean amount of element  $i = K, Mg, Fe, Al, Si$  atoms p. f. u. in biotite. Biotite is involved as a reactant only. Its chemical composition is defined in the protolith (sample 1). Therefore only the biotite composition of sample 1 was used. Small Na and Ca contents in biotite were neglected.

### 3.12.6 Estimation of mass transfer from differences between calculated and observed modal changes

The gains/losses of component  $i$  in the course of a metamorphic transformation are obtained from the difference between observed ( $\Delta n_j$ ) and calculated ( $\xi_k \times \nu_j$ ) changes in mineral modes multiplied by the amount of component  $i$  that is contained in each of the constituent minerals  $j$ :

$$\sum_j [\alpha_{i,j} \times (\Delta n_j - \sum_k \nu_{j,k} \times \xi_k)] = \Lambda_i \quad (8)$$

where  $\xi_k$  is the progress of the  $k$ th net-transfer reaction,  $\nu_j$  is the stoichiometric coefficient of mineral  $j$  in the  $k$ th reaction,  $\alpha_{i,j}$  is number of atom  $i$  in atoms p. f. u. of mineral  $j$  and  $\Delta n_j$  is the observed change in amount of mineral  $j$ .  $\Lambda_i$  equals zero for an isochemical metamorphic transformation, and it has a finite value for an allochemical reaction.

### 3.13 ACKNOWLEDGMENTS

This work has benefited from comments and discussion with M. Engi. A thorough and very constructive review by J. Selverstone and B. Holdsworth helped improve the manuscript substantially. W. Stern and H. Hürlimann from the Geochemical laboratory of Basel University performed the whole rock chemical analyses. K. Waite helped with the microprobe analyses. This study is supported by the Swiss National Foundation Grants Nr. 20-61814.00 and Nr. 2000-063662.00.

## REFERENCES

- Abart, R., Schum, R. & Harlov, D., 2001. Metasomatic coronas around hornblende xenoliths in granulite facies marble, Ivrea zone, N Italy, I: constraints on component mobility. *Contributions to Mineralogy and Petrology*, **141**, 473-493.
- Ashworth, J. H., 1993. Fluid-absent diffusion kinetics of Al inferred from retrograde metamorphic coronas. *American Mineralogist*, **78**, 331-337.
- Baumgartner, L. P. & Olson, S. N., 1995. A Least-Squares Approach to Mass Transport Calculations Using the Isocon Method. *Economic Geology*, **90**, 1261-1270.
- Bearth, P., 1952. Geologie und Petrographie des Monte Rosa. *Beiträge zur Geologischen Karte der Schweiz, Neue Folge*, **96**, 94 p.
- Bearth, P., 1957. Erläuterungen Blatt Saas und Monte Moro, Geologischer Atlas der Schweiz. Nr. **30, 31**. *Schweizerische geologische Kommission*, Basel.
- Bearth, P., 1958. Ueber den Wechsel der Mineralfazies in der Wurzelzone des Penninikums. *Mineralogische und Petrographische Mitteilungen*, **38**, 363-373.
- Berman, R. G., 1988. Internally-consistent Thermodynamic Data for Minerals in the System Na<sub>2</sub>O-K<sub>2</sub>O-CaO-FeO-Fe<sub>2</sub>O-Al<sub>2</sub>O<sub>3</sub>-SiO<sub>2</sub>-H<sub>2</sub>O-CO<sub>2</sub>. *Journal of Petrology*, **29**, 445-552.
- Berman, R. G., 1990. Mixing properties of Ca-Mg-Fe-Mn garnets. *American Mineralogist*, **75**, 328-344.
- Blumenfeld, P., Mainprice, D. & Bouchez, J. L., 1986. C-slip in quartz from subsolidus deformed granite. *Tectonophysics*, **127**, 97-115.
- BOWTELL, S. A., CLIFF, R. A. & BARNICOAT, A. C., 1994. Sm-Nd isotopic evidence on the age of eclogitization in the Zermatt-Saas ophiolite. *Journal of Metamorphic Geology*, **12**, 187-196.
- Brodie, K. H. & Rutter, E. H., 1985. On the relationship between deformation and metamorphism with special reference to the behaviour of basic rocks. In: Thompson, A. B. & Rubie, D. C., (eds). *Metamorphic reactions: kinetics, textures, and deformation*. Berlin Heidelberg New York: Springer, *Advances in physical geochemistry*, **4**, 239-264.
- Chatterjee, N. D. & Froese, E., 1975. A Thermodynamic Study of the Pseudobinary Join Muscovite-Paragonite in the System KAlSi<sub>3</sub>O<sub>8</sub>-NaAlSi<sub>3</sub>O<sub>8</sub>-Al<sub>2</sub>O<sub>3</sub>-SiO<sub>2</sub>-H<sub>2</sub>O. *American Mineralogist*, **60**, 985-993.
- Carlson, W. D., 2002. Scales of disequilibrium and rates of equilibration during metamorphism. *American Mineralogist*, **87**, 185-204.
- Cesare, B., 1999. Multi-stage pseudomorphic replacement of garnet during polymetamorphism: 2. Algebraic analysis of mineral assemblages. *Journal of Metamorphic Geology*, **17**, 735-746.
- Chernoff, C. B. & Carlson, W. D., 1997. Disequilibrium for Ca during growth of pelitic garnet. *Journal of Metamorphic Geology*, **15**, 421-438.

- Dal Piaz, G. V. & Lombardo, B., 1986. Early Alpine eclogite metamorphism in the Penninic Monte Rosa- Gran Paradiso basement nappes of the northwestern Alps. Blueschists and Eclogites. *Geological society of America memoir*, **164**, 249-265.
- De Capitani, C. & Brown, T. H., 1987. The computation of chemical equilibrium in complex systems containing non-ideal solutions. *Geochimica et Cosmochimica Acta*, **51**, 2639-2652.
- De Capitani, C., 1994. Gleichgewichts-Phasendiagramme: Theorie und Software. *Berichte der Deutschen Mineralogischen Gesellschaft, Beihefte zum European Journal of Mineralogy*, **6**, 48.
- Dipple, G. M., Wintsch, R. P. & Andrews, M. S., 1990. Identification of the scales of differential element mobility in a ductile fault zone. *Journal of Metamorphic Geology*, **8**, 645-661.
- Dipple, G. M. & Ferry, J. M., 1992. Metasomatism and fluid flow in ductile fault zones. *Contributions to Mineralogy and Petrology*, **112**, 149-164.
- Dixon, J. & Williams, G., 1983. Reaction softening in mylonites from the Arnaboll thrust, Sutherland. *Scottish Journal of Geology*, **19**, 157-168.
- Engi, M., Scherrer, N. C. & Burri, T., 2001. Metamorphic evolution of pelitic rocks of the Monte Rosa nappe: Constrains from petrology and single grain monazite age data. *Schweizerische Mineralogische und Petrographische Mitteilungen*, **81**, 305-328.
- Escher, A., Hunziker, J. C., Marthaler, M., Masson, H., Sartori, M. & Steck, A., 1997. Geologic framework and structural evolution of the western Swiss-Italien Alps. In: Pfiffner, O. A., Lehner, P., Heitzmann, P., Mueller, St. & Steck, A., (eds). *Deep Structure of the Alps, Results of NRP 20*. Basel Boston Berlin: Birkhäuser, 205-222.
- Evans, J. P. & Chester, F. M., 1995. Fluid-rock interaction and weakening of faults of the San Andreas system: inferences from San Gabriel fault-rock geochemistry and microstructures. *Journal of Geophysical Research*, **100**, 13007-13020.
- Feenstra, A. & Wunder, B., 2002. Dehydration of diasporit to corundite in nature and experiment. *Geology*, **30**, 119-122.
- Ferry, J. M., 1983. Mineral reactions and element migration during metamorphism of calcareous sediments from the Vassalboro Formation, south-central Maine. *American Mineralogist*, **68**, 334-354.
- Ferry, J. M., 1984. A Biotite Isograd in South-Central Main, U. S. A. : Mineral Reactions, Fluid Transfer, and Heat Transfer. *Journal of Petrology*, **25**, 871-893.
- Ferry, J. M., 1986. Reaction Progress: A Monitor of Fluid-Rock Interaction during Metamorphic and Hydrothermal Events. In: Walther, J. V. & Wood, B. J., (eds). *Fluid-Rock Interactions during Metamorphism*. New York Berlin Heidelberg Tokyo: Springer-Verlag, 60-88.
- Frey, M., Hunziker, J. C., Neil, J. R. & Schwander, H. W., 1976. Equilibrium-Disequilibrium Relations in the Monte Rosa Granit, Western Alps: Petrological, Rb-Sr and Stable Isotope Data. *Contributions to Mineralogy and Petrology*, **55**, 147-179.
- Frey, M., Desmons, J. & Neubauer, F. (eds), 1999. Metamorphic maps of the Alps. Published by the

editors and as enclosure to *Schweizerische Mineralogische und Petrographische Mitteilungen*, **79**.

Früh-Green, G. L., 1994. Interdependence of deformation, fluid infiltration and reaction progress recorded in eclogitic metagranitoids (Sesia Zone, Western Alps). *Journal of Metamorphic Geology*, **12**, 327-343.

Fuhrman, M. L. & Lindsley, D. H., 1988. Ternary-feldspar modelling and thermometry. *American Mineralogist*, **73**, 201-215.

Gilotti, J. A., 1989. Reaction progress during mylonitization of basaltic dikes along the Särvi thrust, Swedish Caledonides. *Contributions to Mineralogy and Petrology*, **101**, 30-45.

Grant, J. A., 1986. The Isocon Diagram-A Simple Solution to Gresens' Equation for Metasomatic Alteration. *Economic Geology*, **81**, 1976-1982.

Gratier, J., 1984. La déformation des roches par dissolution-cristallisation. Aspects naturels et expérimentaux de ce fluage avec matière dans la croûte supérieure. *Phd these at université scientifique et médicale de Grenoble*, 315p.

Gresens, R. L., 1967. Composition-Volume Relationships of Metasomatism. *Chemical Geology*, **2**, 47-65.

Huang, W. L. & Wyllie, P. J., 1974. Melting relations of muscovite with quartz and sanidine in the  $K_2O-Al_2O_3-SiO_2-H_2O$  system to 30 kilobars and an outline of paragonite melting relations. *American Journal of Science*, **274**, 378-395.

Hunziker, J. C., 1970. Polymetamorphism in the Monte Rosa, Western Alps. *Eclogae Geologicae Helvetiae*, **63**, 151-161.

Hirth, G. & Tullis, J., 1992. Dislocation creep regimes in quartz aggregates. *Journal of Structural Geology*, **14**, 145-159.

Hutchison C. S., 1974. *Laboratory Handbook of Petrographic Techniques*. New York: John Wiley, 527 p.

JABOYEDOFF, M., BÉGLÉ, P. & LOBRINUS, S., 1996. Stratigraphic et évolution structurale de la zone de Furgg, au front de la nappe du Monte Rosa. *Bulletin de la Société Vaudoise des Sciences Naturelles*, **84.2**, 191-210.

Janecke, S. & U. Evan, J. P., 1988. Feldspar-influences rock rheologies. *Geology*, **16**, 1064-1067.

Joesten, R., 1977. Evolution of mineral assemblage zoning in diffusion metasomatism. *Geochimica et Cosmochimica Acta*, **41**, 649-670.

Johannes, W., 1984. Beginning of melting in the granite system Qtz-Or-Ab-An- $H_2O$ . *Contributions to Mineralogy and Petrology*, **86**, 264-273.

Keller, L. M. & Schmid, S. M., 2001. On the kinematics of shearing near the top of the Monte Rosa nappe and the nature of the Furgg zone in the Val Loranco Antrona valley, N. Italy : tectonometamorphic and paleogeographical consequences. *Schweizerische Mineralogische und Petrographische Mitteilungen*,

**81**, 347-367.

Kerrick, R., Fyfe, W. S., Gorman, B. E. & Allison, I., 1977. Local Modification of Rock Chemistry by Deformation. *Contributions to Mineralogy and Petrology*, **65**, 183-190.

Kerrick, D. M., 1988. Al<sub>2</sub>SiO<sub>5</sub>-bearing segregation in the Lepontine Alps, Switzerland: aluminium mobility in metapelites. *Geology*, **16**, 636-640.

Kerrick, D. M., 1990. The Al<sub>2</sub>SiO<sub>5</sub> polymorphs. *Mineralogical Society of America, Reviews in Mineralogy*, **22**, 406p.

Klein, H. H., 1976. Aluminosilikatführende Knauern im Lepontin. *Schweizerische Mineralogische und Petrographische Mitteilungen*, **56**, 435-456.

Klein, J. A., 1978. Post-nappe folding southeast of the Mischabel Rückfalte (Pennine Alps) and some aspects of the associated metamorphism. *Leidse Geologische Mededelingen*, **51**, 233-312.

Kohler, F., 1960. Zur Berechnung der thermodynamischen Daten eines ternären Systems aus den zugehörigen binären Systemen. *Monatshefte für Chemie*, **91**, 738-740.

Koons, P. O., Rubie, D. C. & Frueh-Green, G., 1987. The Effects of Disequilibrium and Deformation on the Mineralogical Evolution of Quartz Diorite During Metamorphism in the Eclogite facies. *Journal of Petrology*, **28**, 679-700.

Kruhl, J. H., 1996. Prism- and basal-plane parallel subgrain boundaries in quartz: a microstructural geothermobarometer. *Journal of Metamorphic Geology*, **14**, 581-589.

LACASSIN, R., 1987, Kinematics of the ductile shearing from outcrop to crustal scale in the Monte Rosa nappe, Western Alps. *Tectonics*, **6**, 69-88.

Mainprice, D. H., Bouchez, J. L., Blumenfeld, P. & Tubiá, J. M., 1986. Dominant c slip in naturally deformed quartz: implications for dramatic plastic softening at high temperature. *Geology*, **14**, 819-822.

MANCKTELOW, N. S., 1992. Neogene lateral extension during convergence in the Central Alps: Evidence from interrelated faulting and backfolding around the Simplonpass Switzerland. *Tectonophysics*, **215**, 295-317.

Mares, V. M. & Kronenberg, A. K., 1993. Experimental deformation of muscovite. *Journal of Structural Geology*, **15**, 1061-1075.

Markl, G., Abart, R., Vennemann, T. & Sommer, H., 2003. Mid crustal metasomatic reaction veins in a spinel peridotite. *Journal of Petrology*, in press.

Massonne, H. J. & Szpurka, Z., 1997. Thermodynamic properties of white micas on the basis of high-pressure experiments in the system K<sub>2</sub>O-MgO-Al<sub>2</sub>O<sub>3</sub>-SiO<sub>2</sub>-H<sub>2</sub>O and K<sub>2</sub>O-FeO-Al<sub>2</sub>O<sub>3</sub>-SiO<sub>2</sub>-H<sub>2</sub>O. *Lithos*, **41**, 229-250.

Mattey, D., Jackson, D. H., Harris, N. B. W. & Kelly, S., 1994. Isotopic constraints on fluid infiltration from an eclogite-facies shear zone, Holsenoy, Norway. *Journal of Metamorphic Geology*, **12**, 311-325.



McCaig, A. M., Wickham, S. M. & Taylor, H. P., 1990. Deep fluid circulation in alpine shear zones, Pyrenees, France: field and oxygen isotope studies. *Contributions to Mineralogy and Petrology*, **106**, 41-60.

McCaig, A. M., 1997. The geochemistry of volatile fluid flow in shear zones. In: Holness M. B. (eds). *Deformation-enhanced fluid transport in the earth's crust and Mantle*. London: Chapman & Hall, 227-266.

MEANS, W. D., 1995. Shear zones and rock history. *Tectonophysics*, **238**, 229-254.

Milnes, A. G., Greller, M. & Müller, R., 1981. Sequenz and style of major post- nappe structures, Simplon- Pennine Alps. *Journal of Structural Geology*, **3**, 411-420.

Mitra, G., 1992. Deformation of granitic basement rocks along the fault zones at shallow to mid-crustal levels. In: *Structural geology of fold and thrust belts*, (eds Mitra, S. & Fisher, G. W), pp. 123-144. Johns Hopkins University Press, Baltimore.

Nagel, T., De Capitani, C. & Frey, M., 2002. Isograds and *P-T* evolution in the Southeastern Lepontine Dome (Graubünden, Switzerland). *Journal of Metamorphic Geology*, **20**, 309-324.

PFEIFER, H. R., COLOMBI, A. & GANGUIN, J., 1989. Zermatt-Saas and Antrona zone: A petrographic and geochemical comparison of polyphase metamorphic ophiolites of the West-Central Alps. *Schweizerische Mineralogische und Petrographische Mitteilungen*, **69**, 217-236.

O'Hara, K., 1988. Fluid flow and volume loss during mylonitization: an origin for phyllonite in an overthrust setting, North Carolina, U.S.A. *Tectonophysics*, **156**, 21-36.

Potdevin, J-L. & Marquer, D., 1987. Méthodes de quantification des transferts de matière par les fluides dans les roches métamorphique déformées. *Geodinamica Acta (Paris)*, **1**, 193-206.

Ramsay, J. G., 1980. Shear zone geometry: a review. *Journal of Structural Geology*, **2**, 83-99.

RUBATTO, D., GEBAUER, D. & COMPAGNONI, R., 1997. Dating the UHP/HP metamorphism in the western Alps Sesia-Lanzo and Zemat- Saas- Fee: Evidence for subductions events at the Cretaceous-Tertiary boundary in the Middle Eocene. Fifth Internat. Eclogite Conf. Ascona supplement No1 to *Terra Nova*, **9**, 30-31.

Rubie, D.C., 1983. Reaction-enhanced ductility: the role of solid-solid univariant reactions in deformation of the crust and mantle. *Tectonophysics*, **96**, 331-352.

SARTORI, M., 1987. Structure de la zone Combin entre les Diablons et Zermatt (Valais). *Eclogae Geologicae Helvetiae*, **80**, 789-814.

Selverstone, J., Morteani, G. & Staude, J.-M., 1991. Fluid channelling during ductile shearing: transformation of granodiorite into aluminous schist in the Tauern Window, Eastern Alps. *Journal of Metamorphic Geology*, **9**, 419-431

Selverstone, J., 1993. Micro-to macroscale interactions between deformational and metamorphic processes, Tauern Window, Eastern Alps. *Schweizerische Mineralogische und Petrographische*

*Mitteilungen*, **73**, 229-239.

Shea, W. T. & Kronenberg, A. K., 1993. Strength and anisotropy of foliated rocks with varied mica contents. *Journal of Structural Geology*, **15**, 1097-1121.

Spear, F. S., Kohn, M. J., Florence, F. P. & Menard, T., 1991. A model for garnet and plagioclase growth in pelitic schists: implications for thermobarometry and P-T path determinations. *Journal of Metamorphic Geology*, **8**, 683-696.

STECK, A., 1984. Structures de déformation tertiaires dans les Alpes centrales. *Eclogae Geologicae Helvetiae*, **77**, 55-100.

STECK, A., 1987. Le massif du Simplon-Réflexions sur la Cinématique des nappes de gneiss. *Schweizerische Mineralogische und Petrographische Mitteilungen*, **67**, 27-45.

STECK, A., 1989. Structures de déformation alpine dans la région de Zermatt. *Schweizerische Mineralogische und Petrographische Mitteilungen*, **69**, 205-209.

STECK, A., 1990. Une carte des zones de cisaillement ductile dans les Alpes Centrales. *Eclogae Geologicae Helvetiae*, **83**, 603-626.

STECK, A. & HUNZIKER, J. C., 1994. The Tertiary structural and thermal evolution of the Central Alps-Compressional and extensional structures in an orogenic belt. *Tectonophysics*, **238**, 229-254.

Stipp, M., Stünitz, H., Heilbronner, R. & Schmid, S.M., 2002. The Eastern Tonale fault zone: a “natural laboratory” for crystal plastic deformation of quartz over a temperature range from 250 to 700°C. *Journal of Structural Geology*, **24**, 1861-1884

Stünitz, H., 1993. Transition from fracturing to viscous flow in a naturally deformed metagabbro. In: Boland, J. N. & Fitz Gerald, J. D. (eds). *Defects and processes in the solid state: Geoscience Applications*. Amsterdam: Elsevier, 121-150.

Stünitz, H. & Fitz Gerald, J. D., 1993. Deformation of granitoids at low metamorphic grades. II. Granular flow in albite-rich mylonites. *Tectonophysics*, **221**, 299-324

Stünitz, H. & Tullis, J., 2001. Weakening and strain localization produced by syn-deformational reaction of plagioclase. *International Journal of Earth Sciences (Geol. Rundschau)*, **90**, 136-148.

Thompson, A. B., 1975. Calc-Silicate Diffusion Zones between Marble and Pelitic Schist. *Journal of Petrology*, **16**, 314-346.

Thompson, J. B., 1982. Reaction Space: An Algebraic and Geometric Approach. In: Ferry J. M. (ed). *Characterization of Metamorphism through Mineral Equilibria*. Mineralogical Society of America, *Reviews in Mineralogy*, **10**, 33-52.

Tullis, J. & Wenk, H. R., 1994. Effect of muscovite on the strength and lattice preferred orientation of experimentally deformed quartz aggregates. In: Herman, H. (ed). *Materials Science and Engineering*, **A175**, 209-220.

White, S. H. & Knipe, R. J., 1978. Transformation- and reaction-enhanced ductility in rocks. *Journal of the Geological Society London*, **135**, 513-516

Wibberley, C., 1999. Are feldspar-to-mica reactions necessarily reaction-softening process. *Journal of Structural Geology*, **21**, 1219-1227.

Wintsch, R. P., Christoffersen, R. & Kronenberg, A. K., 1995. Fluid-rock reaction weakening of fault zones. *Journal of Geophysical Research*, **100**, 13021-13032.

Woodland, A. B. & Walther, J. V., 1987. Experimental determination of the solubility of the assemblage paragonite, albite, and quartz in supercritical H<sub>2</sub>O. *Geochimica et Cosmochimica Acta*, **51**, 365-372.

## 4. STRUCTURAL AND METAMORPHIC EVOLUTION OF THE CAMUGHERA-MONCUCCO- AND THE MONTE ROSA- UNITS SOUTHWEST OF THE SIMPLON LINE

L. M. Keller, M. Hess, B. Fügenschuh and S. M. Schmid

Department of Earth Sciences, Basel University, Bernoullistrasse 32, CH-4056 Basel

### 4.1 ABSTRACT

This combined structural and petrological study examines relationships between deformation and metamorphism in the Camughera-Moncucco, Antrona and northeastern Monte Rosa units, and it correlates major late stage deformation structures, such as the Vanzone antiform and Simplon normal fault. D1/D2 deformation and related top-N or top-NW thrusting started under high-pressure conditions (12.5-16 kbar) at relatively high temperatures (600-650°C). Petrological and structural data, together with published radiometric data, suggest that top-SE shearing within the structural top of the high-pressure units in the upper Penninic is Alps coeval with top-N or top-NW thrusting at their structural base. This suggests differential ascent of high-pressure units relative to the surrounding units during nappe stacking and associated crustal shortening. Barrovian metamorphism in the upper Penninic Alps is related to a first phase of backfolding, active between c. 35 Ma and c. 29-26 Ma ago (D3). D3 involves dextral shearing in map view, combined with top-WSW shearing and orogen-parallel extension. Unroofing by orogen-parallel extension delays cooling during decompression, which leads to isothermal decompression after the high-pressure stage. Towards deeper structural levels in the east, D3 deformation becomes progressively younger and prevailed at increasingly higher temperatures. Hence, the brittle-ductile transition occurs later in the Ossola valley than at higher structural levels further west. Masera synform and Brevettola antiform form an open fold pair and represent the eastern continuation of the major Vanzone antiform (D4). Normal faulting across the Simplon line overlaps in time with the formation of these major D4 backfolds. Displacement along the Simplon normal fault gradually decreases towards the southeast as it is transformed into syn-D4 dextral shearing of the southern limbs of Vanzone and Brevettola antiforms.

Keywords: Alps, kinematics, metamorphism, exhumation, transpression

## 4.2 INTRODUCTION

For a long time high-pressure metamorphism in the upper Penninic units of Western Switzerland was supposed to be of Cretaceous age (e.g. review by Hunziker et al., 1992). Consequently, parts of the tectonic structures observed west of the Lepontine dome were correlated with a Cretaceous high-pressure metamorphic event. Also, fast exhumation was widely believed to have occurred before the Tertiary (Steck & Hunziker, 1994).

Recently, an increasing amount of isotopic studies, combined with structural arguments, pointed towards a Tertiary age for high-pressure metamorphism in the Western Alps (Froitzheim et al., 1996; Gebauer, 1999). In the Western Alps west of the Lepontine dome re-equilibration occurred under greenschist facies conditions and in the context of backthrusting, dated as late Eocene to Early Oligocene (Barnicoat et al., 1995; Markley et al., 1998). This suggests that Tertiary-age high-pressure metamorphism was immediately followed by fast exhumation.

The studied area is situated southeast of the Simplon line (Fig. 1) and at the eastern margin of the Lepontine dome (Merle et al., 1989), where the metamorphic zonation indicates an eastwards increase of metamorphic grade. While the more western parts reached greenschist facies conditions during decompression (Bearth, 1958; Colombi, 1989; Frey et al., 1999), the more eastern parts reached Barrovian P-T conditions upon decompression from the high-pressure stage (Engi et al., 2001, Keller et al., *subm.*). Such along-strike changes in metamorphic grade upon decompression suggest that the P-T history related to a particular deformation phase may also change from west to east and into the Lepontine dome.

This study, focussing on gneissic units southwest of the Simplon line, aims at revealing relation-

ships between deformation and metamorphism. Deformation phases will be correlated with individual mineral assemblages, based on a microstructural analysis of metapelites. With the help of phase equilibrium diagrams we will infer the P-T histories during individual deformation phases and conclude on the interrelationships between deformation and metamorphic evolution.

From a regional point of view, there is a wealth of studies on the structure and tectonics of the Camughera-Moncucco (CM) unit and adjacent units (Bearth, 1957a; Laduron, 1976; Klein, 1978; Steck, 1984, 1987) in the working area (Fig.1). At least 4 phases of deformation are observed (Milnes et al., 1981). Early shearing and related mylonitisation, related to nappe stacking, started under eclogite facies conditions in the Monte Rosa unit and adjacent Furgg Zone (Keller & Schmid 2001) and continued during D2, still associated with the same kinematic regime (Keller & Schmid, 2001). Note however, that up to now high-pressure metamorphism is not yet documented in the underlying CM unit. A major switch in the kinematic regime occurred after D2, resulting in the formation of a first set of backfolds (D3) and associated dextral shearing. A second backfolding phase D4 formed the major Vanzone antiformal backfold (Bearth, 1957a; Laduron, 1976). However, the location of its axial trace becomes ambiguous towards the east. According to Milnes et al. (1981) the Vanzone backfold is supposed to become increasingly tighter towards the east, associated with a complete transposition of older foliations. On the other hand Klein (1978) proposed open folding during D4 (his "Brevettola antiform") further to the east.

The relative timing and kinematics during the formation of the major Vanzone antiform and normal faulting in the Simplon fault zone, respectively,



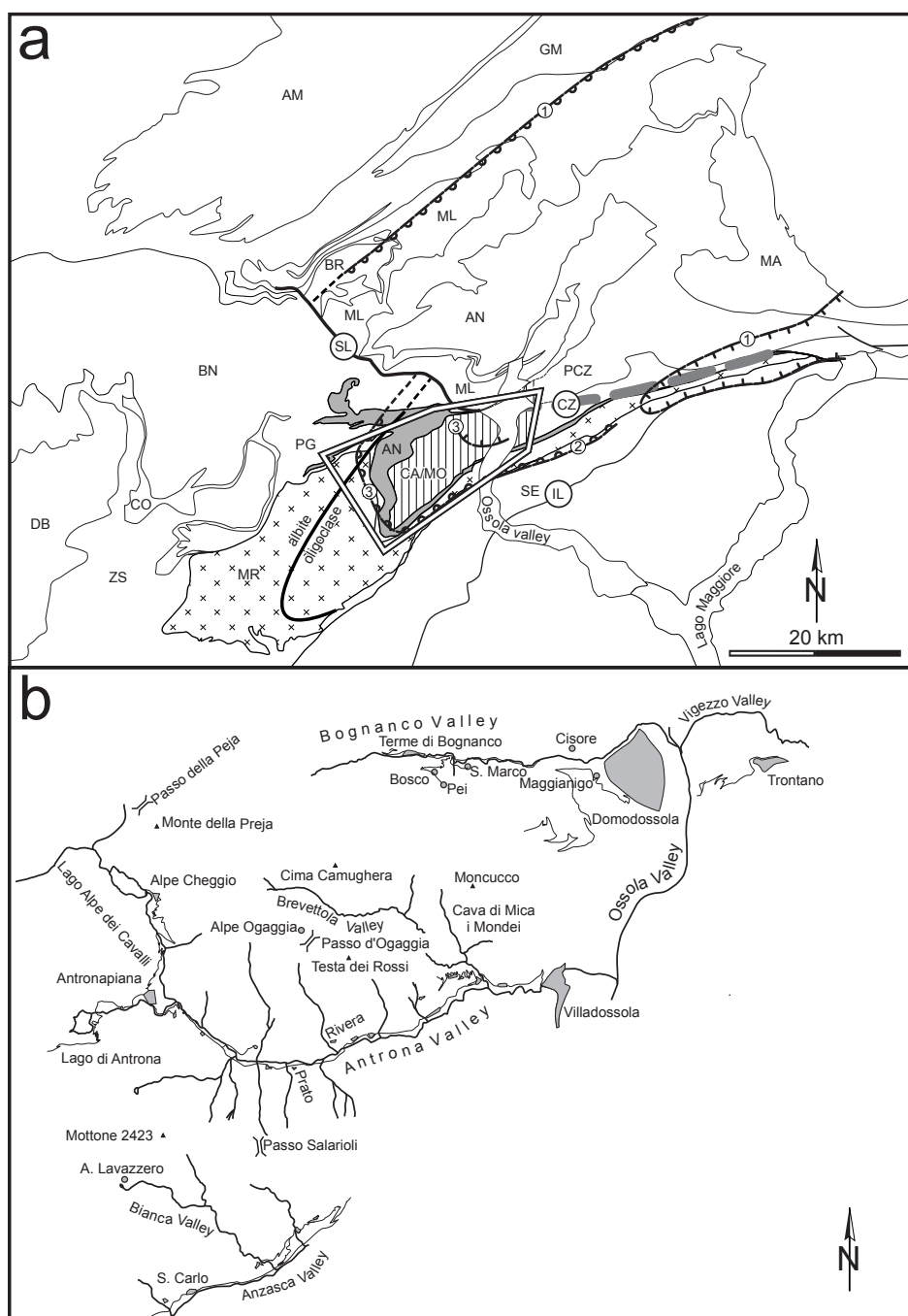


Fig. 1 Tectonic overview and localities in the working area

a) Tectonic map of the western part of the Penninic Alps modified after "Tektonische Karte der Schweiz" (Spicher, 1976) and outline of the study area. The mapped mineral zone boundaries characteristic for Barrovian metamorphism are: 1: sillimanite and staurolite mineral zone boundaries after Niggli (1970), 2: staurolite mineral zone boundary after Reinhardt (1966), 3: staurolite and sillimanite mineral zone boundaries after Keller et al. (subm.), albite-oligoclase: isograd after Bearth (1958). The abbreviations of tectonic units are: MR=Monte Rosa nappe, CA/MO= Camughera-Moncucco unit, ZS=Zermatt-Saas ophiolites, AN=Antrona ophiolites, PG=Portjengrat unit, ML=Monte Leone nappe, AM=Aar Massive, GM=Gotthard Massive, AN=Antigorio nappe, PCZ=Pioda di Crana zone, MA=Maggia nappe, BN=Grand St-Bernhard nappe system, SE=Sesia zone, BR=Berisal nappe

b) River system (black lines) and towns/villages (grey shaded areas and circles, partly connected by roads). White areas: lakes, black triangles: mountain peaks, Parallel lines: passes.

represent a second unresolved issue. Klein (1978) proposed that the Miocene-age Simplon normal fault (Grasemann & Mancktelow 1983) postdated the Vanzone antiform, supposedly cutting its axial plane. Steck & Hunziker (1994) argue along a similar direction by regarding the formation of both generations of backfolds (i.e. the D3 Mischabel and the D4 Vanzone folds) as Oligocene in age, and hence predating the Simplon normal

fault. Furthermore, these authors associate the formation both sets of backfolds with dextral shearing that started as early as 35 Ma ago. A different view is taken by Milnes et al. (1981) and Mancktelow (1992), who propose that the formation of the Vanzone antiform is contemporaneous with the formation of the Simplon normal fault, and hence Miocene in age (Grasemann & Mancktelow, 1983).

In summary, besides understanding the mutual relationships between metamorphism and deformation and at deciding as to how far Tertiary age high-pressure overprint and associated deformation extend into the area of the Lepontine dome, this study also investigates cause and nature of the Vanzone antiform. Thereby, and also regarding nature and timing of late stage back folding and possibly associated normal and/or strike slip faulting, the mapping of the trace of its axial plane in the vicinity of the Simplon normal fault and the Centovalli fault zone is crucial. New fission track data obtained from the area of the Ossola valley (Hess 2003) provide additional constraints regarding the latest stages of the exhumation history.

#### 4.3 GEOLOGICAL SETTING

The Antrona ophiolitic unit separates Monte Rosa nappe and CM unit from each other. All three units belong to the upper Penninic nappe pile located west of the Lepontine dome and southeast of the Simplon line (Fig. 1). Due to S-vergent backfolding and associated axial plunge towards SW the former nappe pile can be seen as a distorted profile in map view (e.g. Klein, 1978; Milnes et al., 1981; Escher et al., 1997). The CM unit forms the core of the Vanzone antiform (e.g. Bearth, 1957) (Fig. 1). Further west the Monte Rosa nappe is overlain by the Zermatt-Saas ophiolites (Fig. 1). Zermatt-Saas ophiolites, Monte Rosa nappe, Antrona ophiolites and CM unit have experienced regional high-pressure metamorphism (Frey et al., 1999; Keller et al., *subm.*). During decompression upon the high-pressure stage the eastern parts of Monte Rosa nappe, Antrona ophiolites and CM unit experienced amphibolite facies metamorphism, whereas the western part of the Monte Rosa nappe only underwent greenschist facies overprint (Frey et al., 1999; Keller et al.

*subm.*). Bearth (1958) recognised this metamorphic zonation first and by mapping the albite-oligoclase boundary in the study area (Fig. 1). This zonation indicates a metamorphic field gradient with temperatures increasing from west to east. Temperatures estimated for the Antrona ophiolites of the study area range between 600-700°C (Colombi, 1989, his Fig. 6-2E). Within the CM unit several occurrences of staurolite and kyanite are known until recently (Merlyn, 1977, his Fig. 14). However, according to Keller et al. (*subm.*) the CM unit west of the Ossola valley reached P-T conditions of about 12.5-16 kbar at 620-700°C during a high-pressure stage. There, sillimanite grade at P-T conditions of about 650°C at 5 kbar, was reached during almost isothermal decompression after the high-pressure stage, and not during a separate “Lepontine” overprint (Fig. 1).

#### 4.4 MAPPING OF THE BOUNDARIES BETWEEN TECTONIC UNITS

The tectonic boundaries drawn in this study (Fig. 2) follow in great part those outlined in the new tectonic map of the Western Alps (Steck et al., 1999), based on the principle that Permo-Mesozoic cover rocks, or ophiolitic remnants of former oceanic crust define major nappe contacts. Some deviations of Fig. (2) from the interpretation given in the new tectonic map of the Western Alps (Steck et al., 1999) are discussed below.

(i) The Furgg zone (Bearth, 1953, 1954a, 1954b, 1956a, 1957b; Wetzel, 1972) is attributed to the continental Portjengrat unit, as suggested by Keller & Schmid (2001), rather than to the Monte Rosa nappe. Based on this interpretation the area around the north-eastern termination of the Monte Rosa nappe is subdivided into Monte Rosa nappe, Portjengrat-Furgg unit and Antrona ophiolites (Fig. 2).

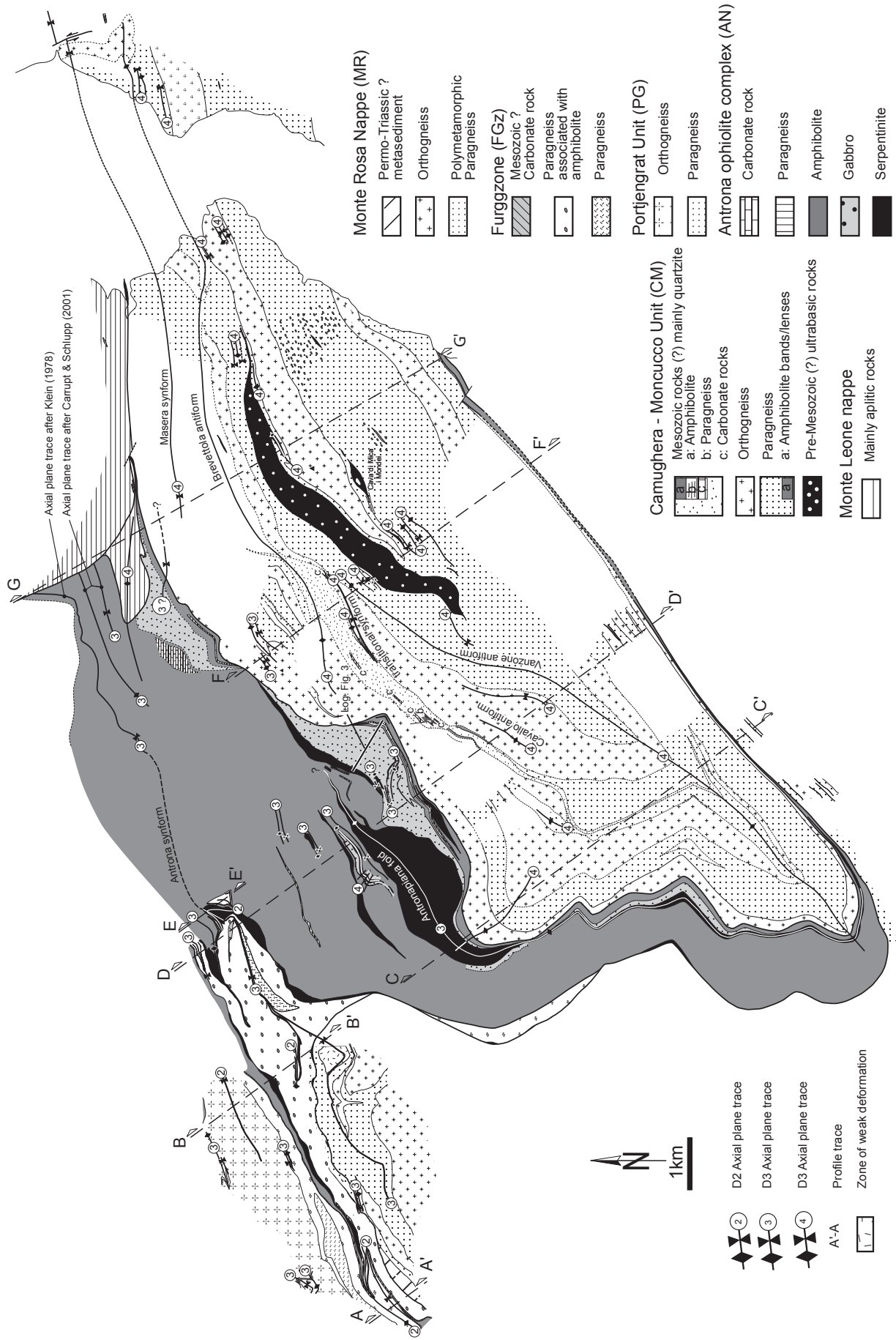


Fig. 2 Map of the study area outlined in Figure 1, indicating tectonic units, fold axial plane traces and lithologies.

(ii) This study verified the observations by Bearth (1939) that the Antrona ophiolites (gabbros, amphibolites and serpentinites) continue along strike much further to the east than shown in the new tectonic map of the Western Alps (Steck et al., 1999) in the Bognanco valley. There, interrelationships between tectonic boundaries have long been debated (e.g. Bearth, 1939; Blumenthal, 1952; Amstutz, 1954; Bearth, 1956b). At the locality “Bosco” (Fig. 1b), situated on the southern slope of the Bognanco valley, rocks derived from the Antrona ophiolite complex still have a thickness of more than one hundred meters (Fig. 2). Further to the east, and along strike of Bosco, ophiolites are again found slightly west and east of the locality S. Marco (Fig. 1b; see also Bearth, 1956b). The easternmost continuation of these ophiolitic rocks (serpentinites), is found on the floor of the river Bogna at the mouth of the Bognanco valley near Cisore (Fig. 1b, see also Novarese & Stella, 1913; Bearth, 1956b). Hence, rocks derived from the Antrona ophiolitic complex can be traced along the lower Bognanco valley and define the contact between CM unit and Monte Leone nappe is formed by (Fig. 2).

(iii) Steck et al., (1999) attribute crystalline rocks situated around Terme di Bognanco to the CM unit. However, these rocks are separated by Antrona ophiolites from the CM unit and are therefore laterally connected with and attributed to the Monte Leone nappe, as previously mapped by Bearth (1939) (his Fig. 6).

#### 4.5 LITHOSTRATIGRAPHY OF THE CAMUGHERA-MONCUCCO UNIT AND THE ANTRONA OPHIOLITES

Concerning the lithostratigraphy of the eastern part of the Monte Rosa Nappe and the Portiengrat-Furgg unit the reader is referred to Jaboyedoff et

al. (1996) and Keller & Schmid (2001). This study primarily addresses the lithostratigraphy of the CM unit and the Antrona ophiolitic unit. The lithostratigraphy of all these units, including that of the Monte Leone unit described by Bearth (1939, 1956b), is an important base of the tectonic map and cross-sections given in Figures 2 and 7.

##### 4.5.1 Camughera-Moncucco unit

The CM gneissic unit may be subdivided into the Moncucco zone and the overlying Camughera zone, the two being partly separated by a series of aligned lenses of marbles and quartzites of supposed Mesozoic age, the so-called “Salioli-Mulde” (Bearth, 1939, 1956b). Both units predominantly comprise different types of paragneisses and orthogneisses of supposed pre-Mesozoic age. Since the same rock types are found in both zones, a difference can only be made on the basis of the relative abundance of paragneisses and orthogneisses, respectively (Figs 2, 3, Bearth, 1956b): orthogneisses (partly coarse-grained augengneisses) are preferentially found in the Camughera zone, paragneisses dominate in the Moncucco zone (Fig. 2). A Rb-Sr age obtained for orthogneisses from the Moncucco zone gives  $271 \pm 4.8$  Ma, indicating a late Variscan age (Bigoggero et al., 1981). Mafic lenses are found in paragneisses of both units, but more frequently in the Moncucco zone (Figs 2, 3). The paragneisses of the Moncucco zone also contain peridotites, which form a larger body, as well as several smaller lenses and boudins mostly located south of this larger body (Fig. 2) (e.g. Bearth, 1956b; Laduron, 1976; Merlyn, 1977). One of these ultramafic boudins, located at I Mondei (“Cava di Mica”), is clearly intruded by a pegmatite (Fig. 2). Rb-Sr dating of coarse-grained muscovite originating from this pegmatite gives ages of about

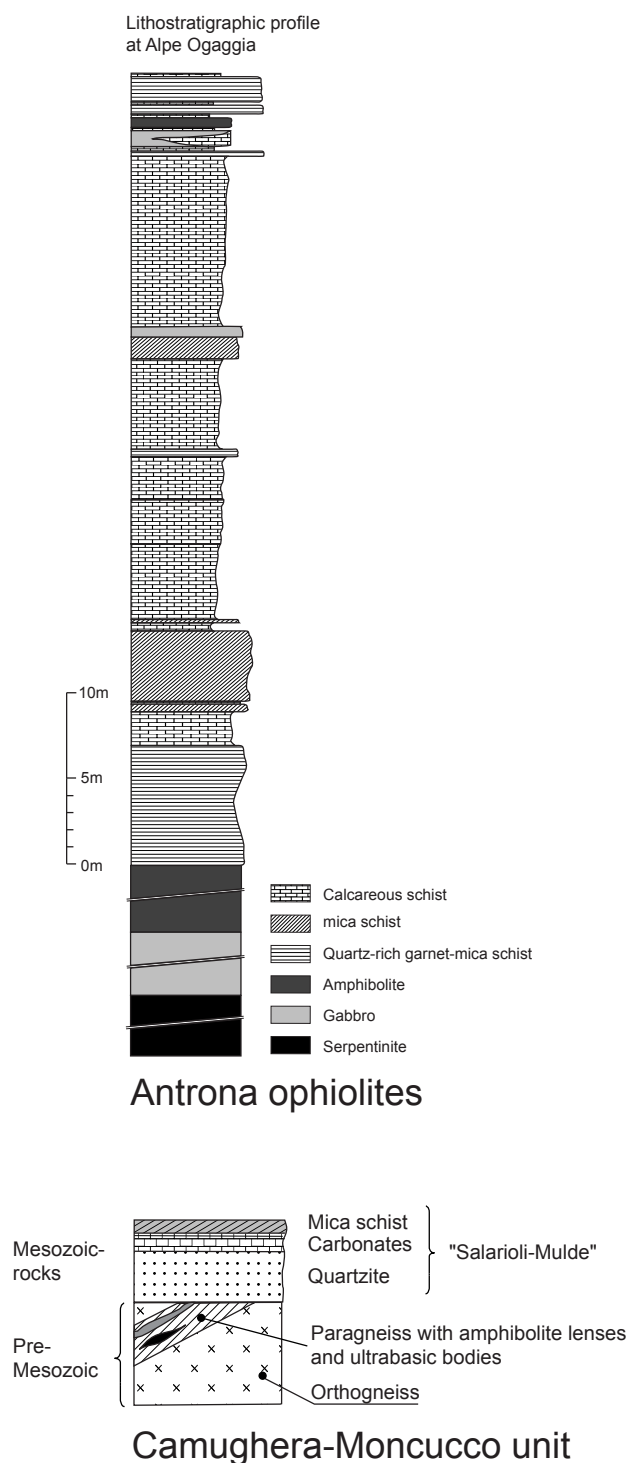


Fig. 3 Lithostratigraphic profile of the Antrona ophiolites taken at Alpe Ogaggia (see Fig. 2 for location and synthetic lithostratigraphic profile of the Camughera-Moncucco unit).

200 Ma (Ferrara et al., 1962). This strongly supports the suggestion by Bearth (1956b) who, contrary to the interpretation of Steck et al. (1999), attributed a pre-Mesozoic age to the peridotites of the Moncucco zone.

The supposed Mesozoic cover of the “Salarioli-Mulde” mainly consists of marbles and quartz-mica schists, the latter being mostly in direct contact with the pre-Mesozoic crystalline basement (Fig. 3). Bearth (1939, his Fig. 7) also reports serpentinites to be associated with the rocks of the “Salarioli-Mulde”, supposedly found between Alpe Cavallo and Passo di Ogaggia (Antrona Valley) (Fig. 1b). However, we could not confirm the existence of such serpentinites. Instead we found greenish coloured metapelites, mainly formed by chlorite, but also containing garnet and staurolite, completely surrounded by the other lithologies of the “Salarioli-Mulde”. Hence, according to our findings, the “Salarioli-Mulde” lacks ophiolitic rocks. Note, that the CM unit is almost completely surrounded by the Mesozoic rocks of the Antrona ophiolites in the study area, while the “Salarioli-Mulde” is nowhere visibly interconnected with the Antrona ophiolitic unit (see also Blumenthal, 1952). Furthermore, the “Salarioli-Mulde” wedges out at Passo Salarioli south of the Antrona valley (Fig. 2) and a tectonic contact between Camughera zone and Moncucco zone can no more be observed farther to the east (see also Bearth, 1939). This, together with the lithological similarities described above, indicates that the “Salarioli-Mulde” formed by infolding or wedging of metasediments into a single Camughera-Moncucco tectonic unit or nappe. Contrary to the interpretation of Steck (1999), Mesozoic ophiolites are restricted to the overlying Antrona ophiolite complex.

#### 4.5.2 Antrona ophiolite complex

Most of the Antrona ophiolite complex is composed of metabasalts, associated with larger bodies of serpentinites and gabbros, as well as remnants of metasedimentary cover rocks (Fig.



2). Fig. 3 presents a lithostratigraphic profile from Alpe di Oggagia (Fig. 1b), situated very close to the tectonic contact with the CM unit. The sequence begins with remnants of oceanic lithosphere. These are, from bottom to top, serpentinites, metagabbros and metabasalts (amphibolites). Then follows relatively homogeneous greyish quartz-rich garnet mica schist, overlain by different types of carbonates, reaching from pure marble to calcareous schist. Metapelites, quartz-rich garnet mica schists and bands of metabasalts or metagabbros are interleaved with these carbonates at different levels (Fig. 3).

This lithostratigraphy of the sedimentary cover of the Antrona ophiolites roughly resembles that reported for the Zermatt-Saas ophiolites only at a first glance. There, Mn-bearing quartzites (metaradiolarites) alternate with marbles, and both are overlain by metapelites and calcareous schists (Bearth, 1973, 1981, his Fig. 1). However, we cannot interpret the quartz-rich garnet mica schist of the study area as the equivalent of the Mn-bearing quartzite or quartz mica schist (metaradiolarites) from the Zermatt-Saas area. This is because the quartz-rich garnet mica schists of the Antrona ophiolitic complex, occurring in map-scale volumes, are nowhere found to be associated with manganese mineralizations or with reddish and finely laminated quartzites, both typical for the metaradiolarites of the Zermatt-Saas area. Instead, we interpret the quartz-rich garnet mica schists, also reported from north of our study area by Carrupt & Schlupp (1998), as derived from impure sandstones. This points to differences between the sedimentary covers of Antrona ophiolites and Zermatt-Saas ophiolites, respectively, and indicates a different paleogeographic origin for the two units (Pfeiffer et al., 1989). The question concerning the paleogeographic origin of the two ophiolitic units

also strongly depends on the interpretation of the nature of the Furgg zone, which only apparently connects the two ophiolitic units according to new findings (Keller & Schmid, 2001, Kramer et al., 2003). In fact the Antrona ophiolites appear to not be connected with the Zermatt-Saas ophiolites via the Furgg zone and they therefore probably represent the remnants of the Valais oceanic domain.

#### 4.6 DEFORMATION HISTORY

The relative timing amongst the individual ductile deformation phases and related structures in the study area largely follows the sequence of four deformation phases described by Milnes et al. (1981) and mainly based on fold overprinting criteria. However, shearing events are also associated with these distinct folding phases (e.g. Müller, 1983; Steck, 1984, 1990; Steck & Hunziker, 1994; Mancktelow, 1992). Hence, we also used correlations between folding and shearing (Keller & Schmid 2001) as a basis for establishing the kinematics of the deformation history. The combination of the above mentioned former studies with the results of our study leads to the following deformation history:

The first deformation phase D1 is associated with a first foliation S1 and contains a stretching lineation X1. This fabric is associated with shear zone formation, isoclinal folds F1 being rare. D1 is associated with top-N to top-NW shearing during nappe stacking and starts under eclogite facies conditions within the entire study area, i.e. including the CM unit (Keller et al., *subm.*).

D2 leads to isoclinal folding (F2) at different scales and under the same kinematic regime as D1 (Keller & Schmid, 2001). Thus, D1 and D2 merely represent progressive stages of the early deformation history, related to nappe stacking. Note, that the major parts of the decompression history are

related to nappe stacking: In the western part of the study area the combined D1/D2 deformation is related to exhumation from eclogite facies to greenschist facies conditions, while cooling during decompression is less pronounced in the eastern part where Barrovian P-T conditions prevailed during exhumation (Keller et al. *subm.*).

A major switch in the kinematic regime occurred during D3. It led to the formation of a first backfolding phase (D3) with associated shearing: dextral within in areas predominated by a subvertically oriented foliation, and top-WSW in flat-lying areas, respectively (Steck, 1984; Keller & Schmid 2001; Kramer, 2002).

A subsequent backfolding phase (D4) clearly overprinted D3 (Kramer, 2002) and shaped the major Vanzone antiform, whose axial plane crosses the CM unit. D4 deformation is also associated with dextral shearing, as can be observed in the southern limb of the major D4 Vanzone antiform in the working area. As will be deduced later, the formation of this antiform overlaps in time with normal faulting across the Simplon line.

#### 4.6.1 D1/D2 structures

The S1/S2 foliation mainly documents shear zone formation during progressive D1/D2 deformation, associated with the X1/X2 stretching lineation that indicates original top-N to top-NW shearing (Keller and Schmid 2001). D2 isoclinal folding is merely regarded as a late stage perturbation during progressive D1/D2 deformation, overprinted by two additional folding phases (D3 and D4), both related to backfolding (Fig. 4). S1 is distinct from S2 only in the hinges of F2 folds, while the transposition of S1 by S2 is complete in F2 fold limbs. Hence the axial planes of F2 folds are parallel to the main S1/S2 composite foliation. The orientation data for the composite S1/S2 foliation

and the D2 folds are presented in Figs. 5 & 6. A major large-scale D2 fold structure was only found in the north of the study area and within the Portjengrat unit (Figs 2, 7; see also Klein, 1978, Milnes et al., 1981, and, Keller & Schmid, 2001).

#### 4.6.2 D3 structures and major folds

During D3 deformation S1/S2 structures were deformed by open to tight asymmetric similar folds (F3) and by associated shearing (see discussion below). At higher structural levels an S3 axial plane foliation is only sporadically established (Klein, 1978; Keller & Schmid, 2001). Towards deeper structural levels D3, however, deformation intensity increases and micro-structural observations indicate that the main foliation is the product of the first three deformation phases (S1-S3), hence D3 overprint is more complete (see below). Fig. 6 illustrates how the D3 structures change from a more unidirectional distribution in subarea I to great circle distributions in subarea III, indicating progressive overprinting of D3 structural elements by D4 deformation towards the south. The major D3 folds within the study area will now be discussed on the base of the tectonic map (Fig. 2), the main S1/S2 foliation map (Fig. 5), and cross-sections (Fig. 7).

The northern part of the study area exhibits a well-known major D3 synformal structure, the Antrona fold, whose northern limb exposes an overturned D1/D2 nappe stack (Figs 2, 7) (Klein, 1978; Milnes et al., 1981; Müller, 1983; Keller & Schmid, 2001). The axial trace of this fold (see Klein 1978 for a more detailed description and mapping of the location of the axial plane trace) runs within the northernmost Monte Rosa nappe in the west (Figs 2, 7) (Klein, 1978; Keller & Schmid, 2001; Kramer, 2002), enters the Antrona unit towards the east, and finally is cut by the Sim-

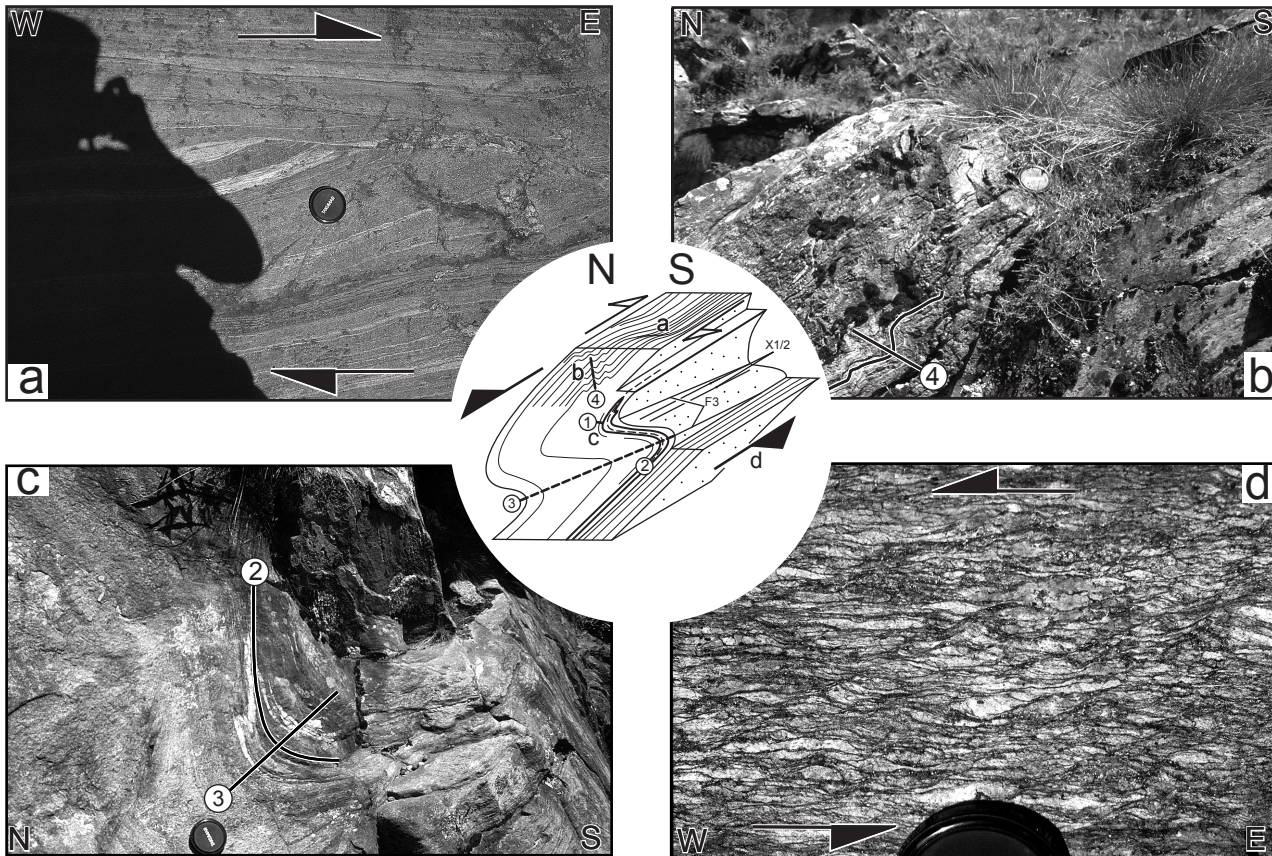


Fig. 4 Outcrop-scale structures within the Camughera-Moncucco unit, all from the same outcrop indicated in Fig. 10, synthesised in the sketch in the centre of the Figure. For orientation data at this outcrop, see pole figure of structural elements also given in Figure 10.  
 a) D1/2 shear band and oblique boudinage, indicating top-ESE transport.  
 b) Open chevron-type D4 crenulation.  
 c) Open D3 fold, overprinting an isoclinal D2 fold within paragneisses. D1 is defined by a still earlier foliation S1.  
 d) D3 shear bands within orthogneiss, indicating top-W transport.

plon normal fault in the east (Figs 2, 7).

A major D3 antiformal fold structure, the Antronapiana antiform, was mapped within the Antrona unit south of the axial plane trace of the Antrona synform, in the vicinity of profile D-D' (Fig. 2). This fold is indicated by the changing asymmetry of parasitic D3 folds, particularly well recognized along profile D-D' of Fig. 7. The asymmetry of parasitic D3 folds within the Antrona unit adjacent to the margin with the CM unit points to a continuation of the axial plane trace of the Antronapiana antiform (Figs 2, 7). The axial plane trace of the Antronapiana antiform can be followed southwards into a thin prolongation of the main ultramafic body (Fig. 2), and still further south it can be mapped as refolded by the Vanzone anti-

form (Fig. 2).

Antronapiana antiform and Antrona synform represent a fold pair. Thereby the nappe stack in the southern limb of the Antrona synform is in an original upright position (Klein, 1978; Milnes et al., 1981; Müller, 1983; Keller & Schmid, 2001). This, together with the facing direction of the folded lithostratigraphic ophiolitic sequence of the Antrona unit (Fig. 3, scheme in Fig. 7) suggests that the D3 Antronapiana fold brings parts of Antrona unit into overturned position. The question whether the D1/D2 tectonic contact between Antrona unit and the CM unit was also inverted, cannot be answered unambiguously. We propose that D3 shearing along the contact between Antrona unit and CM unit only locally overturned



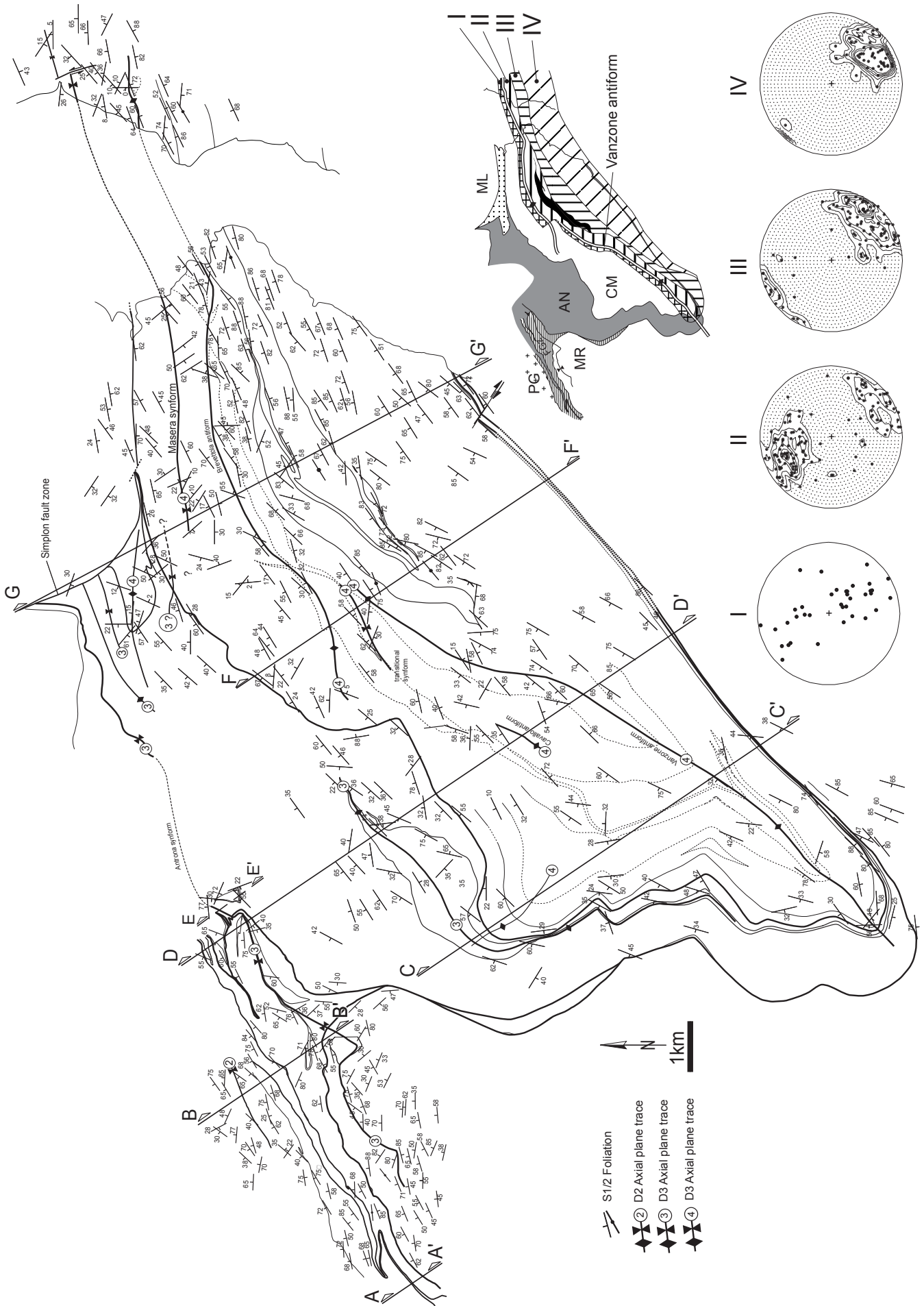


Fig. 5 Map of the composite S1/S2 foliation and stereonets giving orientations of all S1/S2 foliation and stereonets giving orientations of the Vanzone- and Brevettola- major D4 backfolds (areas I and II).

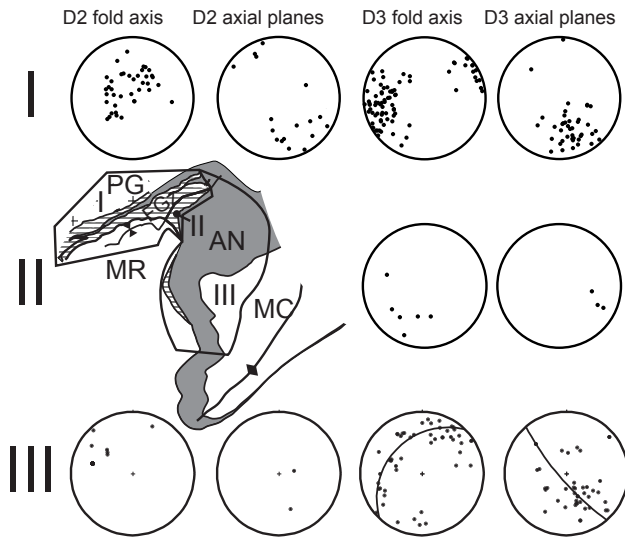


Fig. 6 Orientations of D2 and D3 structural elements (except for stretching lineations and transport directions, given in Fig. 10). There is southwards increase of reorientating D3 axis and D3 axial planes during D4 deformation (compare subarea I and III). Orientation data from subarea I are taken from Keller & Schmid (2001).

the southern limb of the Antronapiana fold, but not the nappe contact (scheme in Fig. 7). Apart from shear indicators (see below) such intense syn-D3 shearing is also evidenced by discordant lithological contacts between rocks derived from the Antrona unit and those derived from CM unit, respectively. Also note, that amphibolites and serpentinites are found again between the overturned top of the sedimentary cover of the ophiolitic sequence below the axial trace of the Antronapiana antiform and immediately above the contact to the CM unit (Fig. 2). This lends additional support to the interpretation that the Antronapiana fold does not invert the polarity of nappe pile.

The original nappe pile, with the Antrona unit being structurally situated above the CM unit, as seen everywhere in the western part of the study area and in the northern flat-lying limb of the D4 Vanzone antiform, however, becomes inverted in the the Bognanco valley further to the east. There, along the southern slope of Bognanco valley, i.e. near profile G-G' indicated in Fig. 2, the Antrona unit laterally changes into a position structurally below the CM unit in the eastern part of the

Bognanco valley. The changeover occurs between profile traces F-F' and G-G' and is indicated in profile G-G' of Fig. 7. This changeover also affects the orientation of the main S1/S2 foliation (Fig. 5), that changes from a dip to the NW in the west to into the SE-dip typical for the eastern part of Bognanco valley. This changeover necessitates the existence of a N-closing post-D1/D2 fold with a sub-horizontal axial plane. Such a fold is indeed indicated by the asymmetry of parasitic folds with subhorizontal axial planes, found in the lower limb of this fold, and sketched in profile G-G' of Fig. 7. The sub-horizontal axial plane orientation differs from the sub-vertical one of the D4 Masera synform, (Fig. 7). Hence, given the lack of D3/D4 overprinting criteria in this area, we favour the interpretation that this fold structure formed during D3 deformation.

An important corollary of the existence of this mega-fold, no matter whether it formed during D3 or D4, is that the Antrona unit appears to have been tightly folded into a structural position below the CM unit, but above the underlying Monte Leone nappe in Bognanco valley. The Monte Leone nappe is commonly regarded as the top unit of a nappe stack with normal polarity, overlain by the Antrona unit (Fig. 7). Hence, given that the nappe polarities indicated in profile G-G' are correct, MC unit and Monte Leone nappe occupy the same original position and have to be connected via a hypothetical synform, which infolds the Antrona unit between those two gneissic units. Assuming the Antrona units to represent the Valais ocean, both MC unit and Monte Leone nappe would have been originally derived from the distal European margin (Fig. 7).



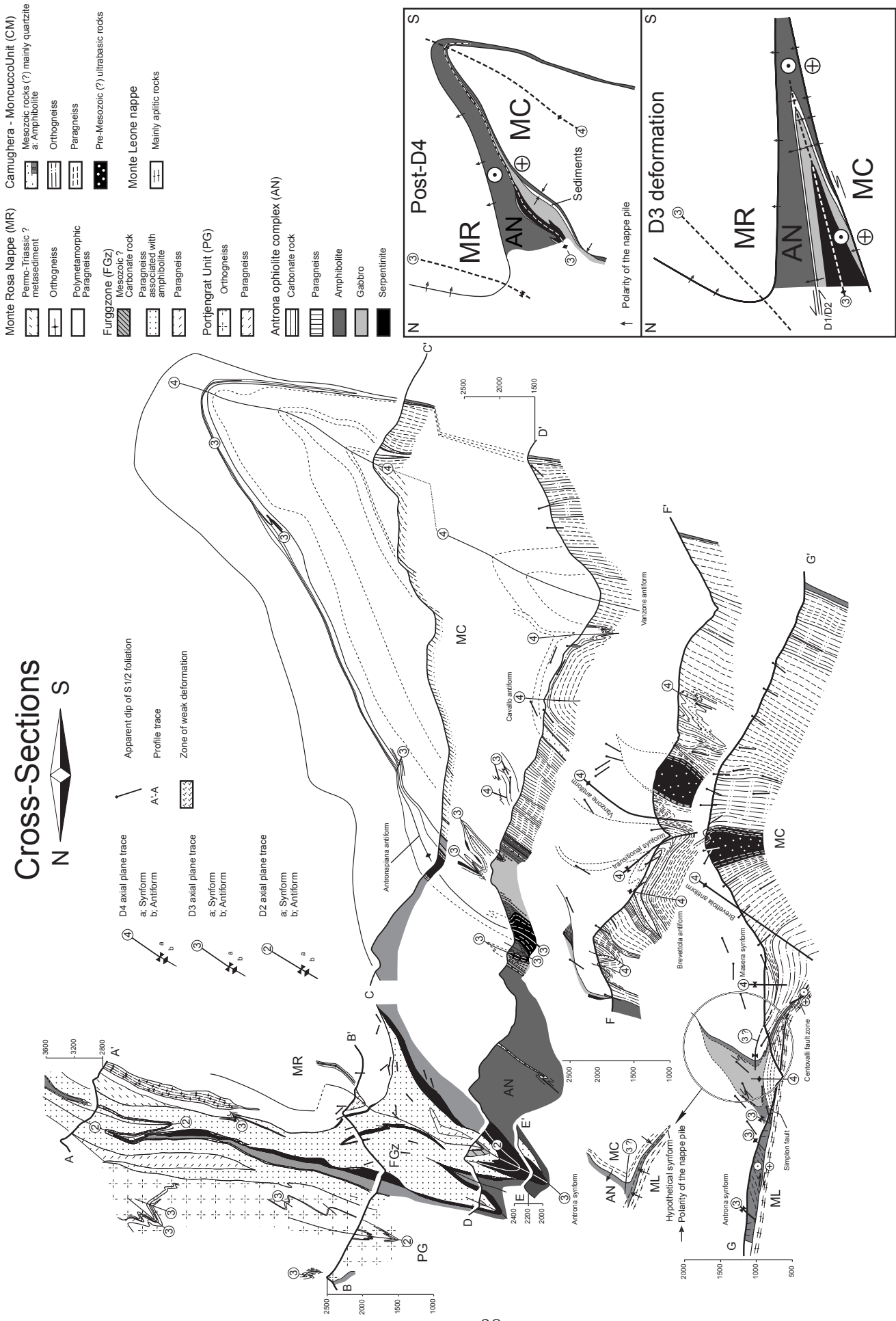


Fig. 7 Cross-sections drawn perpendicular to the WSW-ESE strike of the structural elements. Profile A-A', B-B', C-C', D-D' are stacked assuming a F3 and F4 fold axial plunge of 30°. Profile E-E' was projected into profile D-D' by assuming a F3 fold axial dip of 45°. Profile F-F' and G-G' are stacked assuming a F4 fold axial plunge of 20° (traces indicated in Fig. 2). Schema showing the interpretation how the Antronapiana fold affects the polarity of the nappe pile in the study area. Due to D3 shearing the Antrona unit is locally inverted only, whereby the contact between the Antrona unit and the CM unit remains in an upright position. Note also the schema concerning the polarity of the nappe pile drawn for the profile G-G'.

#### 4.6.3 D4 structures

Lithological variations and deformation gradients led to the formation of different types of F4 folds. Open chevron folds, ranging from small-scale crenulations to sizes of tens of meters, predominate in the northern limb of the major Vanzone D4 antiform and at a large distance to its major axial trace. Towards its major axial plane, D4 deformation intensity increases and open similar folds have also been observed. Furthermore, D4 folding is also seen to be associated with dextral shearing, particularly pronounced in the Antrona valley between the localities Ruginenta and Rivera. There, parasitic folds change asymmetry across the major D4 axial plane, while associated dextral shearing does not (see Figs. 8a-c). Slightly west of the locality Sogno (above Villadossola), located in the southern limb of D4 Vanzone antiform, where many D4 folds associated with dextral shearing can be observed it is evident that D4 folds often nucleate within small-scale dextral D4 shear zones. These shear zones are associated with a sub-horizontal stretching lineation X4. F4 fold axes, which nucleate within such dextral D4 shear zones are often sub-vertical, as can be mainly observed in the southern limb of the Vanzone antiform. In the vicinity of the axial plane the formation a new axial planar foliation S4 occasionally develops within mica rich schists (Fig. 8e). Overprinting criteria often allow to unambiguously distinguish between F3 and F4 folds (Fig. 8b, d). In summary, all this indicates that D4 back-folding and dextral shearing are kinematically linked.

## 4.7 AXIAL TRACES AND KINEMATIC SIGNIFICANCE OF MAJOR D4 FOLDS

### 4.7.1 The eastern continuation of the major D4 Vanzone antiform within the Camughera-Moncucco unit

While the location of the axial trace of the Vanzone antiform is unambiguous within the Antrona ophiolitic units, mapping of its eastern continuation remained ambiguous and controversial so far (compare Klein, 1978 with Milnes et al., 1981 and Steck et al., 1999). Remapping of the major D4 structures led to the following results presented with the help of the foliation map (Fig. 5) and interpretative cross-sections (Fig. 7). The hinge of the Vanzone antiform, still well defined at the western termination of the CM unit (Fig. 2) in Anzasca valley (Bearth, 1957a; Laduron, 1976), enters the Antrona valley at Passo Salarioli. In the floor of the Antrona valley the trace of the major axial plane was mapped between Prato and Rivera (see Figs 1, 2) based on the changing asymmetry of parasitic folds. Note, however, that a second large-scale D4 antiform, referred to as “Cavallo antiform” (Fig. 2), could also be mapped along a distance of approximately 1 km along strike further north. Both D4 antiforms are connected by a relatively tight synform, as is indicated by the asymmetry of parasitic D4 fold structures (profile D-D’ of Fig. 7).

Further to the northeast the axial plane of the Vanzone antiform was mapped along the southern slope of Testa dei Rossi, where the major fold hinge is completely exposed. Here the orientation of the main S1/S2 foliation is seen to continuously change from a moderate NW-dip, typical for the northern limb, into a SE-dip indicative for the southern limb near the hinge zone, just before the southern limb becomes recumbent and also turns

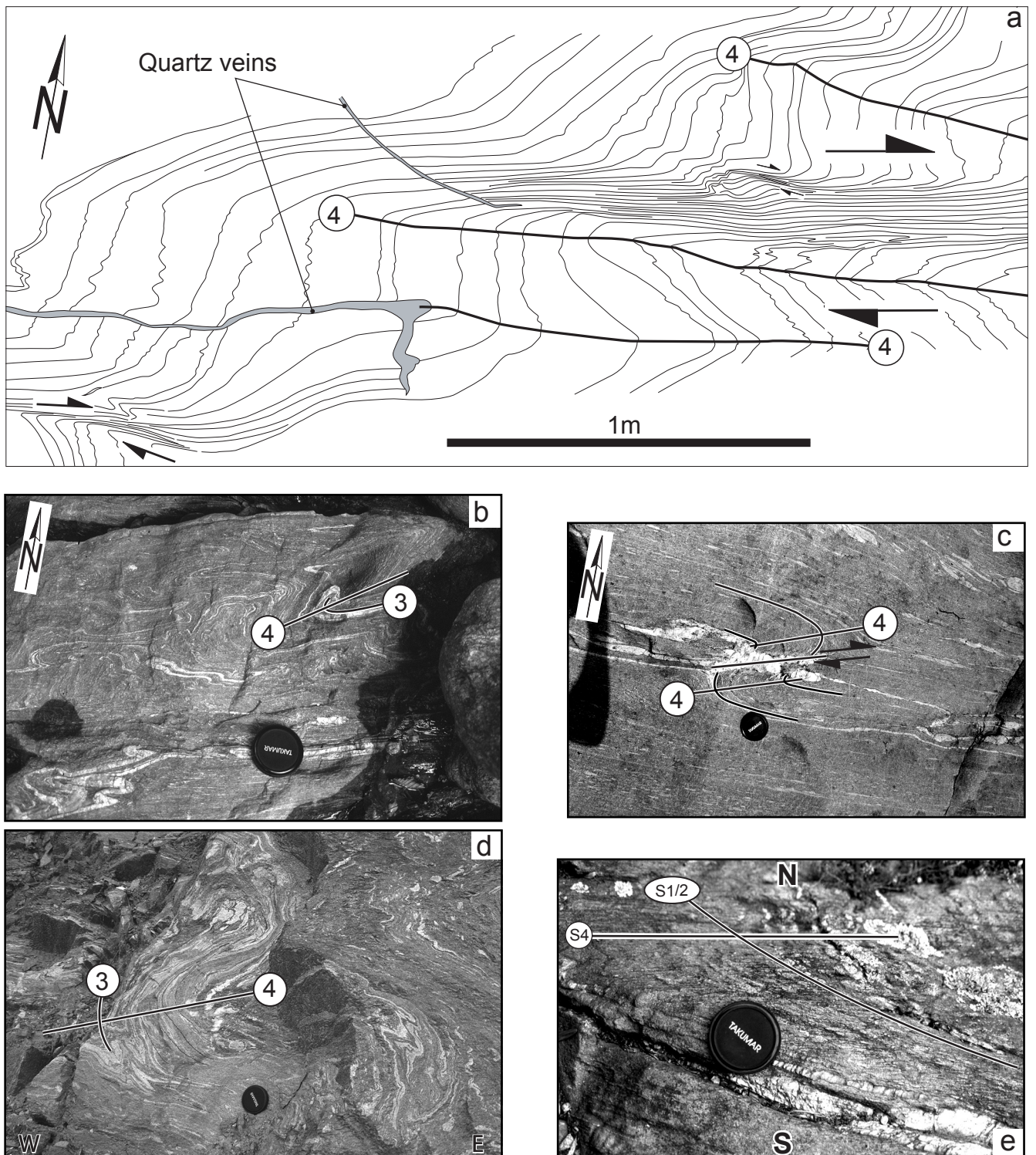


Fig. 8 D4 fold structures from the Camughera-Moncucco unit in Val Antrona. Fig. 8a is from north of the axial plane of the Vanzone antiform; Figs. 8b, c, are from an outcrop situated south of the Vanzone axial plane; Figs. 8d, e are situated south of Vanzone axial plane. Note the changing asymmetry of D4 folds across the hinge of the Vanzone antiform, while the sense of shear (a, c) remains the same. a) Nucleation of the D4 folds evidently being associated with dextral shearing (in map view) and with the injections of quartz veins, which are refolded during later stages of ongoing D4 deformation. b) Overprinting relations between D3 and D4 folds. c) S-type D4 flanking fold (Grasemann & Stüwe, 2001) around rotated quartz vein, indicating dextral shearing (in map view) during vein formation and D4 folding. d) Overprinting relations between D3 and D4 folds. e) Formation of a new axial planar foliation S4 in the vicinity of the trace of the major axial plane of the Vanzone antiform (in map view).



into NW-dip further to the south. The Vanzone axial plane strikes NE from Testa dei Rossi, entering the Brevettola valley north of a major ultrabasic lens within the Moncucco unit (Figs 1, 2), where intense D4 folding is observed.

In the upper part of Brevettola valley another F4 antiform, namely the Brevettola antiform, starts to appear (Fig. 2, Klein, 1978), where it is seen to affect the orientation of the main S1/S2 foliation. Since there is no evidence for the existence of two antiforms further to the NE, it is concluded that the Brevettola D4 major antiform laterally completely replaces the Vanzone antiform. Only in the upper Brevettola valley, i.e. within a transition zone, are the two antiforms connected by a synform. Possibly, this doubling (Cavallo and Vanzone antiform) of the antiform into two closely spaced hinges is caused by the increased thickness of the CM unit, which here becomes wider than half the wavelength of major D4 folds, thereby locally forcing the formation of an additional major fold.

Still further east, the axial trace of the Brevettola antiform almost turns into an E-W strike (Fig. 2) along the southern slope of the Bognanco valley. Mapping of the axial trace was based on the change in orientation of the S1/S2 foliation from flat lying to steeply SE-dipping in the north to an overturned NW-dip in the south (Figs 4, 7). Finally, the axial plane of the D4 Brevettola antiform crosses the Ossola valley around Premone (Fig. 2) and reappears in the northern realms of Trontano on the eastern side of the Ossola valley. Just north of the turn of the Brevettola antiform into an approximate E-W strike the northerly adjacent Masera synform, not present further west, described below, starts to appear (Fig. 2).

#### **4.7.2 Major D4 folds mapped in Bognanco valley**

According to Mancktelow (1990) the mylonitic foliation of the top of the Monte Leone nappe, that is part of this Simplon normal fault zone, gradually changes orientation from a SW-dip to a SSE-dip in the area around Fonti di Bognanco (Fig. 5). Note that this change in orientation occurs near the western termination of the Masera synform, a minor low-amplitude synform (Figs 2, 5). Also note that the Masera synform bends the main S1/S2 foliation of the northern CM unit into parallelism with the foliation in the eastern part of the footwall of the Simplon normal fault at the southern rim of the Monte Leone unit. All this strongly suggests a genetic link between the strongly bent eastern continuation of the Simplon normal fault and the Masera synform. Further to the east the axial plane of this synform is found immediately south of Maggianigo (Figs 2, 5). Finally it crosses onto the eastern side of the Ossola valley, where it corresponds to the "Masera synform" as defined by Milnes et al. (1981).

It is concluded, that D4 deformation on the southern side of the Bognanco valley is characterized by the open Masera-Brevettola synform/antiform pair, oriented parallel to the foliation found at the southern rim of the Monte Leone unit. This fold pair, together with the strongly attenuated eastern continuation of the Antrona ophiolitic unit in lower Bognanco valley, geometrically defines the eastern continuation of the Simplon normal fault (see Fig. 2 and profile G-G' of Fig. 7).

#### **4.7.3 Evidence for dextrally transpressive shearing during D4 deformation**

Approaching the major axial plane of the Vanzone and Brevettola antiforms from the south and perpendicular to the strike of the axial planes,

the orientation of the main S1/S2 foliation successively changes from a steep and overturned NW-dip to a SE-dip, finally turning into sub-horizontal orientation (Fig. 5). The SW-NE strike and the steep NW-dip in the southern limb of the Vanzone antiform gradually swings around to the WSW-ENE strike seen to both sides of the Ossola valley. This is consistent with the observation that dextral shearing is associated with D4 folding (see previous discussion of Fig. 8). All this suggests that dextral shearing occurs at a large scale within southern limb of the Vanzone-Brevettola antiform pair. The stretching lineation X4, associated with this pervasive syn-D4 dextral shearing, plunges moderately to the SW in the western part of this southern limb area and changes into a sub-horizontal WSW-ENE orientation further to the E (see orientations of X4 given in Fig. 10).

The orientation of D4 fold axes changes laterally (see Fig. 9). A moderate plunge to the SW is observed in the western part of the study area (i. e. subarea V of Fig. 9), while further east (subarea VI of Fig. 9) D4 fold axes often nucleate at dextral shear zones and hence exhibit subvertical to steeply NW or NE dipping fold axis orientations. The fold axes within subarea VI, which are not directly associated with dextral shearing, moderately plunge to the SW. Consequently the orientation of D4 fold axes in subarea VI (Fig. 9) indicates a continuous transition from a near-vertical plunge to moderate SW-plunges that are parallel to the X4 stretching lineations of subarea V (compare Fig. 10). This pattern indicates that F4 fold axes may rotate in a clockwise sense during D4 dextral shearing.

In the northern limb of the Brevettola antiform, and along the Masera-synform the plunges of D4 fold axes are gentle to subhorizontal, their strike gradually changing from SW-NE to W-E (Fig. 9).

This change in orientation occurs immediately south of the gradational swing in orientation of the Simplon normal fault and again suggests a direct genetic relationship between D4 folding and normal faulting along the Simplon line.

The D4 fold axial planes (S4) steeply dip to the NW in the southern limb of the Vanzone-Brevettola antiform pair (Fig. 9), also indicating a NW-dip of the above described broad belt that is affected by syn-D4 dextral shearing. However, they steeply to the SW in the northern limb of this antiform pair, indicating a convergent fan of axial planes to be associated with large scale D4 folding.

#### 4.8 COMPILATION OF THE ORIENTATION OF STRETCHING LINEATIONS AND CHANGE IN THE KINEMATICS OF SHEARING

All observed stretching lineations and transport directions are compiled in Fig. 10. Transport directions are inferred from macroscopic and microscopic shear indicators (e.g. Simpson & Schmid, 1983). Fig. 10 includes orientations of X1/X2 lineations that were refolded by minor D3 folds. Such reorientations of older lineations allow for the construction of movement directions related D3 folding (Ramsey & Huber, 1987).

Generally, two principally different kinematic regimes can be inferred for the study area. A first kinematic regime is related to D1/D2 mylonitization. Related stretching lineations and associated senses of shear change orientation from place to place, due to intense overprinting during subsequent deformations. The original transport direction during D1/D2 movement was inferred to have been approximately top-N (see extensive discussion in Keller and Schmid 2001).

The second kinematic regime is related to



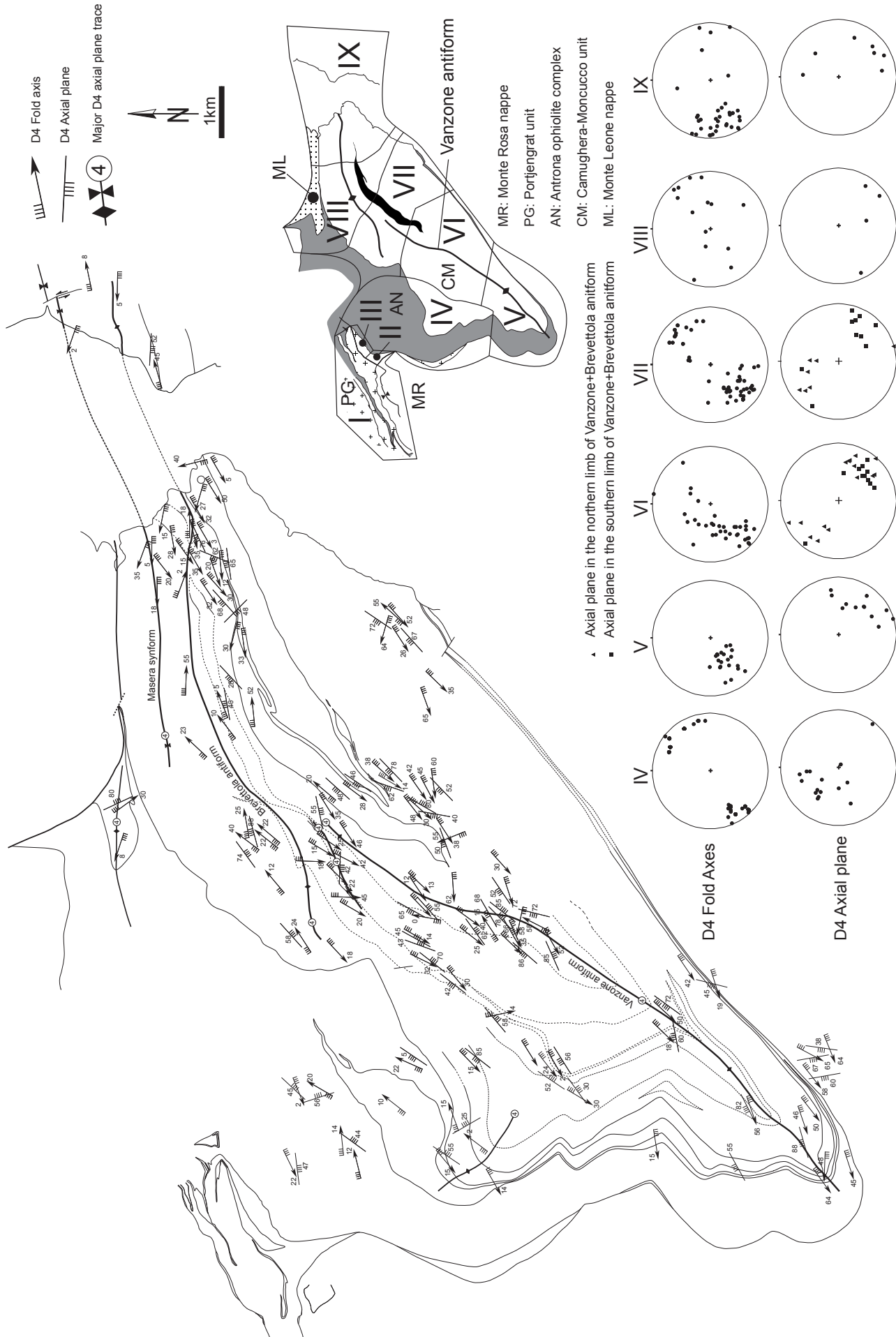


Fig. 9 Orientations data of D4 structural elements (except for stretching lineations and transport directions from the subareas indicated. Fig. 10). Stereonets include all measurements from the subareas indicated.

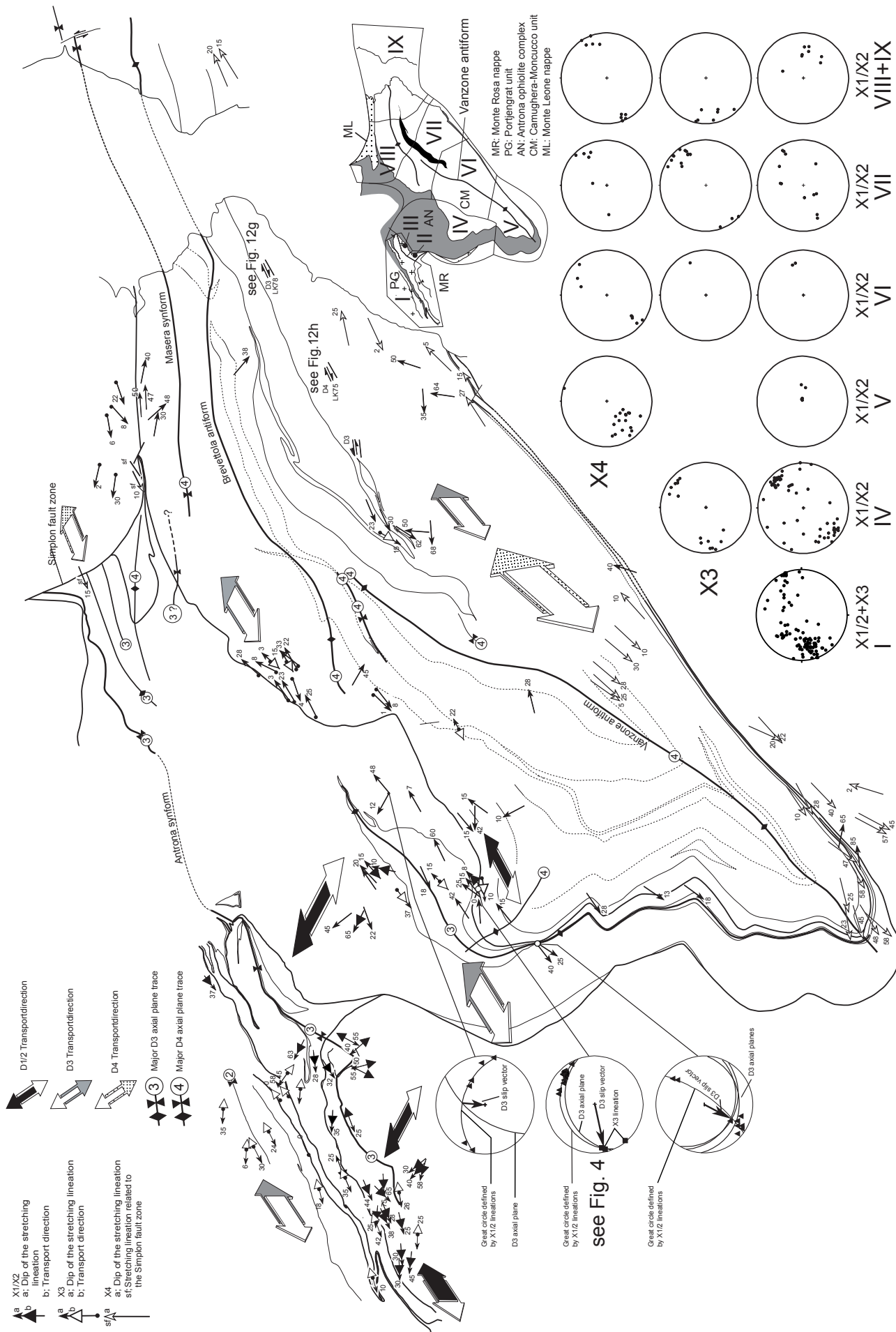


Fig. 10 Orientations of D1/D2, D3 and D4 stretching lineations. Stereonets include all measurements connected to the subareas indicated. The transport directions associated individual measurements refer to the relative displacement direction of the hanging wall. Note that most tectonic contacts have a northerly dip (except for the areas south of the Vanzone and Antrona backfolds, see Figs 5, 7). Large arrow pairs indicate the general transport direction deduced for a larger area. Data from subarea I are after Keller & Schmid (2001). Stereonets, whose location are shown by a tie line show orientations of X1/X2 stretching lineations refolded by minor D3 folds and arrows indicate the movement directions related to D3 folding (given by the intersection of the great circle described by the X1/X2 lineations and the D3 axial plane after Ramsay & Huber 1987).

backfolding during D3 and D4 deformation. In the northern and inverted steep limb of the D3 Antrona backfold this second kinematic regime is characterized by dextral shearing (Fig. 10) (Jaboyedoff et al., 1996; Keller & Schmid, 2001). Interestingly, this same transport direction is inferred for subsequent syn-D4 shearing in the southern limb of the D4 Vanzone antiform, this earlier discussed dextral shearing being directly indicated by rotated feldspar porphyroblasts (Fig. 11b). In between these two steep fold limbs, and within the flat-lying nappe stack, this second kinematic regime is characterized by syn-D3 top-WSW orogen-parallel shearing (Figs. 10, 11a). S to WSW directed movements related to D3 backfolding were also deduced from refolded X1/X2 stretching lineations, measured in the same part of the study area (Fig. 10).

Note that, dextral shearing during this second kinematic regime occurs within steeply inclined and overturned portions of the original D1/D2 nappe stack, while top-WSW characterizes the flat-lying and upright parts of this original nappe stack. Also note that D3 top-WSW shearing appears dextral in map view once it becomes rotated into the southern and overturned limb of the D4 Vanzone antiform (Figs 10, 16b). All this is kinematically consistent with a relative transport the entire Monte Rosa nappe towards the WSW during D3 and D4 deformation, and with respect to the deeper structural units exposed in our area of investigation (Fig. 16b).

On a regional scale the reorientation of X1/X2 stretching lineations is expected to be particularly strong within inverted limbs of major backfolds. In the case of the northern rim (or top in profile view) of the Monte Rosa nappe the original top-N D1/D2 transport direction was reoriented into the presently observed orientation of the D1/D2

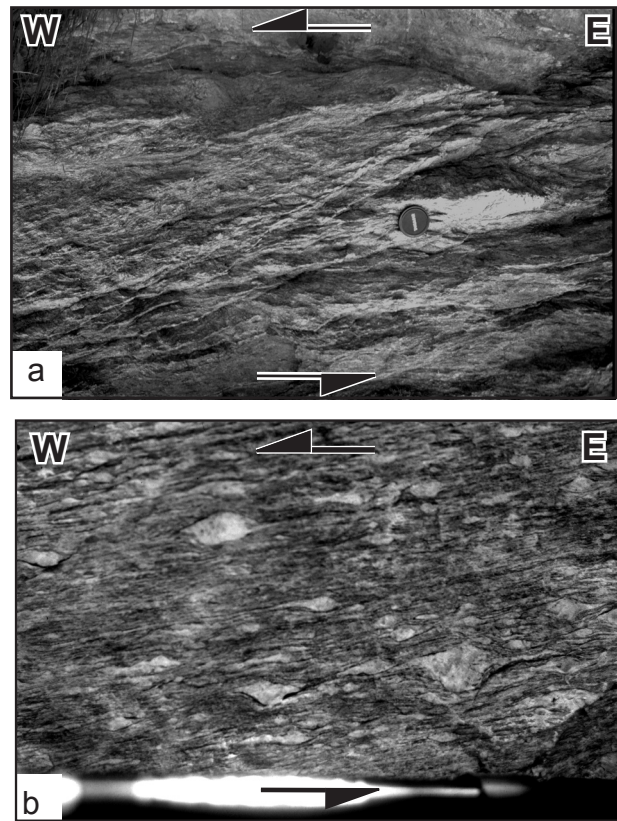


Fig. 11 Illustration of selected transport direction criteria.  
a) D3 shear bands, indicating top-WSW transport within metagabbro.  
b) D4  $\sigma$  clasts, indicating Top-ENE respective dextral transport within orthogneiss of CM unit. Note that the photomicrograph was taken from the bottom to the top, i. e. the opposite of map view.

transport direction which is top-WSW. This reorientation is directly linked to the overturning of the northern limb of the Antrona synform (subarea I in Fig. 10; Keller & Schmid, 2001). The southern limb of the Antrona synform, being in its original position presently often exhibits top-NNW D1/D2 shearing, but top-WSW and top-S shear sense indicators have locally also been observed (subarea I and IV in Fig. 10, see also Keller & Schmid, 2001). The reorientation of X1/X2 stretching lineations measured around small-scale D3 folds indicates a diversification of X1/X2 orientations ranging from an ENE-plunge over a northern plunge to a WSW-plunge (Fig. 10). This range of orientations is in line with the overall pattern of X1/X2 orientations observed in subarea IV of Figure (10), as well as with the one presently

observed at the northern rim of the Monte Rosa nappe (subarea I in Fig. 10, see also Keller & Schmid 2001, their Fig. 12).

We conclude that although 4 phases of deformation can be defined by superposition criteria, the kinematic regime only dramatically changed once. Top-N nappe stacking during progressive D1/D2 was followed by a regime of back-folding during D3/D4, formed in a dextrally transpressive regime and associated with the relative top-WSW movement of higher over lower structural units in the flat-lying parts of the D1/D2 nappe stack. This second kinematic regime involved an orogen-parallel stretch and shaped the “Simplon ductile shear zone” as defined by Steck (1990), denoting the totality of dextral movements which were initially distributed within an approximately 10 km thick deformation zone. This deformation zone shaped the arc of the Western Alps by WNW-directed indentation of the Adria microplate (Schmid & Kissling, 2000; Ceriani et al., 2001).

#### **4.9 LATE STAGE BRITTLE DEFORMATION ASSOCIATED WITH THE CENTOVALLI FAULT ZONE**

Brittle deformation associated to the Centovalli fault zone, an about 2 km wide zone of intense brittle deformation, can be found in the Vigizzo valley. Within and south of the mouth of the Vigizzo valley and along the eastern flank of Vallee d’Ossola, brittle deformation structures associated with the Centovalli fault zone are clearly seen to post-date and overprint D4 folds, including the fold hinge of the Brevettola antiform. Dextral offset on fault planes predominates, but a map scale sinistral offset of the Masera-synform along an antithetic R2 brittle Riedel shear could also be mapped (eastern margin of Fig. 2). Westwards and the across the Ossola valley brittle

deformation becomes less intense and follows the river Bogna along the valley floor of lower Val Bognanco. In the area around Fonti di Bognanco in Val Bognanco a branch of brittle deformation follows the river Bogna uphill, i. e. towards the west into the upper Val Bognanco, whereas another branch is associated to the brittle deformation in the hanging wall of the Simplon normal fault (Bearth, 1956b).

#### **4.10 EARLY STAGES OF METAMORPHISM RELATED TO TOP-N NAPPE STACKING DURING D1/D2 DEFORMATION**

The early Alpine deformation history is particularly well documented by a anastomosing top-WSW (D1/D2) shear zone from the top of Monte Rosa nappe situated in the northern limb of the D3 Antrona synform (Keller & Schmid, 2001). Keller et al. (2004) provide a detailed study of this shear zone, which documents the high-pressure overprint of pre-Alpine metamorphic pelites during an early stage of D1/D2 deformation. In the central parts of the shear zone the Alpine metamorphic overprint is complete and the S1 foliation is mainly composed of Grt + Phe + Pg + Qtz. The P-T conditions for this transformation are estimated at around 650°C at 12.5 kbar. For the chemistry of the minerals, related to this early syn-D1 stage of Alpine metamorphism in the Monte Rosa nappe, the reader is referred to Keller et al. (2004).

In metapelites from the CM unit the assemblage Grt + Phe + Pg + Qtz is again found to represent a first metamorphic stage, documenting peak metamorphic conditions of pressure and temperature within 12.5-16 kbar and 620-700°C (Keller et al. *subm.*). Hence, the early (D1) formed Alpine mineral assemblage Grt + Phe + Pg + Qtz is identical with that found in the eastern part of Monte Rosa nappe (Keller et al., *subm.*). Thus, it is concluded



that S1 formed during peak pressure conditions and at the same P-T conditions within both units. The ongoing D1/D2 deformation is linked to decompression, which is contemporaneous with progressive nappe stacking. In contrast to the early D1 stages occurring under peak-pressure conditions, a spatial diversification of P-T conditions is observed during ongoing D1/D2 deformation and related decompression (Keller et al., *subm.*). In the western part of the study area (i.e. in the staurolite absent mineral zone) cooling is more pronounced during decompression. Further to the east (i.e. within the staurolite mineral zone of the eastern CM unit), and contrary to the observation in the Monte Rosa nappe, decompression is closer to being isothermal (Keller et al., *subm.*).

#### 4.11 CORRELATION BETWEEN DEFORMATION AND METAMORPHISM DURING POLYPHASE DEFORMATION

In order to establish correlations between individual deformation phases of deformation and metamorphism we selected an outcrop, where overprinting relations of deformation phases are particularly well recognized (Fig. 4). This outcrop is located within the staurolite mineral zone of the Camughera-Moncucco metapelites (Fig. 3). Details concerning mineral parageneses, mineral compositions and bulk rock composition of the metapelites at this outcrop are reported elsewhere (Keller et al. *subm.*, their sample LK13). Here, we address the correlation between mineral parageneses and different deformation phases.

Fig. 4 (centre) depicts a composite sketch of all the deformation features observed at this outcrop. Folding phases (F2, F3 and F4) are seen to overprint the early S1 foliation (Fig. 4). Two generations of stretching lineations and associated shear sense indicators are also present. X1/

X2 represents an older stretching lineation and is overprinted by D3 folding, whereby the angle between X1/X2 and the F3 fold axis is quite small. However, a small systematic spread of X1/X2 orientations around the F3 fold hinge is still observable (see stereoplot labelled “see Fig. 4” in Fig. 10). X1/X2 lineations presently dip moderately to between E and NE. Larger systematic spreads of X1/X2 orientations around F3 fold hinges are observed at other outcrops (Fig. 10). Asymmetric boudinage probably related to the X1/X2 stretching lineation presently indicates top ENE D1/D2 transport direction of the hanging wall (Fig. 4a). A second and younger stretching lineation plunges slightly to the west and is associated with shear bands indicating top-W transport (Fig. 4d). This later sense of shearing and associated stretching lineation X3 is correlated to D3 folding because the same kinematic regime is also observed in the overturned limb of the megascopic D3 Antrona synform, interpreted to have formed by shearing during D3 folding (Jaboyedoff et al. 1996; Keller & Schmid, 2001). The great circle defined by the refolded X1/X2 stretching lineation intersects the axial plane of the corresponding D3 fold, and the intersection dips gently to the west, giving the movement direction related to D3 folding (Ramsey & Huber, 1987). Hence, there is similar orientation of the D3 movement directions obtained from refolded X1/X2 stretching lineations and the orientation of X3, supporting the interpretation of top-W shearing during D3 deformation at this outcrop. Note, however, that the angle between the constructed great circles is quite small, causing their intersection to be affected by small angular variance.

The main S1/S2 foliation is well preserved in metapelite sample LK13, which contains garnet, phengite, biotite, kyanite, staurolite, plagioclase,



chlorite, epidote as major minerals and opaque minerals. Garnet, phengite, plagioclase and biotite define the S1/S2 foliation. Paragonite occurs as relict inclusions in garnet and plagioclase, its disappearance being related to ongoing decompression (see later discussion of Fig. 13). Staurolite grows at the rim of kyanite. Staurolite and kyanite grew under static conditions since they postdate the formation of the main S1/S2 foliation (Fig. 12a, c). Garnet is inferred to have decomposed in order to form staurolite. This is based on the observation that garnet predates staurolite, overgrowing the rim of garnets (Fig. 12b, c). Chlorite and associated epidote grow as the latest minerals (Fig. 12e). Chlorite overgrows the main S1/2 foliation, its growth nucleating at grain boundaries of pre-existing garnet, staurolite and biotite (Fig. 12e). A sample taken from the hinge zone of a D3 fold reveals that the S3 axial plane foliation is predominantly defined by biotite, indicating its growth during D3 deformation (Fig. 12d). In this specimen chlorite is seen to also overgrow the S3 foliation (Fig. 12d). Staurolite is found to be stable in D3 fold hinges and hence interpreted to have grown during D3. Apart from this outcrop staurolite is stable during intense D3 deformation, as it defines the foliation in the deeper structural parts, where the foliation is a composite one, formed during the first three deformation phases (see below). Yet another sample, taken from the hinge zone of a D4 fold, shows that D4 folding postdates the formation of chlorite, which is folded during D4 deformation (Fig. 12f).

Fig. 13a shows the equilibrium diagram calculated in the system KNCFMASH for the bulk rock composition of sample LK13 (see Keller et al., in subm., their Table 1) and serves as a basis for discussing the P-T evolution associated with progressive deformation. The grey shaded area

marks peak P-T conditions of metapelites from the study area proposed by Keller et al. (subm.). This P-T area is defined by the overlap of two stability fields of first stage assemblages Keller et al. (subm.). Within errors this P-T-area is compatible with the indication that maximum pressure is likely to range between around 14.5 kbar and 16 kbar (black dots in Fig. 13a), derived from a comparison of calculated end-member isopleths of MgCel with measured XMgCel in phengite cores (0.21 to 0.28).

The P-T conditions of ongoing D1/D2 deformation are reflected by stability fields of the assemblages Grt + Phe + Pg + Pl + Bt + Qtz, later replaced by Grt + Phe + Pl + Bt + Qtz, as paragonite disappears outside the cores of garnets during decompression (assemblages 1 and 2 in Fig. 13a). Both assemblages compose the main S1/S2 foliation that obviously formed during a first stage of progressive decompression. The P-T field related to D1/D2 deformation is limited towards lower pressures of around 10 kbar by the stability fields of kyanite and staurolite (assemblages 3 and 4 in Fig. 13), since both these minerals overgrow the main S1/2 foliation in specimen LK 13.

The assemblages Grt + Phe + Pl + Bt + Ky + Qtz and Grt + Phe + Pl + Bt + St + Qtz are correctly predicted by the phase diagram of Fig. (13a) (assemblages 3 and 4). The subhorizontally orientated calculated mineral abundance isopleths predict the growth of biotite within the stability field of the former two assemblages during further decompression (Fig. 13b). Since this is in accordance with the observation that substantial amounts of biotite grows during D3 folding, we conclude that the assemblages 3 and 4 depicted in Figure (13a) indeed reflect the P-T conditions of D3 deformation. For the CM unit Klein (1978) also suggested the formation of biotite during D3



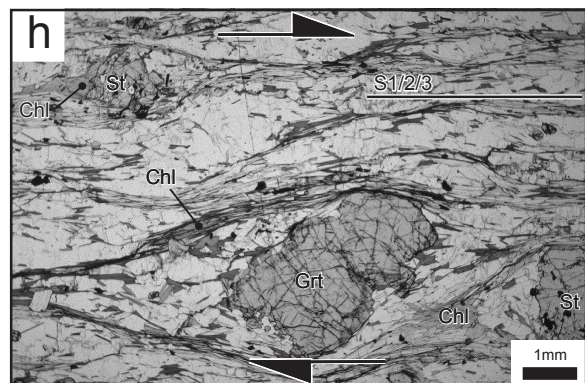
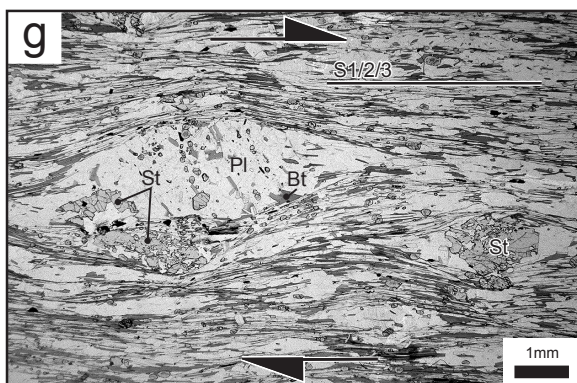
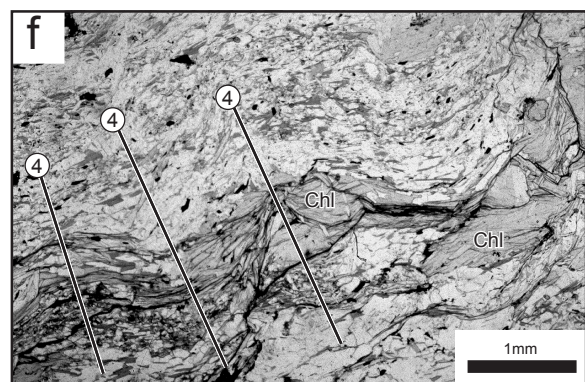
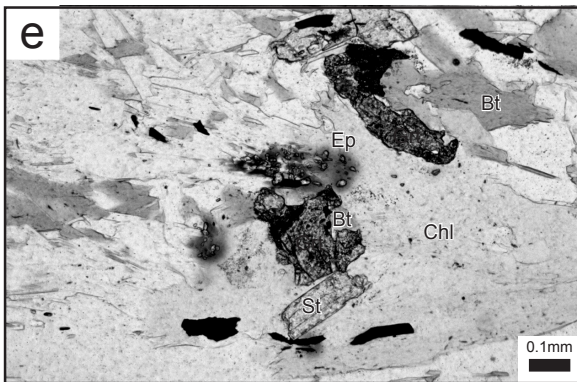
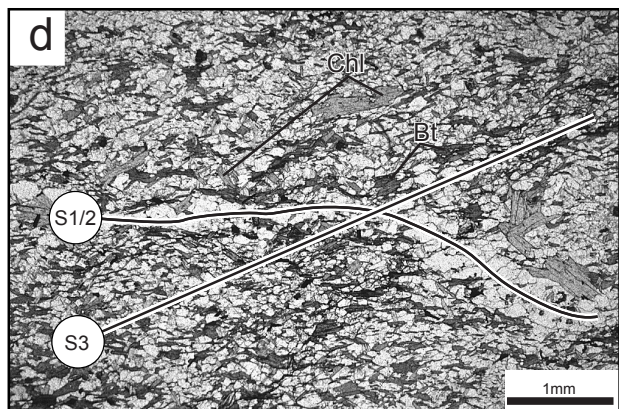
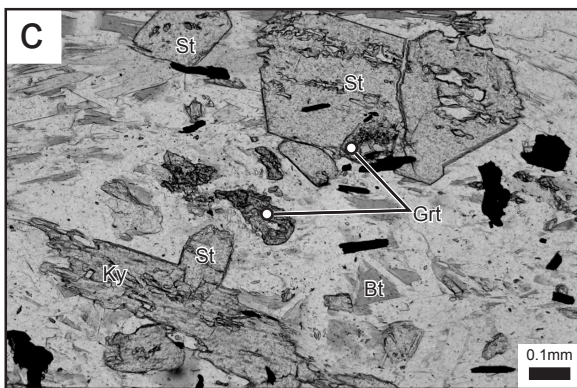
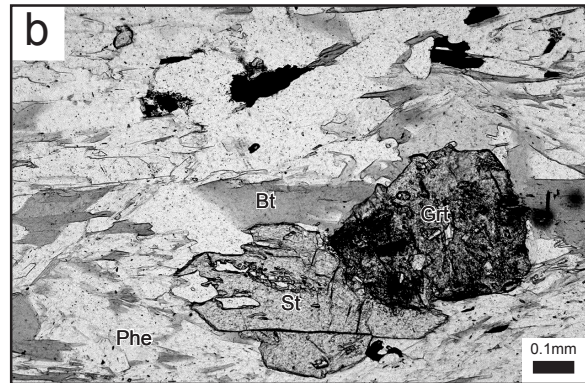
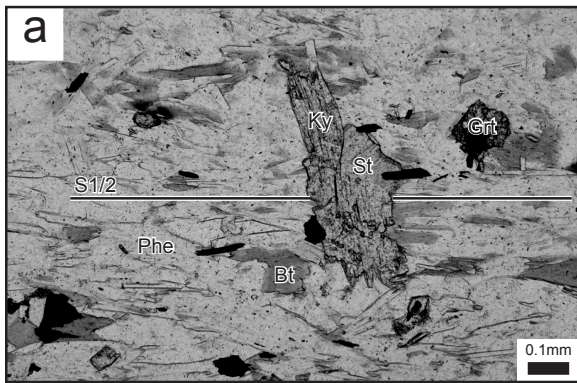




Fig. 12 Photomicrographs of thin sections. Microstructures depicted in Fig. 12a-e are all from the same outcrop illustrated in Fig. 4. For the location of Fig. 12g, h see Fig. 10. a) Kyanite and staurolite overgrowing the main S1/2 foliation, defined by phengite, biotite and plagioclase. Staurolite slightly postdates kyanite as it grows at the rim of kyanite. Garnet is strongly corroded. b) Staurolite growing at the rim of garnet and over phengite. Biotite grows in the pressure shadow of garnet and defines the composite S1/2 foliation. c) Staurolite growing at the rim of kyanite and garnet. d) Schistosity S3, defined by biotite (Bt) in fold limbs of D3 folds. Note that chlorite (Chl) shows no preferred orientation. e) Chlorite growing statically at the rims of garnet, staurolite and biotite. Epidote is associated with chlorite. f) Chlorite, refolded by D4 folds. g) Staurolite and plagioclase as porphyroclasts with asymmetric augen structures within the S1/2/3 foliation plane. Asymmetric augen structures indicate D3 dextral shearing in map view. h) Staurolite and garnet as porphyroclasts with asymmetric augen structures in S1/2/3 foliation defined by chlorite. Asymmetric augen structures indicate dextral shearing during D4 in map view.

folding (his D2). Towards lower pressures the assemblage Grt + Phe + Pl + Bt + Ky + Qtz is limited by the predicted disappearance of kyanite and the growth of staurolite that only coexists in a very narrow P-T intervall with kyanite (Fig. 13a). Formation of staurolite at the expense of kyanite is indeed observed during decompression, as was discussed earlier (Fig. 12a, c). In sample LK13 this former replacement is far from complete, which is interpreted to be due to sluggish replacement of kyanite by staurolite for kinetic reasons, as sample LK 13 underwent ongoing syn-D3

retrogression through the P-T area defined by the assemblage 4 (Fig. 13a) where kyanite can only be metastable. Since LK 13 and surrounding metapelites are devoid of sillimanite, the P-T conditions inferred for D3 are limited towards lower pressures by the stability fields, which involve the growth of sillimanite (Fig. 13a). This indicates that the rocks must have started to cool in the course of ongoing syn-D3 decompression. Because chlorite flakes are seen to overgrow the S3 axial plane foliation, and at the same time the previously formed staurolite (Fig. 12e), we take

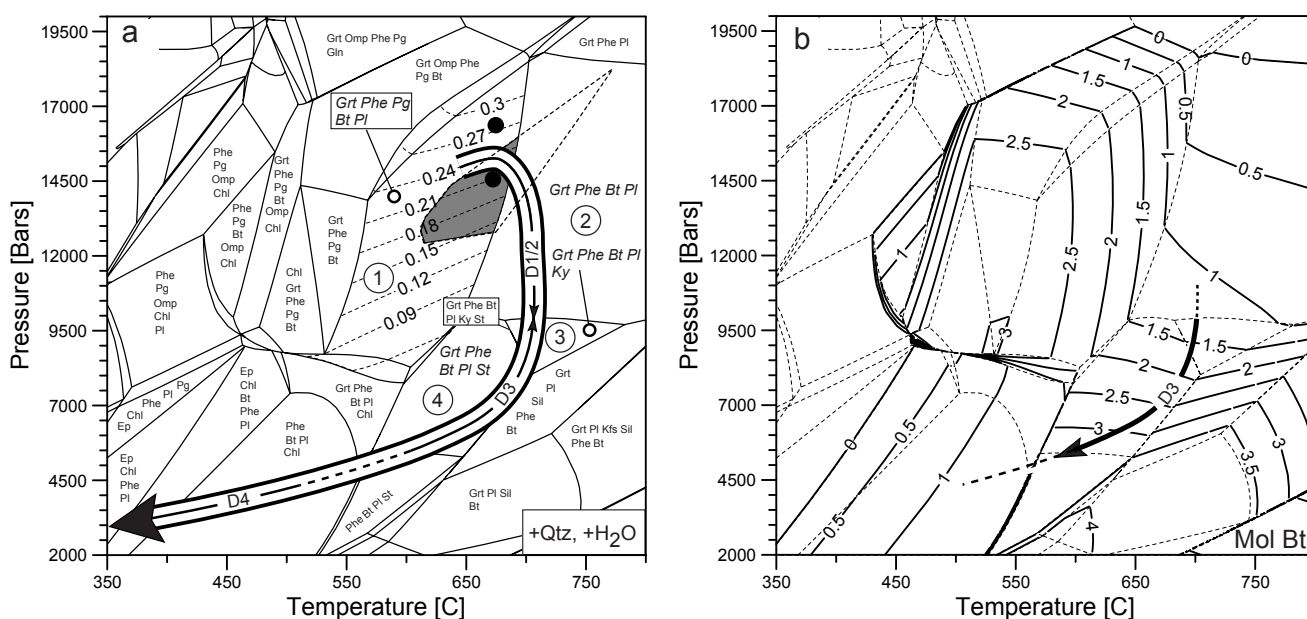


Fig. 13 Equilibrium phase diagrams for the measured bulk rock chemistry of metapelitic sample LK13 taken from the outcrop depicted in Figure 4 (compare micrographs given in Figure 12a-e). The diagrams are calculated with the program DOMINO (De Capitani, 1994) and they postulate distinct stable phase assemblages and corresponding mineral composition based on thermodynamic properties defined in the database (JUN92). Bulk rock chemistry is determined by powder X-ray diffraction and normalized to 100 cations, all iron is taken as Fe2+.

a) Equilibrium phase diagram for the specific bulk rock chemistry of sample LK 13, illustrating the stable mineral assemblages and the proposed P-T-d loop. Water and quartz are stable with all mineral assemblages indicated. Numbers 1, 2, 3, 4 refer to mineral parageneses of sample LK13 discussed in the text. Stippled contours give the calculated Mg-Celadonite content in phengite. Black dots without tie lines indicate the measured XMg-Cel in the cores of phengite. Grey shaded area indicates peak P-T conditions after Keller et al. (subm.) and is defined by the overlap of two first stage assemblages from metapelites with different bulk rock composition.

b) Mineral abundance isopleths of biotite. The diagram is calculated for the measured bulk rock chemistry of sample LK13 with the program DOMINO (De Capitani, 1994). The postulated isopleths are given in moles of a stable phase based on the thermodynamic properties defined in the database (JUN92). Bulk rock chemistry is determined by powder X-ray diffraction and normalized to 100 cations while all iron is taken as Fe2+.

the stability field of assemblage 4 (Grt + Phe + Pl + Bt + St + Qtz) to limit D3 deformation towards lower temperatures. Stability of chlorite at the expense of staurolite is expected to set in at around 570°C and 5.5 kbar (Fig. 13a), i.e. the P-T conditions suggested for the termination of D3 deformation.

From now onwards chlorite is expected to grow at the expense of staurolite, garnet and biotite. According to Fig. 13a the decomposition of staurolite and garnet should theoretically progress to completion as assemblage Grt + Phe + Pl + Bt + Chl + Qtz becomes stable. This is not observed, again for kinetic reasons (slow decomposition progress of garnet and staurolite), these two minerals remaining metastable. We postulate that D4 deformation is likely to immediately follow the termination of D3 ( $P < c. 5.5$  kbar,  $T < c. 570^\circ\text{C}$ ) is indirect but reasonable, given the similar kinematic scenarios for both D3 and D4 discussed earlier. Hence it is proposed in Figure 13a that further cooling of the metapelites below 570°C and down to temperatures of around 280°C, expected for the brittle-viscous transition of quartz (Stipp et al., 2002), predominantly occurred during D4 deformation.

#### 4.12 TECTONIC AND METAMORPHIC EVOLUTION OF THE WORKING AREA IN A REGIONAL CONTEXT

For the western part of Monte Rosa nappe Chopin & Monié (1984) derived P-T conditions for the high-pressure stage of 16 kbar at 500°C. Borghi et al. (1996) derived P-T estimates in the range of 518-546°C at 11-14 kbar for an earliest Alpine mineral assemblage containing Grt + Cld + Chl from a pelitic sample from this same area. Based on the published P-T estimates derived from pelitic rocks we propose that the P-T conditions

for the high-pressure stage of the western part of the Monte Rosa nappe were in the range of 500-550°C at 14-16 kbar, the lower pressures obtained by Borghi et al. (1996) probably indicating early stages of decompression.

For the eastern part of the Monte Rosa nappe and the CM unit almost identical pressures, but higher temperatures, are derived (Keller et al. *subm.*). The area under consideration additionally exhibits a “Barrow-type” metamorphic field gradient, characterized by an eastwards increase in temperatures (Beauregard, 1958; Colombi, 1989; Frey et al., 1999). Hence temperature differences must have persisted during later stages of metamorphism. In theory, these differences could be entirely inherited from the above mentioned temperature differences that prevailed during the precursory high-pressure stage because the index minerals defining the metamorphic zonation grew during decompression and at the expense of the minerals defining the high-pressure assemblages (Keller et al., *subm.*). However, the differences in temperatures during decompression are too large in the study area (Keller et al., *subm.*) for such a simple scenario. Decompression is relatively more isothermal, or even associated with moderate heating, in the more eastern- and structurally-deeper parts of the study area, where sillimanite grade at about 650°C and 5 kbar is reached during decompression (Keller et al., *subm.*). The western parts of the study area (i.e. in the staurolite absent mineral zone), however, experienced substantial cooling during decompression.

In the eastern part of the study area relatively high temperatures at low pressures are reached during D3 deformation (Fig. 13a), which exhibits a NE-SW oriented and orogen-parallel extensional component, characterized by top-WSW, respectively dextral shearing. Because of this syn-D3

component of extensional unroofing component, and following Thompson & England (1984) and England & Thompson (1984), it is proposed that exhumation during D3 deformation progresses much faster in the deeper structural units (i.e. the CM unit) than could be achieved by erosion only. Hence, the deeply buried rocks at the eastern margin of the Lepontine dome (this work) and within this dome (Nagel et al., 2002) experience a much larger amount of decompression before they start to substantially cool, compared to the western areas of the Monte Rosa nappe and the French-Italian Alps in general.

D3 deformation within the staurolite mineral zone occurs over a considerable P-T interval, where the continuous decomposition of phengite forms biotite, staurolite and plagioclase within a wide range of metapelitic compositions (Keller et al., *subm.*). Hence, overprinting in the course of ongoing D3 folding and shearing may progress to completion, thereby causing the main foliation to be a composite foliation formed during the first three deformation phases D1 to D3. Indeed it was frequently observed that staurolite and plagioclase are host porphyroclasts of asymmetric augen structures within the foliation plane in the more eastern parts of the study area, thus defining such a composite main foliation (Fig. 12g). Hence, D3 deformation appears to be more pervasive within deeper structural levels. Within the southern limb of the Vanzone antiform such asymmetric augen structures often indicate dextral shearing. Hence, it is suggested that the main foliation in the eastern area to both sides of the Ossola valley the main foliation is a composite one formed during the first three deformation phases. Many D3 top-WSW shear indicators may have been passively rotated into the southern limb of the D4 Vanzone antiform where they would appear dextral in map

view.

Other asymmetric augen structures are marked by chlorite, which grows at the grain boundaries of staurolite and garnet (Fig. 12h). Such observations indicate the decomposition of staurolite and garnet during ongoing retrogression and dextral shearing during the D4 deformation, which is characterized by a very similar kinematic scenario, as was previously discussed.

Overprinting criteria, orientation data of structural elements and correlations between metamorphism and deformation all indicate that the overprinting of the first backfolding phase (D3) by the second backfolding phase (D4) occurred at lower temperatures compared to those prevailing during D3 deformation. D4 deformation definitely postdates the formation of staurolite. Hence, on a regional scale the relative timing between staurolite growth and D4 deformation is documented by the folded outline of the staurolite mineral zone boundary (Fig. 1), tracing the major D4 Vanzone antiform.

In summary, the exhumation history may be subdivided into the same two stages that were previously deduced for the kinematics of deformation. During a first stage of D1/D2 nappe stacking decompression is near-isothermal in the working area, but not further to the west. The second stage of decompression in the working area is initially associated with a Barrow-type field metamorphic gradient, that is immediately followed by more rapid cooling during ongoing D3 and D4 deformation in a dextrally transpressive scenario, probably due to partial unroofing by an orogen-parallel extensional component of this second kinematic stage.



#### **4.13 CHRONOLOGY OF ALPINE STRUCTURES**

Based on selected published radiometric data, which in part directly date deformation phases, we discuss the timing of the tectonic and metamorphic evolution of the study area and surrounding units based on the compilation of data presented in Fig. 14. We also present new fission track data, established for the area along the Ossola valley (Fig. 15).

##### **4.13.1 Top N-NW thrusting and nappe stacking (D1/D2)**

The first two deformation phases (D1/D2) of the Alpine orogenic cycle are related to top-N nappe stacking in a context of underthrusting of the European plate below the Adriatic margin (e.g. Steck, 1984; 1987; Lacassin, 1987; Steck & Hunziker, 1994; Schmid and Kissling 2000). This top-N shearing (top-NW according to some authors) is associated with nappe stacking, which starts under high-pressure metamorphic conditions in the eclogite bearing units and is immediately followed by a first stage of exhumation. Within the working area the formation of the eclogitic part of D1/D2 shear zone from the Monte Rosa nappe (Keller et al., 2004) was dated as 47 Ma (+1) by  $^{39}\text{Ar}$ - $^{40}\text{Ar}$  dating (Bucher et al., *subm.*). In the Zermatt zone Sm-Nd dating of garnet gives  $51 \pm 18$  Ma for the high-pressure metamorphic stage (Bowtell et al., 1994). A younger age (c. 44 Ma) is obtained from SHRIMP dating of zircon (Rubatto et al., 1997).

However, at the structurally highest level exposing eclogite facies units, namely at the southwestern top of the Monte Rosa and Zermatt zone, Rb-Sr dating of the top-SE movement, linked to the Gressoney shear zone yielded ages that are supposed to date the activity of the Gressoney shear

zone, ranging between 45 and 36 Ma. These ages are interpreted to also date the timing of exhumation of eclogite facies rocks, attributed to normal faulting along this shear zone (Reddy et al., 1999). Assuming that the interpretation of the Rb-Sr isotope ratios and associated tectonic inferences are correct, D1/D2 top-N shearing and associated high-pressure metamorphism at deeper structural levels, including our working area, would overlap in time with top-SE extensional shearing at structurally higher levels such as the Gressoney shear zone, both shearing directions being related to the exhumation of eclogite facies rocks. Such a kinematic situation would result in the differential ascent of the eclogite facies units with respect to over- and underlying tectonic units. Hence, we speculate that exhumation of the eclogitic rocks in the upper Penninic units occurred by active extrusion within a subduction channel, active during overall crustal shortening (e. g. Chemenda et al., 1997).

##### **4.13.2 First phase of backfolding (D3)**

In the structurally higher parts, i. e. in the Zermatt area, greenschist facies top-SE backthrusting related to the D3 Mischabel fold gives an age of about 40 Ma, dated with  $^{40}\text{Ar}/^{39}\text{Ar}$  and Rb/Sr data on white micas and amphiboles (Barnicoat et al., 1995). Field relations suggest that albite veins postdate the activity of syn-Mischabel fold shearing, whereby an absolute age of around 35 Ma (U-Pb) is obtained for vein alteration zones (Barnicoat et al., 1995). Also in the Zermatt area a similar time interval (42-37 Ma) has recently been obtained by Rb-Sr dating of apatite-muscovite pairs for the active stage of greenschist facies top-SE shearing, P-T estimates indicating that shearing started at 400-475°C/4-5 kbar and terminated at 300-350°C/3-3.5 kbar (Cartwright & Barnicoat,

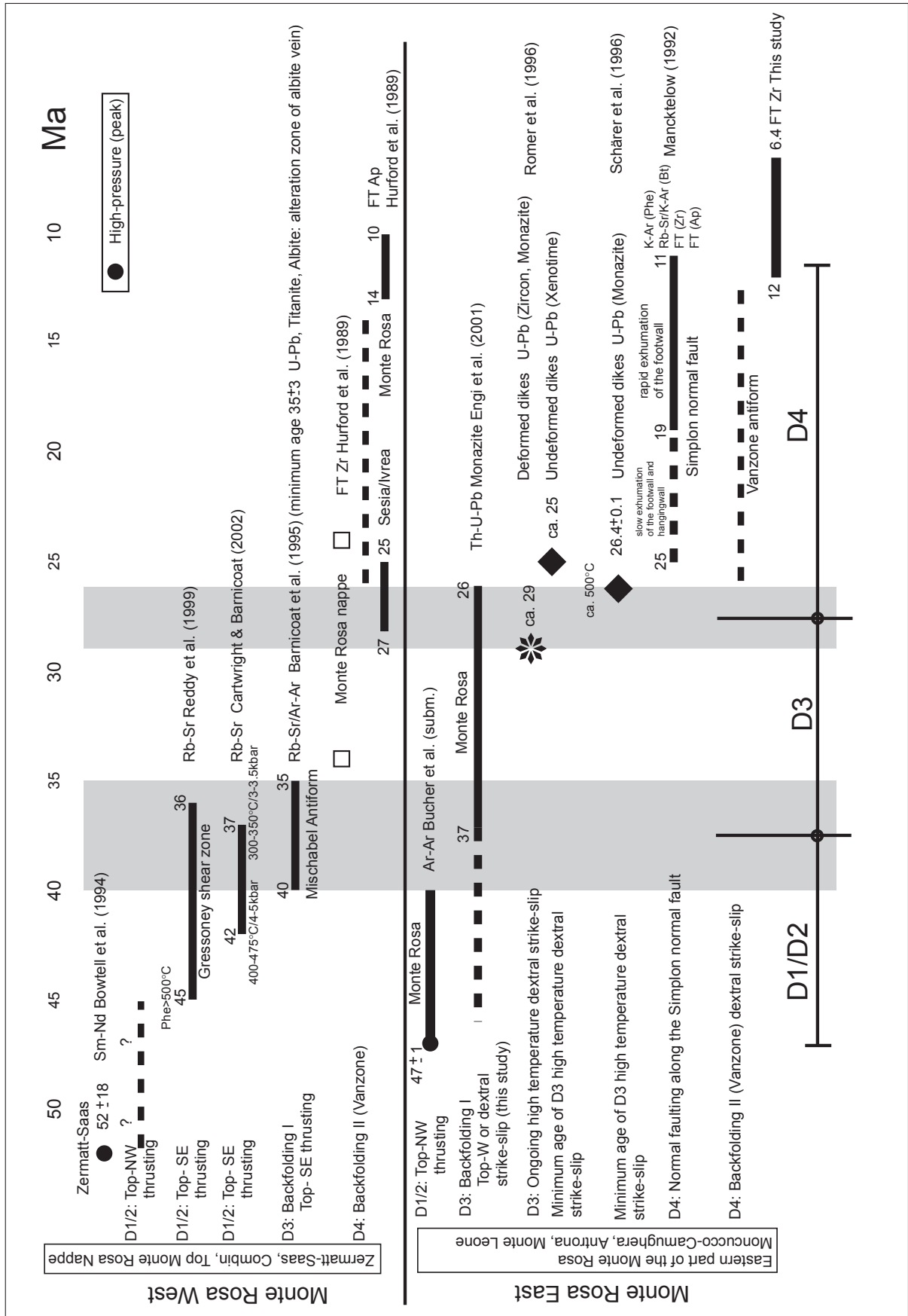


Fig. 14 Table giving available age constraints for the stages of the Alpine tectonic and metamorphic evolution.

2002). Zircon fission track ages (34-24 Ma) from the structural top of the Monte Rosa nappe suggest that these structurally higher parts cooled below c. 250°C during early Oligocene times (Hurford et al., 1989, his Fig. 8). Based on these

published data it is suggested that greenschist facies syn-D3 top-SE backthrusting and backfolding started in the late Eocene and terminated in the early Oligocene in these structurally higher parts, immediately following Eocene D1/D2 top-SE shearing.

However, in the structurally deeper parts (i.e. the eastern part of the Monte Rosa nappe and CM unit), characterized by top-WSW and dextral shearing, respectively, D3 deformation occurred at significantly higher temperatures (i.e. under Barrovian P-T conditions). For the Monte Rosa nappe Engi et al. (2001) provide monazite ages, interpreted by the authors to date an early stage during decompression, ranging between 38 and 32 Ma ago. However, the ages obtained for monazites from staurolite and sillimanite bearing metapelitic samples (sample Bi9801 and Po9703 of Engi et al., 2001, their Fig. 3) from the eastern part of the Monte Rosa nappe range between 37 and 26 Ma and are interpreted to date different re-equilibration stages during decompression. These Barrovian P-T conditions are attained during decompression and are coeval with D3 deformation, which suggests that D3 deformation at deeper structural parts is active within the 37-26 Ma time span. A lower age limit of around (26Ma) for this period correlates well with the termination of dextral respectively top-WSW- and high-temperature- shearing of the Simplon ductile shear zone (Steck, 1990), being constrained by U-Pb dating of the age of post-D3 granitic dike injections into the Isorno-Orselina zone and Monte Rosa nappe (Schärer et al., 1996; Romer et al., 1996; see also Steck & Hunziker, 1994) between 29 Ma and 26 Ma ago.

Hence, the correlation of the Simplon ductile shear zone (D2 of Steck & Hunziker, 1994) with our third deformation phase, i.e. the first back-

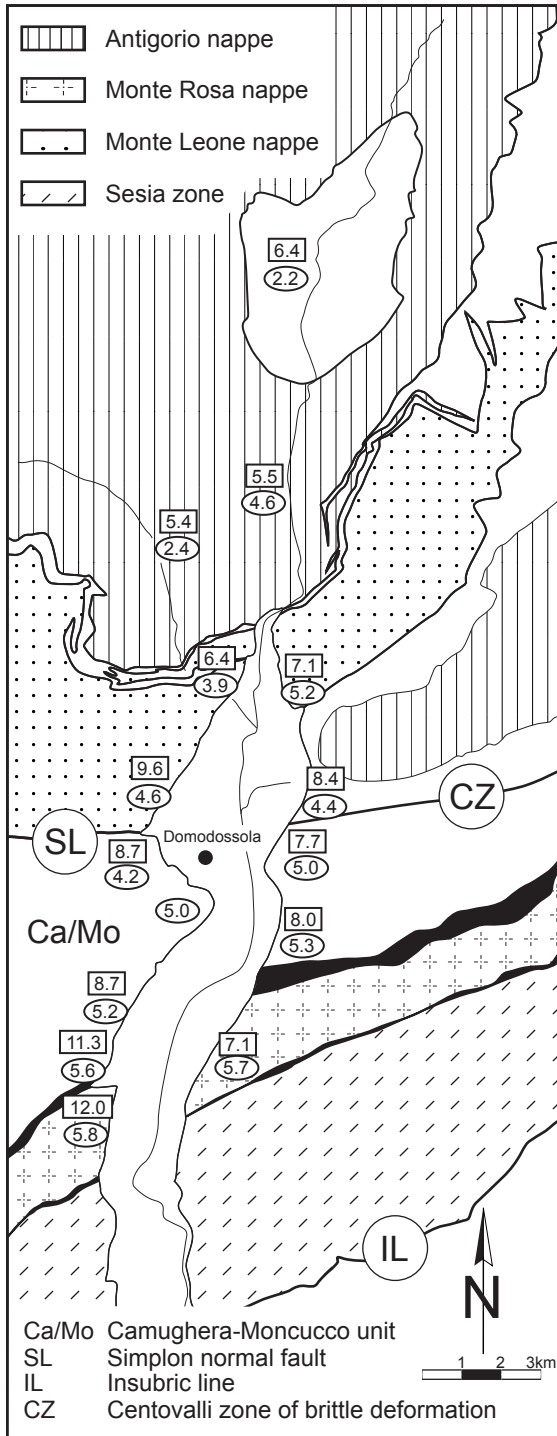


Fig. 15 Tectonic map of the upper part of the Ossola valley, showing available fission track central ages in Ma (see Hess, 2003, deposited at the library of the Geological Institute Basel for more details). Rectangles=zircon fission track ages. Ovals=apatite fission track ages.

folding phase and associated dextral shearing, is supported by these timing constraints. From published and own petrological data it is obvious that temperatures prevailing during D3 deformation increase towards the east, i.e. towards deeper structural levels. In addition, the radiometric data indicate that D3 deformation is heterochronous and becomes increasingly younger towards the east and towards deeper structural levels. Consequently, the first stages of exhumation (D3) related to the new kinematic regime of back-folding and/or -shearing during D3/D4, associated with dextral shearing and/or orogen-parallel stretch of the D1/D2 nappe stack in the working area, is of progressively younger age towards deeper structural levels in the east.

#### **4.13.3 Second phase of backfolding and normal faulting along the Simplon line (D4)**

D4 -folding occurred at lower temperatures (< c. 570°C), related to dextral shearing, particularly in the southern limb of the Vanzone antiform and, as will be discussed below, to contemporaneous normal faulting along the Simplon line.

Gold bearing veins, the ages of which range between around 32 Ma and 25 Ma, tend to become younger towards the east (Pettke et al., 1999) and are found all along the trace of the axial plane of the major Vanzone antiform, suggesting a genetic link with D4-deformation. The area around the southwestern top of the Monte Rosa nappe in the Zermatt area is characterized by a marked gradient in apatite fission track cooling ages. While ages between 10-14 Ma are typical for the northern parts of the western Monte Rosa nappe, ages between 25-27 Ma are found in the southern parts (Hurford et al., 1989, his Fig. 8). This suggests differential exhumation of the northern limb of the Vanzone antiform relative to its southern limb

somewhere within the 27 to 10 Ma time interval. The structural data concerning D4 deformation presented earlier suggest a direct relationship between the formation of D4 backfolds (i.e. the Vanzone, Brevettola and Masera folds) in the south and normal faulting along the Simplon line on the other side. According to Mancktelow (1992) normal faulting along the Simplon line, associated backfolding further to the north (Berisal- and Glishorn- folds), was active between 19 Ma and 11 Ma ago, confirming the postulate of contemporaneous backfolding and orogen-parallel normal faulting. In summary, all these data suggest that D4, (i.e. second backfolding phase and associated dextral shearing) started to be active in late Oligocene times and at about 27 Ma ago, and was still active during Miocene (19-10 Ma) normal faulting along the Simplon line.

Normal faulting in the Simplon domain is marked by jumps in zircon and apatite fission track ages, respectively, allowing to date normal faulting (Mancktelow, 1992), and produces a significant jump in metamorphic grade from greenschist facies conditions in the hangingwall to amphibolite facies conditions in the footwall (Wagner et al. 1977; Soom, 1990; Steck & Hunziker, 1994; Grasemann & Mancktelow, 1983). Our own data from the Ossola valley, however, yielded no jump in zircon- and apatite- fission track ages across the suspected eastern continuation of the Simplon line, central ages ranging between 6.4-12 Ma and 2.2-5.8 Ma, respectively (Fig. 15; Hess, 2003). Note that these ages become continuously and progressively older going from north to south. This indicates late regional uplift of the more northern parts of the area around the Toce culmination. As there is no discrete jump in zircon- and apatite- fission track ages that would mark the eastern continuation of the Simplon line

in the area of the Ossola valley, the discrete Simplon normal fault has no eastward continuation in terms of differential exhumation by tectonic unroofing. It terminates somewhere along the lower Bognanco valley, contrary to the findings of Mancktelow (1990) and Steck (1999), who suggest a continuation of the Simplon line across the Ossola valley and into the Isorno valley.

Temperatures during mylonitisation along the Simplon normal fault and its hypothetical continuation into the Isorno valley increase from the northwest to the southeast and east, but did not exceed 550°C (Mancktelow, 1990). These increasing temperatures would suggest that the differential displacement across this normal fault should theoretically increase across towards the east, differentially exhuming progressively more deeply buried, i.e. higher metamorphic rocks north of this supposed eastern continuation of the Simplon normal fault against lower grade mylonites expected further south. Contrary to this expectation the main foliation is of a high metamorphic grade (sillimanite grade at around 650°C) everywhere south of the eastern continuation of the Simplon normal fault across the Ossola valley. Thus no significant metamorphic “jump” exists either across the supposed eastern continuation of the Simplon normal fault in the Ossola valley.

Fission track data, together with the regional metamorphic pattern, suggest that the rocks all along the Ossola valley have a common retrogression and exhumation history from amphibolite, through greenschist into sub-greenschist facies conditions. Furthermore a broad mylonitic belt in the sense of an eastward continuation of the Simplon normal fault is not observed. Instead, older pre-D4 stretching lineations, steeply plunging to the E to ESE, are observed in the Bognanco valley, indicating that late stage syn-D4 deformation

is not pervasive in the Bognanco valley (Fig. 10, Steck & Hunziker, 1994, their Fig. 3).

In conclusion there is ample evidence that the Simplon normal fault has no eastward continuation and terminates somewhere along lower Bognanco valley. However, the associated displacements and strains associated with D4 Simplon normal faulting must be partitioned into other contemporaneous structures along Bognanco valley. The abrupt change into an E-W-strike of the mylonites related to the Simplon normal fault near Bagni di Bognanco and the eastern termination of this normal fault suggests transformation into dextral shearing further to the south and east, the Simplon normal fault representing a tensile bridge, that links dextral shearing in the working area to that observed further to the NW along the Rhone valley (Steck, 1984, 1987). Note however that such late stage dextral shearing is not localized within our study area, dextral shearing being diffuse and associated with D4-folding of the Masera and Brevettola folds, well documented in case of the southern limbs of the Vanzone- and the Brevettola- antiforms (Figs 8, 10, 11). This second phase of backfolding and associated dextral shearing must have terminated before about 12 Ma ago, when the southern part of the working area situated along the Ossola valley cooled below the zircon fission track temperature ages, no longer allowing for ductile folding. Since brittle deformation along the Centovalli line in Vigizzo valley was shown to clearly overprint D4 folds, the Centovalli line must have been active after the end of D4 deformation, i.e. after 12 Ma ago. Therefore it cannot represent the eastern continuation of the Simplon normal fault either.



## 4.14 DISCUSSION

### 4.14.1 The eastwards continuation of the Simplon normal fault

The fact that our data indicate that the Simplon normal fault apparently has no eastward continuation deserves some discussion, because the Simplon fault zone is often regarded as a transfer zone (“pull-apart”) where dextral strike-slip movements along the Rhone line are transferred to the Insubric line in a overall dextral transpressive regime (e.g. Steck, 1984; Steck, 1987; Schmid & Kissling, 2000). In this context it is interesting to note that the traces of the axial plane of major D4 backfolds show a systematic en-echelon arrangement, accompanied by a change in their strike (Figs 2, 4, 9, 16). In the west the axial plane trace of the Vanzone antiform strikes approximately NE-SW, while towards the east the axial plane traces of the Brevettola antiform and Masera synform tend to strike almost E-W. Note that this pronounced change in strike occurs south of where the Simplon normal fault swings into an E-W orientation near its termination in Bognanco valley (Fig. 16).

The spatial arrangement and the strike- of the D4 axial plane traces suggests that two directions of shortening affected the study area during D4 backfolding. While N-S shortening prevailed in the eastern parts, the western parts underwent NW-SE shortening (Fig. 16). The change in orientation of these D4 axial plane traces roughly coincides with a point where the Adriatic Moho changes its topology, and where the Insubric line changes from an E-W strike to a NE-SW strike (Schmid & Kissling, 2000 their Fig. 5). Because of these remarkable relationships between deep- and shallow- structural features we suggest that the arrangement of the D4 axial plane traces is controlled by the topological change of the Adri-

atic Moho, i.e. by deep-seated structural features. It is proposed that the different directions of shortening and the eastern termination of the Simplon normal fault may both be due to Miocene dextral transpressive indentation of the a bow-shaped complex topology of the Adriatic lower crust represented by the Ivrea zone and geophysical anomaly.

Indentation of a plastic European plate by a rigid African promontory is often used in order to explain the arc of western Alps after collision (e.g. Tapponier, 1977; Regenauer-Lieb, 1996). Analogue experiments suggest that the indentation of India into Asia caused rotation and extrusion of Indochina with respect to the indentation of India (Tapponier et al., 1982). A similar scenario for the Western Alps would be in accordance with recent paleomagnetic data obtained by Collombet et al. (2002), who suggest a large counter-clockwise rotation of the western Alps relative to both Europe and Adria. Thus, we think that the rotation of indented crustal segments is also a viable process for explaining why the Simplon normal fault lacks a southeastern continuation. The Simplon fault zone may also terminate because of a combined effect of transformation into dextral shearing and decreasing amount of extension towards the east. Based on all these considerations we propose a counterclockwise rotation of the hanging block of the Simplon normal fault around a pole situated in the Bognanco valley (Fig. 16). This causes displacement by normal faulting to be highest along the northwestern segment of the Simplon line, where it is transferred into dextral shearing along the Rhone line. Conversely, displacement by normal faulting drops towards the southeastern termination of the Simplon fault zone, in accordance with the presented structural observations, the regional metamorphic pattern and the fission

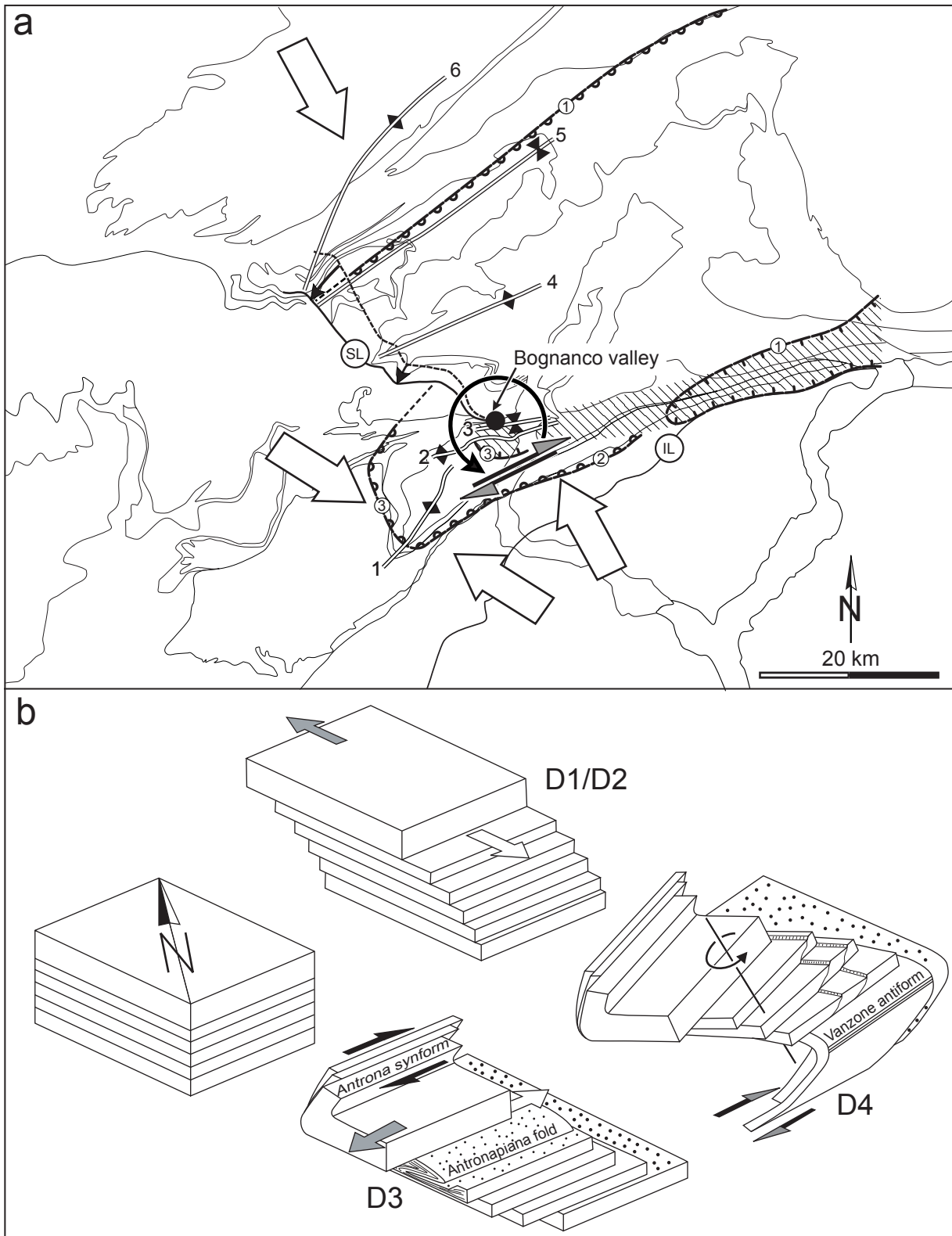


Fig. 16

a) Interpretative tectonic map serving for the discussion of the kinematics during D4 deformation (see text, and Fig. 1 for tectonic units and mineral zone boundaries). Note that the displacement associated with normal faulting along the Simplon line decreases towards the southeast as the upper block of the Simplon line rotates around a pole indicated by the black dot. Dextral shearing occurs particular in the southern limb of the Vanzone- and Brevettola- backfolds and modifies the metamorphic zonation that pre-dates D4 deformation. 1=Vanzone antiform, 2=Brevettola antiform, 3=Masera synform, 4=Toce antiform, 5=Berisal synform 6=Glishorn antiform

b) A card-sliding model to illustrate the kinematic history established in the study area. The original is sheared first by top-NW movements during D1/D2 deformation and associated nappe stacking. During D3 it is sheared towards the west and the first backfolds are formed. At lower structural levels this shearing occurs in a flat lying- or SE dipping- nappe pile. Note that top-west shearing appears dextral in the overturned limb of D3 backfolds. During D4 deformation the second generation of backfolds are formed and the Simplon fault rotates the hanging wall with respect to its footwall.

track data.

#### 4.15 CONCLUSIONS

1) Composite D1/D2 deformation and related top-N or top-NW thrusting started at high-pressure conditions (c. 12.5-16 kbar) and under relatively high temperatures (c. 600-650°C). Published radiometric data for the Eocene high-pressure stage suggest that top-SE shearing at the structural top of the high-pressure units is coeval with top-N or top-NW thrusting at the base. This kinematic situation suggests a differential ascent of high-pressure units relative to the surrounding units during nappe stacking and associated crustal shortening. Thus, exhumation related to D1/D2 deformation rather occurs by extrusion within the subduction channel than by crustal extension.

2) In the higher structural levels D3 backfolding and/or backthrusting start in late Eocene times under greenschist facies conditions. Towards deeper structural levels D3 deformation progressively becomes younger. This is due to the fact that higher temperatures prevailed longer in the east, hence the brittle-viscous transition in the area of the Ossola valley is younger than at higher structural levels in the west. Consequently, the main foliation in the Ossola valley is a composite foliation formed during the first three deformation phases (D1-D3) and is affected by high-temperature metamorphism. Barrovian P-T conditions at deeper structural levels are attained due to an extensional unroofing component during D3 deformation, that delays cooling during decompression and thus causes approximately isothermal decompression. D3 deformation ceased in late Oligocene times.

3) An open fold pair consisting of Masera synform and Brevettola antiform forms the eastern continuation of the major Vanzone antiform. This contradicts the proposition of Milnes et al., (1981), that the D4 Vanzone antiform becomes an isoclinal fold towards the east. Structural arguments, as well as published radiometric data, suggest that the major Vanzone and Brevettola antiforms formed at the same time as the Simplon normal fault. Two geometrical features of D4 deformation change overall style in the Bognanco valley, situated exactly south of the swing in orientation of the Simplon normal fault. Firstly, the Masera synform nucleates and amplifies towards the east into a major D4 fold. Secondly, the D4 fold axes change in strike from SW-NE to W-E.

4) As the Simplon normal fault dies out towards the east, the Masera synform nucleates and amplifies towards the same direction. As hypothesised by Milnes et al. (1981) displacement along the Simplon normal fault (Mancktelow, 1990) is additionally transformed into the southern limb of Vanzone and Brevettola antiforms, where D4 folding is also associated with dextral shearing.

5) It is strongly suggested that paleogeographic reconstructions based on the undoing of all the major fold structures observed in the nappe pile of the upper Penninic Alps and projected onto a single N-S orientated profile plane may lead to ambiguous results. This suggestion is supported by the fact that the two backfolding phases are associated with top-WSW and dextral shearing, and pervasive deformation becomes progressively younger towards the east, i.e. towards deeper structural parts. Hence, there are large out of profile movements during D3 and D4 deforma-

tion that potentially produce suspicious results, if paleogeographic reconstructions are obtained by retro-deformation in profile view only.

6) The Antrona unit in Bognanco valley, which is structurally positioned in the northern limb of the D4 Maserà synform, dipping towards the SE unit, strikes all the way to the mouth of the Bognanco valley. Across the Ossola valley numerous aligned lenses of ophiolitic rocks (amphibolites, ultrabasic rocks and gabbros) in a position identical to that of the Antrona unit in the Bognanco valley, can be found in the southern slope of the Isorno valley (see also Wieland, 1966). There staurolite bearing garnet-mica schists have also frequently been observed (see also Bearth, 1956b). Such staurolite bearing garnet-mica schists are typical rocks for the western parts of CM unit west of the Ossola valley. Thus, it is concluded that the rocks of Antrona unit and the northern rim of the CM unit find their eastern continuation in the southern slope of the Isorno valley and not in the Vigizzo valley as proposed by most tectonic maps (e.g. Steck et al., 1999). Following Bearth (1956b) we suggested that at least parts of the “Pioda di Crana zone” represent the eastern equivalents of the MC unit west of the Ossola valley.

#### **4.16 ACKNOWLEDGMENTS**

This work has benefited from comments and discussions with A. Berger. Furthermore we acknowledge the contributions of the members of the Basel “Western Alps group” and “Monte Rosa group” (R. Bousquet, S. Bucher, S. Ceriani, J. Kramer and N. Froitzheim) which were instrumental for our own thinking. In addition we had support from R. Abart, C. De Capitani, H. Stünitz and K. Waite. This study was supported by the Swiss National Foundation Grants Nr. 20-61814.00 and 2000-068020.02/1.

#### 4.17 REFERENCES

- Amstutz, A. 1954: Pennides dans l'Ossola et problèmes des raciness. Arch. Sci., Genève, 7/6.
- Barnicoat, A. C., Rex, D.C., Guise, P. G. & Cliff, R. A. 1995: The timing of and nature of greenschist facies deformation and metamorphism in the upper Pennine Alps. *Tectonics* 14, 279-293.
- Bearth, P. 1939: Über den Zusammenhang von Monte Rosa- und Bernhard- Decke. *Eclogae geol. Helv.* 32, 101-111.
- 1953: Blatt Zermatt, Geologischer Atlas der Schweiz. Nr. 29. Schweiz. Geol.Kommission, Basel.
- 1954a: Blatt Monte Moro, Geologischer Atlas der Schweiz. Nr. 30. Schweiz. Geol. Kommission, Basel.
- 1954b: Blatt Saas, Geologischer Atlas der Schweiz. Nr. 31. Schweiz. Geol. Kommission, Basel.
- 1956a: Geologische Beobachtungen im Grenzgebiet der lepontinischen und penninischen Alpen *Eclogae geol. Helv.* 49/2, 279-290.
- 1956b: Zur Geologie der Wurzelzone östlich des Ossolatales. *Eclogae geol. Helv.* 49, 267-278.
- 1957a: Die Umbiegung von Vanzone (Valle Anzasca). *Eclogae geol. Helv.* 50, 161-170.
- 1957b: Erläuterungen Blatt Saas und Monte Moro, Geologischer Atlas der Schweiz. Nr. 30, 31. Schweiz. Geol. Kommission, Basel.
- 1958. Ueber den Wechsel der Mineralfazies in der Wurzelzone des Penninikums. *Mineralogische und Petrographische Mitteilungen*, **38**, 363-373.
- 1973: Gesteins- und Mineralparagenesen aus den Ophiolithen von Zermatt. *Schweizerische Mineralogische und Petrographische Mitteilungen* 53, 299-334.
- & Schwander, H. 1981: The post-Triassic sediments of the ophiolite zone Zermatt-Saas Fee and the associated manganese mineralizations. *Eclogae geol. Helv.* 74, 189-205.
- Berman, R. G. 1988. Internally-consistent Thermodynamic Data for Minerals in the System  $\text{Na}_2\text{O}-\text{K}_2\text{O}-\text{CaO}-\text{FeO}-\text{Fe}_2\text{O}_3-\text{Al}_2\text{O}_3-\text{SiO}_2-\text{H}_2\text{O}-\text{CO}_2$ . *Journal of Petrology*, **29**, 445-552.
- 1990. Mixing properties of Ca-Mg-Fe-Mn garnets. *American Mineralogist*, **75**, 328-344.
- Bigioggero, B., Boriani, A., Colombo, A. & Tunesi, A. 1981: Eta e caratteri petrichimici degli ortogneiss della zona Moncucco-Orselina nell' area Ossolana. *Rendiconti Società Italiana di Mineralogia e Petrologia* 38, 207-218.
- Blumenthal, M. M. 1952: Beobachtungen über den Bau und Verlauf der Muldenzone von Antrona. *Eclogae geol. Helv.* 45/2, 220-251.
- Bowtell, S. A., Cliff, R. A. & Barnicoat, A. C. 1994: Sm-Nd isotopic evidence on the age of elongation in the Zermatt-Saas ophiolite. *J. Metamorphic Geol.* 12, 187-196.



- Borghi, A., Compagnoni, R. & Sandrone, R. 1996: Composite P-T paths in the internal Penninic massifs of the western Alps: Petrological constrains to their thermo-mechanical evolution. *Eclogae Geologicae Helvetiae* **89**, 345-367.
- Bucher, S., Villa, I. M., Kleinhanns, I. C., Keller, L. M., Bousquet, R. & Schmid, S. M. subm.: From HP to late stage deformation: Dating the tectono-metamorphic evolution along a transect (ECORS-CROP) through the Italien-French Western Alps. subm.)
- Carrupt, E. & Schlup, M. 1998: Métamorphisme et tectonique du versant sud du Val Bognanco Pennique, (Alpes italiennes). *Bull. Soc. Vaud. Sc. Nat.*, **86**, 29-59.
- Cartwright, J. & Barnicoat, A. C. 2002: Petrology, geochronology, and tectonics of shear zones in the Zermatt-Saas and Combin zones of the Western Alps. *Journal of Metamorphic Geology* **20**, 263-281.
- Ceriani, S., Fügenschuh, B. & Schmid, S. M. 2001: Multi-stage thrusting at the "Penninic Front" in the Western Alps between Mont Blanc and Pelvoux massif. *Int. J. Earth Sci.*, **90**, 685-702.
- Chemenda, A., Matte, P. & Sokolov, V. 1997: A model of Paleozoic obduction and exhumation of high-pressure/low-temperature rocks in the southern Urals. *Tectonophysics* **276**, 217-227.
- Chopin, C. & Monié, P. 1984: A unique magnesiochloritoid-bearing, high-pressure assemblage from the Monte Rosa, Western Alps: petrologic and  $^{40}\text{Ar}$ - $^{39}\text{Ar}$  radiometric study. *Contributions to Mineralogy and Petrology* **87**, 388-398.
- Collombet, M., Thomas, J. C., Chauvin, A., Tricart, P., Bouillin, J. P., Gratier, J. P. 2002: Counterclockwise rotation of the western Alps since the Oligocene: New insights from paleomagnetic data. *Tectonics* **21/4**, 1-15.
- Colombi, A. 1989: Métamorphisme et géochimie des roches mafiques des Alpes ouest-centrales (géoprofil Viège- Domodossola- Locarno). *Mémoires de Géologie* **4**, Imprivite S. A. Lausanne Geneve.
- De Capitani, C. & Brown, T. H. 1987: The computation of chemical equilibrium in complex systems containing non-ideal solutions. *Geochimica et Cosmochimica Acta*, **51**, 2639-2652.
- 1994: Gleichgewichts-Phasendiagramme: Theorie und Software. *Berichte der Deutschen Mineralogischen Gesellschaft, Beihefte zum European Journal of Mineralogy*, **6**, 48.
- England, P. C. & Thompson, A. B. 1984: Pressure-temperature-time paths of regional metamorphism I. Heat transfer during the evolution of regions of thickened continental crust. *Journal of Petrology* **25**, 894-928.
- Engi, M., Scherrer, N. C. & Burri, T. 2001: Metamorphic evolution of pelitic rocks of the Monte Rosa nappe: Constrains from petrology and single grain monazite age data. *Schweizerische Mineralogische und Petrographische Mitteilungen* **81**, 305-328.
- Escher, A., Hunziker, J. C., Marthaler, M., Masson, H., Sartori, M. and Steck, A. 1997: Geologic framework and structural evolution of the western Swiss-Italien Alps. In: Pfiffner, O. A., Lehner, P., Heitzmann, P., Mueller, St., Steck, A. (eds): *Deep Structure of the Alps, Results*

- of NRP 20. Birkhäuser. Basel Boston Berlin, 205-222.
- Ferrara, G., Hirt, B., Jäger, E. & Niggli, E. 1962: Rb-Sr and U-Pb age determination on the pegmatite of I Mondei (Penninic Camughera-Moncucco complex, Italian Alps and some Gneisses from the neighborhood). *Eclogae geol. Helv.* 55, 443-450.
- Frey, M., Hunziker, J. C., Neil, J. R. & Schwander, H. W. 1976: Equilibrium-Disequilibrium Relations in the Monte Rosa Granit, Western Alps: Petrological, Rb-Sr and Stable Isotope Data. *Contrib. Mineral. Petrol.* 55, 147-179.
- Frey, M., Desmons, J. & Neubauer, F. (eds) 1999: Metamorphic maps of the Alps. Published by the editors and as enclosure to Schweizerische Mineralogische und Petrographische Mitteilungen, **79**.
- Froitzheim, N., Schmid, S. M. & Frey, M. 1996: Mesozoic paleogeography and the timing of eclogite facies metamorphism in the Alps: A working hypothesis. *Eclogae geol. Helv.* 89, 81-110.
- Fuhrman, M. L. & Lindsley, D. H. 1988: Ternary-feldspar modelling and thermometry. *American Mineralogist*, **73**, 201-215.
- Gebauer, D. 1999: Alpine geochronology of the Central and Western Alps: new constraints for a complex geodynamic evolution. *Eclogae geol. Helv.* 79, 191-208.
- Grasemann, B. & Mancktelow, N. S. 1983: Two-dimensional thermal modelling of normal faulting: The Simplon fault zone, central Alps, Switzerland. *Tectonophysics*, 225, 155-165.
- & Stüwe, K. 2001: The development of flanking folds during simple shear and their use as kinematic indicators. *J. Struct. Geol.* 23, 715-724.
- Hess, M. 2003: Strukturgeologie und Spaltspurdatierungen an Apatit und Zirkon an der Simplonlinie im Gebiet um Domodossola (I). Unpublished diploma thesis, University of Basel.
- Hunziker, J. C., Desmons, J. & Hurford, A. J. 1992: Thirty-two years of geochronological work in the Central and Western Alps: a review on seven maps. *Mémoires de Géologie* 13, Imprive S. A., Lausanne Geneve.
- Hunziker, P. 2003: The stability of tri-octahedral Fe<sup>2+</sup>-Mg-Al chlorite. A combined experimental and theoretical study. Ph. D., University of Basel, 162pp.
- Hurford, A. J., Flisch, M. & Jäger, E. 1989: Unravelling the thermo-tectonic evolution of the Alps: a contribution from fission track analysis and mica dating. In: Coward, D., Dietrich, D., Park, R. F. (eds): *Alpine tectonics*. *Geol. Soc. Spec. Publ.* 369-398.
- Jaboyedoff, M., Béglé, P. & Lobrinus, S. 1996: Stratigraphic et évolution structurale de la zone de Furgg, au Front de la nappe du Monte Rosa. *Bull. Soc. Vaud. Sc Nat.* 84.2, 191-210.
- Keller, L. M. & Schmid, S. M. 2001: On the kinematics of shearing near the top of the Monte Rosa nappe and the nature of the Furgg zone in Val Loranco (Antrona Valley, N. Italy): tectonometamorphic and paleogeographic consequences. *Schweiz. Mineral. Petrogr. Mitt.* 80, 347-367.

- , Abart, R., Stünitz, H. & De Capitani, C. 2004: Deformation, mass transfer and mineral reactions in an eclogite facies shear zone in a polymetamorphic metapelite (Monte Rosa nappe, Western Alps). *Journal of Metamorphic Geology*, 22, 97-118.
- , Abart, R., Schmid, S. M. & De Capitani, C. subm.: The phengite-paragonite solvus II: Influence of solid solution (phengite-paragonite) on the phase relations in metapelites during decompression (Monte Rosa nappe and Camughera-Moncucco unit, Western Alps). *Journal of Petrology* (subm.)
- , De Capitani, C. & Abart, R. subm.: The phengite-paragonite solvus I: A quaternary solution model for white micas based on natural coexisting phengite-paragonite pairs. *Journal of Petrology* (subm.)
- Kramer, J. 2002: Structural evolution of the Penninic units in the Monet Rosa region (Swiss and Italian Alps). Ph. D., University of Basel
- , J., Abart, R., Müntener, O., Schmid, S. M. & Stern, W. 2003: Geochemistry of metabasalts from ophiolitic and adjacent distal continental margin units: Evidence from the Monet Rosa region (Swiss and Italian Alps). *Schweiz. Mineral. Petrogr. Mitt.* 83, 217-240.
- Klein, J. A. 1978: Post-nappe folding southeast of the Mischabel Rückfalte (Pennine Alps) and some aspects of the associated metamorphism. *Leidse Geol. Meded.* 51, 233-312.
- Lacassin, R. 1987: Kinematics of the ductile shearing from outcrop to crustal scale in the Monte Rosa nappe, Western Alps. *Tectonics* 6, 69-88.
- Laduron, D. 1976: L'antiforme de Vanzone. Etude pétrologique et structurale dans la vallée Anzasca (Province de Novara, Italie). *Mém. Inst. Géol. Univ. Louvain* 28, 1-121.
- Mancktelow, N. S. 1990: The Simplon fault zone. *Beitr. Geol. Karte der Schweiz*, NF 163.
- 1992: Neogene lateral extension during convergence in the Central Alps: Evidence from interrelated faulting and backfolding around the Simplonpass (Switzerland). *Tectonophysics* 215, 295-317.
- Markley, M. J., Teyssier, C., Cosca, M. A., Caby, R., Hunziker, J. C. and Sartori, M. (1998): Alpine deformation and  $^{40}\text{Ar}/^{39}\text{Ar}$  geochronology of synkinematic white mica in the Siviez-Mischabel nappe, Western Pennine Alps, Switzerland. *Tectonics* 17, 407-425.
- Merle, O., Cobbold, P. R. & Schmid, S. M. 1989: Tertiary kinematics in the Lepontine dome. In: *Alpine Tectonics* (Ed. by Coward, M. P., Dietrich, D. & Park, R. G.) Geological Society Special Publication. 45, 113-134.
- Merlyn, M. 1977: Structure et métamorphisme du complexe Camughera-Moncucco entre la Vallée Anzasca et le Val Brevettola (Province de Novara, Italie). PhD thesis, Université catholique de Louvain.
- Milnes, A. G., Greller & M., Müller, R. 1981: Sequenz and style of major post-nappe structures, Simplon- Pennine Alps. *J. Struct. Geol.* 3, 411-420.
- Müller, R. 1983: Die Struktur der Mischabelfalte (Penninische Alpen) *Eclogae geol. Helv.* 79, 391-416.
- Nagel, T., De Capitani, C. & Frey, M. 2002: Isogrades and *P-T* evolution in the Southeastern Lepontine Dome (Graubünden, Switzerland). *Journal of Metamorphic Geology*, 20, 309-

324.

- Niggli, E. 1970: Alpine Metamorphose und alpine Gebirgsbildung. Fortschritt in Mineralogie **47**, 16-26.
- Novarese, A. & Stella, A. 1913: Carta Geologica d'Italia (Domodossola). Istituto Geografico De Agostini.
- Pettke, T., Diamond, L. W. & Villa, I. M. 1999: Mesothermal gold veins and metamorphic devolatilization in the northwestern Alps: The thermal link. *Geology* **27**, 641-644.
- Pfeifer, H. R., Colombi, A. & Ganguin, J. 1989: Zermatt-Saas and Antrona zone: A petrographic and geochemical comparison of polyphase metamorphic ophiolites of the West-Central Alps Schweiz. Mineral. Petrogr. Mitt. **69**, 217-236.
- Ramsay, J. G. & Huber, M.I. 1987: The Techniques of Modern Structural Geology, Vol.2. Academic Press 475-504.
- Reddy, S. M., Wheeler, J. & Cliff, R. A. 1999: The geometry and timing of orogenic extension: an example from the Western Alps. *Journal of Metamorphic Geology* **17**, 573-589.
- Regenauer-Lieb, K. 1996: Plactic velocity vector diagrams applied to indentation and transpression in the Alps. *Journal of Geodynamics* **21**, 339-353.
- Reinhardt, B. 1966: Geologie und Petrographie der Monte Rosa Zone, der Sesia Zone und des Canavese im Gebiet zwischen Valle d'Ossola und Valle Loana. Schweizerische Mineralogische und Petrographische Mitteilungen, **46**, 553-678.
- Romer, R. L., Schärer, U. & Steck, A. 1996: Alpine and pre-Alpine magmatism in the root-zone of the western Alps. *Contrib to Mineral Petrol* **123**, 138-158.
- Rubatto, D., Gebauer, D. & Compagnoni, R. 1997: Dating the UHP/HP metamorphism in the western Alps (Sesia-Lanzo and Zermatt-Saas-Fee): Evidence for subductions events at the Cretaceous-Tertiary boundary in the Middle Eocene. Fifth Internat. Eclogite Conf. Ascona supplement No1 to TERRA nova **9**, 30-31.
- Schärer, U., Cosca, M., Steck, A. & Hunziker, J. 1996: Termination of major ductile strike-slip shear and differential cooling along the Insubric line (Central Alps): U-Pb, Rb-Sr and  $^{40}\text{Ar}/^{39}\text{Ar}$  ages of cross-cutting pegmatites. *Earth and Planetary Sciences letters* **141**, 331-351.
- Schmid, S. M. & Kissling, E. 2000: The arc of the western Alps in the light of geophysical data on deep crustal structure. *Tectonics* **19**, 62-85.
- Simpson, C. & Schmid, S. M. 1983: An evaluation of criteria to deduce the sense of movement in sheared rocks. *Geol. Soc. Am. Bull.* **94**, 1281-1288.
- Soom, M. A. 1990: Abkühlungs- und Hebungsgeschichte der Externmassive und der penninischen Decken beidseits der Simplon-Rhone-Linie seit dem Oligozän: Spaltspurdaterungen an Apatit/Zirkon und K-Ar Datierungen and Biotit/Muskowit (westliche Zentralalpen). PhD thesis, University of Bern, 64pp.
- Spicher, A. 1976: Tektonische Karte der Schweiz 1: 500'000. Schweizerische geologische

Kommission.

- Steck, A. 1984: Structures de déformation tertiaires dans les Alpes centrales. *Eclogae geol. Helv.* 77, 55-100.
- Steck, A. 1987: Le massif du Simplon-Réflexions sur la Cinématique des nappes de gneiss. *Schweiz. Mineral. Petrogr. Mitt.* 67, 27-45.
- Steck, A. 1990: Une carte des zones de cisaillement ductile dans les Alpes Centrales. *Eclogae geol. Helv.* 83, 603-626.
- Steck, A. & Hunziker, J. C. 1994: The Tertiary structural and thermal evolution of the Central Alps-Compressional and extensional structures in an orogenic belt. *Tectonophysics* 238, 229-254.
- Steck, A., Bigioggero, B., Dal Piaz, G. V., Escher, A., Marchant, R., Martinotti, G. & Payot, S. 1999: Carte tectonique des Alpes de Suisse occidentale (1:100'000) Feuille 47 Monte Rosa. Service hydrologique national.
- Stipp, M., Stünitz, H., Heilbronner, R. & Schmid, S. M. 2002: The eastern Tonale fault zone: 'natural laboratory' for crystal plastic deformation in quartz over a temperature range from 250 to 700°C. *J. Struct. Geol.* 24, 1861-1884.
- Tapponier, P. 1977: Evolution tectonique du système alpin en Méditerranée: poinçonnement et écrasement rigid-plastique. *Bull. Soc. geol. France* XIX, n° 3, 437-460.
- Tapponier, P., Peltzer, G., Le Dain, A. Y., Armijo, R. & Cobbold, P. 1982: Propagation extrusion tectonics in Asia: New insights from simple experiments with plasticine. *Geology* 10, 611-616.
- Thompson, A. B. & England, P. C. 1984: Pressure-temperature-time paths of regional metamorphism II. Their inference and interpretation using mineral assemblages in metamorphic rocks. *Journal of Petrology* 25, 929-955.
- Wagner, G. A., Reimer, G. M. & Jäger, E. 1977: Cooling ages derived by apatite fission-track mica Rb-Sr and K-Ag dating: The uplift and cooling history of the Central Alps. *Mem. Ist. Geol. Mineral. Univ. Padova* 30, 1-28.
- Wetzel, R. 1972: Zur Petrographie und Mineralogie der Furggzone (Monte Rosa Decke). *Schweiz. Mineral. Petrogr. Mitt.* 52, 161-236.
- Wieland, H. 1966: Zur Geologie und Petrographie der Valle Isorno (Novara, Italia). *Schweiz. Mineral. Petrogr. Mitt.* 46, 189-303.



#### 4.18 APPENDIX

##### **Thermodynamic calculations**

Equilibrium phase diagrams were calculated for specified bulk rock compositions in the system KNCFMASH. Calculations were made with the DOMINO software (De Capitani & Brown, 1987; De Capitani, 1994). Most thermodynamic data were taken from Berman (1988, update 92); staurolite and chloritoid data are from Nagel *et al.*, (2002), while garnet uses the solution model of Berman (1990). For the biotite binary (Phl, Ann) ideal mixing on three mixing sites, and for chlorite the solution model of Hunziker (2003). For feldspar we used the solution model of Fuhrman & Lindsley (1988), for staurolite the solution model of Nagel *et al.*, (2002). For muscovite/paragonite the solution model of Keller *et al.* (subm.), and for chloritoid the binary ideal mixing on one mixing site were used.

Table 1  
Zircon (Z) and apatite (A) fission track ages

Samples	Altitude [m]	N	N <sub>s</sub>	N <sub>i</sub>	ρ <sub>s</sub> [10 <sup>4</sup> cm <sup>-2</sup> ]	ρ <sub>i</sub> [10 <sup>4</sup> cm <sup>-2</sup> ]	ρ <sub>d</sub> [10 <sup>4</sup> cm <sup>-2</sup> ]	N <sub>d</sub>	P (χ <sup>2</sup> )[%]	Age ± 2σ [Ma]
MH11/00 A	450	30	26	1516	16.20	946.9	799	7700	99.43	2.4 ± 1.0
MH11/00 Z	450	12	404	1611	1561	6224.8	379	2679	33.66	5.4 ± 1.4
MH12/00 A	400	10	36	1368	131	4978.8	849	7700	89.07	3.9 ± 1.4
MH12/00 Z	400	4	97	285	2623.6	7708.5	325	2679	77.32	6.4 ± 2.0
MH13/00 A	350	25	19	797	17.5	733.4	999	4000	98.05	4.2 ± 2.0
MH13/00 Z	350	16	316	823	1490.8	3882.6	396	2679	38.99	8.7 ± 2.2
MH14/00 A	350	11	16	515	19	611.1	843	4000	98.28	4.6 ± 2.4
MH14/00 Z	350	20	2136	4487	3985.5	8372.2	355	2679	4.65	9.6 ± 2.2
MH15/00 A	520	25	6	450	5.4	401.6	947	4000	95.37	2.2 ± 1.8
MH15/00 Z	520	6	110	393	2125.2	7592.6	396	2679	45.58	6.4 ± 2.0
MH16/00 A	420	13	29	1225	41.3	1746.3	1101	7700	99.17	4.6 ± 1.8
MH16/00 Z	420	13	424	1401	1703.2	5627.8	313	2679	22.91	5.5 ± 1.4
MH17/00 A	400	18	30	1163	29.8	1155	1151	7700	100.0	5.2 ± 2.0
MH17/00 Z	400	14	440	1320	1656.7	4970.2	373	2679	97.59	7.1 ± 1.8
MH20/00 A	300	15	32	1225	46	1761.7	1103	4000	99.74	5.0 ± 1.8
MH21/00 A	300	30	43	1667	27.9	1082.7	1156	4000	97.82	5.2 ± 1.6
MH21/00 Z	300	7	268	533	2376.6	4726.7	302	2679	94.42	8.7 ± 2.2
MH22/00 A	350	16	74	2799	101.5	3838.8	1208	4000	100.0	5.6 ± 1.4
MH22/00 Z	350	11	331	624	2174.8	4099.8	384	2679	25.29	11.3 ± 3.0
MH23/00 A	300	28	70	2787	42.7	1698.4	1312	4000	97.85	5.8 ± 1.4
MH23/00 Z	300	20	1969	3190	4044.8	6553	337	2679	47.0	12.0 ± 2.6
MH24/00 A	300	18	47	1947	49.8	2062.4	1364	4000	99.70	5.7 ± 1.8
MH24/00 Z	300	20	1031	3027	2776.9	8152.9	361	2679	4.42	7.1 ± 1.6
MH25/00 A	400	15	41	1914	59.4	2770.9	1416	4000	99.01	5.3 ± 1.6
MH25/00 Z	400	14	595	1586	2165	5770.9	380	2679	16.27	8.0 ± 2.0
MH26/00 A	300	16	39	2000	58.1	2981.5	1468	4000	97.92	5.0 ± 1.6
MH26/00 Z	300	10	350	870	2840	7059.4	331	2679	90.41	7.7 ± 1.8
MH27/00 A	400	38	30	1813	11.1	668.4	1520	4000	99.97	4.4 ± 1.6
MH27/00 Z	400	10	331	835	1950.8	4921.2	367	2679	87.42	8.4 ± 2.0

N=Abundance of dated crystals, N<sub>i</sub>= Abundance of induced fission tracks, ρ<sub>s</sub>=Density of spontaneous fission tracks in the sample, ρ<sub>i</sub>=Density of induced fission tracks in the detector, ρ<sub>d</sub>=Density of fission tracks in the dosimeter, N<sub>d</sub>= Abundance of induced fission tracks in the dosimeter, P (χ<sup>2</sup>)= χ<sup>2</sup>-value in %

## 5. OVERALL CONCLUSIONS

### 5.1 CONCLUSIONS CONCERNING THE HISTORY OF DEFORMATION AND METAMORPHISM

#### 5.1.1 D1/D2 Deformation

Composite D1/D2 deformation and related top-N or top-NW thrusting started at high-pressure conditions (c. 12.5-16 kbar) and under relatively high temperatures (c. 600-650°C) in the nappe pile of the upper Penninic-Alps southwest of the Simplon line .

Published radiometric data for the Eocene high-pressure stage suggest that top-SE shearing within the structural top of the high-pressure units is coeval with top-N or top-NW thrusting at their base. This kinematic situation suggests differential ascent of the high-pressure units relative to the surrounding units during nappe stacking and associated crustal shortening. Thus, early stages of exhumation related to D1/D2 deformation occur by extrusion within the subduction channel rather than by crustal extension.

#### 5.1.2 D3 Deformation

In the higher structural levels of the nappe pile of the upper Penninic-Alps D3 backfolding and/or backthrusting started in late Eocene times and under greenschist facies conditions. Towards deeper structural levels D3 deformation progressively becomes younger. This is due to the fact that higher temperatures prevailed longer in the east, hence the brittle-viscous transition in the area covered by the Ossola valley is of younger age than at higher structural levels in the west. Consequently, the main foliation in the Ossola valley is a composite foliation formed during the first three deformation phases (D1-D3) and

is affected by high-temperature metamorphism. Barrovian P-T conditions at deeper structural levels are attained due to an extensional unroofing component during D3 deformation. This delays cooling during decompression and thus causes approximately isothermal decompression. D3 deformation ceased in late Oligocene time.

#### 5.1.3 D4 Deformation

An open fold pair consisting of Masera synform and Brevettola antiform represents the eastern continuation of the major Vanzone antiform. Structural arguments, as well as radiometric data, suggest that the activity of normal faulting along the Simplon line overlaps the time of the formation of the major D4 backfolds, such as the major Vanzone and Brevettola antiforms.

As the Simplon normal fault dies out towards the east, the Masera synform nucleates and amplifies towards the same direction. As hypothesised by Milnes et al. (1981), displacement along the Simplon normal fault is additionally transformed into the southern limb of Vanzone and Brevettola antiforms, where D4 folding is also associated with dextral shearing. This second phase of backfolding and associated dextral shearing must have terminated before about 12 Ma ago.

### 5.2 CONCLUSIONS REGARDING DEFORMATION, MASS TRANSFER AND MINERAL REACTIONS IN A D1/D2 SHEAR ZONE

In a D1 shear zone situated in the Monte Rosa nappe metapelites, the pre-Alpine assemblage plagioclase + biotite + kyanite is replaced by the assemblage garnet + phengite + paragonite. This represents the first stage Alpine mineral assemblage stable in the S1 foliation also in the metapelites of the MC unit metapelites. At least

---

in the case of the above mentioned shear zone it could be demonstrated that the reaction progress in the metapelites is intimately linked to shearing deformation and restricted to deformed parts of the rock. Shear zone formation facilitated the influx of aqueous fluids into the rock and was the prerequisite for the progress of substantial metamorphic reactions. Gain of silica and loss of Al and K during shear zone formation are indicated by consistent results of two different methods of mass transfer calculations, demonstrating the interplay between mass transfer and net-transfer mineral reactions. Assuming that the marginal parts of the shear zone record earlier parts of the deformation history than the more central parts, the observed mass transfer and modal changes largely occurred during early stages of progressive deformation. The combined infiltration of Si and net transfer mineral reactions cannot account for the observed modal increase of quartz. The Si needed to account for the observed change in modal quartz was largely derived from the dissolution of plagioclase, kyanite and biotite, which released Si, Al and K into the fluid. The Si was immediately re-precipitated within the shear zone, but Al and K remained in the solution and were removed via the pore fluid. Petrological and microstructural data, together with the phase equilibrium diagrams, suggest that the scales over which chemical equilibrium was attained differed between the low- and high-strain domains. Chemical equilibrium was only attained on a sub-grain scale in the low-strain domains, where the Alpine metamorphic overprint occurred at water activities of  $\leq 0.5$ . Bulk equilibration was attained on a hand specimen scale within the shear zone, where the metamorphic transformation occurred under  $H_2O$  saturated conditions.

### **5.3 THE EASTWARDS CONTINUATION OF THE MONCUCCO-CAMUGHERA UNIT**

Structurally positioned in the northern limb of the D4 Masera synform, and dipping towards the SE, the Antrona unit strikes in direction of the mouth of the Bognanco valley. Across the Ossola valley numerous aligned lenses of ophiolitic rocks (amphibolites, ultrabasic rocks and gabbros) can be found in the southern slope of the Isorno valley (see also Wieland, 1966). There they occupy a structural position that is very similar, if not identical, with that of the easternmost occurrences of the Antrona unit in the Bognanco valley. In the Isorno valley staurolite bearing garnet-mica schists have frequently been observed (see also Bearth, 1956). Such staurolite bearing garnet-mica schists are typical rocks in the western parts of CM unit (i. e. west of the Ossola valley). Thus, it is concluded that the rocks of the Antrona unit and the northern rim of the CM unit find their eastern continuation in the southern slope of the Isorno valley and not in the Vigizzo valley, as it for example proposed by the new tectonic map of the Western Alps (Steck et al., 1999). Following Bearth (1956) it is suggested that at least parts of the Pioda di Crana zone “north of the Vigizzo valley” represent the eastern equivalent of the MC unit west of the Ossola valley.

### **5.4 CONCLUSIONS REGARDING THE REGIONAL METAMORPHISM IN GENERAL**

The mineral zones in the study area are characterized by Chl+Bt+Pl through St and Sil zones, indicating a metamorphic field gradient whereby temperatures increases towards the east during decompression. The observed mineral assemblages are compatible with almost isothermal decompression. A heating pulse during

later stages of the metamorphic history is not necessary nor is it indicated. Staurolite grows within a large P-interval during the continuous decomposition of paragonite and phengite, while the growth of staurolite is sensitive to bulk rock composition. This conclusion holds at least for the gneissic units of the upper Penninic-Alps situated southwest of the Simplon line,

### **5.5 CONCLUSIONS REGARDING A NEW SOLUTION MODEL FOR WHITE MICAS**

The solution model for white mica, which is used for calculating equilibrium diagrams, end-member isopleths of phengite and mineral abundance isopleths gives very reasonable results seeing that the calculations coincide with the observations in natural pelitic samples. It turns out that the solution model is an important link in modelling multicomponent equilibrium diagrams for pelitic rocks as it makes the processes understandable, which are related to the decomposition of paragonite and phengite during decompression of pelitic rocks originating from high-pressure areas.



# Curriculum vitae

## AUSBILDUNG

- 1983 – 1987 **Berufsschule für Heizungszeichner in Zürich**
- 1992 – 1995 **Zweitwegmatura, Typus C in Frauenfeld**
- 10/1995 – 03/2000 **Studium der Erdwissenschaften an der Universität Basel**  
Diplomarbeit: Geologie im Grenzbereich zwischen der Monte Rosa Decke und der Furggzone (West Alpen).
- 04/2001 - 04/2004 **Dissertation an der Universität Basel**  
Thema: Tectonometamorphic evolution of the Antrona-Camughera-Moncucco units (Western Alps).  
Betreuer: Prof. S. Schmid, Basel  
Prof. R. Abart, Basel  
Prof. Ch. De Capitani, Basel  
PD Dr. H. Stünitz

## BERUF, PRAXIS UND AUSLAND

- 1983 – 1987 **Heizungszeichner:** Ausbildung bei Fa. Gründler AG, Schaffhausen
- 1988 – 1994 **Heizungszeichner:** Fa. E+H Ingenieurbüro, Schaffhausen
- 04/2000 – 06/2000 **Assistent:** ETH-Zürich
- 07/2000 – 10/2000 **Freier Mitarbeiter:** Kantonsgeologie, Basel-Stadt
- 11/2000 – 12/2000 **Feldarbeit:** in Panama/Mittelamerika für ein biologisches Projekt der Universität Ulm
- 01/2001 – 02/2001 **Feldarbeit:** in Chile (Südamerika) für ein geologisches Projekt der Universität Basel
- 08/2003 - 02/2004 **Mittelschullehrer (Geographie):** an der thurgauisch-schaffhauserischen Maturitätsschule für Erwachsene